Galaxy Evolution in the Local and the High-z Universe Through Optical+near-IR Spectroscopy

by

Bhavin Joshi

A Dissertation Presented in Partial Fulfillment
of the Requirements for the Degree
Doctor of Philosophy

Approved August 2020 by the
Graduate Supervisory Committee:

Rogier Windhorst, Chair
Rolf Jansen
Philip Appleton
Sanchayeeta Borthakur
Evan Scannapieco

ARIZONA STATE UNIVERSITY

August 2020

ABSTRACT

A key open problem within galaxy evolution is to understand the evolution of galaxies towards quiescence. This work investigates the suppression of star-formation through shocks and turbulence at low-redshift, and at higher-redshifts, this work investigates the use of features within quiescent galaxy spectra to redshift estimation, and passive evolution of aging stellar populations to understand their star-formation histories. At low-z, this work focuses on the analysis of optical integral field spectroscopy data of a nearby ($z \sim 0.0145$) unusual merging system, called the Taffy system because of radio emission that stretches between the two galaxies. This system, although a recent major-merger of gas-rich spirals, exhibits an atypically low star-formation rate and infrared luminosity. Strong evidence of shock heating as a mechanism for these atypical properties is presented. This result (in conjunction with many others) from the nearby Universe provides evidence for shocks and turbulence, perhaps due to mergers, as an effective feedback mechanism for the suppression of star-formation. At intermediate and higher-z, this work focuses on the analysis of Hubble Space Telescope (HST) Advanced Camera for Surveys (ACS) G800L grism spectroscopy and photometry of galaxies with a discernible 4000Å break. The usefulness of 4000Å/Balmer breaks as redshift indicators by comparing photometric, grism, and spectrophotometric redshifts (SPZs) to ground-based spectroscopic redshifts, is quantified. A spectral energy distribution (SED) fitting pipeline that is optimized for combined HST grism and photometric data, developed for this project, is presented. This pipeline is a template-fitting based routine which accounts for correlated data between neighboring points within grism spectra via the covariance matrix formalism, and also accounts for galaxy morphology along the dispersion direction. Evidence is provided showing that SPZs typically improve the accuracy of photometric redshifts

by ∼17–60%. For future space-based observatories like the Nancy Grace Roman Space Telescope (formerly the Wide Field InfraRed Survey Telescope, i.e., WFIRST) and Euclid, this work predicts ∼700–4400 galaxies degree^{-2}, within $1.6 \lesssim z \lesssim 3.4$, for galaxies with 4000Å breaks and continuum-based redshifts accurate to $\lesssim$2%. This work also investigates the star-formation histories of massive galaxies ($M_s \geq 10^{10.5}\,M_\odot$). This is done through the analysis of the strength of the Magnesium absorption feature, Mgb, at ∼5175Å. This analysis is carried out on stacks of HST ACS G800L grism data, stacked for galaxies binned on a color vs stellar mass plane.

DEDICATION

To my Parents,

to my Nana and Nani,

and

to my Wife.

ACKNOWLEDGMENTS

This dissertation would not have been possible without the support and guidance of many people who have helped me over the last six and a half years. Firstly, I would like to thank my advisor, Rogier Windhorst, who supported my admission to the PhD program, and has been a source of constant advice on pretty much every aspect of astronomy. Rogier – I would definitely not have gotten through graduate school, or be any good at astronomy, without your mentorship. I really appreciate your understanding and perspective on all things science. To the rest of my committee, Rolf Jansen, Evan Scannapieco, Sanchayeeta Borthakur, and Philip Appleton – your advice and constructive criticism have been invaluable in helping me become a better scientist. I'm very grateful for all that you have taught me and for the significant amount of time and energy that you've invested into me.

A special thanks to Seth Cohen who has had to put up with me and my questions all throughout grad school. Seth – I'm very grateful for your opinion and your patience to work with me through the little details. I will miss our chats in the office (I'm already missing them... as I write this from my couch under Covid-19 restrictions). Also, thanks for (re)introducing me to my love for cycling, and for the introduction to baseball cages!

I would also like to thank my former committee members Phil Mauskopf, Sangeeta Malhotra, and James Rhoads for their advice during the first few years of graduate school and for helpful discussions on some of the work I did for my dissertation. I'm also grateful to the SESE community, particularly Becca Dial and Chris Groppi, and the ISSC at ASU who've worked behind the scenes to ensure that my graduate career went smoothly. I'm also grateful to ASU GPSA for travel funding opportunities to attend AAS meetings. I'd also like to thank Russell Ryan and Nor Pirzkal at the Space

Telescope Science Institute (STScI) for hosting me at the STScI and for teaching me most of what I know on how to reduce grism spectra.

I would also like to thank the Visiting Graduate Fellowship Program, and Philip Appleton in particular, at IPAC/Caltech for allowing me the opportunity to spend 6 months at IPAC. I learned a lot during those 6 months, and that was some of the most productive time of my graduate career. Phil – I couldn't have asked for a better mentor during my time at IPAC and since. Thank you for all you've done to help my career and for your kindness and welcoming demeanor toward me at IPAC.

I would also like to acknowledge my friends from the lab – Duho Kim, Teresa Ashcraft, Kim Emig, and Brent Smith – who've immensely enriched my time in grad school both professionally and personally. I would also like to thank my roommates at Chez Stanko for their friendship and support. To my friends from my time in Pittsburgh (who are too many to mention by name here) when I had only just started on the journey to becoming an astronomer – you helped me stay sane through many highs and lows, and were a family away from my actual family. I'm grateful for all of you, old friends and new.

I must also acknowledge my family, especially my parents and my grandparents, who never stopped me from questioning everything and have always provided me with their unconditional love and support in all my endeavors. I'd especially like to thank my Nana who taught me about the night sky from a very young age.

Finally, I would also like to acknowledge Research Computing at Arizona State University for providing high performance computing resources that have contributed to the research results reported within this dissertation. I'd also like to thank Jason Yalim in particular, who worked through many of the computational aspects of my code with me and got me going on Agave.

TABLE OF CONTENTS

Page

LIST OF TABLES ix

LIST OF FIGURES x

CHAPTER

1 INTRODUCTION 1

1.1 Feedback Mechanisms and Pathways to Quiescence 2

1.2 A Brief Introduction to Integral Field and Slitless Spectroscopy ... 3

2 EVIDENCE FOR SHOCK-HEATED GAS IN THE TAFFY GALAXIES AND BRIDGE FROM OPTICAL EMISSION-LINE IFU SPECTROSCOPY 6

2.1 Introduction 6

2.2 Observations, Data Reduction, and Analysis Methods 10

2.2.1 Flux Calibration and Cube Building 11

2.2.2 Spectral Mapping, Continuum and Emission-Line Fitting ... 12

2.3 Results 16

2.3.1 Emission-Line Gas and Hβ Absorption Within the System .. 16

2.3.2 Dust Extinction From the Balmer Decrement 21

2.4 The Kinematics of the Taffy System 22

2.4.1 Hα Channel Maps 23

2.4.2 Mapping Two-Component Line Profiles in the System 25

2.5 Excitation of the Ionized Gas in the Taffy System 31

2.5.1 Evidence for Shocked Gas in the Taffy System 37

2.5.2 Alternatives to Shock Excitation: Diffuse Lyman Continuum Emission Leaking From HII Regions? 40

CHAPTER Page

2.6 Ionized Gas Fractions, Star formation Rates and Mass in the Ionized Component 44

2.6.1 Star Formation Rate Estimate From Hα Luminosity 45

2.6.2 Ionized Gas Mass 46

2.6.3 Post-Starburst Populations 47

2.7 Conclusions 50

3 SPECTROPHOTOMETRIC REDSHIFTS FOR Z $\sim$ 1 GALAXIES AND PREDICTIONS FOR NUMBER DENSITIES WITH WFIRST AND EUCLID 53

3.1 Introduction 53

3.2 Observations 57

3.3 4000Å Break Measurement and Sample Selection 59

3.3.1 D4000 Measurement 59

3.3.2 Sample Selection 60

3.4 SED Fitting Procedure 62

3.4.1 Template Library 62

3.4.2 Fitting and Error Estimation 65

3.5 The Dependence of Redshift Accuracy on D4000 72

3.6 Estimates of Object Number Densities for Future Surveys 74

3.7 Conclusion 80

4 CONSTRAINING AGN FEEDBACK THROUGH THE THERMAL SUNYAEV-ZEL'DOVICH EFFECT WITHIN STACKED CMB DATA 105

4.1 Background 105

4.2 Stacking Method and Final Result 109

CHAPTER Page

5 STAR-FORMATION HISTORIES OF MASSIVE GALAXIES AT INTERMEDIATE REDSHIFTS 111

5.1 Introduction 111

5.1.1 Cosmic Downsizing and α-Element Enhancement in Massive Galaxies 112

5.2 Data and Sample Selection 114

5.2.1 Stellar Mass Completeness 116

5.2.2 Sample Selection 116

5.3 Stacking Method 117

5.4 Discussion and Results 117

6 CONCLUSION 121

REFERENCES 124

APPENDIX

A ERRORS ON THE D4000 MEASUREMENT 145

B NET SPECTRAL SIGNIFICANCE 147

C COVARIANCE MATRIX ESTIMATION 149

LIST OF TABLES

Table Page

1. Extinction Corrected Fluxes 21

2. LZIFU Parameters 23

3. SPZ Sample Selection 61

4. Redshift Statistics 71

5. SPZ Catalog 83

LIST OF FIGURES

Figure Page

1. Cosmic Star-Formation Rate over Time 2
2. LZIFU Fitting Deep Hβ 13
3. LZIFU Fitting Multiple Components 14
4. Example VIRUS-P Spectra 18
5. Hα Map and Hβ EW 19
6. Dust Extinction 20
7. Velocity Channel Map 26
8. Moment 0, 1, 2 Contour Maps 32
9. Bridge Structure 33
10. Fitting Deep Absorption to Get Accurate Line Fluxes 34
11. Line Diagnostic Diagram: $[NII]$ 41
12. Line Diagnostic Diagram: $[OI]$ 42
13. Line Diagnostic Diagram: $[SII]$ 43
14. Comparing Shock Only to Shock+precursor 49
15. PEARS Coverage on Sky 57
16. D4000 Histogram 63
17. Example SED Fits 67
18. Comparison of Photo-z, Grism-z, and SPZ with Spectroscopic Redshifts for Low D4000 69
19. Comparison of Photo-z, Grism-z, and SPZ with Spectroscopic Redshifts for High D4000 70
20. D4000 and D4000 Significance Dependence on Redshift 75
21. D4000 Significance vs D4000 77

Figure Page

22. D4000 Significance vs i-Band Magnitude 78
23. CMB Temperature Power Spectrum 107
24. The Sunyaev-Zel'dovich Effect 108
25. PEARS vs 3D-HST Mass Comparison 113
26. Stellar Mass Completeness 114
27. $(U - R)$ vs M_s Diagram 115
28. Massive Galaxies Stack 118
29. Fit Result 119

Chapter 1

INTRODUCTION

Over the previous two decades, one crucial observation to emerge is the decline of overall star-formation activity in the universe over the last ∼10 billion years (i.e., since $z \sim 2$, see for example the review by Madau and Dickinson 2014). This key finding, along with our growing understanding of how star-formation in galaxies is extinguished (termed quenching or quiescence), has driven much recent astronomical research. Figure 1 shows the cosmic star-formation rate over time. It can be clearly observed that the average star-formation rate in the universe rose sharply after the Big-Bang, peaking at $z \sim 2$, and has been decreasing ever since. The work presented in this dissertation attempts to build on this collective understanding by (a) addressing how major mergers can inhibit star-formation activity, (b) investigating the different evolutionary pathways that can be taken to quiescence, and (c) investigating how feedback from active galactic nuclei (AGN) has affected the surroundings of quiescent galaxies.

This dissertation is based on ground-based integral field spectroscopy data from the McDonald Observatory (Joshi, Appleton, et al. 2019), and slitless spectroscopy from the Advanced Camera for Surveys (ACS) and the Wide Field Camera 3 (WFC3) on the Hubble Space Telescope (HST; Joshi, Cohen, et al. 2019).

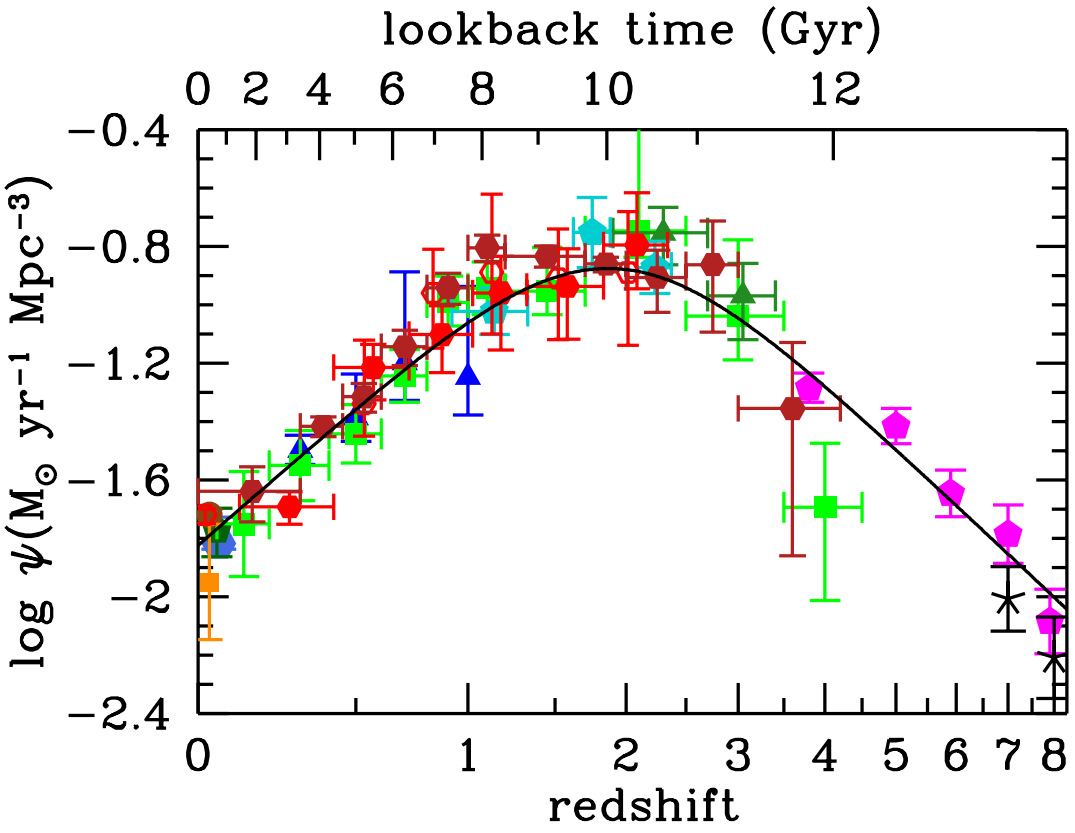

Figure 1. From Madau and Dickinson 2014, showing the volume-averaged cosmic star-formation rate over most of cosmic history from FUV+IR measurements. The many different colored points are from a compilation of studies shown in their Table 1.

1.1 Feedback Mechanisms and Pathways to Quiescence

Galaxies can have their star-formation suppressed due to many effects, generally called feedback mechanisms, either due to internal or environmental factors. Feedback suppresses star-formation by ejecting and/or by heating up cooler atomic and molecular gas rendering it unavailable for star-formation within a galaxy, or by preventing the inflow of cold gas into the galaxy. Internal feedback mechanisms generally comprise of winds due to stellar feedback (i.e., supernovae explosions and stellar winds, see, e.g., Dekel and Silk 1986; Heckman, Armus, and Miley 1990; Mac Low and Ferrara

1999; Heckman et al. 2000; Veilleux, Cecil, and Bland-Hawthorn 2005; Muratov et al. 2015), and winds (or jets) due to AGN feedback (e.g., Silk and Rees 1998; Croton et al. 2006; Schawinski et al. 2007; Fabian 2012; Harrison 2017, also see chapter 4 in this dissertation); although positive AGN feedback, an enhancement in star-formation, is also possible. External feedback mechanisms typically involve interactions between galaxies (e.g., such as major or minor mergers suppressing star-formation on short timescales, Robotham et al. 2014; Joshi, Appleton, et al. 2019, also see chapter 2 in this dissertation), or between a galaxy and the medium surrounding it (e.g., strangulation or ram-pressure stripping of gas from galaxies within galaxy groups and clusters, Fujita 2004; Kawata and Mulchaey 2008; Peng, Maiolino, and Cochrane 2015).

It should also be noted that either internal or external processes can both drive shocks into the interstellar/intergalactic media of galaxies, and cause a suppression of star-formation. For example, I discuss the effects of shocks and turbulence on the Taffy system (a pair of gas-rich spirals with a recent head-on encounter) in chapter 2 where shocks are driven into the intergalactic medium between the two galaxies as a result of their recent collision. The effects of shocks in the Taffy galaxies, in particular, are especially pronounced given the counter-rotation of the two galaxies, since the counter-rotation leads to a boost in the shock velocities (see, e.g., Yeager and Struck 2020).

1.2 A Brief Introduction to Integral Field and Slitless Spectroscopy

Throughout this dissertation, I refer to integral field spectroscopy (in chapter 2) and to slitless (or grism) spectroscopy (in chapters 3 and 5). Here I provide a few sentences of introduction to both spectroscopic techniques. Integral field spectroscopy

is a spectroscopic technique used to obtain spatially resolved spectra, i.e., obtaining a spectrum associated with every location covered within the field-of-view (where the extent of each "location" is determined by the spatial resolution of the instrument). The advantage with this technique is being able to simultaneously obtain spatially resolved spectra for all sources of light within a field-of-view *without* the added difficulty of having spectral overlap (as is the case for slitless spectroscopy) (for a review, see, Allington-Smith 2006). The disadvantage with integral field spectroscopy, however, is the limited observable field-of-view (FoV). This is typically only about 2×2 square arcmin even for integral field units with the largest FoVs.

Slitless spectroscopy (also referred to as grism spectroscopy within this dissertation since slitless spectroscopy on the HST is accomplished using a grism) is also a technique that is used to obtain spatially resolved spectra (e.g., for details on HST grism spectroscopy and reduction, see, Pasquali et al. 2001, 2006). The advantages of slitless spectroscopy are similar to those of integral field spectroscopy. However spectral overlap for sources lying along the dispersion direction is an issue; also see section 3.4 in chapter 3 for a discussion on the nuances of grism data analysis. It is generally the case that ground-based integral field spectroscopy is better at providing high-resolution spectroscopy of faint emission lines within low-redshift objects (as I've done in chapter 2), whereas, space-based slitless spectroscopy is better at providing low-resolution spectroscopy of the stellar continuum and absorption features for fainter objects (as I've done in chapters 3 and 5).

The chapters in this dissertation are organized as follows: in chapter 2, I describe my work on the Taffy galaxies, which are a pair of merging (head-on) gas-rich spiral galaxies with unusually low infra-red (IR) luminosity and star-formation rates. In chapter 3, I describe my work investigating the 4000Å break, a feature that gets

stronger for aging stellar populations, as a redshift indicator within grism spectra. In chapter 4, I describe work I did investigating AGN feedback through the thermal Sunyaev-Zel'dovich (tSZ) effect. In chapter 5, I present my investigation of the star-formation histories (SFHs) and quenching timescales for massive galaxies at intermediate and high-redshifts, and I conclude with a review and summary of my future work in chapter 6.

Chapter 2

EVIDENCE FOR SHOCK-HEATED GAS IN THE TAFFY GALAXIES AND BRIDGE FROM OPTICAL EMISSION-LINE IFU SPECTROSCOPY

This chapter is reproduced from the version published in 2019 in The Astrophysical Journal, Volume 878, Page 161, with permission from the co-authors.

2.1 Introduction

It is now generally accepted that collisions and mergers between gas-rich galaxies often generate intense star-formation activity and associated strong infrared emission (e.g., Joseph and Wright 1985; Soifer et al. 1987; Soifer and Neugebauer 1991). Ultra Luminous Infrared Galaxies, ULIRGs ($L_{IR} > 10^{12}$ $L_{\odot}$) and LIRGS ($10^{12} > L_{IR}/L_{\odot} > 10^{11}$) frequently involve mergers or interactions of gas-rich galaxy pairs, with the likelihood of them being associated with a major merger increasing with infrared (IR) luminosity (Armus, Heckman, and Miley 1987; Sanders, Soifer, Elias, Madore, et al. 1988; Sanders, Soifer, Elias, Neugebauer, et al. 1988; Sanders and Mirabel 1996; Elbaz et al. 2002; Armus et al. 2009). While it is clear that major mergers play an important role in generating high IR luminosities in the local universe, their role at higher redshift is still being explored.

Shocks and turbulence potentially play a role in changing the conditions of the gas in collisional galaxies, not always leading to enhancements in star formation. In the local Hickson Compact Groups, Alatalo et al. 2015 found evidence that multiple collisions can quench or significantly suppress star formation in some systems where

turbulence and shocks are present (see also Lisenfeld et al. 2017). These galaxies had previously been found to contain large volumes of warm molecular hydrogen that emit their energy mainly in the mid-IR, and were believed to be shock-heated (Cluver et al. 2013). An extreme example is found in the Stephan's Quintet system. Here, a large filament of molecular gas is found in the intergalactic medium in which a large fraction of the gas is warm and in a shock-heated phase (Appleton et al. 2006; Guillard et al. 2009; Cluver et al. 2010; Appleton et al. 2017). Shocks, though hard to detect in LIRGs and ULIRGs because of the dominant effects of star formation on optical emission-line diagnostics, are being increasingly detected with the advent of spatially resolved optical integral field unit (IFU) spectroscopy (Rich, Kewley, and Dopita 2011, 2014, 2015). How large-scale shocks and turbulence affect the star formation in such galaxies, and how important this process is in higher-redshift systems is currently unknown.

An interesting example of an ongoing major merger that may be caught in a highly disturbed state is the Taffy galaxy pair UGC 12915/4 (hereafter Taffy-N and Taffy-S for simplicity). Despite having recently undergone a strong head-on collision, the Taffy system appears surprisingly normal in its IR properties, with a total $L_{IR} = 4.5 \times 10^{10}$ $L_{\odot}$ summed over the whole system based on multi-wavelength *S*pitzer and *H*erschel SED photometric fitting Appleton et al. 2015; (see also Jarrett et al. 1999; Sanders et al. 2003). The reason that the system is so normal in the IR, despite its recent violent history, is not known. It may be that the Taffy system is in a peculiar moment where most of its gas is so disturbed that it cannot yet generate significant star formation. If so, studying the conditions of the gas in between the galaxies (referred to as the bridge) may well yield interesting insight into how shocks and turbulence can inhibit star formation in violently colliding galaxies.

The Taffy galaxies were named for the discovery of a bridge of radio continuum emission, stretching, like salt-water taffy (candy), between the galaxies (Condon et al. 1993). Evidence suggests that the two galaxies collided 25-30 Myr ago, allowing their stellar components to pass through each other, but stripping $\sim$ 7 x 10^9 $M_\odot$ of molecular and atomic gas into a bridge between them (Braine et al. 2003; Gao, Zhu, and Seaquist 2003; Zhu et al. 2007). There is more gas in the bridge than in the two galaxies combined.

The bridge appears to be strongly disturbed (and probably turbulent), based on kinematically-broad CO line studies of the bridge, and strong mid-IR H_2 emission and [CII]157.7μm lines suggestive of shocks (Peterson et al. 2012, 2018). Despite its high gas mass, the average star formation rate (SFR) in the entire bridge through SED fitting is quite low, $\sim$0.45 $M_\odot$ yr^{-1}, excluding the prominent extragalactic HII region seen south-west of UGC 12915, which was separately found to have a SFR of 0.24 $M_\odot$ yr^{-1} (Appleton et al. 2015). Numerical models of such a head-on collision between two gas rich galaxies (e.g., Struck 1997) and a detailed model of the Taffy system (Vollmer, Braine, and Soida 2012) provide strong support for the idea that the gas left behind in the center of mass frame of the collision would be highly turbulent, and that some would be strongly shock heated. Appleton et al. 2015 detected faint extended soft X-ray emission, and several compact point X-ray sources in the bridge, the former being consistent with shock-heated gas that has not had time to completely cool since the collision occurred. Finally, Lisenfeld and Völk 2010 concluded that the radio emission in the bridge could be explained in terms of cosmic rays accelerated in magnetic fields compressed in shocks.

Although the Taffy galaxies have been studied quite extensively at longer wavelengths (Condon et al. 1993; Jarrett et al. 1999), very little work has been done at

visible or near-IR wavelengths. Howard A. Bushouse 1987 presented early digital video camera observations which showed Hα emission from the inner disks of both galaxies and emission from the extragalactic HII regions in the bridge. Paα observations from the ground were also made by Komugi et al. 2012. The galaxies show strong disturbances in their optical structure, including rings and loops, and the possible recent onset of star formation in the bridge, including at least one prominent extragalactic HII region, and fainter clusters–some of which are seen in archival NICMOS observations from HST (Appleton et al. in preparation).

This paper represents the first major study of the ionized gas phase in the Taffy system and bridge. I provide, for the first time, a detailed exploration of both the kinematics and excitation properties of the optical emission line gas in the Taffy system. The paper is organized as follows: §2.2 describes the observations and methods used in the paper. I describe the fitting process used on the double line profiles and the gas kinematics through Hα channel maps and velocity field moment maps in §2.3.1 and §2.4, respectively. The effects of dust extinction on the measured line fluxes are discussed in §2.3.2. I describe the results from the line diagnostic diagrams in §2.5. In §2.6, I discuss the results on the properties of the ionized gas and its excitation mechanisms through the use of emission-line ratio diagnostic diagrams and comparison with shock models. In §2.6 and §2.6.1 I discuss the estimates of the ionized gas fraction from star formation and the SFR in the system. I discuss the evidence for a post-starburst population in the underlying starlight in §2.6.3. In §2.7 I present the conclusions. I assume a comoving distance to the galaxies of 62 Mpc based on a mean heliocentric velocity for the system of 4350 km s^{-1}, and a Hubble constant of 70 km s^{-1}Mpc^{-1}.

2.2 Observations, Data Reduction, and Analysis Methods

The IFU data presented in this work were obtained with the VIRUS-P Spectrograph at McDonald Observatory (Hill et al. 2008; G. A. Blanc et al. 2010). VIRUS-P is the Visible Integral-field Replicable Unit Spectrograph prototype (now called the George and Cynthia Mitchell Spectrograph, GCMS) mounted on the 2.7 m Harlan J. Smith telescope. The IFU has 246 fibers (each fiber has an angular diameter of $4\farcs16$ on the sky) with a $\frac{1}{3}$ filling factor. Several cycles of a 3-point dither pattern to completely cover the 2.8 sq. arcminute field of view were used. The VP2 and VP4 gratings were used for the blue and red channel spectra respectively. VP2 and VP4 have a spectral resolution of 1.6 and 1.5 Å and covered a range of 4700–5350 Å and 6200–6850 Å, respectively. This spectral resolution corresponds to a velocity resolution of $\sim$100 km s^{-1}and $\sim$70 km s^{-1}at the wavelengths of Hβ in VP2 and Hα in VP4, respectively.

Observations of the Taffy galaxies were made on 2012 Jan 31 and Feb 2 (blue spectrometer) and 2012 Feb 01 (red spectrometer) with a total exposure time per dither position of 2200s (blue) and 1200s (red). Conditions were photometrically good at the time of the observations with moderate seeing of 1.8-2.5 arcseconds (less than the diameter of a fiber).

These data were processed using the VACCINE pipeline which identified and traced each fiber on the CCD chip, and performed bias, flat-field and wavelength calibration (based on lamp spectra) on a fiber-by-fiber basis for the science frames. VACCINE is a Fortran-based reduction package developed for the HETDEX Pilot Survey (Adams et al. 2011) and the VENGA project (G. A. Blanc et al. 2010). Cosmic-ray removal was then performed using the IDL routine LA-Cosmic (van Dokkum 2001).

2.2.1 Flux Calibration and Cube Building

The flux calibration and pointing refinements and final cube construction of these data was performed in three steps following the methods described by Guillermo A. Blanc et al. 2013: i) Relative spectrophotometric calibration was performed which is applied to all the fibers. Observations were made in a 6-point dither pattern (including several fibers) of the standard star Hz 15 (HIP 21776). An algorithm was used to solve for the position of the star on the fibers and determine the spectrophotometric transformation from native (ADU) units across the spectrum to units of erg s^{-1} cm^{-2} $Å^{-1}$. The results were applied to all the fibers irrespective of throughput. This step resulted in a relative flux uncertainty across the band of ∼8%; ii) astrometry and absolute flux calibration, using a bootstrapping method, was used to effectively cross-correlate a reconstructed image of the galaxy derived by integrating the light from each fiber, with a calibrated images of Taffy from the SDSS (York et al. 2000) in the g- and r-band, suitably convolved to the resolution of the VIRUS-P fiber system. This helped refine the astrometry, and the assembly of the final cube from the individual observations of each field. The cross-correlation also allowed the spectrum in each fiber to be absolutely scaled to the SDSS band in question. The details of this procedure are given in Guillermo A. Blanc et al. 2013. Tests performed in that paper show that the absolute spectrophotometric flux calibration has a typical accuracy of 15-30%, after taking into account the uncertainties in SDSS calibration and the VIRUS-P relative spectrophotometric accuracy; iii) a final flux-calibrated 3-d spectral cube was created by combining all the various observational pointing frames into a single interpolated cube with resulting 2 x 2 $arcsec^2$ spaxels (∼0.3 kpc $arcsec^{-1}$ based

on the assumed distance of 62 Mpc). These processes were repeated for the red and blue channels, creating final flux-calibrated blue and red spectral cubes.

2.2.2 Spectral Mapping, Continuum and Emission-Line Fitting

The processing and extraction of astrophysical information from the data cubes was done using a combination of IRAF/PyRAF, IDL and Python routines. Before beginning the analysis I smoothed the data cubes spatially, but *not* in the spectral direction, using a Gaussian kernel with a standard deviation of 1.47 pixels. This was done to boost the signal-to-noise ratio in areas that I was interested in; particularly the Taffy bridge region which has relatively low signal-to-noise compared to the galaxies. This spatial smoothing effectively reduces the noise in spectra from individual spaxels by a factor of $\sim$2. I used these spatially smoothed cubes for all of the analysis done in this work.

For fitting each individual spaxel in the IFU data I used the IDL software toolkit LZIFU (LaZy-IFU) (Ho et al. 2016). LZIFU automates fitting multiple emission lines superimposed on a continuum for multiple spaxels in each channel and provides 2D maps of continuum and line fluxes, velocities and velocity dispersion. It is capable of fitting emission lines that are superimposed on deep absorption features and also emission lines with multiple velocity components. Figures 2 and 3 show the fitting results for two individual spaxels that show these features in their spectra. Figure 2 shows a spaxel that has strong Hβ absorption and Hβ emission superimposed on the absorption trough. This spaxel lies very close to the center of Taffy-N. This absorption must be accounted for with the continuum fitting to get accurate emission line fluxes as well as an accurate line profile. The emission lines also show evidence for double

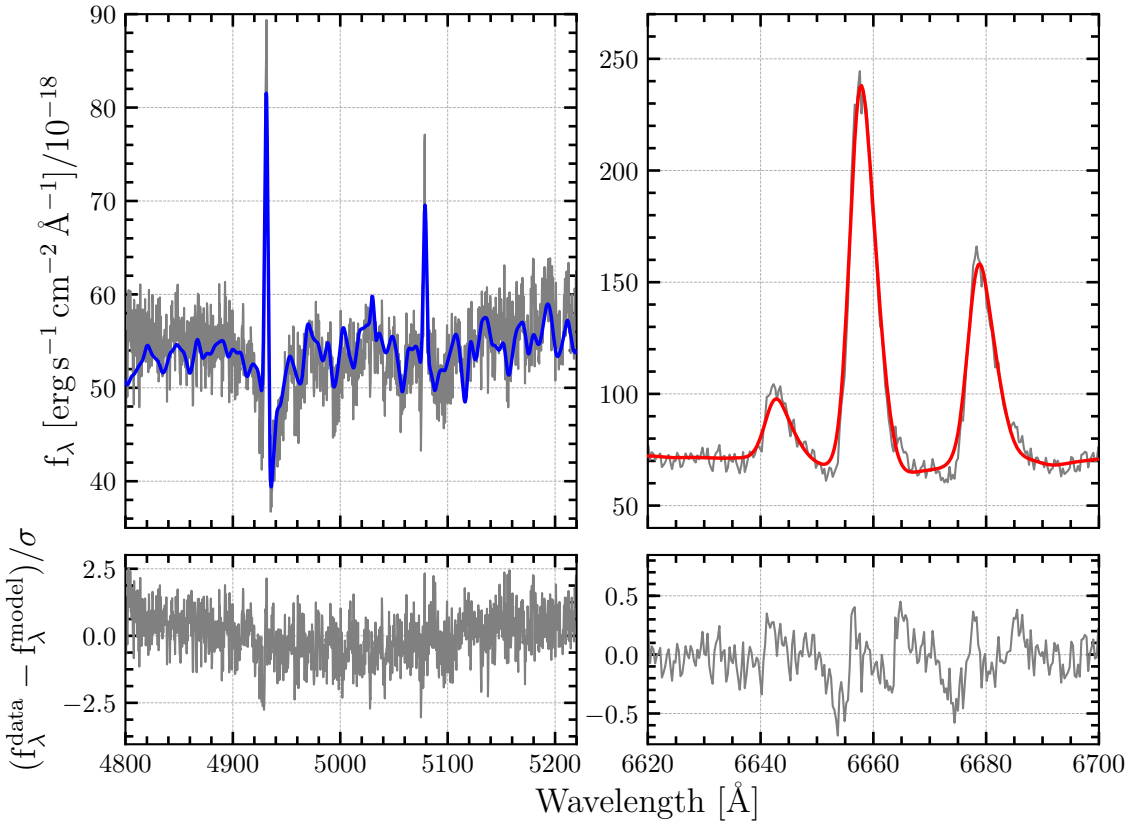

Figure 2. LZIFU fitting results for a spaxel that has deep Hβ absorption and Hβ emission superimposed on the absorption trough. The top left and right panels show the blue and red data respectively, along with their model fits. The bottom panels show the corresponding residuals from the fitting. The gray line shows the raw data from the spaxel and the blue and red lines show the model fits to the respective channels. Note that the Figure does not show the full wavelength coverage of the data but instead is focused on showing the relevant absorption and emission features i.e. Hβ and the [OIII]$\lambda\lambda$4959,5007 doublet in the blue channel and Hα and its neighboring [NII]$\lambda\lambda$6548,6583 doublet lines in the red channel.

line profiles in many positions across the system. As an example, Figure 3 shows a spaxel which lies close to the edge of the extragalactic HII region which clearly shows two separate velocity components.

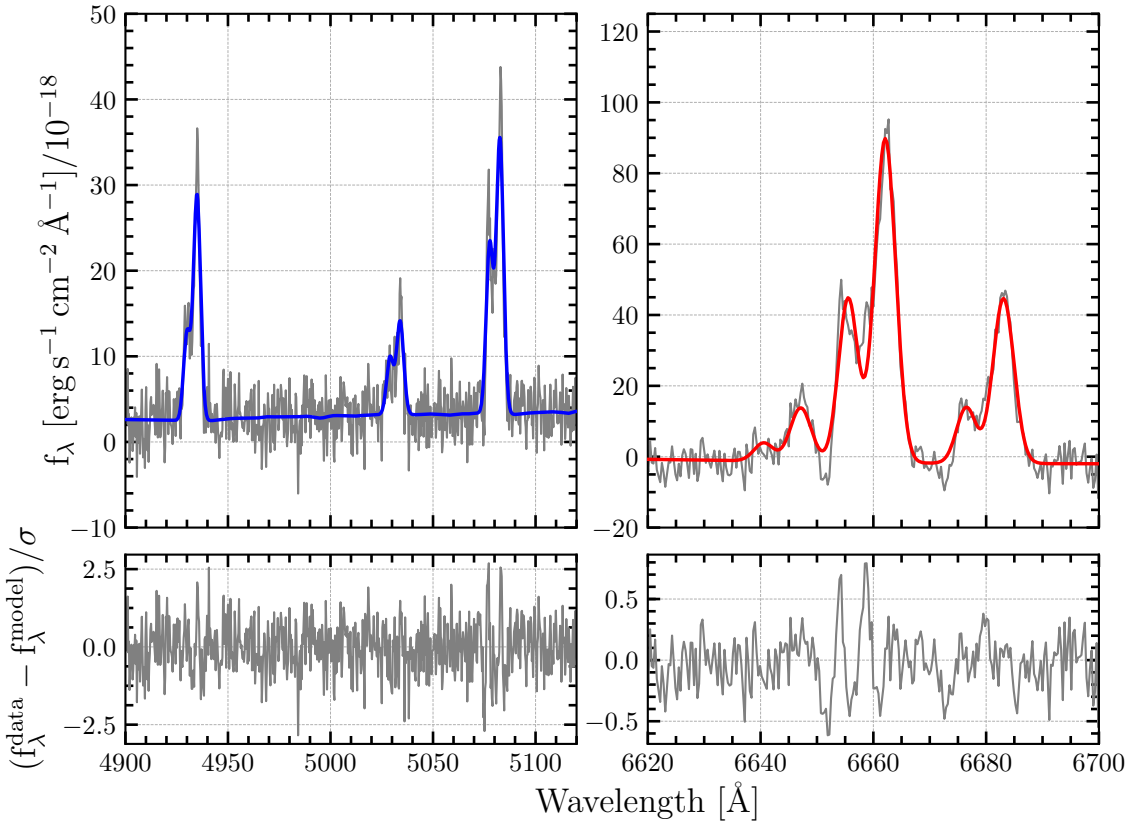

Figure 3. Same as Figure 2 but now showing the LZIFU fitting results for another spaxel which displays distinct velocity components more clearly.

LZIFU works by first fitting the continuum with a custom implementation of the PPXF code (Cappellari and Emsellem 2004) within LZIFU and then fitting the emission lines after subtracting the continuum model. The continuum fitting uses a set of model templates that are fit to a combined blue+red channel spectrum. LZIFU also accounts for systematic errors in the models and non-stellar contributions to the continuum data by fitting a multiplicative polynomial simultaneously with the continuum models. The emission lines along with residuals from sky line subtraction are masked during the continuum fitting process. I also specified the following lines to be fit (and masked during continuum fitting) - Hβ, the [OIII]$\lambda\lambda$4959,5007 doublet, [OI]λ6300, [OI]λ6364, Hα, the [NII]$\lambda\lambda$6548,6583 doublet, and the [SII]$\lambda\lambda$6716,6731 doublet. The extinction corrected emission line fluxes for all the lines detected in different regions of the Taffy system (as defined in Figure 4) are tabulated in Table 1.

I ran LZIFU on the entire IFU data cube for the Taffy galaxies which is 58×58 and 59×59 spaxels with 2227 and 2350 spectral elements for the blue and red channels respectively. The process of fitting the full cube was not straightforward for several reasons relating to the peculiar kinematics of the Taffy system. The LZIFU software was designed to work best with a galaxy showing slowly-varying velocity centroids relatively close to the initial guess for the velocity of the system. In the Taffy system, the velocity range of the emission lines over the whole system was large, with the emission lines sometimes exhibiting complex behavior, in addition to occasionally being observed superimposed on deep Balmer absorption lines. Furthermore, in a large number of spaxels, I found multiple velocity components which did not always move together as a function of position. As a result, a single set of initial guesses for the various starting parameters did not work for the whole cube, but had to be adjusted spatially to achieve good fits, especially in specific regions showing double

line profiles. After an iterative process of fitting with different starting parameters tuned to particular regions, I was able to get a consistent set of smoothly varying results across the whole system. I provide the most relevant LZIFU parameters and their starting guesses in Table 2.

2.3 Results

2.3.1 Emission-Line Gas and Hβ Absorption Within the System

Previous observations of the Taffy system in the visible wavelength range had reported the detection of ionized gas within the galaxies and the extragalactic HII region (H. A. Bushouse 1986; Howard A. Bushouse 1987). Because of the sensitivity of the VIRUS-P instrument to very faint diffuse emission, I report the presence of ionized gas throughout the Taffy system – both within the galaxies, the so-called extragalactic HII region, and also *in the bridge between the galaxies*. I detect emission from many lines, including Hα, Hβ, the [OIII]$\lambda\lambda$4959,5007 doublet, the [NII]$\lambda\lambda$6548,6583 doublet, and the [SII]$\lambda\lambda$6716,6731 doublet lines (see Figures 2 and 3). I also detect strong emission from the atomic oxygen line [OI]λ6300 and sometimes the weaker [OI]λ6364 line in the galaxies and the extragalactic HII region in the bridge. Although emission lines dominate in many of the locations across the system, in some cases Hβ emission is observed superimposed on a broad absorption trough indicative of a post-starburst population (as seen in Figure 2).

In Figure 4 I present some extracted spectra in several places in the system to provide an overview of the complexity of the kinematics in this system. The spectra show expanded views of the [OIII]λ5007 and Hα lines along the major axis of both

galaxies and a sampling of the bridge. As with the previous HI investigations of Taffy by Condon et al. 1993; Braine et al. 2003, the ionized gas spectra along the major axis of Taffy-N (N1-N5) show clear rotation from low to high velocities as one proceeds northwards, whereas in Taffy-S (S1-S5), the rotation is also obvious, but in the opposite sense. This confirms the suggestion that the galaxies were counter-rotating when they collided. Many of the line profiles are complex, and contain multiple components. Of special note are the broad lines in the bridge (especially B1 and B2) as well as complex multi-component structures in the north-west of both galaxies (N4, N5, S4 and S5). The nucleus of Taffy-S (S2) also shows very broad strong [OIII] emission, and weaker broad wings in Hα (especially when a correction is made for Hα absorption–see §4.2). I also show polygons marking additional regions of interest on the SDSS image in Figure 4. These polygons show regions which are investigated in the emission-line diagnostic diagrams in §2.5. In the emission-line diagnostic diagrams, I investigate the excitation mechanisms for the western regions of Taffy-N and the bridge separately because these regions exhibit peculiar kinematics distinct from the rest of Taffy-N and the bridge (see the detailed discussion in §2.4.1 and §2.4.2).

Figure 5a shows total Hα emission contours overlaid on a SDSS i-band image. The two galaxies and the area near the extragalactic HII region can clearly be distinguished as regions with the brightest Hα emission, with extended emission spread between the galaxies. For Taffy-S, the brightest Hα lies on either side of the nucleus with fainter emission from the direction of the nucleus. It is noticeable that there is no obvious ionized gas associated with the faint southern part of the outer ring in Taffy-S, although there may be some associated with the northern part of the ring between the galaxies. Taffy-N has a very different distribution of ionized gas, with a strong

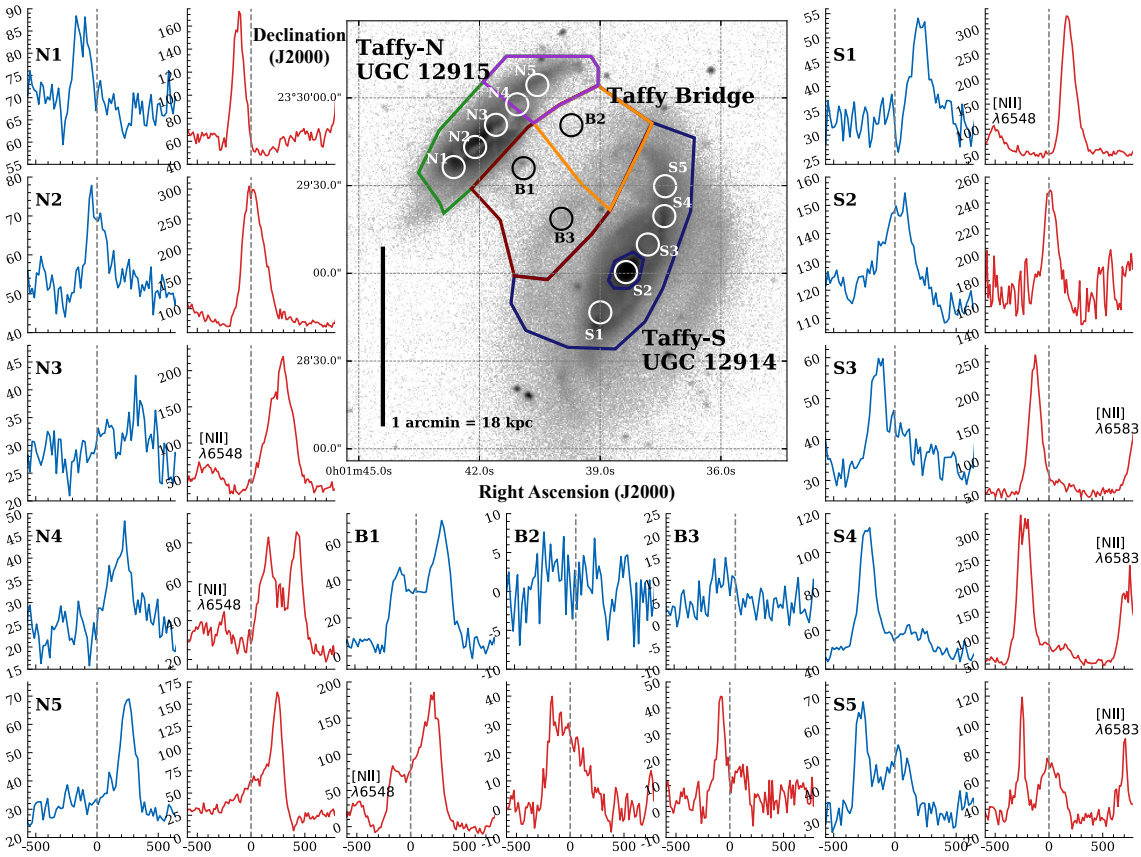

Figure 4. Some examples of integrated VIRUS-P spectra from the Taffy system expanded to emphasize the kinematics. The galaxies UGC 12915/4 referred to as Taffy-N and Taffy-S respectively for clarity in the text are shown in this SDSS i-band image. Spectra are shown extracted from the regions of the black and white colored circles. The blue and red spectra correspond to the [OIII]5007 and Hα lines. The flux axis is in units of $10^{-18}\,\mathrm{erg\,s^{-1}\,cm^{-2}\,\AA^{-1}}$. The polygon regions refer to the regions that are color coded, using the same colors, in the later discussion of the emission-line diagnostic diagrams (with the exception of the western part of Taffy-N which is shown as green pluses in the line diagnostic diagrams). I denote Taffy-N, the western part of Taffy-N, Taffy-S, the eastern bridge, and the western bridge by green, magenta, blue, red, and orange colored polygons respectively. The nucleus of Taffy-S is also denoted by a small blue polygon. The justification for selecting these regions is discussed in the text. The region shown here as B1 is centered on a faint extragalactic HII region discussed in the text. The gray dashed line denotes the systemic recessional velocity for the Taffy pair at 4350 km/s.

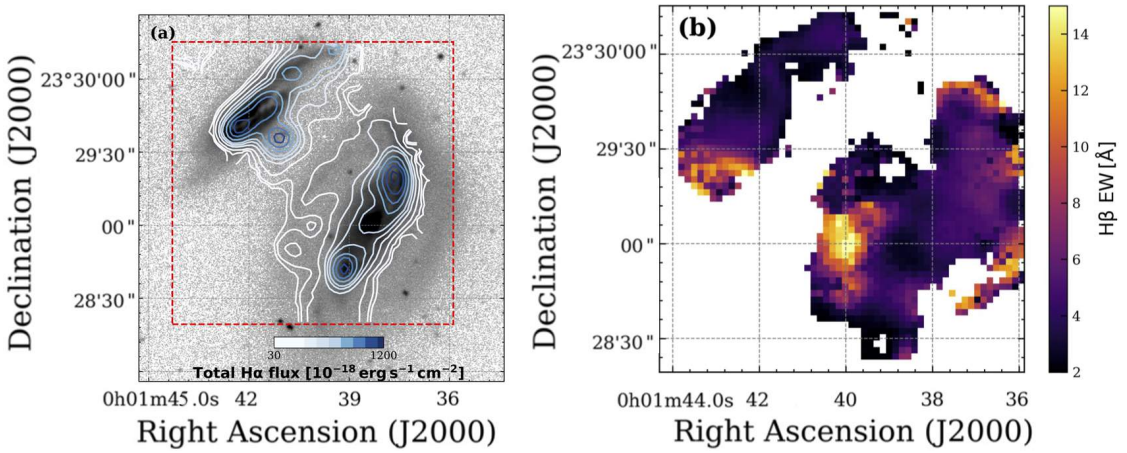

Figure 5. (a) Integrated Hα emission contours from the IFU data overlaid on an SDSS i-band image. The contour levels are 30, 50, 100, 200, 300, 400, 600, 800, 1000, and 1200, in units of 10^{-18} $erg\,s^{-1}\,cm^{-2}$. The lowest contour level corresponds to an approximately 2σ detection. The red rectangle shows the IFU coverage. The Hα emission was summed over the two velocity components in spaxels where there were double profiles. (b) The measured Hβ absorption-line equivalent width (EW) in Angstroms across the Taffy system based on the ppxf fitting of the absorption lines and continuum.

concentration in the inner disk, and fainter emission extending along the north-west major axis where it appears to join with bridge material.

Figure 5b shows a map of the equivalent width of the Hβ absorption across the system. In contrast to the lack of emission lines in the southern ring of Taffy-S, strong stellar absorption is seen there, along the extreme north-westerly edge of the galaxy, and in an extended region north-east of the faint stellar ring. In Taffy-N the strongest absorption is seen at the south-eastern end of the major axis in the region outside the main body of Hα emission, although it extends at lower equivalent width as far as the center of the galaxy. I will discuss the implications of this Hβ absorption in §2.6.3.

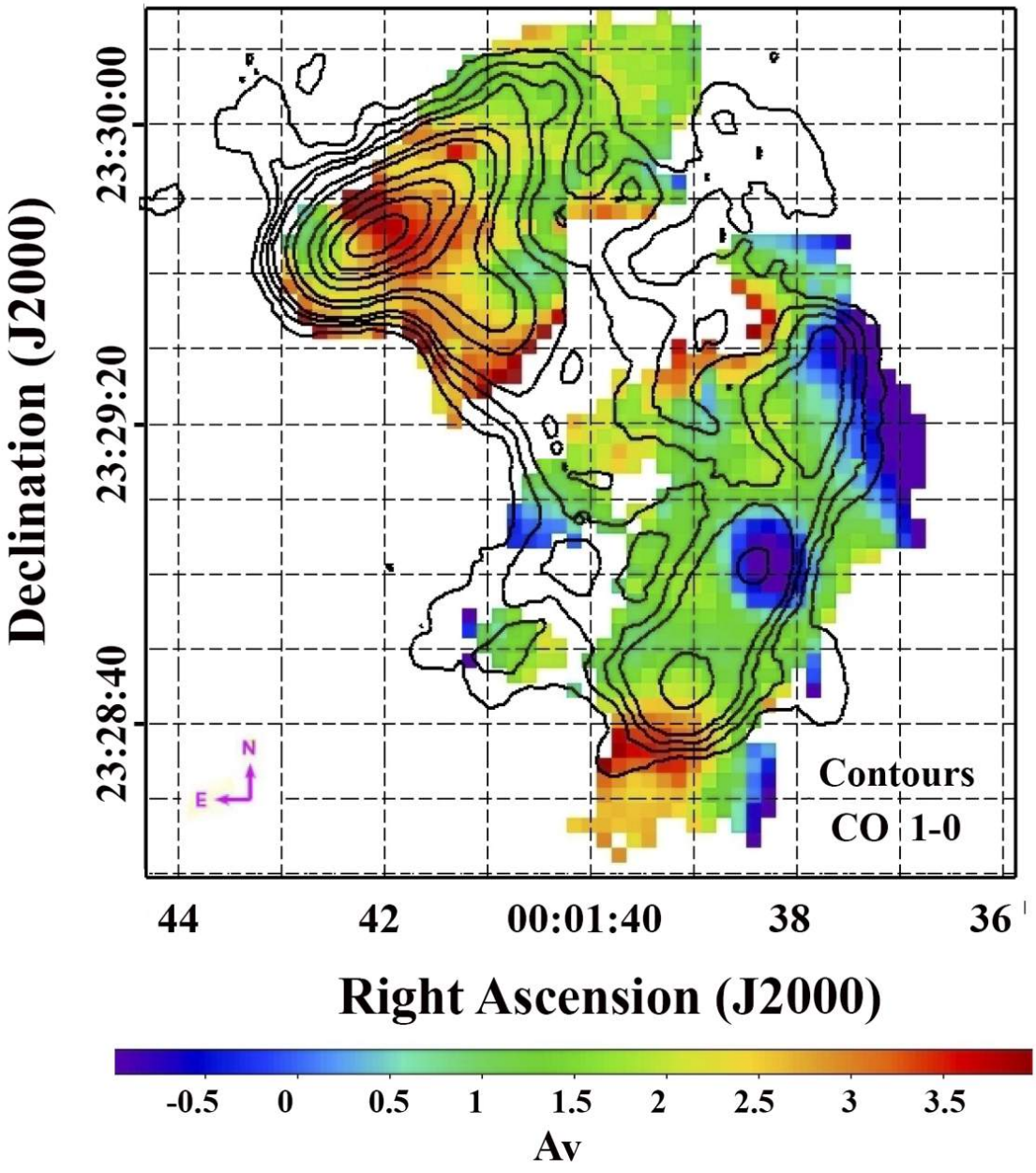

Figure 6. Map of visual extinction, A_V, with superimposed CO (1-0) (black) contours from Gao, Zhu, and Seaquist 2003. The A_V map was created as per the calculation described in §2.3.2. The contour levels are 35, 40, 45, 50, 65, 75, 100, 120, 140, and 160, in units of [Jy km s^{-1}beam^{-1}].

Table 1. Visual dust extinction corrected emission line fluxes divided by region [10^{-16} W/m^2].

Region	A_V	Hβ	[OIII]λ5007	[OI]λ6300	Hα	[NII]λ6583	[SII]λ6716	[SII]λ6731
Taffy-N	2.29	3.2 ± 0.23	1.98 ± 0.2	0.59 ± 0.16	9.12 ± 0.16	4.34 ± 0.14	2.24 ± 0.14	1.35 ± 0.16
Taffy-S	0.94	1.67 ± 0.13	0.67 ± 0.11	0.39 ± 0.11	4.78 ± 0.11	2.70 ± 0.1	1.38 ± 0.1	1.18 ± 0.12
Bridge	1.89	1.42 ± 0.19	1.48 ± 0.16	0.55 ± 0.14	4.05 ± 0.13	1.89 ± 0.11	1.25 ± 0.11	0.81 ± 0.13

Fluxes quoted for Taffy-N are from the combined Taffy-N and west-bridge regions, i.e., including the western parts defined in Figure 4.

2.3.2 Dust Extinction From the Balmer Decrement

I estimate the extinction caused by dust by examining the line ratio of the Balmer lines, Hα and Hβ, referred to as the Balmer decrement, and assume Case B recombination. The color excess E(B − V) is given by,

$$\mathrm{E(B-V)} = 1.97 \log_{10} \left(\frac{(\mathrm{H}\alpha/\mathrm{H}\beta)_{\mathrm{obs}}}{2.86} \right). \tag{2.1}$$

The extinction at wavelength λ is related to the color excess by,

$$\mathrm{A}_\lambda = \mathrm{k}(\lambda)\, \mathrm{E(B-V)}. \tag{2.2}$$

I assume a reddening curve k(λ) of the form given by Calzetti et al. 2000. Adopting the same method for all the observed lines allows us to correct, spaxel by spaxel, the observed line fluxes for dust extinction to arrive at intrinsic line fluxes.

A map of the dust extinction at visual wavelengths, A_V, derived from the Balmer decrement is shown in Figure 6 and superimposed on the map are CO (1-0) contours from Gao, Zhu, and Seaquist 2003 using data from the Berkeley-Illinois-Maryland-Association (BIMA) interferometer. It can be seen that the dust extinction map follows reasonably well the CO (1-0) surface density map, with a peak at the center of Taffy-N (as expected since the H_2 surface density is very high there). A high value of extinction is also seen at the southern tip of Taffy-S. This extends beyond the

CO column density contours, but I note that the VLA maps of HI in this region by Condon et al. 1993 show a peak column density there of 1.8×10^{21} cm^{-2}, which would imply an A_V of ~ 1 mag integrated over a 18 x 18 arcsec^2 beam (Güver and Özel 2009).

Interestingly, I observe a low value of A_V at the center of the Taffy-S, and along the northern edge of the spiral arm of that galaxy. The latter result is consistent with a low H_2 column there, although the low A_V in the nucleus may imply different conditions in the gas excitation (deviations from the assumed Case B recombination–perhaps due to a low-luminosity AGN) or a significantly reduced dust to gas ratio there.

Given that dust opacity measurements depend strongly on galaxy inclination (see e.g., Simon P. Driver et al. 2007; Unterborn and Ryden 2008), I caution that the dust extinction estimates for both galaxies should be treated as lower limits and that actual A_V values could be much higher. For example, Gao, Zhu, and Seaquist 2003 estimate A_V values could be higher than 10 mag for both galaxies. The low A_V values for the Taffy galaxies could be because measuring the dust extinction from the Hα and Hβ lines involved in the Balmer decrement effectively only probes the effects of dust superficially (essentially a "skin" effect; e.g., Calzetti 2001). It also assumes a simplistic dust geometry – a screen of dust between the observer and the Balmer line emitting regions. Such an assumption might not be true for the complicated kinematics within the post collision Taffy system.

2.4 The Kinematics of the Taffy System

As Figure 4 has shown, the spectra are quite complex in the system, and so I present the kinematic results in two ways. Firstly, I present the channel maps of one

Table 2. LZIFU parameters supplied to the configuration file.

Parameter name	Value	Description
only_1side	0	0: 2-sided data. 1: 1-sided data
z	0.0145	Redshift
fit_ran	[4700,6855]	Fitting range
Continuum fitting with PPXF		
mask_width	12	Full width to mask around emission lines defined in lzifu_linelist.pro
cont_vel_sig_guess	[0., 50.]	Starting guess of delV and vel_dispersion of continuum (in km/s)
cont_ebv_guess	0.1	Starting guess of ebv
Emission fitting with MPFIT		
fit_dlambda	22.	Full width around line centers to be fitted. (A)
ncomp	2	Number of component.
line_sig_guess	70.	Initial guess of velocity dispersion for emission line (km/s)
vdisp_ran	[-50,500.]	Velocity dispersion constraints in km/s.
vel_ran	[-600.,+600.]	Velocity contriants in km/s. 0 is systemic velocity from set.z
Variation in initial guess		
comp_2_damp	[0.6]	Initial guess for amplitude of 2^{nd} component as fraction of 1^{st} component amplitude
comp_2_dvel	[-150,-50,+50,+150]	Initial guess range for velocity of 2^{nd} component; given as difference between velocities of 1^{st} and 2^{nd} components
comp_2_dvdisp	[+20]	Initial guess for velocity dispersion of 2^{nd} component

LZIFU explores all possible combinations of initial guesses of 1^{st} and 2^{nd} components.

of the lines (in this case Hα) to provide a large-scale view of the gas distribution as a function of radial velocity channel. Secondly, I explore the spatial distribution of the gas associated with different kinematic components, especially those associated with multiple lines.

2.4.1 Hα Channel Maps

Figure 7 shows the Hα emission channel maps integrated over channels of width 70 km s^{-1}. It is well known that the two galaxies are counter-rotating (e.g. Vollmer, Braine, and Soida 2012), and the brightest ionized gas in the two systems reflects this.

Ionized gas in Taffy-S is seen in the lowest velocity channel (3806-3876 km s^{-1}) in the north-west on the inside edge of the faint stellar ring, and progresses in a south-easterly direction with increasing velocity eventually showing a major component of emission in the south-east disk which fades away around 4780 km s^{-1}. Taffy-S also has some peculiar kinematics. For example, in the NW part of the disk, faint gas emission is seen over a wide range of velocities along the northern major axis even at the highest velocities. This would not be expected for gas in normal rotation. Taffy-N is even more peculiar. The main centroid of emission from the south-east disk appears at around 4016-4086 km $s^{-1}$and progresses steadily towards the north-west, showing the counter-rotation. In addition, there is a peculiar region of emission which appears at even lower velocities on the north-west extreme tip of Taffy-N, and cannot be part of the normal rotation of the galaxy. Indeed, that structure appears to be part of the bridge, since as velocities increase it becomes more extended and eventually connects to the north-western region of Taffy-S. In addition to this bridge feature, a second bridge component starts to appear between the galaxies at velocities of 4000 km s^{-1}, and at higher radial velocities it becomes quite strong in the region of the extragalactic HII region. The emission bridges the two galaxies where it joins with emission that potentially is associated with the faint stellar ring in the north-eastern part of Taffy-S. The connection between the galaxies disappears at velocities in excess of 4650 km s^{-1}.

The faint stellar ring in the northern half of Taffy-S exhibits some peculiar emission. Features that can be associated with this ring can be seen most clearly appearing from velocities around 4000 km s^{-1}. Moving to higher velocities shows several clumps that appear to follow the ring from NW to SE. These clumps also appear to be surrounded by emission that blends with the emission from the bridge. These features hint that this ring was strongly influenced by the collision and shows a discernible transition

from material that is clearly associated with Taffy-S to material clearly associated with the bridge. A similar argument could also apply to Taffy-N although such a transition is much harder to observe in Taffy-N which is highly inclined. It is clear that the velocity structure of the gas in both galaxies and the bridge is very complex, and so I will now explore the gas in terms of its spectral profiles–which allows us to more easily separate normal regular rotation in the galaxies from peculiar motions.

2.4.2 Mapping Two-Component Line Profiles in the System

As I have shown previously, there are regions in the full data cube where the emission-line spectra show more than one component. Similar, double line-profiles were noticed in both the HI (Condon et al. 1993) spectra, and in spectra taken in the far-IR [C II] and [O I] lines with *Herschel* (Peterson et al. 2018). Some regions of the bridge also show two components in the CO 1-0 molecular gas observations of Gao, Zhu, and Seaquist 2003. These observations (consistent with those of Gao, Zhu, and Seaquist 2003; Peterson et al. 2018) show that the double-line profiles in the ionized gas are not just confined to the bridge, but are also seen projected against parts of the galaxy disks, especially Taffy-N.

To explore the kinematics further, I performed line fitting in two distinct passes. Firstly I ran LZIFU, forcing it to fit only one component across the whole system. This worked well in regions where the lines were single-valued, but produced poor results in regions where the lines were double-profiled. The output from LZIFU at this stage was a model data cube built from the model fits, as well as the best fitting continuum cube. Also included were additional data products, including integrated line maps for each of the lines fitted.

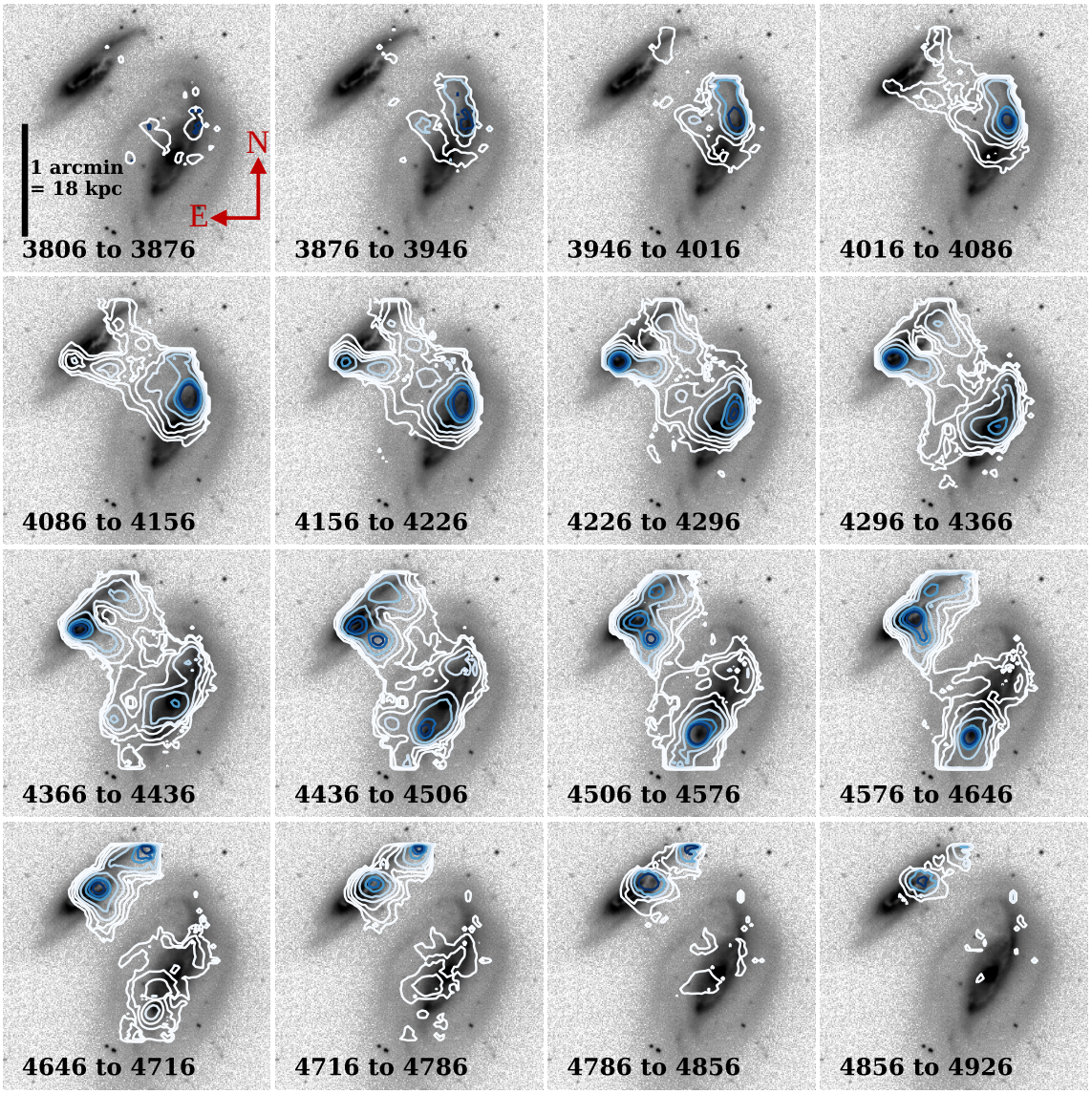

Figure 7. Velocity channel map showing the Hα emission over -540 to +510 km s^{-1} with respect to the (optically defined) systemic recessional velocity of $\sim$ 4350 km s^{-1}. The contours have been overlaid on a SDSS i-band image of the Taffy galaxies. The color of the contours, going from white to blue, indicates the intensity of the Hα emission going from low to high intensity. The contour levels are 1, 4, 10, 20, 40, 80, 105, and 135 in units of $erg\,s^{-1}\,cm^{-2}/(70\,km\,s^{-1})$. Note that every contour level is not visible in each panel because the Hα intensities change for each panel. The velocity range shown for each panel (heliocentric velocity) is 70 km s^{-1}. The LZIFU emission line cube was stitched as described in §2.4.2. The scale bar in the top left-hand panel is 1 arcmin (18 kpc for D = 62 Mpc) in length.

Secondly, I ran LZIFU again, but this time I required it to fit two components for everything. In this case, the fitting worked well for the case of two components, but I found that it performed poorly in places where the profiles were singular. In this mode, since the software was fitting two separate line profiles, the output included two sets of data products (model line cubes, integrated line and velocity field maps), one set for each component–a low and high-velocity component.

I was able to interrogate the model results to determine, spaxel by spaxel, the mean, standard deviation, and amplitudes for each of the single and two component fits. This allowed us to divide the results into three classes of kinematic behavior:

1. Spectra consistent with a single Gaussian component, V_s
2. Spectra consistent with two components, V_1 and V_2, at different velocities (V_1 represents the lowest velocity component, and V_2 the highest).
3. Spectra consistent with two components with nearly the same mean velocity, but exhibiting both a narrow V_{1n} and broad V_{2b} component.

To qualify as two components, the two Gaussian line centers, V_1 and V_2, were required to differ by at least 35 km s^{-1}, or one-half of the velocity resolution at Hα wavelengths. In practice, the lines were generally further apart than this and clearly separated. Similarly, for a second component to be considered broad, V_{2b} must have a FWHM of at least 1.5$\times$ that of V_{1n}. In a few cases, the LZIFU modeling failed to fit two components to cases where a single line profile would have been more appropriate. In these small number of cases, I inspected the profiles by eye to perform what I considered to be the most reasonable classification.

In general when there was doubt about the classification, I inspected the profiles by eye to confirm the classification. Overall the separation between single and two-

components seemed reasonable, although I realize that there may be some areas where the distinction is somewhat subjective. Less subjective methods of deciding whether to fit single or multiple components to optical IFU data have been explored by Hampton et al. 2017 using Artificial Neural Networks. These methods, which currently rely on training sets using "expert" astronomer guidance, are encouraging for the future, especially since such methods can classify velocity profiles faster than a human, and with statistically similar outcomes. As IFU data becomes more common, and as the amount of data increases with time, such methods may eventually be needed to replace human classifications. In this paper, in most cases, the classification of a two-component versus single Gaussian component was relatively unambiguous.

In order to explore the relationship between the regions of emission where a single component is most appropriate compared with a region with two components, I have created composite moment maps (intensity, mean velocity and velocity dispersion) by *combining* those positions consistent with a single profile V_s with those consistent with one or other of the double profile cases. The reason I combined the single component data with the two velocity components separately, was to look for continuity between the single component gas and one or other of the double-lines. For example, if the single component data mapped smoothly into velocity field of one of the two double components, this might suggest they are really part of one single dynamical system, whereas a sudden discontinuity would suggest no such regularity.

These "merged" single and double profile moment maps are shown in Figure 8. Figures 8 a,b and c represent moment maps created by combining spaxels containing components V_s with V_1 and V_{1n}, whereas Figures 8 d,e and f, represent the combination of spaxels containing V_s with V_2 and V_{2b}. To make it clear where the different kinds of profiles fall in the maps, I indicated in the Figure those regions enclosed within the red

polygon that are consistent with Class-2 above (two components at different velocities). Those regions of the maps consistent with a single line, Class-1, are colored with a red background color. Finally, those regions where a narrow and broad component were present, Class-3, are shown with a green background color.

Given that the kinematics are quite complex, I start by identifying those regions which may show regular galactic rotation. The simplest kinematics to understand are those of Taffy-S in the *low-velocity component* of Figure 8b. Here, the increasing iso-velocity contours, going from yellow to dark blue progress regularly in the double-line region, merging smoothly with the V_{1n} (green underlying color) and single-component V_s (red underlying color) contours. The velocity dispersion in the *low-velocity component* in Taffy-S is also low across most of its disk. Concentrating only on the *low-velocity component* for Taffy-S, it is clear that the velocities and dispersions shown in Figures 8b and c look like a somewhat-warped, but regular rotating disk. In contrast, Taffy-S is much more peculiar in the *high-velocity component* of Figures 8e and f, where the galaxy shows only a small amount of obvious rotation, as well as exhibiting a high velocity dispersion in a large part of the disk. It also has a band of spectra classified as broad-line (Class-3 type; green underlying color) in the nuclear regions.

I now turn my attention to Taffy-N which has more complex kinematics. This galaxy is quite edge-on and may be expected to show regular rotation along its major axis. Evidence of rotation is seen in the *high velocity component* of Taffy-N in the southern part of the disk centered on the dense dust lane and nucleus. Figure 8e, shows a clear rotation signature where the velocities (starting with the pale blue contours in the south-east) increase along the major axis (dark-blue contours in the north-west of the inner disk). Although this apparent regular rotation in the *high*

velocity component is confined to the inner parts of the Taffy-N disk, the increasing trend in velocity shows a reversal towards the north-western extended disk. This might be interpreted as a turn-over in the rotation curve there.

Next I consider those parts of the velocity field that cannot be considered normal, and are most likely caused by the strongly collisional nature of the Taffy pair. I have already pointed out in the discussion of the channel maps that the north-western part of Taffy-N has a peculiar low-velocity structure which is not part of the normal rotation. This can be seen in Figure 8b (*low velocity component*) where much of the NW disk of Taffy-N shows very little rotation, and also shows high velocity dispersion (Figure 8c). Here I see that the gas extends as a finger towards the south-west, where it forms a western bridge with Taffy-S. A second eastern bridge structure, is seen associated with the extragalactic HII region, which is strongest in the *high-velocity component*. The two structures are graphically emphasized in Figure 9. Much of the gas between the two galaxies is seen in the eastern high-velocity bridge component, and shows a velocity gradient which extends between the two galaxies along direction of the radio-continuum bridge discovered by Condon et al. 1993. Some regions of the high-velocity component bridge material have a high velocity dispersion–as was noted in the spectra in Figure 4. I will show that much of the bridge gas in the *high velocity component* has the excitation properties consistent with shocked gas.

Several regions also show Class-3 spectra–which means that one component is broad. These regions (color green in all the panels of Figure 8) are confined to positions along the minor axis of Taffy-S, and to a small region at the north-west tip of the same galaxy. I show an example of these kind of spectra in Figure 10. Here I show how LZIFU has fit two components to the Hα profile from the nucleus of Taffy-S after correcting for weak Balmer absorption. This appears as a region of high velocity

dispersion in Figure 8c and f. The Hα line profile shown is an average over a 4 x 4 spaxel region centered on the X-ray hot-spot in Taffy-S. The two components have a FWHM of 320 $\pm$ 70 km s^{-1}and 205 $\pm$ 70 km s^{-1}, with a small offset in velocity between the two.

2.5 Excitation of the Ionized Gas in the Taffy System

I next consider the possible excitation mechanisms for the ionized gas within the Taffy system by constructing emission line diagnostic diagrams based on LZIFU fitting of each spaxel in the data cube (sometimes called BPT or VO diagrams; Baldwin, Phillips, and Terlevich 1981; Veilleux and Osterbrock 1987; L. J. Kewley et al. 2001). I construct emission line diagnostic diagrams using the [OIII]λ5007/Hβ, [NII]λ6583/Hα, [OI]λ6300/Hα, and [SII]λ,λ6716,6731/Hα ratios. I have significant detections of the [NII] and [SII] lines in most spaxels that fall on the galaxies and bridge, whereas the [OI]λ6300Å line is detected in fewer spaxels because it is not as strong. I require every emission line used in the diagrams to be detected at the 3σ level.

In order to look for differences in excitation properties between the low and high velocity components where the lines are double, I show line diagnostic diagrams for each of the components separately (top panels a and b) in each of the Figures 11, 12, and 13 for the [NII], [OI], and [SII] plots respectively. I also show the diagnostic diagrams for the total emission (sum of the two components plus those fitted by a single line) as a third panel (c) in each of the same Figures. These diagrams use classifications from Lisa J. Kewley et al. 2006. In all three line diagnostic diagrams, I plot spaxels associated with different spatial regions of the Taffy-system. The

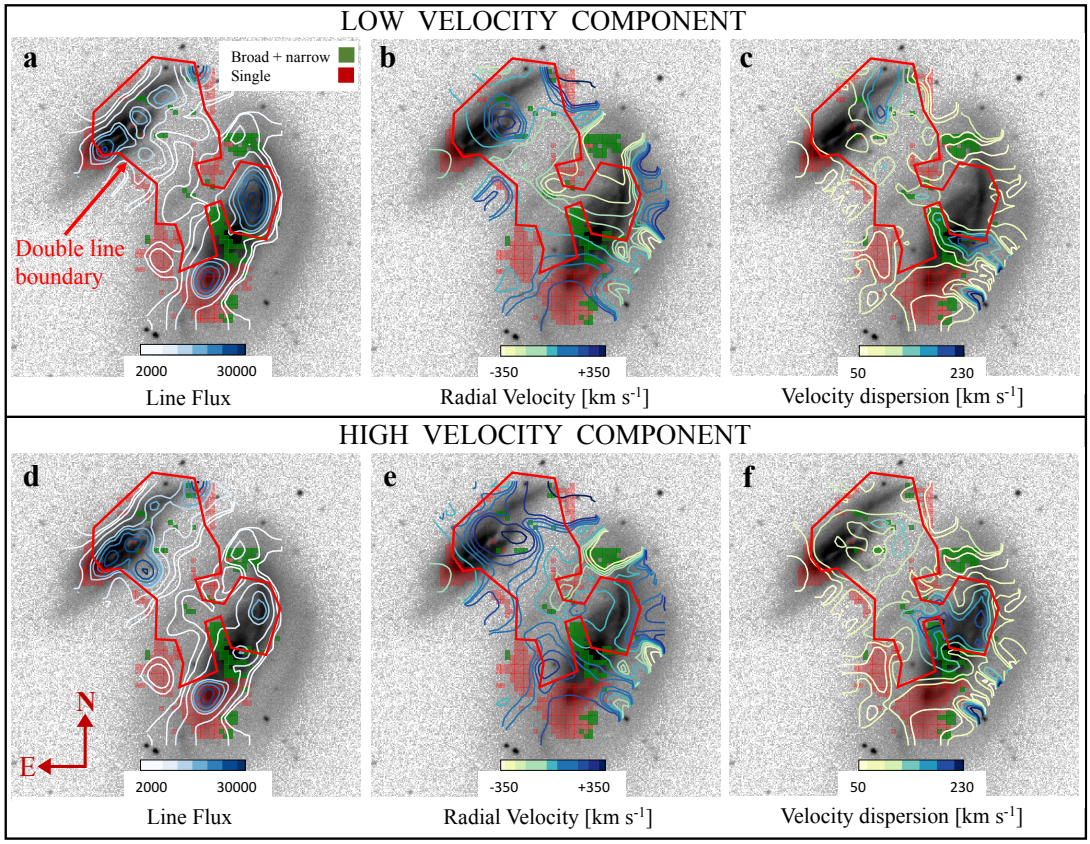

Figure 8. Contour maps, overlaid on a SDSS i-band image of the Taffy system, of the moments of the velocity field. Zero velocity corresponds to an (optically defined) recession velocity of 4350 km s^{-1}. The top and bottom rows correspond to the low and high velocity component as shown. From left to right, the column panels show the integrated flux in Hα, radial velocity (with respect to systemic velocity), and velocity dispersion, respectively. The contour levels for the integrated line flux maps are: 2000, 3000, 6000, 12000, 15000, 20000, 25000, and 30000 in units of $erg\,s^{-1}\,cm^{-2}\,km\,s^{-1}$. The contour levels for the velocity maps are: -350, -250, -200, -150, -100, 0, 100, 150, 200, 250, and 350 in units of $km\,s^{-1}$. The contour levels for the velocity dispersion maps are: 50, 70, 90, 130, 160, 190, and 230 in units of $km\,s^{-1}$. The red polygon demarcates the boundary where I see two line components in the profiles of the emission lines. The red spaxels outside the double line boundary indicate spaxels where I see only a single velocity component. The green spaxels indicate spaxels where I see two components but with significantly different widths (i.e., Class-3; I define the three line profile classes in §2.4.2).

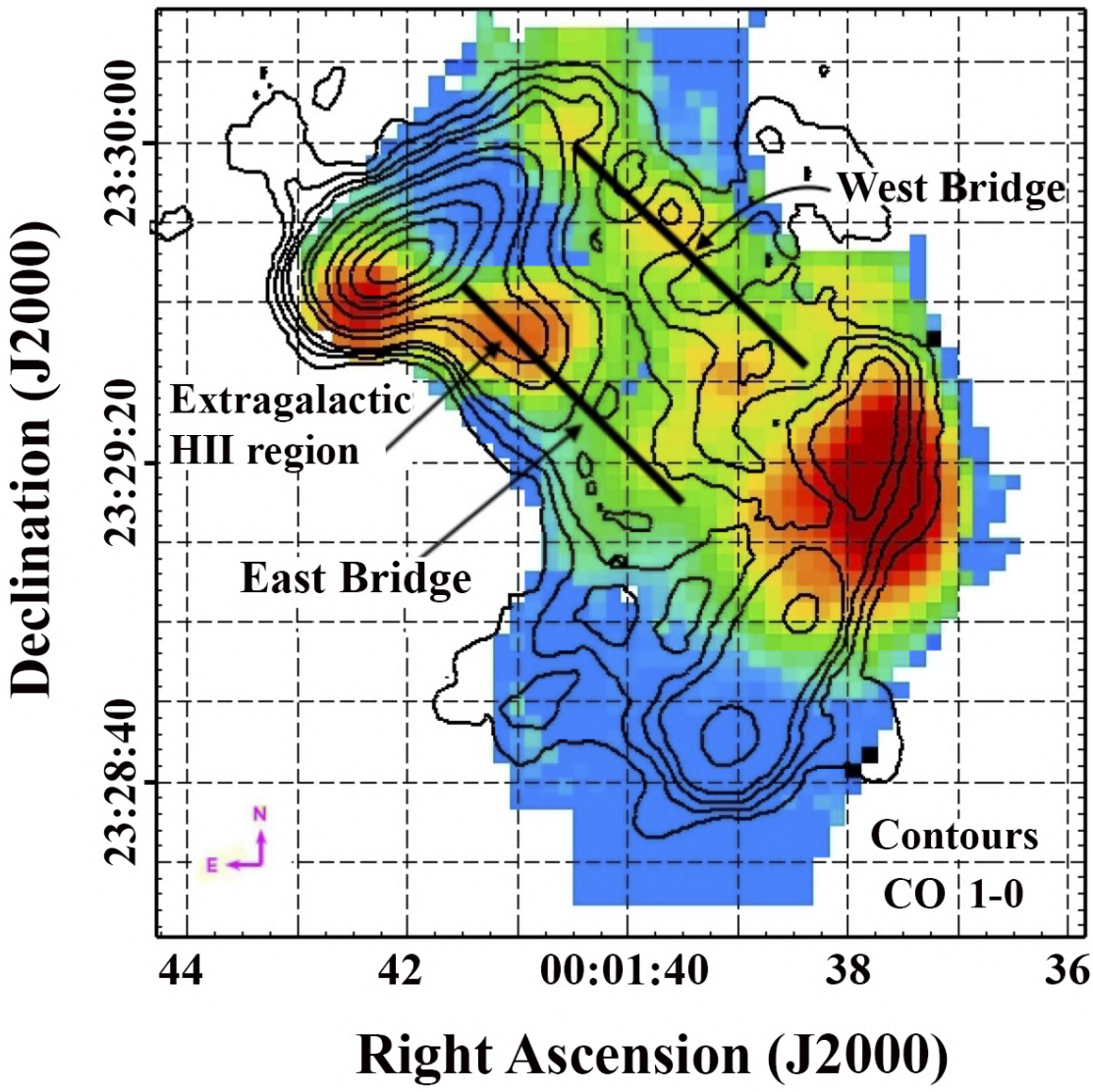

Figure 9. The emission between the galaxies can be decomposed into two kinematically different bridges of emission, seen represented in this single channel map of the Hα for velocities 4156 to 4226 km s^{-1}where parts of them both happen to appear at the same velocity. The two separate filaments are best defined by looking at the full range of channel maps shown in Figure 7. The eastern bridge structure extends from the southern part of Taffy-N and extends down through the extragalactic HII region until eventually it merges with the south-eastern disk of Taffy-S. The western bridge extends from the north-west of Taffy-N into the bridge and eventually connects with the north-western tip of Taffy-S. The eastern bridge is more closely associated with the CO emission than the western bridge, although some clumpy regions are seen in CO even in the west (black contours are from Gao, Zhu, and Seaquist 2003, see text for more details).

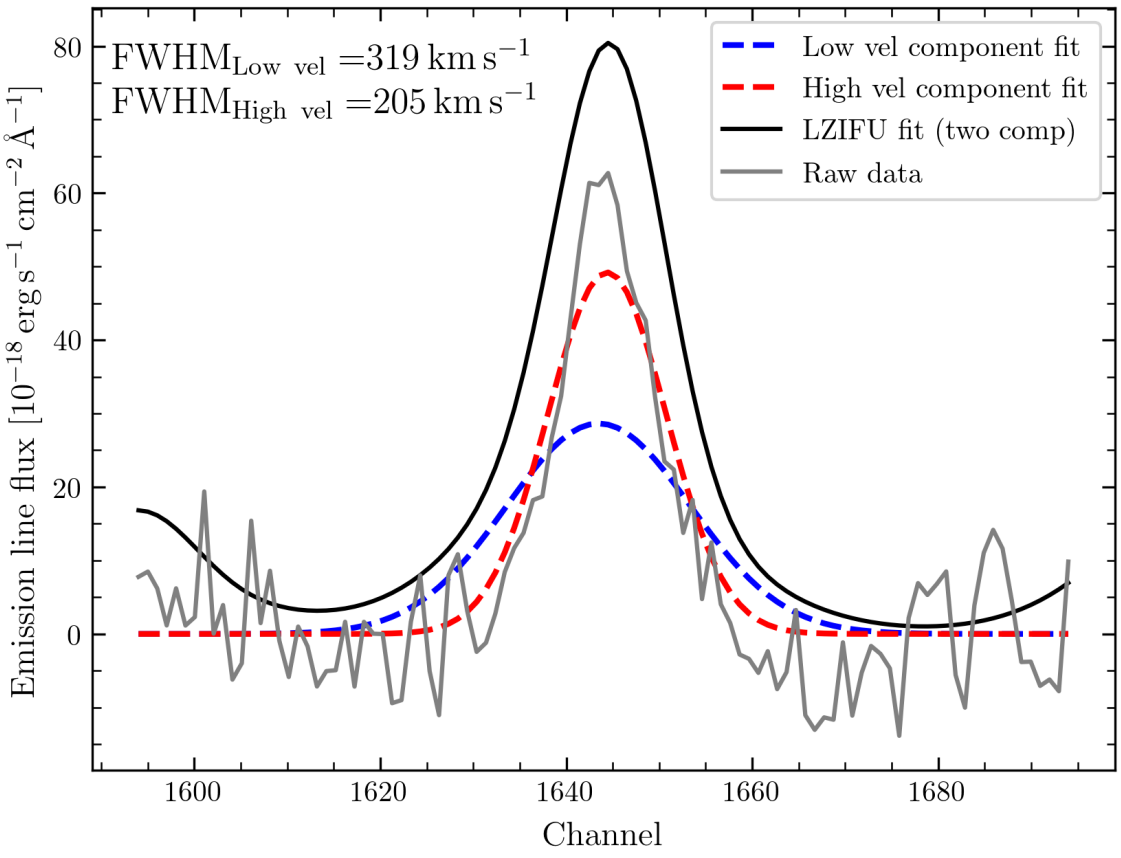

Figure 10. The Hα nuclear spectrum of Taffy-S (UGC 12914). The raw spectrum is shown (grey solid line), as well as the spectrum after correction by LZIFU for Hα absorption (solid black line). I show the decomposition into two profiles, one with a broad lower-velocity component (blue dashed line) and a narrower slightly higher-velocity component (red dashed line)-see text. The spectrum emphasizes the importance of correcting for the continuum (driven mainly by the fit in the blue), since in this case the Balmer absorption masked a broader component in the emission line.

symbols shown in the excitation diagrams are labelled in each Figure based on the regions defined in Figure 4. For example, green points and crosses represent regions in Taffy-N, while blue points represent Taffy-S (the nuclear region is distinguished as blue diamonds). The Taffy bridge is shown as red crosses (east bridge), and filled orange circles (west bridge). Because the west bridge contains fewer points than its eastern counterpart, I also present the integrated line ratio for the western bridge as a single larger open orange circle.

The line diagnostic diagrams show that the low and high velocity components often behave differently, indicating a difference in their respective excitation mechanisms. For the two galaxies (blue and green symbols), all three sets of line diagnostic diagrams show spaxels mainly distributed within the HII, HII+AGN-composite or LINER part of the diagnostic diagram, with little hint of any pure AGN component. Much recent work has shown that excitation by shocks can resemble excitation by an AGN. Rich, Kewley, and Dopita 2011, 2014, 2015 showed that composite line ratios i.e., HII + AGN, can be due to HII + shocks. This is particularly true for merging galaxies, for example Rich, Kewley, and Dopita 2014 showed that merging U/LIRGS can present "composite" optical spectra in the absence of any AGN contribution, with increasing contribution from shocks as the merger stage progresses from early to late-mergers. I will argue below that much of the LINER emission, with the possible exception of the nucleus of Taffy-S, is likely the result of fast shocks exciting the ionized gas in the bridge and in significant parts of the galaxy disks.

I will first concentrate on describing excitation in Taffy-N. I decided to split Taffy-N into two parts, one part covering the main disk of the galaxy and the other part covering the western extension which appears to connect with the western bridge. The emission from the main disk of Taffy-N (green points) is largely consistent with

emission from HII-regions. This is true in all of the diagnostic diagrams in the low, high, and summed components. The western extension of Taffy-N shows a mix of HII and LINER emission. This is especially evident in Figure 12 where the western extension of Taffy-N falls clearly in the LINER area in the low velocity component which I have previously noted from the channel maps may be associated with the western bridge.

Next I consider Taffy-S (blue points and diamonds). There appears to be a strong mix of HII-region and LINER/composite excitation for Taffy-S in all diagnostic diagrams. Despite the fact that the nucleus of Taffy-S does not show evidence for a powerful AGN in the gas excitation diagrams, this does not necessarily preclude a low-luminosity active nucleus being present-especially given the broader line-widths discussed previously. Taffy-S's nucleus (blue diamonds on Figures 11, 12, 13) does show some evidence of being a LINER, especially in the low-velocity regime. I find that most of the spaxels located on the nucleus of Taffy-S in the low-velocity (V_1) line diagnostic diagrams are in the LINER area in the [OI] and [SII] diagnostic diagrams, and close to the AGN line in the [NII] diagram for both the low and high velocity components. However, as previously noted, the velocity difference between the two components is small (< 20 km s^{-1}), with the main difference being in the width of the lines, the V_1 component having a broader width than the V_2 component (see Figure 10). This is consistent with Chandra X-ray observations (Appleton et al. 2015), which showed the possible existence of a low-luminosity AGN based on the X-ray hardness ratio.

I divide the bridge into two parts (east and west) as discussed previously. The eastern bridge (red crosses) shows clear evidence of being HII-region excited in the low-velocity component. The situation is quite different for the *high-velocity* V_2

component ('b' panels) in Figure 11b, 12b. Here, I observe sets of east-bridge spaxels that deviate strongly from the HII area locus. For example, in the [OIII]λ5007/Hβ ratio, the east-bridge points are spread out along the [NII]/Hα and [OI]/Hα line, extending strongly into the LINER area. The western bridge (orange filled circles) show a mix of HII-region and composite/LINER behaviour in all diagrams. This is quite similar to what I find for the western extension of Taffy-N indicating that they might be excited by the same processes. Because there are so few points from the western bridge, I also plot an average of the entire western bridge as an orange open circle which is only shown in the 'all' components diagram. This falls in the composite/LINER area for the [NII] and [OI] diagrams but in the HII area for the [SII] diagram.

2.5.1 Evidence for Shocked Gas in the Taffy System

I first explore the possibility that the gas is excited by shocks. I over-plot predicted line ratios from shocks on Figures 11, 12, and 13, taken from the MAPPINGS III library of models (Allen et al. 2008). The model line ratios are plotted for different shock velocities as solid colored lines. Based on the models of Vollmer, Braine, and Soida 2012, I assume that much of the gas in the bridge and throughout the galaxies is close to solar metallicity, since the gas has been stripped from the galaxies or has been excited *in situ*. For the shock models I therefore assume solar metallicity. The other parameters of the models include the pre-shock gas densities in the range $0.1 < \mathrm{n\,[cm^{-3}]} < 1000$ (stepping by a factor of 10 each time), and an assumed constant magnetic field of B=5 μG (this is close to the equipartition magnetic field strength of 8 μG measured by Condon et al. 1993 through radio continuum measurements).

I have plotted only the line ratios for the shock itself while excluding the precursor component of the shock. For the moderate shock velocities that seem compatible with the Taffy excitation velocities, it may be reasonable to ignore the effect of a strong ionizing shock-precursor, as I shall discuss later.

For the east bridge points (red crosses), in the high-velocity component ('b' panels), it is clear that the east bridge points fall relatively neatly between the solid lines for shock velocities 175 km/s and 200 km/s (green and orange lines). For the west bridge points, in cases where the points deviate from the HII-region area they are consistent with the same shock velocity, e.g., the low-velocity components in all diagrams. *Thus the high-velocity east bridge component and the low-velocity west bridge component seem consistent with shock excitation for all the line diagnostic diagrams.*

The situation is mixed for the disks of galaxies themselves. As Figures 11b, 12b and 13b show, there are some points within the disks of both galaxies which fall in the composite region of the diagnostic diagram. Some of these points would be consistent with a mixture of HII region and shocked gas excitation. The nucleus of Taffy-S is an ambiguous case, because it could be excited by shocks in a mild outflow, or may be gas excited by UV emission from a weak LLAGN.

The spreading of the points along lines of constant [OIII]λ5007/Hβ ratio in the high-velocity component in the bridge has a number of possible interpretations if I assume that shocks are involved. Firstly, the spread might imply that the shocks are occurring in an ensemble of gas clouds with different pre-shock densities. Such a picture is consistent with previous observations of the Taffy bridge (Peterson et al. 2012, 2018) where I have observed gas in many different excited phases, from HI (Condon et al. 1993) to warm molecular gas from the *Spitzer* IRS; along with the detection of [CI] and [CII] emission (Peterson et al. 2018), and boosted values of

[CII]/FIR and [CII]/PAH ratios. The existence of a highly multi-phase (and multi-density) medium is also very consistent with the detection of soft X-ray emission from the bridge. Thus it might be expected that shocks moving through such a multi-phase gas would encounter a range of pre-shock densities–which would spread the points along lines of constant shock velocity–as observed in Figures 11 and 12 especially.

An alternative explanation might be that some of the gas is of lower metallicity. As the models of Allen et al. 2008 show, reducing the metallicity of the shocked gas moves the points in the diagnostic diagrams to the left at roughly constant values of [OIII]λ5007/Hβ ratio. However, if the collisional models of Vollmer, Braine, and Soida 2012 are correct, the gas in the bridge should have come from many different places within the original pre-collisional disks, and deviations of factors of 100 in metallicity in the bridge seem unlikely. I conclude that it is much more likely that I are observing shocks within the bridge and parts of the galaxy disks which encounter clumps of material at different densities.

What is the effect of ignoring the possible influence of a hot shock precursor in the models? This is an effect where, in high velocity shocks, the gas in the shock is so strongly heated that UV radiation from the shocked gas ionizes large amounts of pre-shocked gas upstream of the shock. I show in Figure 14, an example of the [NII] line diagnostic diagram, the effect of including the shock and the shock precursor (Allen et al. 2008). As can be seen by comparison with Figure 11 the behaviour when I include the shock precursor with velocities < 300 km s^{-1} is very similar to the case with no shock precursor, which fits the data well. At shock velocities > 300 km s^{-1} the models including the shock precursor diverge significantly from these data. Similar behaviour is noted in the other diagnostic diagrams (not shown). This implies that the shock models between 100-300 km s^{-1} fit the bridge data well regardless of whether

the precursor is included. I note, however, that in dense gas (e.g. molecular gas known to also be present in the bridge) the velocity at which a shock precursor may become important will be much lower. Therefore future modeling the molecular shocks may have to take precursor activity into account.

2.5.2 Alternatives to Shock Excitation: Diffuse Lyman Continuum Emission Leaking From HII Regions?

In a recent paper by Weilbacher et al. 2018, it was noted that the Antennae galaxies (NGC 4038/39), like the Taffy system, also exhibit significant diffuse ionized gas emission. Although several mechanisms were put forward to explain the emission, including the possibility of shocks, the authors favor an interpretation that much of the diffuse gas is ionized by Lyman-continuum photons (hereafter Ly-C) "leaking" from large numbers of HII regions found primarily in the disks of both galaxies, as well as HII regions found within the "overlap region". Much (but not all) of the diffuse component was found close to massive star formation complexes in the system. Using multi-color HST imaging of the clusters, the authors were able to compare the luminosity of the Hα emission associated closely with a cluster with theoretical models of the Ly-C flux from the clusters to determine whether the clusters were "leaking" Ly-C photons into the surrounding gas. It was found that many of the HII regions had non-zero escape fractions of Ly-C UV radiation, especially in the center of NGC 4038 and also in the "overlap" region. Thus, for the Antennae system, it was found that the excess diffuse emission within the system could be explained as gas excited by UV radiation escaping from the clusters.

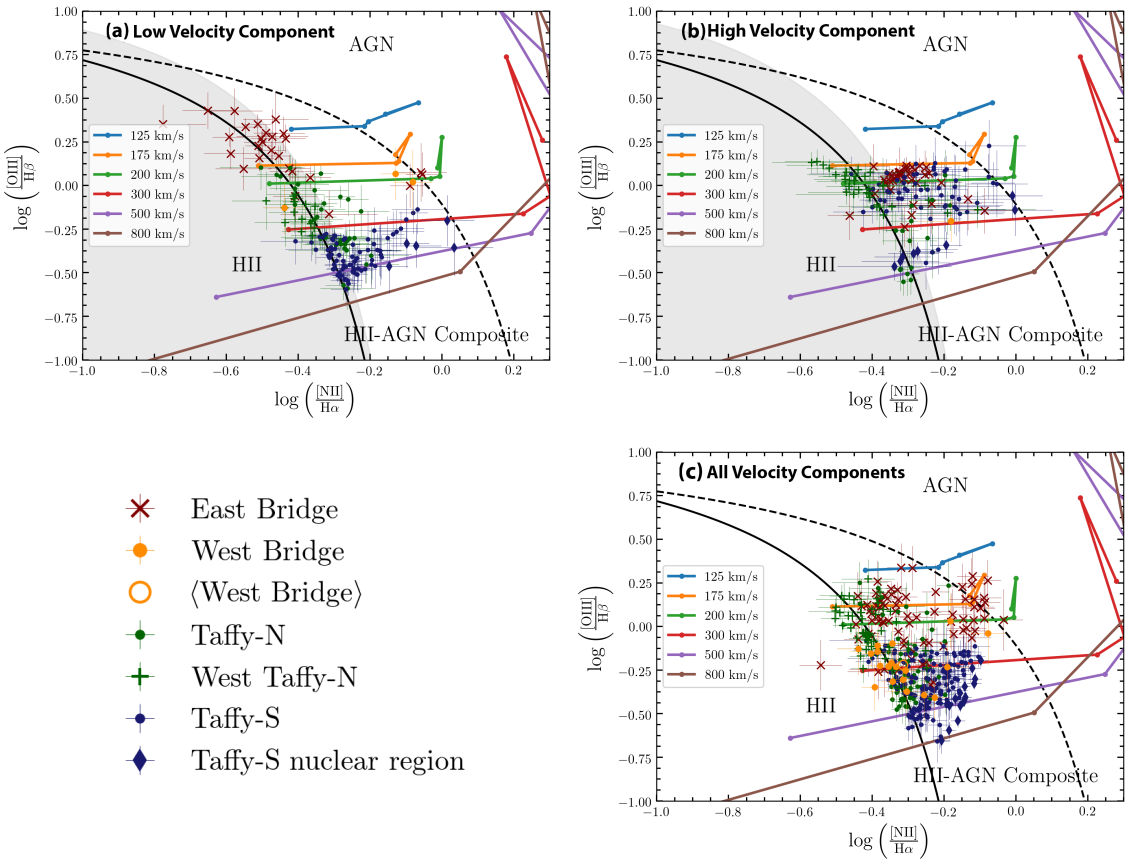

Figure 11. [NII]λ6583Å line diagnostic diagrams. (a): for the low velocity component, (b): for the high velocity component, and (c): total, i.e. sum of both velocity components and also including line ratios from spaxels which show a single component. Each point here represents the line ratios from a single spaxel. The red crosses, green points, and blue points correspond to the eastern bridge, Taffy-N, and Taffy-S, respectively. The blue diamonds are spaxels that fall within the nuclear region of Taffy-S. The green pluses are spaxels from the western part of Taffy-N. The orange circles are spaxels from the western part of the bridge. The unfilled orange circle is the average of line ratios from all the spaxels within the western bridge. These colors are consistent with those used to denote the corresponding regions in Figures 4 and 9, with the exception of the western part of Taffy-N which is shown as a magenta polygon in Figure 4. The panels also show line ratios from the MAPPINGS III shock models (Allen et al. 2008) overlaid on the measured line ratios i.e. colored solid lines. The parameters assumed in the models are Z=Z$_\odot$ and B=5 μG. Along each shock velocity line the points are marked by increasing number density. The classifications are from Lisa J. Kewley et al. 2006. The shaded gray area around the solid black line classifying the HII-region excited gas marks the area I used to put a lower limit on the fraction of gas excited by star formation (see §2.6). The width of the shaded area (above the HII classification line) is twice the size of the average error bar in each panel.

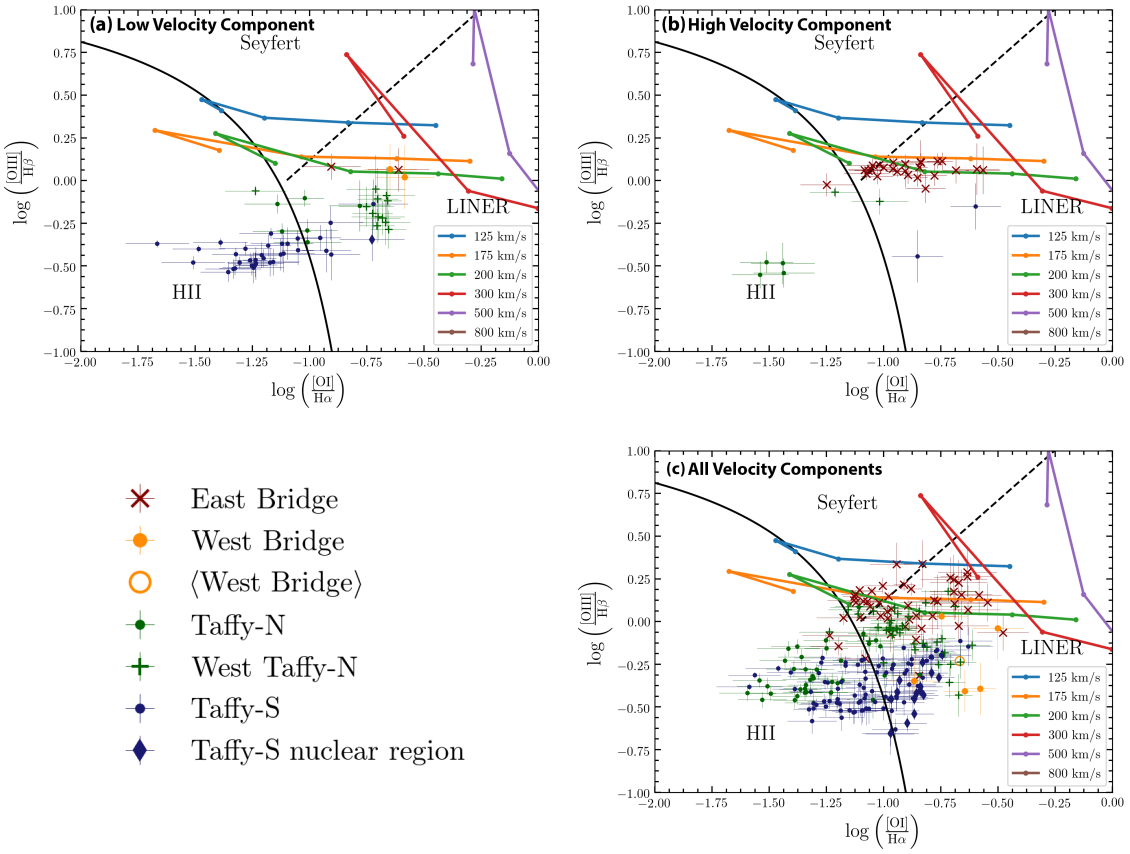

Figure 12. Same as Figure 11 but using the [OI]λ6300Å line. This Figure contains fewer points than the [NII] and [SII] line diagnostic diagrams due to the [OI] line being much weaker than the [NII] and [SII] lines and therefore being undetected in many spaxels.

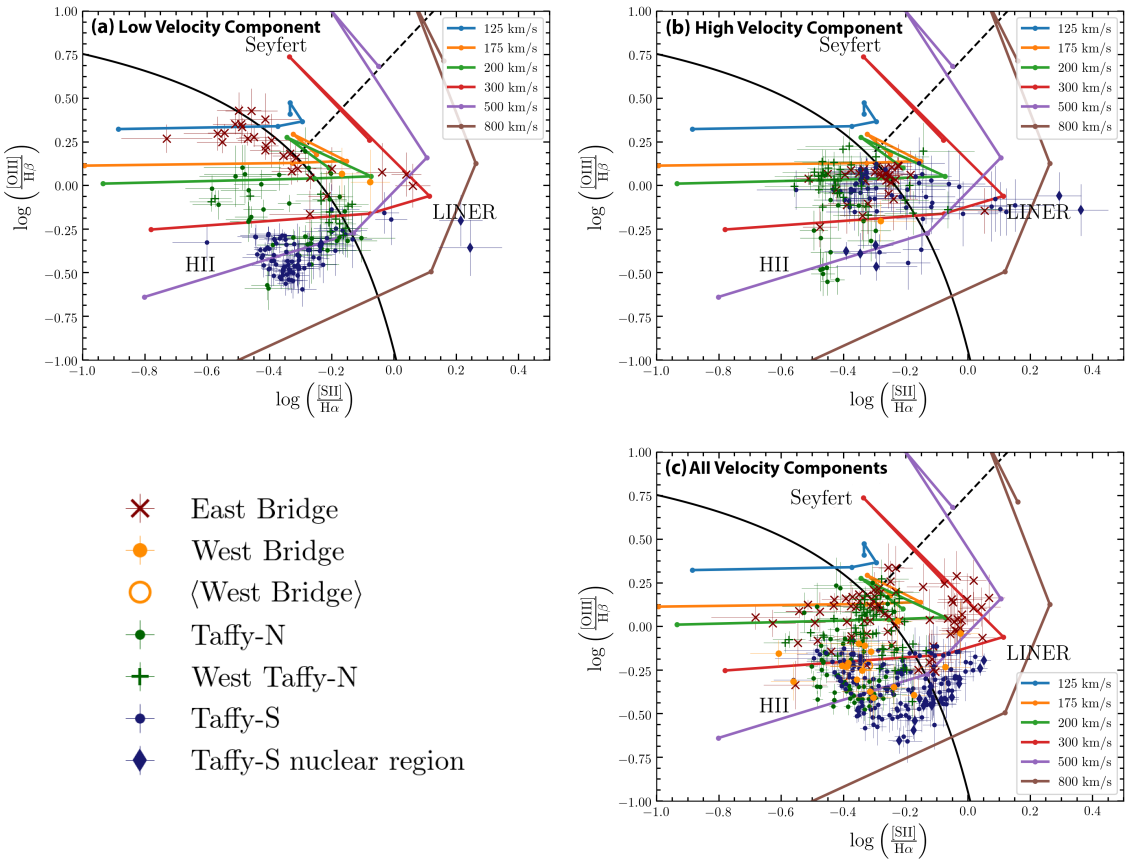

Figure 13. Same as Figure 11 but using the sum of the [SII]$\lambda\lambda$6716,6731 lines.

Could some, or all of the extended ionized gas emission seen in the Taffy come from similarly degraded UV light from HII regions in the disks of the Taffy galaxies that might diffuse outwards and ionize large parts of the Taffy bridge? I estimate (Table 1) that the amount of Hα emission coming from the bridge, after correcting for extinction, is similar to that from Taffy-S and roughly 50% of the emission from Taffy-N. In this case the majority of the escaping photons would have to come from the galaxies themselves, since the star formation rate in the Taffy bridge is very low. Unfortunately, unlike the case of the Antennae, I do not have multi-color high resolution images of the individual star clusters, and this means that it is difficult to perform the same kind of test that was applied, for all individual HII regions, by Weilbacher et al. 2018. As a result, I cannot completely rule out a significant contribution to the ionized medium in the Taffy coming from leaky HII regions. Nevertheless, many other lines of evidence already suggest that shocks must be present in the Taffy bridge, and so I prefer the shock explanation for the excitation of the high-velocity component, rather than leaky HII regions. Future observations will be needed to attempt to model the history of star formation in the clusters in the galaxies, which will allow us to estimate the fraction of UV emission which may escape into the surround gas. This is beyond the scope of the current paper.

2.6 Ionized Gas Fractions, Star formation Rates and Mass in the Ionized Component

Here I describe the method that I employed to estimate a lower limit to the fraction of ionized gas excited by star-formation (as opposed to being shock excited) using the [NII] line diagnostic diagram. I use the [NII] line diagnostic diagram since it contains the most number of points. I start by defining an effective HII-region excitation area.

This is shown as a shaded gray region in the [NII] line diagnostic diagrams of Figure 11. I defined this area simply by "padding" the HII classification line (Lisa J. Kewley et al. 2006) by twice the size of the average error in the y-direction (the y-error being the larger error). I sum up the Hα flux in each spaxel that falls within this region. This flux is divided by the total Hα flux to arrive at the lower limit for the fraction of ionized gas excited by star-formation. This process is repeated independently on each velocity component.

The fraction derived this way is a lower limit because the other spaxels, outside of the shaded area (i.e. in the HII+AGN area) will contain emission from gas excited by star-formation, and I cannot accurately disentangle the excitation from shocks and star-formation (also see text in §2.5.1). The lower limits for the fraction of ionized gas excited by star-formation that I derived are 64% and 46% for the lower and higher velocity component, respectively. For the purposes of the calculations of star formation rate (in §2.6.1) and ionized gas mass (in §2.6.2) I estimate the Hα luminosity, coming only from star-formation, by $\mathrm{L(H}\alpha)_{\mathrm{SF}} = 0.64\,\mathrm{L(H}\alpha)_{\mathrm{low}} + 0.46\,\mathrm{L(H}\alpha)_{\mathrm{high}}$; where $\mathrm{L(H}\alpha)_{\mathrm{low}}$ and $\mathrm{L(H}\alpha)_{\mathrm{high}}$ are the extinction corrected total Hα luminosities in the low and high velocity components, respectively.

This gives us an extinction-corrected value of $\mathrm{L(H}\alpha)_{\mathrm{SF}} = 4.99 \pm 0.54 \times 10^{41}\,\mathrm{erg\,s^{-1}}$ for the lower limit to the Hα luminosity resulting from star-formation for the Taffy system.

2.6.1 Star Formation Rate Estimate From Hα Luminosity

Using the following relation from Kennicutt 1998 I estimate the star formation rate (SFR) in the entire Taffy system and the bridge region (using the entire region

defined as the bridge in Figure 4), including Hα emission from the extragalactic HII region.

$$\psi[\mathrm{M}_\odot\,\mathrm{yr}^{-1}] = 7.9 \times 10^{-42}\,\mathrm{L(H}\alpha)[\mathrm{erg\,s}^{-1}] \tag{2.3}$$

I obtain $\mathrm{L(H}\alpha)_{\mathrm{SF}} = 4.99 \pm 0.54 \times 10^{41}\,\mathrm{erg\,s}^{-1}$ and $\mathrm{L(H}\alpha)_{\mathrm{SF;bridge}} = 1.02 \pm 0.14 \times 10^{41}\,\mathrm{erg\,s}^{-1}$ for the extinction-corrected Hα luminosity coming from star-formation for the entire Taffy system and bridge respectively, using the method described previously. This translates to SFRs of 3.94 $\pm$ 1.0 $\mathrm{M}_\odot\ \mathrm{yr}^{-1}$ and 0.81 $\pm$ 0.22 $\mathrm{M}_\odot\ \mathrm{yr}^{-1}$ respectively for the entire Taffy system and the bridge. These SFRs agree well with previous estimates derived from UV-FIR SED fitting (Appleton et al. 2015) of 3.65 $\pm$ 0.03 $\mathrm{M}_\odot\ \mathrm{yr}^{-1}$ and 0.69$\pm$0.06 $\mathrm{M}_\odot\ \mathrm{yr}^{-1}$ respectively for the total system and the bridge.

Interestingly, recent observations with the Atacama Large Millimeter Array (ALMA) show dense filaments of molecular gas, in the Taffy bridge, with little star-formation in them. These ALMA observations and the overall star-formation properties will be discussed in a future paper (Appleton et al. in preparation).

2.6.2 Ionized Gas Mass

The mass of ionized gas in the Taffy system, and in the bridge assuming Case B recombination (Macchetto et al. 1996; Kulkarni et al. 2014) is given by :

$\mathrm{M}_{ion} = 2.33 \times 10^3\ (\mathrm{L}_{\mathrm{H}\alpha}/10^{39})(10^3/\mathrm{n}_e)\ \mathrm{M}_\odot$

where $\mathrm{L}_{\mathrm{H}\alpha}$ is the extinction corrected Hα luminosity in units of erg s^{-1}, and n_e is the electron density. For the bridge, from the lower limits to the ionized gas fractions from star-formation (see above) I obtained $\mathrm{L(H}\alpha)_{\mathrm{SF;bridge}} = 1.02 \pm 0.14 \times 10^{41}\,\mathrm{erg\,s}^{-1}$. I also have n_e=200 cm^{-3}, based on the ratio of the [SII] lines. This then gives us

$M_{ion} = 1.19 \pm 0.22 \times 10^6$ $M_\odot$. This calculation is uncertain because the Hα emission originates from two different processes – HII regions and very likely shocks. However, it does show that the ionized gas mass is an insignificant fraction ($\sim$0.2%) of the total mass of gas in the bridge ($\sim 7 \times 10^9$ $M_\odot$; made up of a mix of HI and H_2). This is in agreement with the very low ionized gas fraction responsible for exciting the [C 2]157.7μm far-IR cooling line in the bridge (Peterson et al. 2018) determined from the upper limit to the detection of [N 2]206μm in the bridge. For the Taffy system as a whole, using the extinction corrected Hα luminosity coming from star-formation, $L(H\alpha)_{SF} = 4.99 \pm 0.54 \times 10^{41}\,erg\,s^{-1}$, I get $M_{ion} = 5.8 \pm 1.0 \times 10^6$ $M_\odot$ for the mass of ionized gas in the entire Taffy system. Again, this is an insignificant fraction ($\sim$0.8%) of the total gas mass in the Taffy system.

2.6.3 Post-Starburst Populations

I detect Hβ absorption lines within many spaxels on the galaxies. The spectra of post-starburst galaxies are known to contain strong Balmer absorption lines due to their stellar populations being dominated by A type stars. Evidence of a post-starburst population is not uncommon in merging galaxies (e.g. Zabludoff et al. 1996; Yang et al. 2004, 2008), but attempts to measure the age of the stellar population are difficult, especially when only Hβ is observed (see for e.g. Worthey and Ottaviani 1997). Since the spectral coverage did not include other post-starburst indices, I can only provide preliminary results here. Further observations using full UV-optical SED, better absorption line indices, and detailed modeling (e.g. French, Arcavi, and Zabludoff 2016) will be needed to obtain a better estimate for the age for the population which is responsible for the Hβ absorption.

I measured the EW of the Hβ absorption line for each spaxel that contained either the galaxies or the bridge. The EW was measured using,

$$\mathrm{W(H}\beta\mathrm{)\ [\AA]} = \frac{\int_{line} f_\lambda d\lambda}{\langle f_{\lambda;cont} \rangle} \tag{2.4}$$

where the integral is done over the continuum subtracted absorption line fit and $\langle f_{cont} \rangle$ is the average continuum value measured on either side of the Hβ line. LZIFU provides as output the fit to the stellar continuum and the nebular emission lines separately. I use the continuum fit cube to refit a Gaussian absorption line to the region centered on the Hβ absorption. The parameters from this fit then give the area within the absorption line and the average continuum is measured in a band of $\sim$10 spectral elements on both sides of the line.

Figure 5b shows the measured EW map for the Taffy system. Relatively deep Hβ absorption (W(Hβ) > 10) occurs where there is little Hα emission. Two regions of high W(Hβ) lie in the northern and southern parts of the faint stellar ring that surrounds Taffy-S. Another region, in the south-eastern part of Taffy-N, does extend into regions where there is some star formation and older stellar populations are probably present, with the deepest absorption lying outside of the main star formation disk.

It is generally true that values of W(Hβ) of $10 <$ W(Hβ) < 20 implies stellar evolutionary ages for the post-starburst populations of several 100 Myr, and this would imply that there is no connection between the post-starburst population and the current collision between the two galaxies (e.g. Worthey and Ottaviani 1997). From dynamical arguments it has been argued that the collision between the two Taffy galaxies is quite recent (approximately 25-30 Myrs; Vollmer, Braine, and Soida 2012), and so the fact that the outer ring of Taffy-S shows an old population would lead to an apparent problem, *if* the stellar population of the ring was created in the collision.

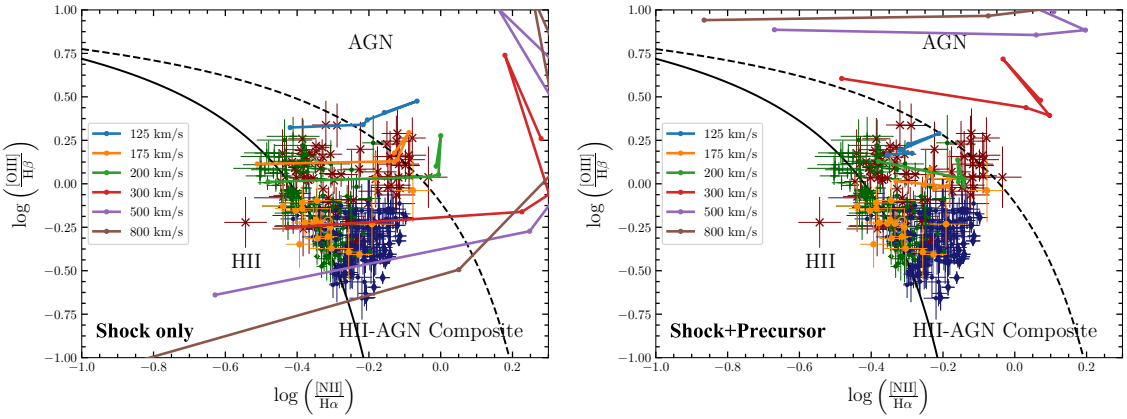

Figure 14. The effect of including the only the shocks compared to including shocks with the shock precursor, from the models of Allen et al. 2008, for the [NII] diagnostic diagram. The symbols (and their colors) and shock model parameters are the same as the line diagnostic diagrams of Figures 11, 12, and 13. The included data points are the same as those on the "All Velocity Components" diagram of Figure 11.

However, one solution might be that the stellar population of the ring is a stellar density wave containing a much older pre-collisional system which had undergone star formation a long time in the past. This is also the conclusion reached by Jarrett et al. 1999 who argue that the ring consists of stars from an old disk population from the pre-collision disk.

The fact that both galaxies contain evidence of post-starburst activity might imply that the galaxies underwent a high-speed encounter in the more distant past which triggered star formation, but did not lead to immediate merger. If that is the case, then we are probably currently witnessing the second (probably final) collision before full merger. Broader wavelength coverage in the blue, to detect more absorption lines and better characterize the age of the post-starburst population, will be needed to test this idea.

2.7 Conclusions

Using visible IFU data from the VIRUS-P instrument on 2.7m telescope at McDonald Observatory for the Taffy system, I have shown the results summarized below.

- Detection of widespread ionized gas within the disks of the Taffy galaxies and the bridge which exhibit very disturbed kinematics, including many regions with double line profiles and emission regions that do not follow regular rotation. Although both galaxies show velocity components that approximate gas rotation around their centers, both galaxies also show peculiar motions, often associated with gas which extends into the bridge between them. The gas associated with Taffy-N (UGC 12915) contains a major kinematic component that does not take part in regular rotation, but exhibits a high velocity dispersion and forms a narrow western bridge to Taffy-S (UGC 12914). Taffy-S, although showing the kinematics of a likely tidally-warped but regular (counter-)rotating disk, also contains a peculiar kinematic component that is associated with a second ionized gas bridge. This eastern bridge component, which extends from Taffy-N, through the region containing the extragalactic HII region and eventually connecting with the Taffy-S, is more closely associated with the molecular bridge seen previously to extend between the galaxies. On the other hand, the western bridge, which is much fainter, appears to be kinematically linked with the western extension of Taffy-N (and the western part of Taffy-S) and shows a mix of HII-region and composite/LINER excitation unlike the main disk of Taffy-N which is largely consistent with HII-region excitation.

- An analysis of the excitation of the ionized gas through diagnostic line ratios shows that a significant fraction of the emission shows a mix of HII-region and LINER-type emission, especially in the areas where two velocity components can be clearly distinguished. The LINER-type emission is especially dominant in the high velocity component in the east-bridge region, but also over significant portions of both galaxies. I observe emission line ratios in the high-velocity component, for the east bridge and the low-velocity component of the west bridge, that are consistent with the gas being excited by shocks with velocities of ∼175-200 km/s, and a range of pre-shock densities. Such evidence for shocks permeating clouds of varying density is consistent with previous observations of the bridge by *Spitzer* and *Herschel*, where strong mid- and far-IR cooling lines are detected from warm molecular and diffuse atomic gas heated by turbulence. While I cannot rule out a contribution to the diffuse ionized emission from Lyman-continuum photons leaking from young HII regions embedded in the disks of both galaxies, the weight of evidence, from previous multi-wavelength observations of the bridge, suggests that shocks are a more likely explanation for the LINER-type emission line ratios seen in the bridge and in parts of the disks of both galaxies. Given the violence of the collision based on previous numerical models of head-on collisions which suggest that the bridge is still in a highly disturbed state, such shocks may not be unexpected.
- Strong Balmer absorption lines ($10 < \mathrm{W(H}\beta)[\text{Å}] < 15$) are observed in parts of the ring associated with Taffy-S (UGC 12914), as well as the south-east portion of the edge-on disk of Taffy-N (UGC 12915). The absorption lines are strongest in regions where the ionized and molecular gas distributions are weak, suggesting that parts of the Taffy system have experienced a burst of star

formation in the past, perhaps from a previous close passage of the two galaxies. If so, it is possible that the current collision may be a second, more dissipative collision, that will likely lead to merger in the near future. Further observations, with a broader blue wavelength coverage than the current observations, will be necessary to better determine the age of the post-starburst populations in both galaxies.

- Although there has been only weak evidence in the past for the nucleus of Taffy-S (UGC 12914) containing a low-luminosity AGN from X-ray properties (Appleton et al. 2015), I detect line widths in the nucleus as large as 320 km s^{-1}. These line-widths are typical of narrow-line Seyfert galaxies. The broad lines appear to extend over 6-10 arcsecs along the minor axis. The excitation properties of the nuclear gas are consistent with LINER emission, but without higher spatial and velocity resolution data I cannot determine whether the Taffy-S nucleus hosts a weak shocked highly confined outflow from a nuclear starburst, or is excited by UV radiation from a LLAGN.
- I provide evidence, supporting much previous work, that the Taffy system has atypically low SFRs for a system having recently undergone a recent major-merger. I find SFRs of 3.94 ± 1.0 $M_\odot$ yr^{-1} and 0.81 ± 0.22 $M_\odot$ yr^{-1} in the entire Taffy system and the bridge (including the extragalactic HII region), respectively. Low star formation rates in this recent post-collisional remnant may result from the highly disturbed nature of the gas in the galaxies and bridge.

Chapter 3

SPECTROPHOTOMETRIC REDSHIFTS FOR Z $\sim$ 1 GALAXIES AND PREDICTIONS FOR NUMBER DENSITIES WITH WFIRST AND EUCLID

This chapter is reproduced from the version published in 2019 in The Astrophysical Journal, Volume 883, Page 157, with permission from the co-authors.

3.1 Introduction

Galaxy evolution studies and cosmological measurements require redshift accuracy at the few-percent level or better. In particular, cosmological measurements such as measurements of the baryon acoustic scale (e.g., Eisenstein et al. 2005; Weinberg et al. 2013), and weak lensing tomography (e.g., Hildebrandt et al. 2012), require redshift accuracy at the percent or better level, and outlier fractions at the sub-percent level (Weinberg et al. 2013). Measurements of galaxy overdensities also require redshifts accurate at the level of a few percent. For example, Pharo et al. 2018, identify overdensities using redshifts estimated from low-resolution grism spectra combined with broad-band photometry. Accurate redshifts (typically with accuracy of $\Delta z/(1+z) \simeq 0.001$) can be obtained by using high-resolution spectroscopic data that allow for the precise fitting of high-resolution synthetic spectra of stellar populations. These can distinguish between synthetic stellar population models from different regions of parameter space, and simultaneously provide accurate redshifts and stellar population parameters. In practice, it is extremely difficult and very expensive to conduct a large scale spectroscopic survey of faint and distant galaxies that is both

unbiased and sufficiently deep to analyze the stellar continua, in order to secure both accurate redshifts *and* detailed stellar population properties. Wide-field large scale ground-based spectroscopic campaigns, e.g., SDSS (York et al. 2000), 6dF (Jones et al. 2004), GAMA (S. P. Driver et al. 2011), have been conducted to obtain high-resolution spectra and accurate redshifts. These spectroscopic ground-based surveys, however, are limited to the relatively brighter sources ($\sim$ 21–22 mag) at lower redshifts ($z \lesssim 0.5$).

In addition, large scale Hubble Space Telescope (*HST*) photometric and grism spectroscopic surveys have obtained photometric redshifts accurate to within a few percent, and have led to a better understanding of the stellar populations of a substantial number of galaxies at intermediate and high redshifts ($z > 1.5$). Notable examples include the Wide Field Camera 3 (WFC3) Early Release Science (ERS) field (Windhorst et al. 2011) and the Cosmic Assembly Near-infrared Deep Extragalactic Survey (CANDELS; Grogin et al. 2011; Koekemoer et al. 2011) which used imaging from WFC3/IR and the Advanced Camera for Surveys (ACS) on the *HST*, while the GRAPES (N. Pirzkal et al. 2004; Pasquali et al. 2006; Ryan et al. 2007; Hathi et al. 2009), PEARS (Ferreras et al. 2009), and FIGS (Norbert Pirzkal et al. 2017) surveys invested 40, 200, and 160 *HST* orbits, covering 11.6, 119, 18.6 arcmin^2, respectively to do slitless spectroscopy with the ACS/G800L and WFC3/G102 grisms. Similarly the 3D-HST survey (Brammer et al. 2012; Skelton et al. 2014; Bezanson et al. 2016), which is a *HST* survey with the WFC3/G141 grism, also invested 248 orbits to conduct WFC3/G141 spectroscopy of the CANDELS fields covering 600 arcmin^2.

The 4000Å break is the strongest absorption feature in rest-frame visible spectra of galaxies, particularly in early-type galaxies whose optical light is dominated by older stars, and also to a lesser extent and more varying extent in late-type star forming galaxies (Hathi et al. 2009). The break is expected to be stronger for later

stellar spectral types and higher metallicities (see, e.g., Bruzual A. 1983; Hamilton 1985), and therefore for galaxies dominated by old and metal-rich stellar populations. It is caused by the superposition of multiple absorption features within a narrow wavelength range close to 4000Å. The H and K absorption lines of Ca II, at 3969Å and 3934Å respectively, make up a significant part of the amplitude of the 4000Å break, which is why it is sometimes also referred to as the Ca H and K break. The strength of the 4000Å break is an excellent proxy for the age of the stellar population, and for the lack of recent star formation activity (e.g., Bruzual A. 1983; Hamilton 1985; Poggianti and Barbaro 1997; Kauffmann, Heckman, White, Charlot, Tremonti, Brinchmann, et al. 2003; Kauffmann, Heckman, White, Charlot, Tremonti, Peng, et al. 2003; Hernán-Caballero et al. 2013). Similar to the 4000Å break, the Balmer break at 3646Å— caused by strong Balmer absorption lines in younger stellar populations ($\lesssim$0.3 Gyr) — is also a useful feature for redshift determination. The 4000Å/Balmer breaks are useful as photometric redshift indicators to achieve accuracy of better than a few percent, particularly if the photometry bands straddle the 4000Å/Balmer breaks.

In this paper, I combine grism spectra, containing a 4000Å/Balmer break, and photometric data to derive spectrophotometric redshifts (SPZs) and compare the accuracy of SPZs to redshifts derived from only photometric data (photo-z) and examine the dependence of redshift accuracy on D4000.

The deep grism data I use in this paper come from the Probing Evolution And Reionization Spectroscopically (PEARS) survey done with the ACS/G800L grism on *HST* (Ferreras et al. 2009; Straughn et al. 2009; Xia et al. 2011; Nor Pirzkal et al. 2013). These slitless grism spectra are much lower in resolution (R$\sim$100 for ACS Wide Field Channel WFC/G800L; Pasquali et al. 2006) than traditional slit-spectroscopy

(which typically have R$\gtrsim 10^3$), but clearly have higher spectral resolution than broad-band filters. While traditional slit-spectroscopy is inherently restricted to pre-selected objects in the Field-of-View (FoV), slitless grism spectroscopy is capable of providing spectra for nearly *all* sources in the FoV, after accounting for spectral overlap (e.g., Ryan, Casertano, and Pirzkal 2018).

I use PEARS grism spectra for galaxies within $0.600 \leq z \leq 1.235$. This redshift range is selected so that the 4000Å break, if present, falls within the ACS/G800L grism wavelength coverage of 0.6–0.95 μm. I also restrict our sample further by selecting galaxies which have a discernible 4000Å break, i.e., having D4000$\geq$1.1 (see §3.3.1 and 3.3.2 for details on our measurements and our sample selection). I note that our results are based on grism spectra with a resolution of R$\simeq$100 and a wavelength coverage of $6000 \leq \lambda[\text{Å}] \leq 9500$. If either or both of these parameters increases i.e., a higher resolution and/or larger wavelength coverage for grism spectra, I expect the SPZ accuracy to improve over photo-z accuracy in absolute terms and also for lower D4000 values, as will be the case for the planned Wide Field InfraRed Survey Telescope (WFIRST) and the Euclid space-based observatories.

This paper is structured as follows: in §3.2 I provide details of the slitless spectroscopy data and the PEARS survey. In §3.3, I explain the methods used for measurements of the 4000Å break and our sample selection, and in §3.4, I describe our SED fitting procedure for estimating redshifts. In §3.5, I evaluate the dependence of our photo-z, grism-z, and SPZ accuracy with D4000 by comparing to ground-based spectroscopic redshifts. In §3.6, I provide the number density predictions based on continuum derived redshifts for observations by future observatories, such as WFIRST and Euclid. I conclude in §3.7. Wherever needed, I used the following cosmology: a flat Universe with $H_0 = 67.4\ \mathrm{km\,s^{-1}\,Mpc^{-1}}$, $\Omega_m = 1 - \Omega_\Lambda = 0.315$, from the Planck

2018 results (Planck Collaboration et al. 2018a). All magnitudes quoted in this paper are AB magnitudes (Oke and Gunn 1983).

3.2 Observations

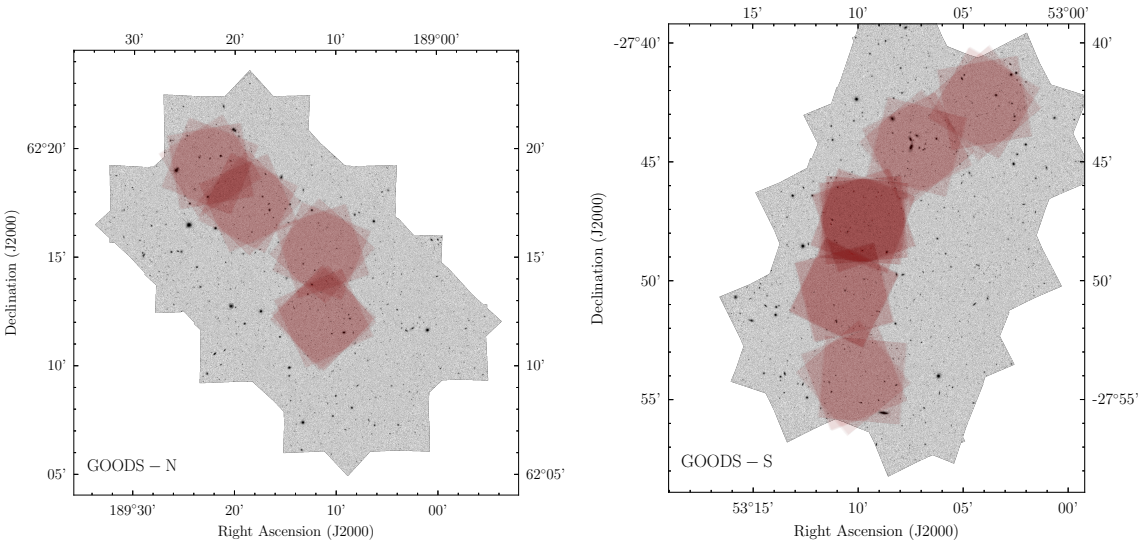

Figure 15. The coverage of the PEARS survey within the GOODS fields. The red pointings, superimposed on a HST/ACS/F606W mosaic from the 3D-HST collaboration, show the primary coverage of the PEARS survey with the ACS G800L grism.

I use slitless spectroscopy obtained with the *HST* as part of the PEARS survey (GO 10530; PI - S. Malhotra). The PEARS survey was awarded 200 orbits in Cycle 14 to cover 8 fields in the Great Observatories Origins Deep Survey (GOODS) North (GOODS-N) and South (GOODS-S) regions (Giavalisco et al. 2004) to a depth of $z'_{AB} \leq$ 27 mag with the ACS/WFC G800L grism. A ninth ultra-deep field to $z'_{AB} \lesssim$ 28 mag overlaps the Hubble Ultra Deep Field (HUDF; Beckwith et al. 2006). The total area covered is $\sim$119 arcmin^2. The G800L grism delivers $+1^{st}$ order spectra with a dispersion of about 40Å per pixel (Pasquali et al. 2006). The best resolution of

R$\sim$100 is achieved for point sources, but for most of the sources considered in this paper (see §3.3.2 for details on our selected sample), which are spatially extended, the effective resolution is lower because the spectrum is convolved with the object morphology along the dispersion direction (Pasquali et al. 2001).

The ACS G800L grism nominally covers 0.55–1.05 μm (for spectra dispersed in the positive first order). The useful wavelength range, where the throughput of the grism exceeds 10%, is 0.60–0.95 μm. While somewhat dependent on the exact bandpasses used to measure the break strength, this allows one to trace the 4000Å break uninterrupted from $z \simeq 0.600$ to $z \simeq 1.235$. I refer to §3.3.1 for the definition of the break indices and for the justification of our use throughout this paper of D4000 over D_n4000. If the D_n4000 index is used, instead of D4000, then the redshift range is $0.558 \leq z \leq 1.317$.

Fig. 15 shows the footprints of the PEARS pointings within the GOODS-N and GOODS-S regions. Each of the 8 deep PEARS pointings were observed for a total of 20 *HST* orbits, while the ultra-deep pointing on the HUDF totaled 40 orbits. In order to mitigate contamination of galaxy spectra that may (partially) overlap at any given dispersion direction, each pointing was visited at three different position angles (PAs), except for 2 fields in GOODS-S which were observed at four PAs. Direct images through the ACS/WFC F606W filter were taken to astrometrically align the G800L grism exposures and to provide the zeropoint of the grism wavelength solution.

For more details about slitless spectroscopy with the ACS/G800L grism and its data reduction the reader is referred to N. Pirzkal et al. 2004 and Pasquali et al. 2006. I refer to Nor Pirzkal et al. 2013 for a description of the reduction and analysis specific to PEARS data. Pasquali et al. 2006 describe the basics of ACS grism observations and the strategy used to calibrate grism observations in orbit.

3.3 4000Å Break Measurement and Sample Selection

3.3.1 D4000 Measurement

I measure the 4000Å break in the rest-frame of the galaxies that were in the PEARS survey, and which also had measured photometry from the 3D-HST and CANDELS surveys. The galaxies are distributed over the redshift range $0.600 \leq z \leq 1.235$. In this work, the 4000Å break is measured by the D4000 (Bruzual A. 1983; Hamilton 1985), as opposed to the D_n4000 index (Balogh et al. 1999; see below). The D4000 index (see, e.g., Bruzual A. 1983; Hamilton 1985) measures the ratio of the integrated continuum flux density (in f_ν units) in the bandpass from 4050Å to 4250Å to the integrated continuum flux density in the bandpass from 3750Å to 3950Å (Eq. 3.1). The D_n4000 index, where the n stands for "narrow", measures the ratio of the integrated continuum flux density in the bandpass from 4000Å to 4100Å to the flux in the bandpass from 3850Å to 3950Å (Eq. 3.2).

$$\mathrm{D4000} = \int_{4050\text{Å}}^{4250\text{Å}} f_\nu d\lambda \Big/ \int_{3750\text{Å}}^{3950\text{Å}} f_\nu d\lambda \tag{3.1}$$

$$\mathrm{D_n4000} = \int_{4000\text{Å}}^{4100\text{Å}} f_\nu d\lambda \Big/ \int_{3850\text{Å}}^{3950\text{Å}} f_\nu d\lambda \tag{3.2}$$

The narrower definition, D_n4000, is less sensitive to reddening effects, and is used relatively more in recent literature (e.g, Li et al. 2015; Zahid and Geller 2017). Because I am using low-resolution grism spectra, the measurement of D_n4000 is more likely to be less accurate. This is because the break must fall in a relatively narrower wavelength range (as compared to D4000) for the measurement to be accurate. Since the spectrum must also be deredshifted before measuring the break strength, this

"narrow" constraint also requires the redshift estimate to be more accurate in order for the D_n4000 measurement to be robust. Furthermore, there are fewer flux measurements within each wavelength bin to integrate over while using D_n4000 compared to D4000, which could again lead to the D_n4000 to be less robust than D4000. Therefore, when comparing the accuracy of spectrophotometric redshifts with photometric redshifts for different 4000Å break strengths, I prefer to measure these break strengths in the grism spectra of our galaxies using the D4000 index rather than the D_n4000 index. Appendix A provides details on the error analysis for the D4000 measurement.

3.3.2 Sample Selection

The sample of galaxies used in this paper comes from the public master catalog of galaxies and their grism spectra released by the PEARS survey[1]. This catalog contains 9551 galaxies (4082 in GOODS-N and 5469 in GOODS-S). I matched the PEARS master catalogs (using a matching radius of 0.″3) with photometry catalogs from the 3D-HST survey (Skelton et al. 2014) and our catalog of ground-based spectroscopic redshifts in the GOODS regions. This gives us all galaxies which have measured photometry, grism spectra, and ground-based spectroscopic redshifts. The matching with the ground-based spectroscopic redshift catalog is done so that I can check the accuracy of our redshifts (see §3.5). The 3D-HST photometry catalog contains photometry from multiple ground and space-based surveys. I use 12-band photometry from u-band (ground-based) to 8μm (*Spitzer* IRAC). I refer the reader to the 3D-HST photometry paper for details on the imaging sources (Table 3 in Skelton et al. 2014). This matching results in a sample of 1863 galaxies.

[1]https://archive.stsci.edu/prepds/pears/

Table 3. Summary of sample selection cuts

	Selection cut	Number of galaxies remaining after cut
1.	PEARS master catalog	9551
2.	Matching with 3D-HST photometric catalog and ground-based spectroscopic redshift catalog	1863
3.	Redshift cut i.e., $0.600 \leq z_{spec} \leq 1.235$	790
4.	Combined cuts: a) $\mathcal{N} > 10$ b) Contamination $< 33\%$	602
5.	Final sample for which I measured photometric, grism, and spectrophotometric redshifts. a) 1.1≤D4000<2.0 b) None/incomplete flux measurements within D4000 bandpass c) Remove worst quality spectroscopic redshifts	497

I then applied a redshift cut of $0.600 \leq z \leq 1.235$ to the ground-based spectroscopic redshifts to get galaxies which could contain a 4000Å break in their grism spectra. This results in a sample of 790 galaxies. A note on GOODS-N astrometry is in order here: because the PEARS catalogs were made with pre v2.0 ACS GOODS images, before matching the PEARS catalog with 3D-HST and ground-based spectroscopic redshift catalogs, I also corrected for the known offset in the declination of pre v2.0 ACS images for GOODS-N. This offset is ∼0.3 arcsec (see the readme file for v2.0 ACS images[2]).

I also apply a cut on the Net Spectral Significance, $\mathcal{N} \geq 10$. Briefly, the Net Spectral Significance is a proxy for the useful information content within a spectrum. For example, from N. Pirzkal et al. 2004, $\mathcal{N} > 8.5(n_{pix}/100)^{1/2}$ corresponds to the

[2]https://archive.stsci.edu/pub/hlsp/goods/v2/h_goods_v2.0_rdm.html

detection of at least a 3σ signal in the grism data; where n_{pix} is the number of independent spectral elements. In our case, I typically have $n_{pix}\sim88$, which implies that a value of $\mathcal{N} > 8$ corresponds to at least a 3σ detection of signal in the grism data. I refer the reader to appendix B for the definition and also to N. Pirzkal et al. 2004 for details. I also reject galaxies with excessive contamination (as measured by the PEARS pipeline reduction) – defined here as any galaxy which has more than 33% of its continuum flux contaminated i.e., likely coming from its line-of-sight neighbors (N. Pirzkal et al. 2004; Nor Pirzkal et al. 2013; Norbert Pirzkal et al. 2017). I also reject an additional 5 galaxies that have a D4000 error larger than 0.5. These cuts give us 602 galaxies. Finally, before I run the code to estimate the three types of redshifts (i.e., photometric, grism, and spectrophotometric), I restrict the range to D4000$\geq$1.1. This "color" cut is used to remove grism spectra of galaxies that would not be useful in determining redshifts, since they do not contain a discernible 4000Å break. This brings the final sample of galaxies for which I estimate redshifts to 497 galaxies. Table 3 summarizes our selection cuts. Figure 16 shows the distribution of D4000 in our sample (note that this figure includes galaxies with D4000$<$1.1 to clearly show the distribution).

3.4 SED Fitting Procedure

3.4.1 Template Library

I use the Bruzual and Charlot (2003; hereafter BC03) library of stellar population synthesis (SPS) models (Bruzual and Charlot 2003) to compare with the observed grism and photometric data of a galaxy to infer its redshift. The synthetic spectra

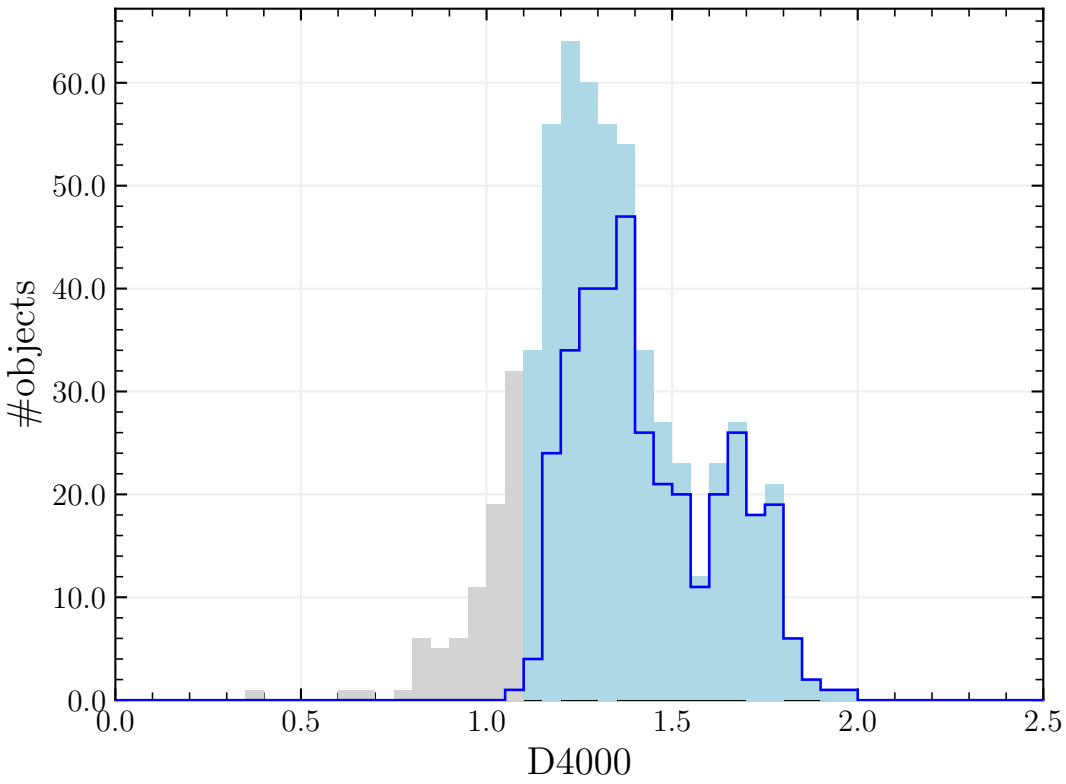

Figure 16. The distribution of D4000 for all 602 galaxies within our redshift range and which also passed our Net Spectral Significance and contamination cuts. The light blue shaded area shows the D4000 range for galaxies included in our final sample, i.e., D4000≥1.1. The overlaid blue histogram shows the distribution of those galaxies that have a 3σ or better measurement of D4000, i.e., $(\mathrm{D4000}-1.0)/\sigma_{D4000} \geq 3.0$ (see §3.5).

include models with 3 different star formation histories (SFHs): 1) instantaneous burst also referred to as Simple Stellar Populations (SSPs); 2) exponentially declining SFH also referred to as Composite Stellar Populations (CSPs); and 3) constant SFH, where the upper limit of the time scale (τ) on our exponentially declining models is ∼63 Gyr. This is much older than the current age of the Universe, so that this model effectively has a constant SFH.

I generate a grid of templates with the age, metallicity, dust extinction (as measured by A_V) and SFH as parameters. All the models are normalized to form a total stellar

mass of 1 $M_\odot$. The models are restricted to an age range of 10 Myr to 7.95 Gyr. This upper limit is decided by the age of the Universe at the lowest value in our redshift range, i.e., this is the oldest possible age for any galaxy in our sample. However, while fitting each individual galaxy, the age of the model is restricted to be less than the age of the Universe, depending on the redshift of the galaxy under consideration. The SSP models have 6 metallicity values: $0.005\,Z_\odot$, $0.02\,Z_\odot$, $0.2\,Z_\odot$, $0.4\,Z_\odot$, $Z_\odot$, and $2.5\,Z_\odot$. The CSP models, however, are restricted to solar metallicity values for the sake of computational efficiency. For the exponentially declining SFHs I use a grid for the e-folding time τ (in Gyr) that has a range of $-2 < \log\tau < +2$ and a step-size $\Delta\log(\tau)$ of 0.02. For a screen of dust, the optical depth, τ_V, is related to visual dust extinction, A_V, by $A_V = 1.086\tau_V$. For τ_V I adopt a grid with a range of $0.0 \leq \tau_V \leq 2.9$ and a step size of 0.2. The BC03 models use the prescription given by Charlot and Fall 2000 to include the effect of dust extinction on the stellar light. The wavelength range for all the models generated by BC03 is 91Å to 160μm. The total number of templates used is 37761.

Since the BC03 templates do not contain emission lines, I manually add emission lines to the model spectra. Following the prescription given by Anders and Fritze-v. Alvensleben 2003, I relate the number of Lyman continuum photons (N_{Lyc}) and the strength of non-Hydrogen emission lines to the Hβ line strength.

$$f(H\beta) = 4.757 \times 10^{-13} \,.\, N_{Lyc} \tag{3.3}$$

For each template, the BC03 code gives N_{Lyc} as one of its output parameters, and this allows us to get the Hβ and metal emission line fluxes. The ratios of the Hydrogen recombination lines are related to the Hβ flux as given by Hummer and Storey 1987, assuming ISM conditions of $n_e = 10^2 cm^{-3}$ and $T_e = 10^4 K$ and Case B recombination. For the sake of computational efficiency I only include typically observed optical

emission lines such as Hα, Hβ, Hγ, Hδ, [MgII]λ2800, [OII]λ3727, [OIII]$\lambda\lambda$4959,5007, [NII]$\lambda\lambda$6548,6583, and [SII]$\lambda\lambda$6716,6731.

3.4.2 Fitting and Error Estimation

The procedure I follow to arrive at the best fit BC03 model is a χ^2 minimization method which accounts for correlated data in the grism spectrum. For every galaxy, I compare the entire model set to the observed data of the galaxy to get a χ^2 value for each model. The χ^2 statistic is defined by,

$$\chi^2 = (F - \alpha M)^T \; C^{-1} \; (F - \alpha M)\,, \tag{3.4}$$

where F and M are the flux and model SED vectors, respectively, which are in flux density units (i.e., $\mathrm{erg\,s^{-1}\,cm^{-2}\,\AA^{-1}}$), and C^{-1} denotes the inverse of the covariance matrix. There is only a single free parameter for each model, the vertical scaling factor α, the value of which is found by finding where the first order derivative of χ^2 vanishes:

$$\frac{\partial \chi^2}{\partial \alpha} = 0 \Rightarrow \alpha = \frac{\sum_{ij} \left(F_i\, M_j + F_j\, M_i\right) / \sigma_{ij}^2}{2 \sum_{ij} M_i\, M_j / \sigma_{ij}^2} \tag{3.5}$$

Here, $1/\sigma_{ij}^2$ is the 'ij'th element in the inverse of the covariance matrix. On the diagonal of the covariance matrix this corresponds to the variance on each individual flux point in the observed data. Details on the covariance matrix estimation (to account for correlated data in the extracted slitless spectra) and a brief explanation for Eq. 3.5 are given in Appendix C. To arrive at the redshift estimate I choose the redshift corresponding to the best-fit model which has an age that does not exceed the age of the Universe at that redshift.

This procedure remains the same in essence regardless of the redshift that is being computed, i.e., photometric, grism, or spectrophotometric. To estimate photometric redshifts, one needs to (i) redshift the high-resolution model spectra, and (ii) compute fluxes for the redshifted models through all filters for which photometry is available, before the comparison with the photometric data is performed. The only simplification in the case of photometric redshifts is that the covariance matrix is taken to be diagonal for photometric data, since the CANDELS/*HST* filters are all essentially non-overlapping and therefore largely independent. In the case of grism redshift estimates, one must (i) redshift the high-resolution model spectra, (ii) convolve the models with the Line Spread Function (LSF), and (iii) resample the redshifted, convolved model spectra to the grism spectral dispersion of 40Å per pixel. Finally, when estimating spectrophotometric redshifts from the combination of grism and photometric data, I apply all these modifications to the models before performing the χ^2 minimization.

I consider a range of possible redshifts for each galaxy within $0.30 \leq \mathrm{z} < 1.50$ with a step size of $\Delta \mathrm{z} = 0.01$. I experimented with $\Delta \mathrm{z} = 0.005$ and found no significant improvement in the redshift estimates at significant cost of computing time. The larger redshift range is required to properly sample the redshift probability distribution, p(z) curve, in cases where the galaxy redshift is at the edge of the redshift range over which the 4000Å break is visible, i.e., $0.600 \leq z \leq 1.235$. The redshift in step (i) above comes from iterating over all the redshifts in this range, i.e., for each redshift in this range I carry out the three steps mentioned above, and construct a map of χ^2 values.

The convolution of the models with the LSF of the galaxy is done to take into account the effects of the morphology of an object on its spectrum. Because of the absence of a spectroscopic slit in grism data, the orientation of the object with respect to the dispersion direction can cause the LSF and hence the resulting spectrum to be

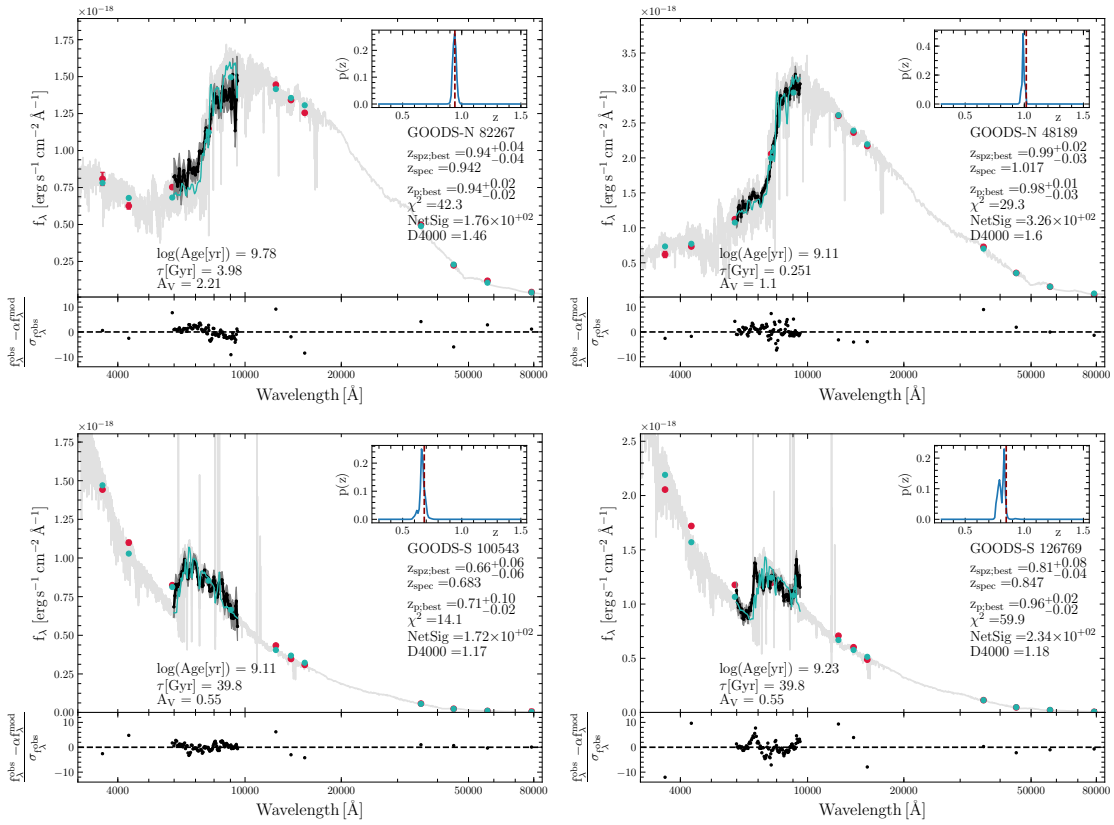

Figure 17. Example spectra and fit residuals from our SPZ fitting procedure for four galaxies in our sample at various D4000 values. The black solid line is the grism data with error bars shown in gray. The observed photometry is shown as red points with error-bars. The light gray line is the best fit high-resolution BC03 model at the estimated redshift. The light green solid line and points are the best fit BC03 model downsampled to the grism redshift and the model photometry. The "best" spectrophotometric redshift from our code, which is the redshift corresponding to the minimum χ^2, is shown on the plot legend along with the ground-based spectroscopic redshift as well as the photometric redshift. The p(z) curve for the galaxy is shown in the upper right corner as an inset figure with the ground-based redshift shown as a red dashed line. The plot legend also shows the galaxy ID, Net Spectral Significance ($\mathcal{N}$), D4000 (based on the ground-based spectroscopic redshift), and other derived parameters from the fitting routine. The bottom panels show the residuals for the fit, i.e., $(f_\lambda^{obs} - f_\lambda^{model})/\sigma_{f_\lambda^{obs}}$. Note that the flux axis is plotted here in f_λ units for visual clarity since the 4000Å break is more prominent in f_λ units, but that the D4000 measurement is done in f_ν units.

quite different at different position angles. This knowledge of the LSF is important because the LSF will cause any absorption or emission features that might be present — like the 4000Å break — to be diluted, and therefore cause a significant variation in the measurement of indices such as D4000. This effect is even more pronounced for an index with narrower wavelength bandpasses, such as D_n4000. In our case, for the PEARS data, I evaluate the Net Spectral Significance, $\mathcal{N}$ (appendix B), for the spectrum at each position angle and select the spectrum with the highest $\mathcal{N}$ to compare to the BC03 SPS models.

Apart from the LSF convolution, it is also necessary that the SED models and the grism data are sampled to the same spectral resolution before being compared to find a best fitting model. The spectral resolution of the BC03 models is 3Å in the range $3200 < \lambda\,[\text{Å}] < 9500$, and lower outside this range (Bruzual and Charlot 2003). A mismatch in resolution would lead to an improper comparison between the high-resolution model and the low-resolution data, because spectral features in the model would remain much sharper than in the data yielding larger values of the χ^2 statistic that I am attempting to minimize. The models are therefore re-sampled to the wavelength resolution of the grism spectrum. This re-sampling of the model is done simply by taking the average flux of all points in the model that fall within the wavelengths of two adjacent points on the grism spectrum. This is done for all points within the grism spectrum wavelength coverage. For the purposes of finding a best-fit model, I only consider the part of the model spectrum that has the same wavelength range as the grism spectra.

I derive redshift uncertainties analytically, by first deriving errors on the reduced χ^2 (see, e.g., Andrae, Schulze-Hartung, and Melchior 2010; Hogg, Bovy, and Lang 2010), and then deriving the corresponding error on the redshift. The error on the

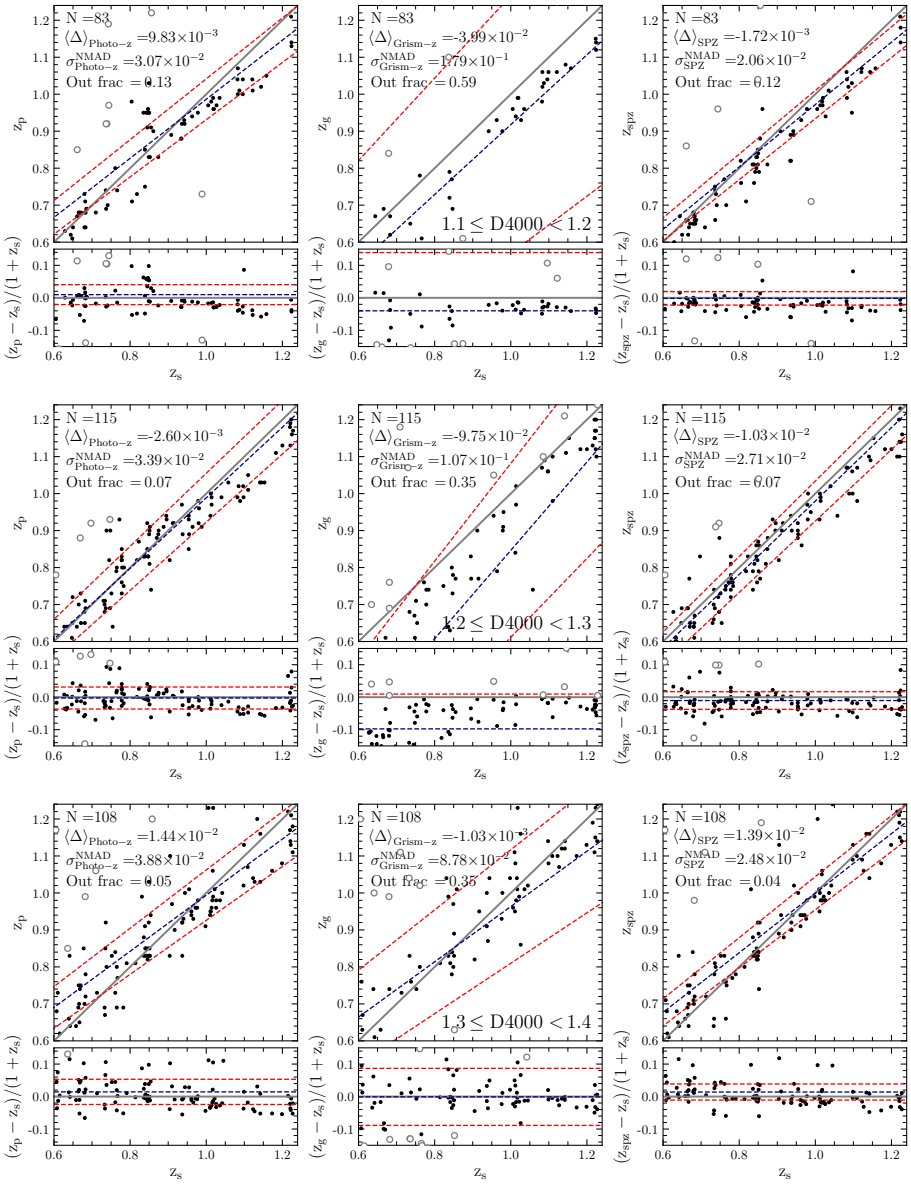

Figure 18. Photo-z (z_p), grism-z (z_g), and SPZ (z_{spz}) redshift accuracy for different D4000 bins by comparing to ground-based spectroscopic redshifts (z_s). Each row on this figure contains galaxies that fall in the D4000 range shown in the middle subplot. Within each row are three subplots: photo-z on the left, grism-z in the middle, and SPZ on the right. The top panels within each subplot show each of the three redshifts vs. the ground-based spectroscopic redshift. The bottom panels show the residuals, i.e., $(z_* - z_s)/(1+z_s)$, where z_* is either z_p, z_g, or z_{spz}. The D4000 bins sizes are steps of 0.1, except at the two bins with largest D4000 (in Figure 19), where I have a larger bin size to get a comparable number of galaxies in each bin. The gray solid line in the top panels is the 1:1 line. The blue and red dashed lines are the mean and $\pm 1\sigma_{\rm NMAD}$ spread, respectively. The gray open circles are $>3\sigma$ outliers.

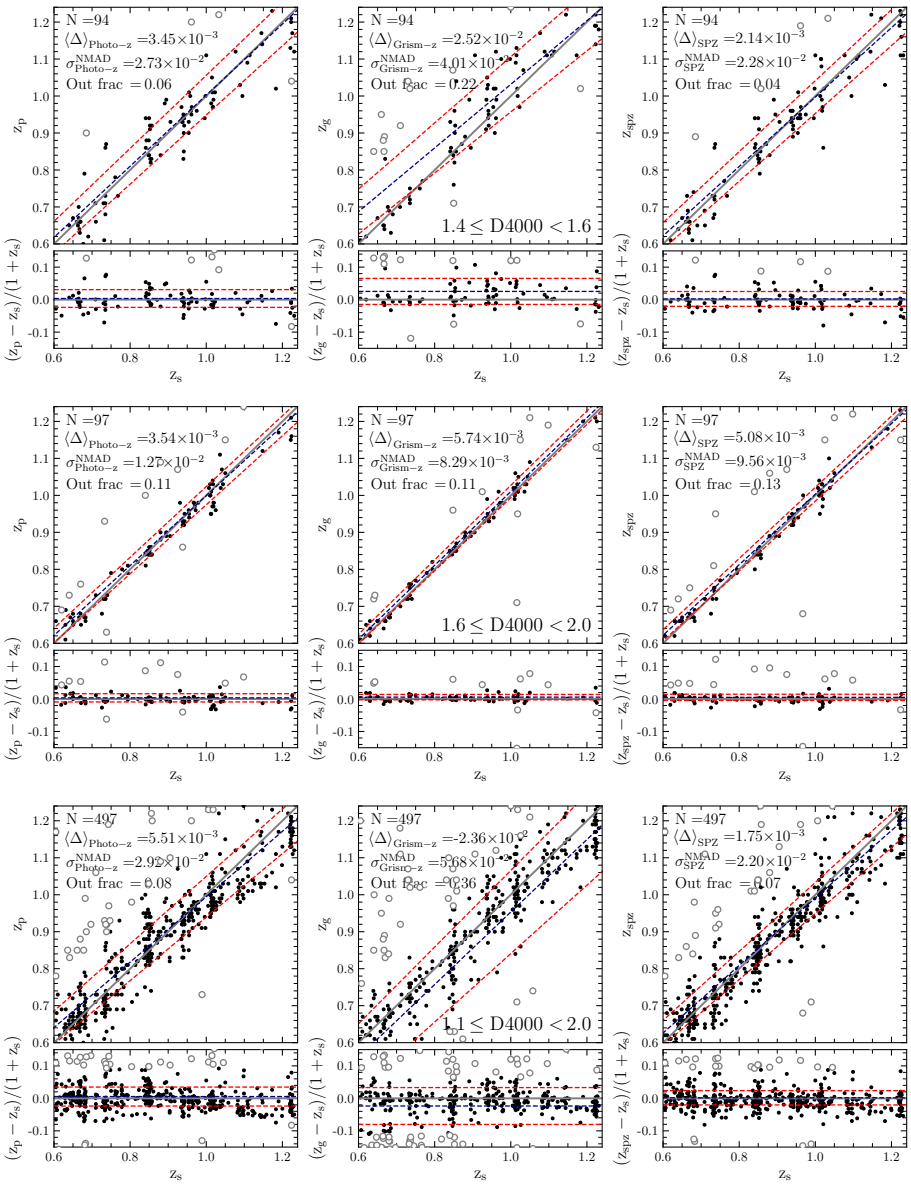

Figure 19. Same as Figure 18 but for the two larger D4000 bins (top and middle) and the entire D4000 range (bottom).

Table 4. Redshift statistics

D4000 range	N	Outlier fraction			Photo-z residuals		Grism-z residuals		SPZ residuals	
		Photo-z	Grism-z	SPZ	Mean	$\sigma_{\rm NMAD}$	Mean	$\sigma_{\rm NMAD}$	Mean	$\sigma_{\rm NMAD}$
$1.1 \leq$ D4000 ≤ 1.2	83	0.13	0.59	0.12	$+0.010$	0.031	-0.040	0.179	-0.002	0.021
$1.2 \leq$ D4000 ≤ 1.3	115	0.07	0.35	0.07	-0.003	0.034	-0.098	0.107	-0.010	0.027
$1.3 \leq$ D4000 ≤ 1.4	108	0.05	0.35	0.04	$+0.014$	0.039	-0.001	0.088	$+0.014$	0.025
$1.4 \leq$ D4000 ≤ 1.6	94	0.06	0.22	0.04	$+0.003$	0.027	$+0.025$	0.040	$+0.002$	0.023
$1.6 \leq$ D4000 ≤ 2.0	97	0.11	0.11	0.13	$+0.004$	0.013	$+0.006$	0.008	$+0.005$	0.010
Full D4000 range:										
$1.1 \leq$ D4000 ≤ 2.0	497	0.08	0.36	0.07	$+0.006$	0.029	-0.024	0.057	$+0.002$	0.022

Quantifying the accuracy of the three different redshifts while stepping through D4000 bins.

reduced χ^2 is given by $\sqrt{2/d.o.f.}$, where d.o.f. is the number of degrees of freedom. Our model has one free parameter, the vertical scaling factor α, and the d.o.f. is given by the difference between number of observed flux points ($\rm N_{data}$) and the number of parameters in fit which gives d.o.f. $= (\rm N_{data} - 1)$. This also allows us to accurately estimate asymmetric uncertainties in cases where the χ^2 minimum is asymmetric.

Figure 17 shows four example spectra and photometry, with varying D4000 values, to show results from our SED fitting routine. It can be seen that our fitting process gives decent results for both 4000Å (top row) and Balmer breaks (bottom row). Although it does not appear to affect the fitting results, I note that the χ^2 values for SPZ and photo-z are much larger than the optimal value of 1.0. This is likely due to systematic errors in the absolute photometric calibration, because our photometric data come from multiple different instruments and observatories. It can also be seen that the residuals for the grism data are scattered tightly around zero, whereas the photometric points can have much larger residuals. As another visual check, I also compute the p(z) curves for each galaxy. This is done by first converting the χ^2 map to a likelihood map, $\mathcal{L} \sim e^{-\chi^2/2}$, which is then marginalized over all model parameters to convert it to a redshift probability distribution, i.e., a p(z) curve. In Table 5 I

provide our redshift estimates and their uncertainties along with the other relevant parameters.

3.5 The Dependence of Redshift Accuracy on D4000

I now investigate the dependence of the accuracy of the three types of redshifts on the 4000Å break strength, D4000. Our derived redshifts are compared to ground-based spectroscopic redshifts which are often based on emission lines.

Figures 18 and 19 show this comparison of accuracy between the photometric (broad-band), grism (only), and spectrophotometric (broad-band plus grism) redshifts while stepping through bins of increasing D4000. I quantify the outlier fraction and the mean and spread of our sample for our three types of redshifts, for different bins of D4000, in Table 4. The mean of the residuals is given by $\langle \Delta z/(1+z_s) \rangle$, where Δz is $(z_{p;g;spz} - z_s)$. The spread in the distribution of redshift residuals is measured by using the Normalized Median Absolute Deviation (σ_{NMAD}; see, for e.g., Brammer, van Dokkum, and Coppi 2008). The σ_{NMAD} is given by:

$$\sigma_{NMAD} = 1.48 \times \text{median}\left(\frac{\Delta z - \text{median}(\Delta z)}{1+z_s}\right). \tag{3.6}$$

A redshift value is defined as an outlier when its $|\Delta z/(1+z_s)|$ value is greater than $3\sigma_{NMAD}$ away from the mean. For the sake of consistency I use the σ^{phot}_{NMAD}, for photometric redshifts, as the σ_{NMAD} in the definition of outlier. The entire sample of 497 galaxies over the D4000 range of $1.1 \leq D4000 < 2.0$ is shown in the bottom three panels in Figure 19.

It can be seen that the grism redshifts at values D4000<1.3 show a $\Delta z/(1+z_s)$ offset at the level of < -0.1. This is due to a significant number of outliers toward

the blue end of the redshift range. This occurs because, for galaxies with a relatively weaker 4000Å/Balmer break – and therefore lower significance (see following discussion and Figure 20b) on the measured value of D4000 – our fitting routine is driven to the blue edge of the redshift grid. This is also the reason why the middle subplot in the first two rows, of Figure 18, has somewhat fewer points than the other two subplots. For D4000$\gtrsim$1.3 this offset is significantly diminished, and is similar for all three types of redshifts. From Figures 18 and 19 and Table 4, it can be seen that the SPZ improves over the photo-z, as measured by the spread in the residuals, i.e., $\sigma_{\rm NMAD}$, for all D4000 values by $\sim$17–60%. In the D4000 bin with the largest values, 1.6$\leq$D4000$<$2.0, the SPZ improves over the photo-z by 30%.

A general trend for lower or similar SPZ outlier fractions as compared to photo-z outlier fractions can also be observed. For the bin with the largest D4000 values the outlier fraction for SPZs is $\sim$2% higher than photo-z (i.e., the SPZ method has 2 additional objects which are counted as outliers). The photo-z method is expected to work well with the largest breaks and therefore shows a roughly equivalent outlier fraction for the largest D4000 bin. It therefore appears that the outlier fractions are less dependent on the method than the adopted definition of outlier.

The dependence of redshift accuracy on D4000 also prompted us to attempt to quantify the value of D4000 at which the measurement of the break strength is significant enough for a redshift to be accurately estimated in Figure 20b. For this, I quantify the D4000 measurement significance by $({\rm D4000}-1.0)/\sigma_{\rm D4000}$, which is plotted vs. redshift in Figure 20b, where the points are colored with their D4000 value ($\sigma_{\rm D4000}$ is the error in our D4000 measurement). In Figure 20a, I show the average error for all our D4000 measurements as the point with red error-bars. This average error is $\sim$0.1. I define the significance threshold then as the level of 3σ above the flat

spectrum line of D4000=1.0, shown as the pink dash-dot line at D4000$\simeq$1.3. This agrees well with the decreased offset in the grism redshifts which occurs at D4000$\geq$1.3 (Figures 18 and 19). Figure 21 shows this dependence between D4000 measurement significance and the redshift accuracy more explicitly. It can be seen that at larger D4000 values and larger significance of the D4000 measurements, the redshift accuracy improves dramatically, while at lower D4000 values and lower D4000 measurement significance, there exists a larger scatter in the redshift accuracy.

In Figure 22 I investigate the effect of source brightness on the significance of the D4000 measurement. The figure shows a strong correlation between i_{AB} mag and $(\mathrm{D4000}-1.0)/\sigma_{\mathrm{D4000}}$. It can be seen that at fluxes fainter than $i_{AB} \sim$ 23–24 mag, there are far more galaxies with lower D4000 significance, i.e., $(\mathrm{D4000}-1.0)/\sigma_{\mathrm{D4000}} < 3.0$ than with higher D4000 significance.

This idea of D4000 significance is analogous to the measurement of the significance of emission lines when determining redshifts based on emission lines. Essentially, for an accurate redshift to be measured, the emission line must be measured at a significance of *at least* 3σ above the continuum level. I conclude here that a similar requirement is needed on the D4000 measurement for accurate redshifts based on absorption features. Therefore, using the robustness of D4000 measurements will be a useful tool for future WFIRST and Euclid redshift surveys.

3.6 Estimates of Object Number Densities for Future Surveys

The Wide Field Infrared Survey Telescope (WFIRST) was ranked as the highest priority space mission in the Astro2010 decadal survey, "New Worlds New Horizons" (National Research Council 2010). One of the primary drivers of both WFIRST and

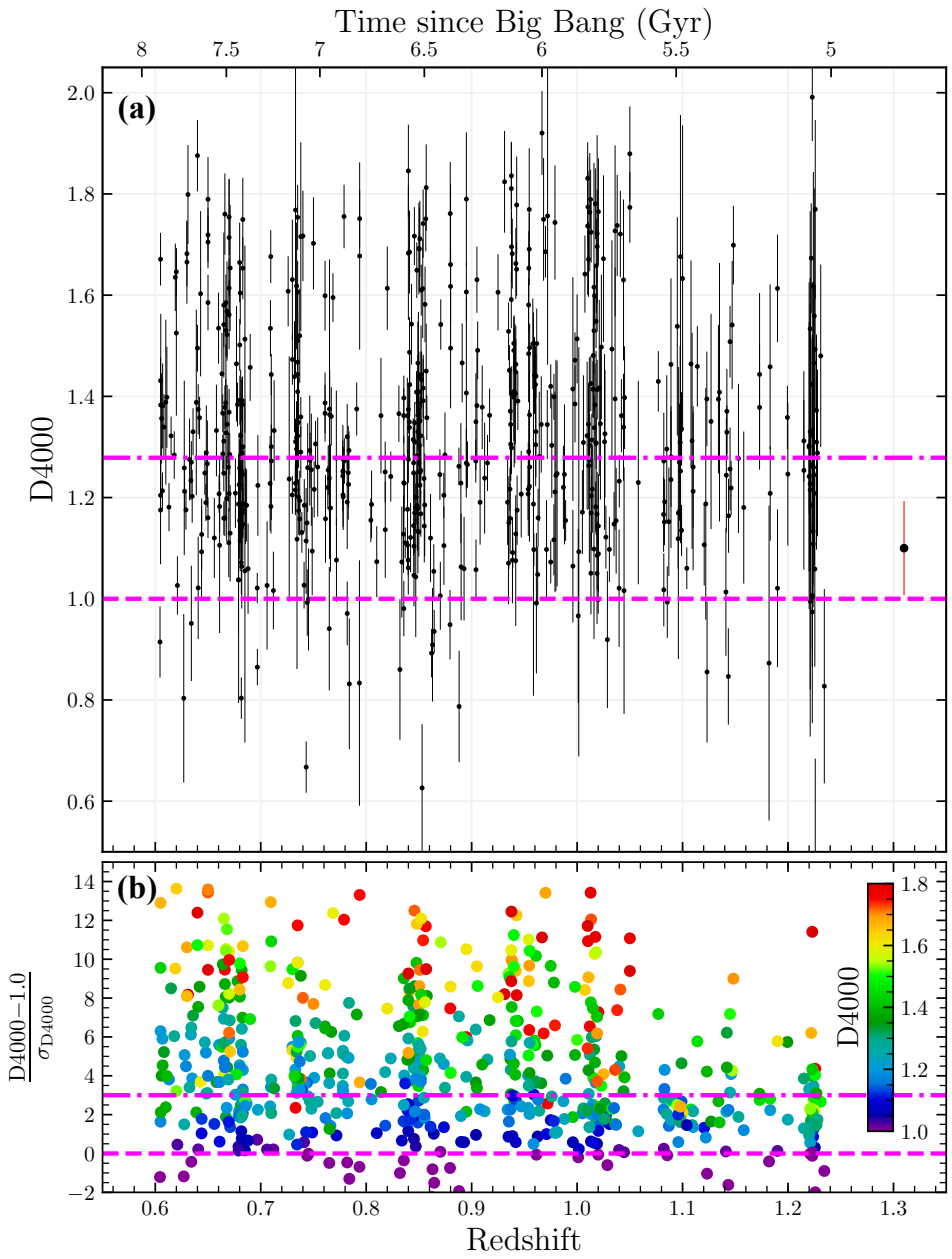

Figure 20. (a) The distribution of D4000 values with spectroscopic redshift. The black points show the D4000 measurements from our PEARS data for all the 602 galaxies which were within our redshift range and passed the Net Spectral Significance and contamination cuts. The horizontal pink dashed line at D4000 = 1.0 shows the D4000 value for a flat spectrum, in f_ν. The pink dash-dot line is 3σ away from 1.0, where 1σ is the average error-bar for all D4000<1.3 shown by the point with the red error-bar. (b) The significance of the D4000 measurement, as measured by $(D4000 - 1.0)/\sigma_{D4000}$, vs. redshift. The points are colored with their D4000 values as shown. The horizontal dashed and dash-dot lines show the null-measurement and 3σ level, respectively.

the European Space Agency's Euclid mission is to measure the growth of structure and cosmic expansion over a large period of cosmic history. To achieve this, accurate redshift measurements are necessary – within 0.1% accuracy for baryon acoustic scale measurements (BAO) and ∼1-3% for weak lensing and galaxy overdensity measurements. In this section, I estimate the expected number density of objects by future redshift surveys that will achieve a redshift accuracy of ∼2% or better based on the 4000Å/Balmer breaks.

As a first step to estimate the number density for future redshift surveys, I investigate any possible evolution of the 4000Å break strength, D4000, with redshift at intermediate redshifts. Figure 20a shows the distribution of D4000 vs. redshift for all galaxies in our sample that had ground-based spectroscopic redshifts, and that passed our Net Spectral Significance and contamination cuts. Figure 20a shows that the strength of the 4000Å break remains roughly constant between $0.600 \leq z \leq 1.235$. It can also be seen that most of the galaxies at these redshifts have a red slope at ∼4000Å, since they lie above the value of 1.0 (red dashed horizontal line) that represents a flat spectrum (in f_ν) between 3750Å and 4250Å (equal integrated flux density in the two bandpasses used in the D4000 definition).

The method presented in this work relies on the presence of a discernible 4000Å break. Hence, the number density of galaxies with accurate 4000Å break redshifts observable by WFIRST and Euclid will depend on the fraction of galaxies that contain a discernible 4000Å break at the redshifts being probed. For WFIRST and Euclid (Laureijs et al. 2011), the wavelength coverage of the grism is 1.0 to 1.93 μm (for the WFIRST Wide Field Instrument, WFI)[3], and 0.92 to 1.85 μm (for the Euclid Near

[3]https://wfirst.ipac.caltech.edu/sims/Param_db.html

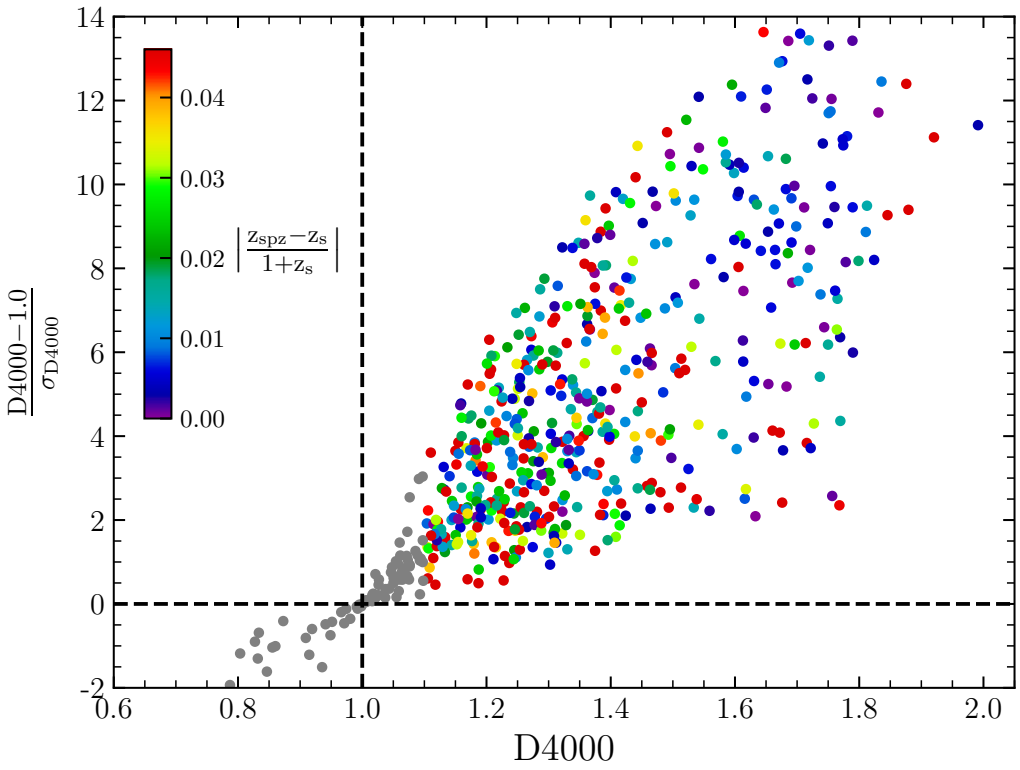

Figure 21. The significance of the D4000 measurement vs. the D4000 value. The points are colored according with the accuracy of their spectrophotometric redshifts. The horizontal dashed line is the null-measurement level of D4000, and the vertical dashed line is D4000=1.0 i.e, a flat spectrum. The gray points are galaxy spectra with D4000<1.1 for which I did not estimate a spectrophotometric redshift with our routine. This shows that the signal-to-noise of D4000 can indicate the quality of redshift.

Infrared Spectrometer and Photometer, NISP)[4], respectively. These grism wavelength coverages translate to redshift ranges that are sensitive to the 4000Å break, i.e., $1.67 \leq z \leq 3.45$ and $1.45 \leq z \leq 3.35$ for WFIRST and Euclid, respectively. These ranges are derived from wavelength coverage for the grisms and the D4000 definition (see Eq. 3.1).

[4]https://www.euclid-ec.org/?page_id=2490

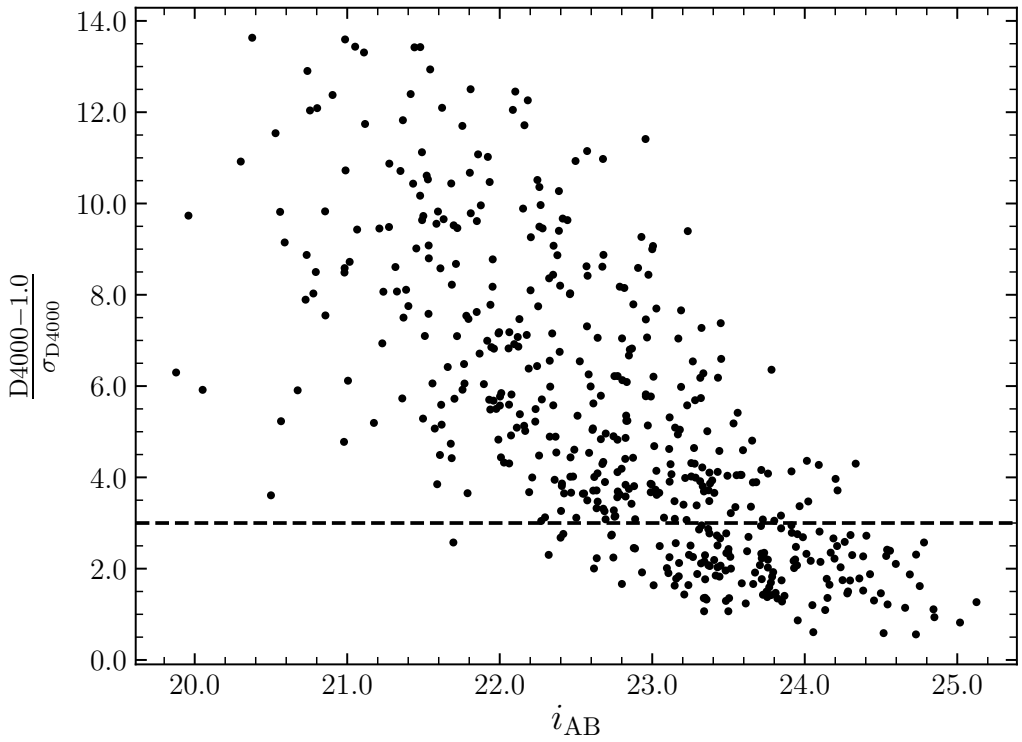

Figure 22. Significance of the D4000 measurement vs. i_{AB} magnitude. The horizontal dashed line is at $(D4000 - 1.0)/\sigma_{\mathrm{D4000}} = 3.0$. This plot includes all the 497 galaxies in our sample with $1.1 \leq \mathrm{D4000} < 2.0$.

Given the results from Figure 20a — the absence of a strong trend in D4000 with redshift for the intermediate redshift values I consider — and also for simplicity, I assume that the fraction of galaxies with a 4000Å or Balmer break available to provide accurate redshifts is roughly constant between the WFIRST and Euclid redshift ranges. I am allowing for the possibility that the abundance of 4000Å break galaxies should drop at higher redshifts, but the abundance of Balmer break galaxies (due to post starburst populations dominated by A-type stars) should increase due to the increased overall star formation activity in the Universe (e.g., Madau and Dickinson 2014).

Based on the results from Figure 22, for the remainder of this work, I will only consider the subsample of galaxies within our sample that are brighter than i_{AB}=24

mag. There are 464 galaxies, representing ∼72% of all galaxies in the PEARS area (464 out of 646 galaxies), that are within $0.600 \leq z \leq 1.235$ and contain a discernible 4000Å/Balmer break, i.e., D4000>1.1, and also have i_{AB}≤24 mag. I assume that this is the fraction of galaxies within any given area that will contain 4000Å/Balmer breaks available to determine accurate redshifts.

I estimate the number density of objects with accurate 4000Å/Balmer break redshifts by integrating measured luminosity functions (LFs) over the WFIRST and Euclid redshift ranges covering the 4000Å break. The measured LFs come from Kelvin et al. 2014, who report LFs measured for elliptical galaxies (among others) at local redshifts, using data from the GAMA survey (S. P. Driver et al. 2011). The LFs are assumed to follow a Schechter form (Schechter 1976) parameterized by the characteristic magnitude M*, the characteristic number density ϕ^* [M$pc^{-3}mag^{-1}$], and the faint-end slope α. While the choice of LF does impact the predicted number counts, the effects of LF-evolution will be minor, and the largest uncertainty is currently the unknown survey completeness.

Following the prescription in Gardner 1998, I integrate the adopted LF and differential volume element, giving the number density out to the specified magnitude limit. The BC03 SED I used has the following stellar population parameters: age, $t = 4\,\mathrm{Gyr}$, exponential SFH timescale, $\tau = 0.1\,\mathrm{Gyr}$, $A_V = 0$, and solar metallicity. To predict the number density of galaxies that contain a discernible 4000Å break and also allow for a redshift estimate with accuracy $|\Delta z/(1+z_s)| \leq 0.02$, I multiply the number densities obtained from the LF integration with the fraction of galaxies with D4000>1.1 (denoted f_{D4000}) and the fraction of galaxies with $|\Delta z/(1+z_s)| \leq 0.02$ (denoted f_{acc}) determined from our sample. These fractions are $f_{D4000} = 0.72$ (see preceding

discussion) and $f_{acc}^{SPZ} = 0.575$ (286 out of 497 galaxies) for spectrophotometric redshifts or $f_{acc}^{zg} = 0.36$ (180 out of 497 galaxies) for grism-only redshifts.

Therefore, based on the calculation described above, I predict a total of ∼700–4400 galaxies/degree^2 which can be used to obtain redshifts accurate to $|\Delta z/(1+z_s)| \leq 0.02$, within the WFIRST and Euclid redshift ranges to a limiting depth of i_{AB}=24 mag. Our predicted number density of galaxies with accurate continuum derived redshifts is comparable to the expected number density of emission line redshifts. For example, our expected number density agrees reasonably well, at the higher end of our prediction, with the expected number density of Hα emitting galaxies predicted by Merson et al. 2018, who find a number density between 3900 and 4800 galaxies/degree^2 for a Euclid-like survey, and a number density between 10400 and 15200 galaxies/degree^2 for a WFIRST-like survey. Our expected number density also agrees well with estimates of line-emitting galaxies from the WFC3 Infrared Spectroscopic Parallels (WISP) survey collaboration (see for e.g., Colbert et al. 2013; Mehta et al. 2015) and also with the number counts of line emitters at $0.9 < z < 1.8$ estimated by Valentino et al. 2017.

3.7 Conclusion

I note three important aspects of our continuum derived redshifts relevant to future redshift surveys –

(i) **Complementarity with emission line redshifts**: As I have shown, the expected number density of galaxies with redshifts derived from the 4000Å/Balmer breaks is comparable to that of galaxies with Hα based redshifts. Our redshift fitting method relies on absorption features in the continuum to minimize χ^2, while also accounting for the effects of correlated data in the grism spectra and galaxy morphology. Since

the two methods rely on very different features present in galaxy spectra, these methods individually access very different galaxy populations. Therefore, the two methods combined can comprehensively sample the galaxy population. I have also shown, that the D4000 measurement significance can be used as a proxy for expected continuum-based redshift accuracy.

(ii) **Redshifts based on grism data alone**: For galaxies that contain strong emission lines, using grism data alone, a redshift accuracy of $\sim$0.1% can be achieved, by employing 2-dimensional grism spectra to detect individual emission line regions in galaxies (Norbert Pirzkal et al. 2018). I have shown that continuum-based redshifts derived using only grism data, for galaxies *without* strong emission lines, can still achieve an accuracy of $\sigma^{NMAD}_{\Delta z/(1+z)}$$\sim$6% (Table 4), down to $i_{AB}$$\sim$23–24 mag. This is when using ACS/G800L spectra that have R$\simeq$100 and a typical rest-frame coverage around the 4000Å break of $\sim$1500Å. This is especially important, given that much of the area covered by WFIRST and Euclid will not have supporting 12-band (or more) photometry, and therefore must rely on grism-based redshifts alone.

(iii) **Grism redshifts for fainter continua**: Accurate grism continuum redshifts can be achieved for *continua* that are fainter (i_{AB}=24 mag for this paper) than those that can be done from the ground. Given the steep slope in the luminosity function at the faint end (e.g., Finkelstein et al. 2015), this is particularly important because sampling fainter magnitudes will allow for obtaining continuum-based redshifts for much larger numbers of galaxies.

While programs targeting Hα and [OIII]λ5007 lines are being planned for both the WFIRST (see e.g., High Latitude Survey, Spergel et al. 2015) and Euclid missions, I show that redshifts obtained with the 4000Å/Balmer breaks can also be accurate to at least $\lesssim$2%. I argue that – (i) since the expected number densities of objects with

redshifts based on the 4000Å/Balmer breaks and objects with emission line redshifts are comparable, and (ii) since grism continuum redshifts can be done from space to fainter continuum levels compared to continuum-based redshifts from the ground (e.g., this work goes as faint as i_{AB}=24 mag) – continuum-based redshifts can thus provide redshifts for galaxies which will not have emission line based redshifts from grism observations with WFIRST and Euclid, and therefore contribute additional redshifts which would otherwise not be available.

Table 5. Redshift and D4000 catalog for our sample. I also provide the Net Spectral Significance ($\mathcal{N}$), D4000, and the i-band magnitude for each galaxy. A machine readable version of this table is available from the journal website.

PearsID	Field	RA	DEC	z_{spec}	z_{phot}	z_{grism}	z_{SPZ}	$\mathcal{N}$	D4000	$\sigma_{\rm D4000}$	i(AB)
85422	GOODS-N	189.2827329	62.268248	0.936	$0.93^{+0.01}_{-0.00}$	$0.99^{+0.00}_{-0.00}$	$0.93^{+0.00}_{-0.01}$	437.05	1.45	0.05	21.53
114657	GOODS-S	53.0456393	−27.724930	1.215	$1.22^{+0.02}_{-0.07}$	$1.19^{+0.00}_{-0.01}$	$1.22^{+0.02}_{-0.07}$	198.59	1.31	0.08	22.99
35878	GOODS-S	53.1750819	−27.873892	0.650	$0.64^{+0.00}_{-0.00}$	$0.30^{+0.01}_{-0.00}$	$0.62^{+0.00}_{-0.00}$	383.65	1.16	0.04	22.21
90546	GOODS-S	53.1549743	−27.768908	1.050	$1.06^{+0.00}_{-0.00}$	$1.09^{+0.01}_{-0.00}$	$1.06^{+0.00}_{-0.00}$	577.57	1.77	0.07	21.86
83248	GOODS-S	53.1616316	−27.780247	0.619	$0.59^{+0.01}_{-0.00}$	$0.62^{+0.00}_{-0.00}$	$0.59^{+0.00}_{-0.00}$	588.09	1.64	0.07	21.70
57014	GOODS-S	53.1845635	−27.836041	1.038	$1.02^{+0.00}_{-0.02}$	$1.03^{+0.00}_{-0.00}$	$1.02^{+0.01}_{-0.00}$	164.86	1.74	0.10	23.45
132104	GOODS-S	53.0610491	−27.688081	0.818	$0.82^{+0.03}_{-0.01}$	$0.59^{+0.01}_{-0.00}$	$0.79^{+0.00}_{-0.00}$	188.17	1.25	0.06	22.80
89573	GOODS-N	189.2496182	62.274447	1.012	$0.95^{+0.11}_{-0.00}$	$1.06^{+0.00}_{-0.02}$	$0.95^{+0.18}_{-0.00}$	136.31	1.76	0.12	23.27
109151	GOODS-S	53.1409173	−27.736119	0.667	$0.64^{+0.00}_{-0.00}$	$0.65^{+0.14}_{-0.00}$	$0.64^{+0.00}_{-0.00}$	520.90	1.59	0.06	21.53
32497	GOODS-N	189.1665811	62.174797	0.935	$0.97^{+0.02}_{-0.00}$	$0.91^{+0.10}_{-0.00}$	$0.96^{+0.00}_{-0.00}$	315.51	1.53	0.06	22.20
36418	GOODS-N	189.1941824	62.180293	0.940	$0.93^{+0.13}_{-0.00}$	$0.87^{+0.01}_{-0.01}$	$0.94^{+0.00}_{-0.00}$	148.40	1.40	0.09	23.11
126415	GOODS-S	53.0474116	−27.701823	0.733	$0.93^{+0.01}_{-0.05}$	$0.76^{+0.00}_{-0.03}$	$0.81^{+0.00}_{-0.00}$	63.59	1.77	0.33	24.17
94085	GOODS-N	189.2999221	62.283150	1.142	$1.03^{+0.01}_{-0.02}$	$1.12^{+0.00}_{-0.01}$	$1.04^{+0.00}_{-0.02}$	360.69	1.33	0.05	22.77
132474	GOODS-S	53.0865015	−27.687486	0.683	$0.64^{+0.02}_{-0.01}$	$0.62^{+0.00}_{-0.00}$	$0.66^{+0.00}_{-0.01}$	174.31	1.19	0.07	22.73
33414	GOODS-N	189.1540648	62.175396	1.016	$0.97^{+0.02}_{-0.01}$	$0.71^{+0.65}_{-0.01}$	$1.00^{+0.00}_{-0.03}$	89.50	1.62	0.25	23.43
74987	GOODS-N	189.2407802	62.248600	0.849	$0.92^{+0.00}_{-0.00}$	$0.97^{+0.01}_{-0.02}$	$0.92^{+0.00}_{-0.03}$	293.54	1.36	0.05	22.12
21592	GOODS-S	53.1459236	−27.901462	0.670	$0.66^{+0.00}_{-0.00}$	$0.83^{+0.04}_{-0.03}$	$0.66^{+0.00}_{-0.01}$	443.13	1.56	0.07	21.69
34821	GOODS-S	53.1652086	−27.873947	1.096	$1.04^{+0.00}_{-0.01}$	$1.04^{+0.00}_{-0.01}$	$1.03^{+0.00}_{-0.00}$	249.11	1.12	0.06	22.62
83499	GOODS-N	189.1973120	62.274485	0.871	$0.87^{+0.00}_{-0.00}$	$0.87^{+0.03}_{-0.01}$	$0.87^{+0.00}_{-0.00}$	603.06	1.54	0.05	21.28
125098	GOODS-N	189.3846421	62.342237	1.223	$1.21^{+0.00}_{-0.00}$	$1.30^{+0.00}_{-0.00}$	$1.23^{+0.00}_{-0.00}$	319.61	1.99	0.09	22.96
124386	GOODS-N	189.3902768	62.344510	0.841	$0.86^{+0.01}_{-0.02}$	$0.93^{+0.02}_{-0.09}$	$0.86^{+0.01}_{-0.06}$	222.50	1.49	0.07	22.80

continued ...

. . . continued

PearsID	Field	RA	DEC	z_{spec}	z_{phot}	z_{grism}	z_{SPZ}	$\mathcal{N}$	D4000	$\sigma_{\rm D4000}$	i(AB)
86522	GOODS-N	189.3232826	62.268957	0.710	$0.68^{+0.02}_{-0.00}$	$1.32^{+0.02}_{-0.04}$	$0.64^{+0.04}_{-0.01}$	269.71	1.18	0.05	22.86
68612	GOODS-N	189.1965577	62.237297	0.610	$0.73^{+0.02}_{-0.07}$	$0.63^{+0.02}_{-0.02}$	$0.68^{+0.02}_{-0.06}$	124.64	1.39	0.16	23.62
109794	GOODS-S	53.1431093	−27.730585	0.667	$0.65^{+0.00}_{-0.00}$	$1.49^{+0.00}_{-1.11}$	$0.64^{+0.00}_{-0.00}$	519.81	1.39	0.05	21.24
118100	GOODS-S	53.0703038	−27.717853	0.644	$0.62^{+0.02}_{-0.01}$	$0.67^{+0.00}_{-0.00}$	$0.67^{+0.00}_{-0.00}$	159.11	1.13	0.07	23.16
113700	GOODS-N	189.4055414	62.315743	1.085	$1.02^{+0.04}_{-0.02}$	$1.10^{+0.39}_{-0.03}$	$1.07^{+0.01}_{-0.05}$	85.51	1.30	0.15	24.23
135087	GOODS-S	53.0807722	−27.681003	0.682	$0.99^{+0.00}_{-0.00}$	$0.46^{+0.23}_{-0.01}$	$0.98^{+0.00}_{-0.00}$	714.63	1.39	0.04	21.07
76405	GOODS-N	189.1780463	62.250802	0.697	$0.92^{+0.01}_{-0.01}$	$0.44^{+0.01}_{-0.01}$	$0.83^{+0.00}_{-0.01}$	119.74	1.22	0.10	23.11
19226	GOODS-S	53.1412561	−27.907070	0.663	$0.65^{+0.01}_{-0.01}$	$1.32^{+0.00}_{-0.00}$	$0.73^{+0.00}_{-0.00}$	324.85	1.44	0.08	22.23
126762	GOODS-S	53.0823701	−27.701108	1.044	$1.03^{+0.03}_{-0.02}$	$1.05^{+0.01}_{-0.01}$	$1.04^{+0.00}_{-0.00}$	90.52	1.63	0.16	24.20
118459	GOODS-S	53.0952520	−27.717270	0.671	$0.68^{+0.00}_{-0.01}$	$0.38^{+0.05}_{-0.01}$	$0.65^{+0.01}_{-0.00}$	104.73	1.13	0.10	23.35
108892	GOODS-S	53.0779324	−27.736875	0.958	$1.00^{+0.00}_{-0.05}$	$0.90^{+0.05}_{-0.01}$	$0.94^{+0.03}_{-0.04}$	144.69	1.50	0.09	22.61
92378	GOODS-N	189.1805813	62.281280	0.944	$1.00^{+0.05}_{-0.03}$	$1.04^{+0.01}_{-0.00}$	$1.02^{+0.09}_{-0.04}$	288.62	1.39	0.06	22.06
47038	GOODS-S	53.1338939	−27.851542	0.683	$0.72^{+0.01}_{-0.04}$	$0.31^{+0.01}_{-0.00}$	$0.72^{+0.01}_{-0.06}$	153.20	1.30	0.10	22.30
82816	GOODS-N	189.3380698	62.262313	0.778	$0.82^{+0.01}_{-0.00}$	$0.70^{+0.01}_{-0.00}$	$0.78^{+0.01}_{-0.00}$	154.46	1.20	0.07	22.69
72524	GOODS-S	53.1303304	−27.805615	1.173	$1.06^{+0.01}_{-0.03}$	$1.10^{+0.00}_{-0.04}$	$1.08^{+0.00}_{-0.01}$	111.31	1.38	0.12	23.73
58856	GOODS-N	189.1602768	62.220296	0.635	$0.58^{+0.00}_{-0.01}$	$0.40^{+0.00}_{-0.00}$	$0.60^{+0.01}_{-0.00}$	287.12	1.20	0.05	22.41
89031	GOODS-S	53.1016142	−27.773408	0.895	$0.90^{+0.00}_{-0.00}$	$0.89^{+0.01}_{-0.00}$	$0.90^{+0.00}_{-0.00}$	150.49	1.79	0.13	22.60
70857	GOODS-N	189.1161525	62.246957	0.680	$0.70^{+0.01}_{-0.02}$	$0.99^{+0.01}_{-0.03}$	$0.71^{+0.00}_{-0.00}$	547.56	1.39	0.05	21.33
96844	GOODS-S	53.1523301	−27.761868	0.710	$0.41^{+0.00}_{-0.01}$	$0.31^{+0.01}_{-0.00}$	$0.31^{+0.01}_{-0.00}$	165.48	1.27	0.07	23.33
113678	GOODS-S	53.0611747	−27.726963	0.910	$0.97^{+0.01}_{-0.01}$	$1.49^{+0.00}_{-1.13}$	$0.94^{+0.01}_{-0.00}$	142.71	1.38	0.08	23.44
39728	GOODS-N	189.1700185	62.185821	0.765	$0.80^{+0.03}_{-0.02}$	$0.51^{+0.00}_{-0.01}$	$0.76^{+0.01}_{-0.00}$	124.88	1.36	0.09	23.43
120726	GOODS-N	189.3316295	62.330061	0.778	$0.82^{+0.01}_{-0.03}$	$0.35^{+0.01}_{-0.00}$	$0.76^{+0.01}_{-0.01}$	169.07	1.24	0.07	23.15
98131	GOODS-N	189.2542330	62.291574	0.710	$0.73^{+0.00}_{-0.00}$	$0.70^{+0.01}_{-0.00}$	$0.72^{+0.00}_{-0.00}$	739.18	1.67	0.05	21.54

continued . . .

. . . continued

PearsID	Field	RA	DEC	z_{spec}	z_{phot}	z_{grism}	z_{SPZ}	$\mathcal{N}$	D4000	$\sigma_{\rm D4000}$	i(AB)
119616	GOODS-N	189.3631438	62.327969	1.010	$0.94^{+0.03}_{-0.06}$	$1.11^{+0.00}_{-0.01}$	$1.01^{+0.01}_{-0.01}$	82.46	1.32	0.15	23.94
35853	GOODS-N	189.1421243	62.179438	1.011	$0.94^{+0.01}_{-0.01}$	$0.38^{+0.00}_{-0.01}$	$0.93^{+0.00}_{-0.00}$	129.19	1.26	0.09	23.23
117608	GOODS-S	53.0816361	−27.717718	0.640	$0.73^{+0.00}_{-0.00}$	$0.72^{+0.01}_{-0.00}$	$0.72^{+0.00}_{-0.00}$	618.65	1.88	0.07	21.42
82141	GOODS-N	189.1952610	62.261281	0.917	$0.90^{+0.00}_{-0.00}$	$0.95^{+0.00}_{-0.01}$	$0.88^{+0.00}_{-0.01}$	302.61	1.36	0.05	22.12
47355	GOODS-N	189.1542324	62.199884	0.779	$0.80^{+0.00}_{-0.02}$	$0.30^{+0.00}_{-0.00}$	$0.77^{+0.00}_{-0.01}$	361.90	1.27	0.04	21.56
100572	GOODS-S	53.1371579	−27.754179	0.765	$0.80^{+0.01}_{-0.05}$	$0.37^{+0.01}_{-0.00}$	$0.75^{+0.02}_{-0.05}$	181.72	1.24	0.07	22.79
88929	GOODS-N	189.2792124	62.274477	0.943	$0.95^{+0.01}_{-0.00}$	$0.93^{+0.01}_{-0.00}$	$0.94^{+0.00}_{-0.00}$	197.35	1.78	0.10	22.82
109967	GOODS-S	53.1558608	−27.735275	1.017	$1.06^{+0.01}_{-0.08}$	$1.01^{+0.00}_{-0.01}$	$1.05^{+0.01}_{-0.07}$	147.74	1.38	0.08	23.01
98048	GOODS-S	53.1095470	−27.760050	1.050	$1.15^{+0.00}_{-0.00}$	$1.21^{+0.01}_{-0.00}$	$1.21^{+0.00}_{-0.00}$	227.42	1.88	0.09	23.23
36989	GOODS-N	189.1697691	62.180284	1.006	$1.23^{+0.05}_{-0.24}$	$0.96^{+0.01}_{-0.14}$	$1.20^{+0.09}_{-0.19}$	82.90	1.31	0.13	24.01
107010	GOODS-N	189.2552092	62.306395	0.942	$0.93^{+0.00}_{-0.04}$	$0.90^{+0.00}_{-0.00}$	$0.90^{+0.00}_{-0.00}$	270.77	1.13	0.05	22.42
45026	GOODS-N	189.1799942	62.196666	1.007	$1.02^{+0.00}_{-0.00}$	$1.02^{+0.00}_{-0.00}$	$1.02^{+0.00}_{-0.00}$	228.58	1.64	0.08	22.58
118642	GOODS-N	189.3352811	62.325305	0.836	$0.83^{+0.00}_{-0.06}$	$0.37^{+0.00}_{-0.01}$	$0.74^{+0.04}_{-0.01}$	212.96	1.23	0.06	22.48
117225	GOODS-S	53.1081977	−27.720155	0.972	$0.96^{+0.02}_{-0.00}$	$0.98^{+0.00}_{-0.01}$	$0.97^{+0.01}_{-0.00}$	55.39	1.76	0.29	24.78
107208	GOODS-S	53.0971826	−27.742252	1.221	$1.14^{+0.05}_{-0.01}$	$1.30^{+0.01}_{-0.06}$	$1.19^{+0.05}_{-0.02}$	60.75	1.33	0.25	24.45
17022	GOODS-S	53.1918766	−27.912430	0.733	$0.69^{+0.00}_{-0.00}$	$1.04^{+0.00}_{-0.00}$	$0.64^{+0.02}_{-0.00}$	454.47	1.31	0.05	21.96
121439	GOODS-N	189.3093396	62.332923	0.888	$0.91^{+0.02}_{-0.03}$	$1.27^{+0.05}_{-0.17}$	$0.93^{+0.00}_{-0.00}$	974.50	1.26	0.04	22.64
126365	GOODS-S	53.0748433	−27.701080	0.643	$0.67^{+0.01}_{-0.01}$	$0.73^{+0.01}_{-0.25}$	$0.66^{+0.01}_{-0.01}$	125.78	1.60	0.16	23.34
23595	GOODS-S	53.2106591	−27.899203	0.976	$0.96^{+0.01}_{-0.02}$	$0.93^{+0.00}_{-0.01}$	$0.93^{+0.01}_{-0.01}$	94.61	1.30	0.10	23.71
98698	GOODS-S	53.1119356	−27.757828	0.831	$0.99^{+0.04}_{-0.06}$	$1.04^{+0.00}_{-0.00}$	$1.01^{+0.03}_{-0.05}$	291.56	1.37	0.06	22.33
97568	GOODS-S	53.1252542	−27.756535	0.955	$1.37^{+0.03}_{-0.10}$	$1.05^{+0.00}_{-0.01}$	$1.36^{+0.00}_{-0.07}$	371.51	1.26	0.05	21.93
88858	GOODS-N	189.1765570	62.272816	0.854	$0.94^{+0.01}_{-0.01}$	$0.38^{+0.01}_{-0.00}$	$0.92^{+0.03}_{-0.02}$	133.03	1.39	0.09	23.28
109170	GOODS-N	189.2956885	62.309360	0.631	$0.69^{+0.01}_{-0.01}$	$0.64^{+0.01}_{-0.01}$	$0.66^{+0.00}_{-0.00}$	308.04	1.80	0.10	22.79

continued . . .

. . . continued

PearsID	Field	RA	DEC	z_{spec}	z_{phot}	z_{grism}	z_{SPZ}	$\mathcal{N}$	D4000	$\sigma_{\rm D4000}$	i(AB)
50214	GOODS-N	189.1413327	62.204732	1.016	$1.01^{+0.01}_{-0.07}$	$1.26^{+0.00}_{-0.00}$	$1.08^{+0.00}_{-0.01}$	476.25	1.53	0.09	22.80
91474	GOODS-N	189.2850939	62.277525	1.222	$1.13^{+0.01}_{-0.00}$	$1.15^{+0.00}_{-0.00}$	$1.15^{+0.01}_{-0.00}$	98.78	1.32	0.19	23.59
40991	GOODS-N	189.1849611	62.192549	1.013	$1.01^{+0.00}_{-0.00}$	$1.02^{+0.00}_{-0.01}$	$1.01^{+0.00}_{-0.00}$	496.61	1.79	0.06	21.48
94097	GOODS-N	189.2203911	62.281966	0.761	$0.80^{+0.04}_{-0.05}$	$0.78^{+0.00}_{-0.07}$	$0.77^{+0.00}_{-0.01}$	101.45	1.16	0.09	23.79
108922	GOODS-S	53.1382054	−27.737523	0.665	$0.70^{+0.00}_{-0.00}$	$0.65^{+0.27}_{-0.00}$	$0.69^{+0.01}_{-0.04}$	131.91	1.58	0.14	23.55
117825	GOODS-N	189.3957805	62.323567	0.634	$0.58^{+0.00}_{-0.00}$	$0.70^{+0.00}_{-0.01}$	$0.61^{+0.00}_{-0.02}$	490.62	1.27	0.04	21.77
117180	GOODS-S	53.1507119	−27.716204	0.967	$0.98^{+0.00}_{-0.00}$	$1.40^{+0.00}_{-0.00}$	$0.68^{+0.00}_{-0.00}$	214.00	1.92	0.08	21.49
57792	GOODS-N	189.2310375	62.219798	0.955	$0.94^{+0.00}_{-0.00}$	$0.94^{+0.00}_{-0.00}$	$0.94^{+0.00}_{-0.00}$	296.22	1.69	0.07	22.41
103139	GOODS-N	189.2447370	62.299235	0.942	$0.92^{+0.00}_{-0.00}$	$0.92^{+0.00}_{-0.00}$	$0.92^{+0.00}_{-0.00}$	222.05	1.45	0.07	22.87
105547	GOODS-S	53.1375911	−27.743506	0.605	$0.66^{+0.00}_{-0.00}$	$0.61^{+0.00}_{-0.00}$	$0.62^{+0.00}_{-0.00}$	910.71	1.67	0.05	20.74
71200	GOODS-S	53.1996796	−27.810448	0.682	$0.71^{+0.03}_{-0.06}$	$0.51^{+0.00}_{-0.00}$	$0.61^{+0.00}_{-0.03}$	80.85	1.29	0.15	23.79
87000	GOODS-N	189.1375951	62.271215	0.853	$0.83^{+0.00}_{-0.00}$	$0.90^{+0.00}_{-0.00}$	$0.83^{+0.00}_{-0.01}$	284.67	1.43	0.06	22.25
89993	GOODS-N	189.1793699	62.275523	0.870	$0.88^{+0.01}_{-0.01}$	$0.41^{+0.00}_{-0.01}$	$0.81^{+0.00}_{-0.00}$	248.84	1.25	0.05	22.37
62107	GOODS-N	189.1603789	62.227500	1.018	$1.03^{+0.00}_{-0.00}$	$0.95^{+0.00}_{-0.00}$	$1.03^{+0.00}_{-0.00}$	177.73	1.66	0.09	22.97
39842	GOODS-N	189.1831814	62.185293	0.845	$0.95^{+0.00}_{-0.01}$	$0.51^{+0.01}_{-0.00}$	$0.83^{+0.00}_{-0.00}$	200.38	1.10	0.05	22.93
62122	GOODS-S	53.1916475	−27.828335	0.627	$0.64^{+0.08}_{-0.06}$	$0.45^{+0.14}_{-0.03}$	$0.68^{+0.06}_{-0.04}$	81.70	1.26	0.17	24.28
23142	GOODS-S	53.1606733	−27.897112	0.620	$0.69^{+0.00}_{-0.00}$	$0.65^{+0.00}_{-0.00}$	$0.69^{+0.00}_{-0.00}$	1358.70	1.65	0.05	20.38
90388	GOODS-S	53.1059353	−27.771416	0.896	$0.93^{+0.00}_{-0.01}$	$0.77^{+0.08}_{-0.00}$	$0.92^{+0.01}_{-0.03}$	353.71	1.27	0.05	22.08
60709	GOODS-S	53.1909224	−27.831035	1.228	$1.17^{+0.02}_{-0.03}$	$1.24^{+0.00}_{-0.00}$	$1.16^{+0.08}_{-0.03}$	92.70	1.29	0.16	24.25
79903	GOODS-N	189.1893278	62.256443	0.682	$0.71^{+0.00}_{-0.01}$	$0.40^{+0.00}_{-0.00}$	$0.67^{+0.03}_{-0.01}$	283.14	1.14	0.05	22.27
102163	GOODS-S	53.1152531	−27.751588	1.110	$1.01^{+0.01}_{-0.04}$	$0.98^{+0.00}_{-0.00}$	$0.98^{+0.01}_{-0.00}$	68.63	1.21	0.16	24.15
106649	GOODS-S	53.1587815	−27.742386	1.190	$1.17^{+0.00}_{-0.00}$	$1.20^{+0.01}_{-0.01}$	$1.18^{+0.01}_{-0.00}$	150.54	1.61	0.11	22.96
61172	GOODS-S	53.1647452	−27.824545	0.650	$0.67^{+0.00}_{-0.00}$	$0.67^{+0.22}_{-0.00}$	$0.67^{+0.00}_{-0.00}$	625.22	1.59	0.05	21.35

continued . . .

. . . continued

PearsID	Field	RA	DEC	z_{spec}	z_{phot}	z_{grism}	z_{SPZ}	$\mathcal{N}$	D4000	$\sigma_{\rm D4000}$	i(AB)
133802	GOODS-S	53.0777266	−27.683883	0.710	$1.06^{+0.01}_{-0.02}$	$1.11^{+0.00}_{-0.00}$	$1.11^{+0.00}_{-0.00}$	91.48	1.30	0.14	23.37
106067	GOODS-S	53.0940969	−27.740505	0.738	$0.80^{+0.00}_{-0.03}$	$0.76^{+0.01}_{-0.05}$	$0.80^{+0.00}_{-0.01}$	882.60	1.36	0.04	20.59
84520	GOODS-N	189.1592064	62.268062	0.857	$0.84^{+0.00}_{-0.01}$	$0.85^{+0.01}_{-0.00}$	$0.84^{+0.00}_{-0.00}$	444.25	1.75	0.06	21.75
18260	GOODS-S	53.1933713	−27.903872	0.664	$0.69^{+0.00}_{-0.00}$	$1.49^{+0.00}_{-0.00}$	$0.69^{+0.00}_{-0.00}$	1314.17	1.37	0.04	19.96
60481	GOODS-S	53.1462700	−27.831469	1.096	$1.00^{+0.04}_{-0.04}$	$1.32^{+0.17}_{-0.01}$	$0.95^{+0.14}_{-0.00}$	41.12	1.17	0.29	24.52
126406	GOODS-S	53.0221164	−27.701411	0.861	$0.90^{+0.02}_{-0.02}$	$1.40^{+0.00}_{-0.08}$	$0.96^{+0.01}_{-0.00}$	176.41	1.12	0.09	23.75
53708	GOODS-N	189.2094343	62.212731	0.681	$0.67^{+0.00}_{-0.00}$	$0.68^{+0.24}_{-0.01}$	$0.67^{+0.00}_{-0.00}$	501.56	1.60	0.06	21.50
41115	GOODS-S	53.2136575	−27.864474	0.980	$0.92^{+0.02}_{-0.03}$	$0.91^{+0.09}_{-0.00}$	$0.93^{+0.01}_{-0.03}$	45.55	1.24	0.23	23.50
108510	GOODS-S	53.1477213	−27.739197	0.880	$0.88^{+0.00}_{-0.00}$	$0.90^{+0.00}_{-0.01}$	$0.89^{+0.00}_{-0.01}$	223.49	1.62	0.07	22.91
112789	GOODS-S	53.1061108	−27.724322	0.668	$0.66^{+0.00}_{-0.00}$	$0.89^{+0.02}_{-0.03}$	$0.63^{+0.01}_{-0.00}$	956.00	1.52	0.05	20.53
72905	GOODS-S	53.1802421	−27.798928	0.666	$0.70^{+0.01}_{-0.06}$	$0.50^{+0.00}_{-0.01}$	$0.67^{+0.01}_{-0.04}$	680.72	1.38	0.04	21.02
88671	GOODS-S	53.1197250	−27.772304	0.735	$0.72^{+0.00}_{-0.00}$	$0.73^{+0.25}_{-0.00}$	$0.74^{+0.00}_{-0.02}$	423.41	1.61	0.06	21.59
90557	GOODS-N	189.3143761	62.275709	0.852	$0.83^{+0.01}_{-0.00}$	$0.59^{+0.01}_{-0.10}$	$0.79^{+0.00}_{-0.00}$	271.02	1.17	0.05	22.61
83503	GOODS-N	189.2025506	62.264620	0.852	$0.84^{+0.00}_{-0.00}$	$0.85^{+0.00}_{-0.00}$	$0.84^{+0.00}_{-0.00}$	534.24	1.61	0.05	21.62
117632	GOODS-S	53.0471377	−27.709112	0.607	$0.58^{+0.01}_{-0.02}$	$0.34^{+0.00}_{-0.01}$	$0.56^{+0.00}_{-0.00}$	885.11	1.21	0.04	20.68
119764	GOODS-N	189.3263534	62.327299	1.225	$1.30^{+0.03}_{-0.03}$	$1.31^{+0.05}_{-0.02}$	$1.22^{+0.10}_{-0.00}$	82.39	1.56	0.25	24.20
111648	GOODS-N	189.3538023	62.312340	1.224	$1.14^{+0.03}_{-0.01}$	$1.12^{+0.06}_{-0.01}$	$1.18^{+0.00}_{-0.01}$	137.36	1.13	0.11	23.61
91095	GOODS-S	53.1363113	−27.763179	0.955	$1.01^{+0.00}_{-0.06}$	$1.02^{+0.00}_{-0.06}$	$1.01^{+0.00}_{-0.00}$	546.42	1.50	0.05	21.43
58703	GOODS-N	189.1399619	62.222202	0.845	$0.83^{+0.06}_{-0.02}$	$0.78^{+0.02}_{-0.03}$	$0.83^{+0.02}_{-0.02}$	494.69	1.31	0.04	21.53
134389	GOODS-S	53.0854533	−27.683033	0.895	$0.94^{+0.01}_{-0.01}$	$0.83^{+0.00}_{-0.00}$	$0.90^{+0.02}_{-0.04}$	170.14	1.27	0.07	22.36
95002	GOODS-N	189.4097481	62.288231	0.880	$0.90^{+0.00}_{-0.00}$	$0.88^{+0.01}_{-0.01}$	$0.89^{+0.00}_{-0.00}$	205.49	1.76	0.10	22.13
83106	GOODS-N	189.1455086	62.263566	0.854	$0.82^{+0.02}_{-0.00}$	$0.92^{+0.02}_{-0.00}$	$0.79^{+0.01}_{-0.01}$	267.69	1.42	0.06	22.18
79928	GOODS-N	189.1813500	62.258988	0.847	$0.83^{+0.00}_{-0.00}$	$0.73^{+0.00}_{-0.02}$	$0.76^{+0.00}_{-0.00}$	213.68	1.20	0.05	22.64

continued . . .

. . . continued

PearsID	Field	RA	DEC	z_{spec}	z_{phot}	z_{grism}	z_{SPZ}	$\mathcal{N}$	D4000	$\sigma_{\rm D4000}$	i(AB)
42014	GOODS-N	189.1773335	62.189407	0.845	$0.91^{+0.01}_{-0.02}$	$0.77^{+0.01}_{-0.00}$	$0.80^{+0.00}_{-0.01}$	186.01	1.14	0.06	22.88
75653	GOODS-N	189.1605828	62.248679	0.849	$0.88^{+0.00}_{-0.05}$	$0.84^{+0.01}_{-0.00}$	$0.85^{+0.02}_{-0.03}$	166.10	1.47	0.08	23.28
81513	GOODS-N	189.2327902	62.259489	0.850	$0.84^{+0.02}_{-0.01}$	$0.71^{+0.01}_{-0.02}$	$0.83^{+0.01}_{-0.00}$	94.80	1.44	0.13	24.02
112617	GOODS-S	53.0393961	−27.726626	1.023	$1.01^{+0.01}_{-0.01}$	$0.97^{+0.00}_{-0.00}$	$1.02^{+0.00}_{-0.05}$	84.58	1.50	0.14	23.37
17024	GOODS-S	53.1533697	−27.913962	0.661	$0.67^{+0.00}_{-0.02}$	$0.41^{+0.00}_{-0.00}$	$0.66^{+0.00}_{-0.00}$	278.36	1.18	0.05	22.19
63227	GOODS-N	189.1535471	62.229405	0.846	$0.85^{+0.01}_{-0.03}$	$0.32^{+0.02}_{-0.00}$	$0.85^{+0.00}_{-0.04}$	417.67	1.31	0.04	21.72
59024	GOODS-N	189.1431247	62.220131	0.845	$0.92^{+0.00}_{-0.01}$	$0.80^{+0.00}_{-0.10}$	$0.86^{+0.00}_{-0.06}$	179.28	1.27	0.07	22.85
50799	GOODS-N	189.2360180	62.205595	0.954	$0.96^{+0.00}_{-0.00}$	$0.96^{+0.02}_{-0.00}$	$0.96^{+0.00}_{-0.00}$	219.24	1.65	0.07	22.68
115781	GOODS-S	53.1484734	−27.719482	1.222	$1.15^{+0.00}_{-0.00}$	$1.21^{+0.00}_{-0.00}$	$1.15^{+0.00}_{-0.00}$	156.30	1.67	0.11	23.01
76592	GOODS-S	53.1736667	−27.797363	0.668	$0.58^{+0.07}_{-0.02}$	$0.36^{+0.00}_{-0.00}$	$0.64^{+0.00}_{-0.00}$	132.67	1.20	0.08	23.50
26158	GOODS-S	53.1785644	−27.890211	0.650	$0.66^{+0.00}_{-0.00}$	$0.66^{+0.00}_{-0.00}$	$0.66^{+0.00}_{-0.00}$	842.00	1.70	0.05	20.99
111741	GOODS-S	53.0454611	−27.728629	0.998	$1.00^{+0.03}_{-0.02}$	$1.10^{+0.01}_{-0.00}$	$1.02^{+0.01}_{-0.03}$	330.77	1.47	0.05	21.61
112509	GOODS-N	189.4184551	62.314892	0.955	$1.01^{+0.01}_{-0.06}$	$1.46^{+0.01}_{-0.01}$	$1.00^{+0.03}_{-0.05}$	141.09	1.36	0.09	23.03
79185	GOODS-N	189.1656552	62.263279	0.848	$0.84^{+0.00}_{-0.00}$	$0.96^{+0.00}_{-0.11}$	$0.85^{+0.00}_{-0.00}$	528.87	1.65	0.05	21.36
54598	GOODS-N	189.2245564	62.215020	0.642	$0.64^{+0.03}_{-0.02}$	$0.61^{+0.01}_{-0.01}$	$0.64^{+0.01}_{-0.03}$	694.02	1.36	0.04	20.98
121302	GOODS-N	189.3372338	62.332220	0.778	$0.76^{+0.00}_{-0.02}$	$0.30^{+0.00}_{-0.00}$	$0.72^{+0.01}_{-0.00}$	311.43	1.25	0.05	22.16
119879	GOODS-N	189.3599907	62.329089	1.010	$1.00^{+0.00}_{-0.00}$	$1.00^{+0.00}_{-0.00}$	$1.00^{+0.00}_{-0.00}$	284.78	1.78	0.07	22.50
41630	GOODS-N	189.1987192	62.188955	1.223	$1.20^{+0.12}_{-0.06}$	$1.12^{+0.00}_{-0.00}$	$1.23^{+0.09}_{-0.09}$	111.73	1.27	0.14	23.17
31899	GOODS-S	53.1398202	−27.880603	1.077	$1.12^{+0.00}_{-0.04}$	$1.17^{+0.00}_{-0.11}$	$1.11^{+0.02}_{-0.03}$	354.71	1.43	0.06	22.06
95449	GOODS-N	189.3288829	62.287190	0.935	$0.88^{+0.07}_{-0.06}$	$0.36^{+0.00}_{-0.01}$	$0.89^{+0.00}_{-0.00}$	105.59	1.15	0.09	23.24
13543	GOODS-S	53.1314798	−27.921453	1.134	$1.20^{+0.02}_{-0.30}$	$1.12^{+0.01}_{-0.07}$	$1.16^{+0.03}_{-0.09}$	87.55	1.39	0.15	23.99
93602	GOODS-N	189.1672976	62.282149	0.943	$0.93^{+0.00}_{-0.00}$	$0.94^{+0.00}_{-0.00}$	$0.93^{+0.00}_{-0.00}$	471.82	1.65	0.05	22.18
46765	GOODS-N	189.2579665	62.197271	1.020	$0.96^{+0.01}_{-0.01}$	$0.99^{+0.00}_{-0.00}$	$0.99^{+0.00}_{-0.01}$	92.69	1.14	0.10	23.87

continued . . .

. . . continued

PearsID	Field	RA	DEC	z_{spec}	z_{phot}	z_{grism}	z_{SPZ}	$\mathcal{N}$	D4000	$\sigma_{\rm D4000}$	i(AB)
104774	GOODS-S	53.0861053	−27.746234	0.726	$0.68^{+0.00}_{-0.02}$	$0.72^{+0.00}_{-0.01}$	$0.68^{+0.00}_{-0.00}$	365.72	1.61	0.07	21.95
93627	GOODS-S	53.1090557	−27.767658	1.221	$1.19^{+0.10}_{-0.15}$	$1.17^{+0.01}_{-0.14}$	$1.10^{+0.07}_{-0.07}$	36.90	1.23	0.41	24.73
88020	GOODS-N	189.1544383	62.270859	0.852	$0.83^{+0.02}_{-0.01}$	$0.63^{+0.01}_{-0.00}$	$0.74^{+0.00}_{-0.01}$	128.18	1.32	0.08	23.38
93815	GOODS-S	53.1812066	−27.765670	1.220	$1.18^{+0.00}_{-0.06}$	$1.20^{+0.01}_{-0.00}$	$1.20^{+0.02}_{-0.08}$	231.97	1.24	0.07	22.68
102847	GOODS-S	53.1001026	−27.751121	1.110	$1.05^{+0.02}_{-0.02}$	$1.10^{+0.00}_{-0.00}$	$1.07^{+0.03}_{-0.00}$	97.39	1.26	0.12	23.93
92535	GOODS-N	189.1767644	62.279170	0.836	$0.83^{+0.02}_{-0.01}$	$0.83^{+0.01}_{-0.00}$	$0.83^{+0.01}_{-0.01}$	234.15	1.36	0.05	22.85
85920	GOODS-N	189.2502329	62.268303	1.014	$0.96^{+0.00}_{-0.00}$	$0.98^{+0.00}_{-0.00}$	$0.98^{+0.00}_{-0.00}$	274.63	1.31	0.05	22.33
91148	GOODS-N	189.1672069	62.276870	0.849	$1.03^{+0.03}_{-0.20}$	$0.80^{+0.01}_{-0.01}$	$0.82^{+0.08}_{-0.01}$	134.89	1.39	0.09	23.38
103146	GOODS-S	53.1527857	−27.750513	1.019	$0.98^{+0.03}_{-0.02}$	$1.01^{+0.01}_{-0.00}$	$1.01^{+0.00}_{-0.00}$	76.02	1.72	0.19	24.21
79351	GOODS-N	189.1574350	62.256407	1.221	$1.13^{+0.06}_{-0.00}$	$1.15^{+0.04}_{-0.01}$	$1.14^{+0.00}_{-0.00}$	96.38	1.22	0.16	23.82
25184	GOODS-S	53.1426003	−27.895068	0.685	$0.90^{+0.00}_{-0.07}$	$0.63^{+0.15}_{-0.00}$	$0.89^{+0.01}_{-0.08}$	97.96	1.51	0.19	23.48
65022	GOODS-N	189.2313299	62.231529	1.145	$1.03^{+0.01}_{-0.03}$	$1.11^{+0.00}_{-0.00}$	$1.09^{+0.00}_{-0.00}$	163.89	1.26	0.08	22.75
105048	GOODS-N	189.2771661	62.305090	0.856	$0.83^{+0.02}_{-0.00}$	$0.85^{+0.00}_{-0.00}$	$0.85^{+0.00}_{-0.01}$	235.86	1.58	0.07	22.88
22402	GOODS-S	53.1418669	−27.901909	0.823	$0.87^{+0.00}_{-0.02}$	$0.75^{+0.01}_{-0.00}$	$0.83^{+0.01}_{-0.03}$	259.59	1.24	0.05	22.33
107136	GOODS-S	53.1073466	−27.741929	0.891	$0.98^{+0.00}_{-0.00}$	$0.99^{+0.00}_{-0.08}$	$0.99^{+0.00}_{-0.00}$	163.54	1.47	0.08	23.19
98420	GOODS-N	189.3300095	62.291136	1.200	$1.13^{+0.03}_{-0.13}$	$1.12^{+0.01}_{-0.00}$	$1.12^{+0.02}_{-0.03}$	109.52	1.25	0.14	23.85
25390	GOODS-S	53.1307081	−27.888658	1.000	$1.11^{+0.02}_{-0.03}$	$1.24^{+0.01}_{-0.00}$	$1.11^{+0.02}_{-0.02}$	197.11	1.51	0.09	22.01
33294	GOODS-S	53.1586671	−27.880188	1.035	$0.99^{+0.00}_{-0.01}$	$0.96^{+0.00}_{-0.00}$	$1.01^{+0.00}_{-0.00}$	176.43	1.15	0.06	23.49
43997	GOODS-S	53.1618662	−27.858128	0.754	$0.64^{+0.02}_{-0.00}$	$0.65^{+0.03}_{-0.01}$	$0.65^{+0.00}_{-0.00}$	132.38	1.26	0.10	23.45
111030	GOODS-S	53.0425693	−27.733020	1.058	$1.03^{+0.03}_{-0.04}$	$0.74^{+0.01}_{-0.29}$	$0.94^{+0.13}_{-0.00}$	47.18	1.23	0.20	24.66
93239	GOODS-N	189.3436071	62.280933	0.841	$0.85^{+0.02}_{-0.03}$	$0.81^{+0.03}_{-0.02}$	$0.84^{+0.01}_{-0.04}$	171.31	1.35	0.07	22.75
66256	GOODS-S	53.1932050	−27.820214	0.683	$0.66^{+0.03}_{-0.00}$	$0.68^{+0.01}_{-0.00}$	$0.69^{+0.00}_{-0.00}$	367.00	1.75	0.08	22.35
45496	GOODS-N	189.2052291	62.196807	0.960	$0.96^{+0.00}_{-0.02}$	$1.02^{+0.01}_{-0.07}$	$0.95^{+0.01}_{-0.01}$	179.82	1.44	0.08	22.96

continued . . .

. . . continued

PearsID	Field	RA	DEC	z_{spec}	z_{phot}	z_{grism}	z_{SPZ}	$\mathcal{N}$	D4000	$\sigma_{\rm D4000}$	i(AB)
61291	GOODS-N	189.1623525	62.224831	1.011	$1.00^{+0.00}_{-0.00}$	$1.00^{+0.00}_{-0.00}$	$1.00^{+0.00}_{-0.00}$	241.50	1.67	0.07	23.00
108987	GOODS-S	53.1570855	−27.737865	1.215	$1.36^{+0.03}_{-0.02}$	$1.13^{+0.32}_{-0.15}$	$1.10^{+0.01}_{-0.07}$	76.98	1.25	0.20	23.48
112840	GOODS-S	53.1347278	−27.729402	1.026	$0.98^{+0.02}_{-0.01}$	$0.86^{+0.00}_{-0.00}$	$0.98^{+0.00}_{-0.01}$	75.77	1.31	0.17	24.36
123476	GOODS-N	189.3758964	62.342342	0.634	$0.64^{+0.01}_{-0.02}$	$0.34^{+0.15}_{-0.00}$	$0.60^{+0.03}_{-0.03}$	611.24	1.23	0.04	21.00
120825	GOODS-S	53.0960605	−27.707305	0.733	$0.70^{+0.00}_{-0.00}$	$0.37^{+0.17}_{-0.00}$	$0.66^{+0.01}_{-0.02}$	272.75	1.22	0.05	22.03
34128	GOODS-S	53.1589571	−27.877881	0.734	$0.67^{+0.01}_{-0.01}$	$0.83^{+0.03}_{-0.00}$	$0.66^{+0.00}_{-0.00}$	228.19	1.32	0.06	22.83
46766	GOODS-N	189.1889185	62.198477	0.968	$0.98^{+0.01}_{-0.01}$	$1.01^{+0.00}_{-0.01}$	$1.00^{+0.00}_{-0.00}$	156.58	1.75	0.12	23.32
78475	GOODS-N	189.1491249	62.253905	0.854	$0.84^{+0.01}_{-0.00}$	$0.85^{+0.00}_{-0.00}$	$0.85^{+0.00}_{-0.01}$	165.46	1.61	0.10	23.34
62388	GOODS-N	189.1976740	62.225022	0.964	$0.91^{+0.04}_{-0.02}$	$0.79^{+0.00}_{-0.00}$	$0.86^{+0.01}_{-0.00}$	82.35	1.28	0.13	23.76
67582	GOODS-N	189.2202524	62.234699	1.014	$0.99^{+0.01}_{-0.01}$	$1.02^{+0.00}_{-0.02}$	$0.98^{+0.01}_{-0.01}$	139.62	1.22	0.09	23.25
81749	GOODS-N	189.1758510	62.262638	0.858	$1.20^{+0.00}_{-0.00}$	$1.01^{+0.00}_{-0.01}$	$1.19^{+0.00}_{-0.01}$	514.03	1.36	0.04	21.39
99490	GOODS-S	53.1065888	−27.758035	0.667	$0.58^{+0.15}_{-0.05}$	$0.53^{+0.17}_{-0.01}$	$0.70^{+0.02}_{-0.02}$	62.97	1.33	0.17	24.43
76125	GOODS-S	53.1385500	−27.799460	1.098	$1.02^{+0.06}_{-0.06}$	$1.14^{+0.14}_{-0.02}$	$1.09^{+0.05}_{-0.09}$	72.02	1.31	0.19	24.75
70232	GOODS-S	53.1564022	−27.810814	0.665	$0.68^{+0.00}_{-0.00}$	$0.37^{+0.00}_{-0.01}$	$0.66^{+0.01}_{-0.01}$	726.89	1.16	0.03	20.98
86999	GOODS-N	189.3033036	62.271670	0.851	$0.83^{+0.00}_{-0.01}$	$0.89^{+0.00}_{-0.00}$	$0.89^{+0.00}_{-0.00}$	363.46	1.35	0.05	22.34
93364	GOODS-N	189.3841570	62.282941	0.975	$0.96^{+0.00}_{-0.05}$	$1.10^{+0.07}_{-0.07}$	$0.95^{+0.02}_{-0.04}$	761.60	1.42	0.04	21.63
62376	GOODS-N	189.1804328	62.225739	0.904	$0.83^{+0.01}_{-0.01}$	$0.34^{+0.00}_{-0.01}$	$0.89^{+0.00}_{-0.00}$	116.69	1.35	0.10	23.41
54405	GOODS-N	189.1663611	62.213902	0.846	$0.82^{+0.00}_{-0.00}$	$0.84^{+0.00}_{-0.00}$	$0.82^{+0.00}_{-0.01}$	575.11	1.35	0.04	21.32
122766	GOODS-S	53.0717630	−27.708439	0.605	$0.50^{+0.02}_{-0.02}$	$0.33^{+0.00}_{-0.01}$	$0.55^{+0.00}_{-0.01}$	128.00	1.18	0.11	23.01
94812	GOODS-N	189.1614505	62.285139	0.682	$0.59^{+0.05}_{-0.00}$	$0.42^{+0.00}_{-0.00}$	$0.65^{+0.00}_{-0.00}$	526.09	1.25	0.04	21.66
36110	GOODS-S	53.1724271	−27.873753	0.611	$0.59^{+0.00}_{-0.01}$	$0.67^{+0.00}_{-0.00}$	$0.62^{+0.00}_{-0.00}$	161.95	1.40	0.10	23.22
52896	GOODS-N	189.1991331	62.209159	0.961	$0.94^{+0.01}_{-0.01}$	$0.37^{+0.01}_{-0.01}$	$0.91^{+0.01}_{-0.01}$	133.80	1.30	0.08	23.37
27974	GOODS-S	53.1466117	−27.889677	0.670	$0.76^{+0.00}_{-0.01}$	$0.66^{+0.00}_{-0.00}$	$0.75^{+0.00}_{-0.03}$	254.65	1.71	0.11	22.75

continued . . .

. . . continued

PearsID	Field	RA	DEC	z_{spec}	z_{phot}	z_{grism}	z_{SPZ}	$\mathcal{N}$	D4000	σ_{D4000}	i(AB)
86604	GOODS-S	53.1452229	−27.777903	1.099	$1.13^{+0.04}_{-0.09}$	$1.08^{+0.01}_{-0.00}$	$1.13^{+0.02}_{-0.10}$	189.38	1.34	0.07	23.27
117865	GOODS-S	53.1300388	−27.719551	1.022	$1.01^{+0.02}_{-0.05}$	$0.99^{+0.00}_{-0.60}$	$0.99^{+0.00}_{-0.02}$	81.77	1.35	0.15	24.73
30763	GOODS-S	53.1654674	−27.885331	0.685	$0.69^{+0.02}_{-0.02}$	$0.53^{+0.08}_{-0.01}$	$0.65^{+0.05}_{-0.00}$	176.29	1.18	0.08	22.89
94231	GOODS-N	189.3795897	62.287426	1.013	$0.98^{+0.01}_{-0.05}$	$1.09^{+0.02}_{-0.01}$	$1.00^{+0.00}_{-0.05}$	358.40	1.43	0.05	21.94
71071	GOODS-S	53.1323007	−27.810923	0.996	$0.94^{+0.01}_{-0.00}$	$1.49^{+0.00}_{-0.71}$	$0.94^{+0.03}_{-0.01}$	51.92	1.41	0.22	24.69
127226	GOODS-S	53.0617823	−27.699201	0.680	$0.67^{+0.00}_{-0.00}$	$0.67^{+0.03}_{-0.00}$	$0.67^{+0.00}_{-0.00}$	357.05	1.66	0.08	22.35
52460	GOODS-N	189.2315221	62.212656	0.791	$0.81^{+0.00}_{-0.00}$	$0.36^{+0.00}_{-0.00}$	$0.78^{+0.01}_{-0.00}$	315.63	1.37	0.05	21.99
77821	GOODS-S	53.1376154	−27.791914	0.998	$0.91^{+0.01}_{-0.00}$	$1.04^{+0.00}_{-0.00}$	$0.99^{+0.00}_{-0.01}$	224.23	1.39	0.08	22.61
62223	GOODS-S	53.1418806	−27.827172	0.840	$0.84^{+0.01}_{-0.01}$	$0.85^{+0.00}_{-0.05}$	$0.84^{+0.01}_{-0.03}$	151.41	1.68	0.13	23.53
77555	GOODS-N	189.1353010	62.253679	0.683	$0.78^{+0.00}_{-0.02}$	$0.35^{+0.00}_{-0.05}$	$0.78^{+0.00}_{-0.01}$	352.75	1.38	0.05	21.92
89112	GOODS-N	189.3512440	62.275530	0.852	$0.91^{+0.01}_{-0.00}$	$0.31^{+0.00}_{-0.01}$	$0.86^{+0.05}_{-0.00}$	296.18	1.25	0.05	22.13
79587	GOODS-N	189.3103218	62.258285	0.857	$0.84^{+0.00}_{-0.00}$	$0.87^{+0.00}_{-0.00}$	$0.83^{+0.00}_{-0.00}$	275.63	1.81	0.09	22.26
117715	GOODS-N	189.4000044	62.322069	1.026	$0.96^{+0.05}_{-0.03}$	$1.16^{+0.07}_{-0.01}$	$0.98^{+0.06}_{-0.02}$	100.71	1.33	0.13	24.26
58222	GOODS-S	53.2087572	−27.834432	0.713	$0.73^{+0.01}_{-0.01}$	$0.73^{+0.01}_{-0.07}$	$0.72^{+0.01}_{-0.01}$	146.05	1.33	0.10	23.55
121733	GOODS-S	53.0399146	−27.711628	0.683	$0.68^{+0.02}_{-0.02}$	$0.67^{+0.00}_{-0.00}$	$0.67^{+0.00}_{-0.00}$	171.17	1.15	0.07	23.38
98209	GOODS-N	189.3194843	62.292583	1.146	$1.49^{+0.00}_{-0.06}$	$1.47^{+0.01}_{-0.00}$	$1.49^{+0.00}_{-0.09}$	286.62	1.22	0.05	22.64
112448	GOODS-S	53.1554831	−27.726190	0.660	$0.66^{+0.00}_{-0.01}$	$0.95^{+0.00}_{-0.14}$	$0.66^{+0.00}_{-0.01}$	371.84	1.53	0.07	21.85
109900	GOODS-S	53.1128097	−27.734630	0.739	$0.92^{+0.00}_{-0.02}$	$0.41^{+0.00}_{-0.00}$	$0.73^{+0.00}_{-0.01}$	370.58	1.13	0.04	22.40
113555	GOODS-S	53.1148764	−27.725394	0.607	$0.68^{+0.03}_{-0.01}$	$0.45^{+0.00}_{-0.00}$	$0.71^{+0.01}_{-0.00}$	237.33	1.38	0.08	22.59
47101	GOODS-S	53.2063098	−27.851605	0.783	$0.75^{+0.01}_{-0.01}$	$0.45^{+0.00}_{-0.01}$	$0.76^{+0.01}_{-0.00}$	303.79	1.23	0.05	22.07
91947	GOODS-N	189.1685725	62.278265	0.849	$0.95^{+0.02}_{-0.01}$	$0.53^{+0.00}_{-0.01}$	$0.85^{+0.00}_{-0.00}$	120.13	1.18	0.09	23.95
45451	GOODS-N	189.1595647	62.197454	0.841	$0.94^{+0.00}_{-0.06}$	$0.85^{+0.00}_{-0.01}$	$0.94^{+0.00}_{-0.05}$	257.71	1.42	0.06	22.39
90536	GOODS-N	189.2420607	62.277510	1.017	$1.04^{+0.00}_{-0.00}$	$1.03^{+0.00}_{-0.01}$	$1.03^{+0.00}_{-0.00}$	278.02	1.78	0.07	22.57

continued . . .

. . . continued

PearsID	Field	RA	DEC	z_{spec}	z_{phot}	z_{grism}	z_{SPZ}	$\mathcal{N}$	D4000	$\sigma_{\rm D4000}$	i(AB)
38445	GOODS-N	189.2005634	62.183952	0.649	$0.72^{+0.02}_{-0.03}$	$0.38^{+0.00}_{-0.01}$	$0.69^{+0.03}_{-0.04}$	191.30	1.27	0.09	22.50
68525	GOODS-S	53.1711820	−27.814712	0.683	$0.45^{+0.00}_{-0.00}$	$0.35^{+0.00}_{-0.00}$	$0.46^{+0.00}_{-0.00}$	979.91	1.17	0.03	20.57
96423	GOODS-N	189.3643627	62.287230	0.778	$0.85^{+0.13}_{-0.00}$	$0.37^{+0.00}_{-0.00}$	$0.83^{+0.19}_{-0.00}$	191.74	1.21	0.06	22.69
76094	GOODS-S	53.1554484	−27.791484	0.710	$0.66^{+0.00}_{-0.00}$	$0.92^{+0.00}_{-0.04}$	$0.65^{+0.00}_{-0.00}$	1269.14	1.44	0.04	20.30
109851	GOODS-N	189.2711498	62.312059	0.875	$0.90^{+0.03}_{-0.01}$	$0.33^{+1.08}_{-0.03}$	$0.88^{+0.00}_{-0.01}$	141.76	1.28	0.08	23.29
17495	GOODS-S	53.1303655	−27.913615	0.661	$0.85^{+0.04}_{-0.07}$	$1.42^{+0.01}_{-0.01}$	$0.86^{+0.02}_{-0.08}$	74.49	1.11	0.17	24.06
123538	GOODS-N	189.3931748	62.341860	0.938	$0.93^{+0.00}_{-0.00}$	$1.05^{+0.05}_{-0.02}$	$0.93^{+0.00}_{-0.00}$	385.52	1.59	0.06	21.93
66708	GOODS-S	53.1617076	−27.819261	0.669	$0.88^{+0.01}_{-0.02}$	$0.34^{+0.01}_{-0.00}$	$0.77^{+0.00}_{-0.01}$	244.11	1.26	0.07	22.88
88347	GOODS-N	189.3539121	62.273490	0.709	$0.59^{+0.01}_{-0.02}$	$1.18^{+0.01}_{-0.02}$	$0.57^{+0.02}_{-0.01}$	127.94	1.23	0.09	23.50
85256	GOODS-S	53.1288245	−27.780420	1.173	$1.23^{+0.12}_{-0.20}$	$1.11^{+0.10}_{-0.01}$	$1.21^{+0.12}_{-0.09}$	90.82	1.44	0.16	23.95
50670	GOODS-N	189.1624276	62.205493	0.608	$0.55^{+0.01}_{-0.01}$	$0.76^{+0.00}_{-0.00}$	$0.59^{+0.00}_{-0.00}$	302.61	1.34	0.06	22.23
43618	GOODS-N	189.1825663	62.195238	0.768	$0.73^{+0.00}_{-0.00}$	$0.77^{+0.01}_{-0.01}$	$0.73^{+0.00}_{-0.00}$	795.94	1.60	0.05	20.90
107263	GOODS-N	189.3201245	62.306652	0.839	$0.91^{+0.00}_{-0.00}$	$1.37^{+0.00}_{-0.00}$	$0.84^{+0.00}_{-0.00}$	264.20	1.36	0.07	22.77
117725	GOODS-S	53.0404348	−27.713365	0.735	$0.71^{+0.06}_{-0.06}$	$1.02^{+0.02}_{-0.02}$	$0.73^{+0.03}_{-0.03}$	701.90	1.47	0.05	20.86
36708	GOODS-N	189.1417078	62.181841	0.764	$0.79^{+0.01}_{-0.02}$	$0.47^{+0.00}_{-0.00}$	$0.74^{+0.01}_{-0.01}$	356.96	1.22	0.04	21.62
93811	GOODS-S	53.1460878	−27.766564	0.954	$0.85^{+0.04}_{-0.02}$	$0.32^{+0.03}_{-0.00}$	$0.92^{+0.02}_{-0.00}$	106.31	1.22	0.09	23.73
116636	GOODS-N	189.3095285	62.320093	1.224	$1.04^{+0.03}_{-0.02}$	$1.19^{+0.01}_{-0.02}$	$1.11^{+0.01}_{-0.00}$	98.01	1.47	0.16	23.84
48229	GOODS-N	189.1915296	62.200388	0.679	$0.56^{+0.02}_{-0.03}$	$0.84^{+0.00}_{-0.01}$	$0.65^{+0.00}_{-0.00}$	93.88	1.19	0.10	23.67
121095	GOODS-S	53.0792362	−27.711868	1.019	$0.97^{+0.00}_{-0.00}$	$1.01^{+0.00}_{-0.01}$	$0.97^{+0.05}_{-0.00}$	151.16	1.70	0.11	23.43
97879	GOODS-N	189.3980533	62.301465	0.840	$0.85^{+0.00}_{-0.04}$	$1.49^{+0.00}_{-0.00}$	$0.84^{+0.01}_{-0.03}$	586.22	1.37	0.05	20.73
78300	GOODS-N	189.2256455	62.254197	0.849	$0.83^{+0.13}_{-0.01}$	$0.49^{+0.00}_{-0.00}$	$0.81^{+0.00}_{-0.00}$	250.04	1.18	0.05	22.77
112486	GOODS-N	189.3236425	62.314013	0.835	$0.95^{+0.01}_{-0.04}$	$0.49^{+0.01}_{-0.00}$	$0.81^{+0.00}_{-0.00}$	123.66	1.13	0.08	23.66
103037	GOODS-S	53.1594073	−27.748641	0.666	$0.67^{+0.02}_{-0.00}$	$0.64^{+0.01}_{-0.00}$	$0.67^{+0.00}_{-0.00}$	385.98	1.76	0.08	21.72

continued . . .

. . . continued

PearsID	Field	RA	DEC	z_{spec}	z_{phot}	z_{grism}	z_{SPZ}	$\mathcal{N}$	D4000	σ_{D4000}	i(AB)
89845	GOODS-N	189.3358390	62.274894	0.840	$0.83^{+0.00}_{-0.01}$	$0.63^{+0.01}_{-0.02}$	$0.81^{+0.02}_{-0.05}$	312.40	1.28	0.05	21.76
58181	GOODS-S	53.1680222	−27.832514	0.650	$0.65^{+0.02}_{-0.00}$	$0.66^{+0.01}_{-0.00}$	$0.66^{+0.01}_{-0.00}$	362.04	1.79	0.08	22.28
76098	GOODS-N	189.2013683	62.252073	0.938	$0.86^{+0.00}_{-0.00}$	$0.94^{+0.00}_{-0.01}$	$0.92^{+0.00}_{-0.00}$	429.93	1.84	0.07	22.10
86357	GOODS-N	189.1617285	62.268264	0.854	$0.86^{+0.00}_{-0.00}$	$0.86^{+0.00}_{-0.00}$	$0.86^{+0.00}_{-0.00}$	317.54	1.74	0.07	22.68
79426	GOODS-N	189.2179819	62.260341	0.939	$0.93^{+0.01}_{-0.00}$	$0.95^{+0.01}_{-0.00}$	$0.95^{+0.00}_{-0.02}$	285.63	1.68	0.07	22.15
48189	GOODS-N	189.1667451	62.202052	1.017	$0.97^{+0.00}_{-0.00}$	$1.02^{+0.00}_{-0.00}$	$0.99^{+0.00}_{-0.00}$	326.23	1.60	0.06	22.39
26891	GOODS-S	53.1441777	−27.890151	1.099	$1.28^{+0.01}_{-0.09}$	$1.06^{+0.00}_{-0.00}$	$1.27^{+0.01}_{-0.17}$	312.58	1.14	0.05	22.40
97070	GOODS-N	189.2308114	62.288324	0.941	$0.90^{+0.20}_{-0.00}$	$0.96^{+0.00}_{-0.01}$	$0.89^{+0.21}_{-0.00}$	127.94	1.41	0.10	23.59
92108	GOODS-N	189.3597889	62.279739	1.183	$1.11^{+0.02}_{-0.03}$	$1.12^{+0.04}_{-0.00}$	$1.12^{+0.04}_{-0.00}$	138.73	1.21	0.09	23.72
74133	GOODS-S	53.1489575	−27.799680	0.665	$0.67^{+0.00}_{-0.00}$	$0.88^{+0.03}_{-0.04}$	$0.67^{+0.00}_{-0.00}$	1056.98	1.54	0.04	20.80
56190	GOODS-N	189.1981062	62.214635	0.681	$0.57^{+0.02}_{-0.04}$	$0.74^{+0.01}_{-0.28}$	$0.70^{+0.00}_{-0.00}$	102.98	1.32	0.13	23.94
78710	GOODS-S	53.1491348	−27.792985	1.223	$1.21^{+0.01}_{-0.05}$	$1.14^{+0.13}_{-0.01}$	$1.23^{+0.01}_{-0.10}$	67.81	1.42	0.20	24.60
109885	GOODS-S	53.0713359	−27.735481	0.730	$0.72^{+0.00}_{-0.03}$	$0.72^{+0.01}_{-0.00}$	$0.72^{+0.00}_{-0.00}$	165.99	1.63	0.12	23.11
84001	GOODS-N	189.2388180	62.266877	0.940	$0.83^{+0.06}_{-0.04}$	$0.94^{+0.00}_{-0.01}$	$0.96^{+0.01}_{-0.02}$	81.43	1.41	0.15	23.42
122616	GOODS-N	189.3817051	62.335724	1.153	$1.03^{+0.03}_{-0.01}$	$1.15^{+0.00}_{-0.00}$	$1.15^{+0.00}_{-0.01}$	96.93	1.28	0.15	23.30
74641	GOODS-N	189.1747314	62.249069	0.850	$0.94^{+0.00}_{-0.06}$	$0.76^{+0.22}_{-0.01}$	$0.94^{+0.01}_{-0.06}$	176.49	1.41	0.08	22.97
76917	GOODS-N	189.1814877	62.251585	0.848	$0.83^{+0.03}_{-0.01}$	$0.78^{+0.00}_{-0.14}$	$0.82^{+0.00}_{-0.01}$	150.28	1.28	0.08	23.02
113361	GOODS-S	53.1132340	−27.726632	0.668	$0.74^{+0.00}_{-0.00}$	$1.49^{+0.00}_{-0.01}$	$0.73^{+0.01}_{-0.05}$	235.84	1.35	0.08	22.46
14386	GOODS-S	53.1397446	−27.920454	0.658	$0.64^{+0.01}_{-0.02}$	$0.63^{+0.01}_{-0.00}$	$0.66^{+0.00}_{-0.02}$	177.05	1.33	0.09	22.99
27994	GOODS-S	53.1335325	−27.890769	0.988	$0.91^{+0.03}_{-0.05}$	$0.43^{+0.00}_{-0.07}$	$0.95^{+0.00}_{-0.01}$	77.04	1.25	0.14	24.14
57446	GOODS-S	53.1521569	−27.835112	0.989	$0.73^{+0.01}_{-0.00}$	$0.43^{+0.00}_{-0.02}$	$0.71^{+0.00}_{-0.05}$	466.03	1.15	0.04	21.59
17704	GOODS-S	53.1847841	−27.913397	0.732	$0.61^{+0.01}_{-0.02}$	$0.73^{+0.04}_{-0.01}$	$0.67^{+0.01}_{-0.01}$	151.80	1.44	0.11	23.28
55923	GOODS-N	189.1138417	62.216061	1.223	$1.21^{+0.01}_{-0.00}$	$1.15^{+0.00}_{-0.01}$	$1.21^{+0.00}_{-0.00}$	328.03	1.19	0.06	22.76

continued . . .

. . . continued

PearsID	Field	RA	DEC	z_{spec}	z_{phot}	z_{grism}	z_{SPZ}	$\mathcal{N}$	D4000	$\sigma_{\rm D4000}$	i(AB)
68675	GOODS-S	53.1745112	−27.814960	0.666	$0.68^{+0.00}_{-0.00}$	$0.69^{+0.00}_{-0.00}$	$0.62^{+0.00}_{-0.00}$	510.38	1.16	0.04	22.01
37181	GOODS-N	189.1591231	62.181325	0.766	$0.74^{+0.06}_{-0.05}$	$0.61^{+0.01}_{-0.00}$	$0.70^{+0.00}_{-0.01}$	75.12	1.18	0.13	23.73
119723	GOODS-N	189.3504106	62.327519	0.804	$0.98^{+0.00}_{-0.00}$	$0.48^{+0.01}_{-0.00}$	$0.82^{+0.01}_{-0.01}$	292.28	1.15	0.04	22.82
122560	GOODS-N	189.3970214	62.335577	1.083	$1.07^{+0.00}_{-0.01}$	$1.06^{+0.01}_{-0.00}$	$1.04^{+0.03}_{-0.00}$	389.61	1.19	0.04	22.06
61447	GOODS-S	53.1852305	−27.827841	0.840	$1.00^{+0.02}_{-0.00}$	$0.85^{+0.00}_{-0.00}$	$1.01^{+0.00}_{-0.00}$	241.49	1.85	0.09	22.93
43816	GOODS-S	53.1378275	−27.856631	0.735	$0.73^{+0.03}_{-0.09}$	$0.72^{+0.20}_{-0.00}$	$0.72^{+0.00}_{-0.08}$	133.66	1.44	0.12	21.79
123843	GOODS-S	53.1053746	−27.706719	0.613	$0.36^{+0.00}_{-0.00}$	$0.32^{+0.01}_{-0.00}$	$0.30^{+0.00}_{-0.00}$	322.49	1.18	0.05	22.41
70787	GOODS-N	189.2451694	62.243034	0.678	$0.85^{+0.02}_{-0.03}$	$0.39^{+0.36}_{-0.00}$	$0.84^{+0.02}_{-0.02}$	778.78	1.38	0.04	20.73
35765	GOODS-S	53.1631421	−27.873062	0.761	$0.84^{+0.00}_{-0.00}$	$1.02^{+0.00}_{-0.01}$	$0.83^{+0.12}_{-0.00}$	288.77	1.39	0.06	22.25
65620	GOODS-S	53.1649789	−27.819329	0.970	$0.97^{+0.00}_{-0.00}$	$0.97^{+0.00}_{-0.00}$	$0.97^{+0.00}_{-0.00}$	657.50	1.69	0.05	21.44
85298	GOODS-S	53.1790635	−27.780521	1.036	$1.11^{+0.00}_{-0.00}$	$1.01^{+0.00}_{-0.00}$	$1.10^{+0.01}_{-0.00}$	83.61	1.73	0.17	24.33
123472	GOODS-S	53.0930594	−27.707373	1.010	$1.03^{+0.01}_{-0.01}$	$0.99^{+0.00}_{-0.00}$	$1.04^{+0.01}_{-0.00}$	118.60	1.74	0.14	23.56
123290	GOODS-N	189.3980521	62.338414	1.142	$1.16^{+0.00}_{-0.05}$	$1.14^{+0.00}_{-0.07}$	$1.16^{+0.00}_{-0.04}$	165.23	1.37	0.08	22.87
83237	GOODS-N	189.1616765	62.263124	0.904	$0.82^{+0.02}_{-0.00}$	$0.32^{+0.00}_{-0.00}$	$0.82^{+0.00}_{-0.00}$	382.63	1.27	0.04	22.19
92860	GOODS-S	53.1614988	−27.767621	0.680	$0.64^{+0.03}_{-0.02}$	$0.39^{+0.00}_{-0.00}$	$0.68^{+0.00}_{-0.00}$	149.48	1.15	0.08	23.76
94544	GOODS-S	53.1946158	−27.765542	1.095	$1.00^{+0.12}_{-0.00}$	$1.11^{+0.00}_{-0.01}$	$1.00^{+0.13}_{-0.00}$	55.14	1.54	0.22	24.21
91800	GOODS-N	189.2262114	62.281970	0.942	$0.92^{+0.00}_{-0.04}$	$0.93^{+0.00}_{-0.00}$	$0.92^{+0.00}_{-0.00}$	271.82	1.66	0.07	22.39
78077	GOODS-S	53.1841650	−27.792630	0.737	$0.92^{+0.00}_{-0.00}$	$0.46^{+0.01}_{-0.00}$	$0.74^{+0.00}_{-0.00}$	782.83	1.16	0.03	21.68
36842	GOODS-N	189.1851440	62.181358	0.937	$0.83^{+0.03}_{-0.01}$	$0.34^{+0.00}_{-0.01}$	$0.90^{+0.00}_{-0.00}$	155.64	1.31	0.07	23.26
70156	GOODS-N	189.1614500	62.239445	0.966	$0.93^{+0.01}_{-0.00}$	$0.35^{+1.14}_{-0.00}$	$0.94^{+0.00}_{-0.00}$	161.50	1.34	0.10	23.03
75762	GOODS-N	189.1127342	62.252615	0.794	$0.79^{+0.00}_{-0.00}$	$0.80^{+0.00}_{-0.00}$	$0.79^{+0.00}_{-0.00}$	643.12	1.75	0.06	21.11
51356	GOODS-S	53.1566795	−27.843269	0.628	$0.57^{+0.00}_{-0.00}$	$0.45^{+0.02}_{-0.01}$	$0.58^{+0.00}_{-0.00}$	427.14	1.21	0.04	21.57
85491	GOODS-N	189.2247125	62.268616	0.850	$0.95^{+0.00}_{-0.00}$	$0.51^{+0.00}_{-0.01}$	$0.84^{+0.00}_{-0.00}$	212.08	1.13	0.05	22.73

continued . . .

. . . continued

PearsID	Field	RA	DEC	z_{spec}	z_{phot}	z_{grism}	z_{SPZ}	$\mathcal{N}$	D4000	$\sigma_{\rm D4000}$	i(AB)
115288	GOODS-S	53.1309357	−27.723377	1.025	$0.96^{+0.17}_{-0.00}$	$1.15^{+0.00}_{-0.02}$	$1.15^{+0.00}_{-0.10}$	92.76	1.67	0.16	23.76
42119	GOODS-N	189.2095962	62.190913	0.954	$0.93^{+0.01}_{-0.00}$	$1.48^{+0.01}_{-0.00}$	$0.88^{+0.00}_{-0.00}$	152.40	1.29	0.08	22.57
114628	GOODS-N	189.3971628	62.321637	0.836	$0.88^{+0.02}_{-0.00}$	$0.99^{+0.01}_{-0.00}$	$0.88^{+0.00}_{-0.02}$	541.75	1.40	0.04	21.45
86173	GOODS-N	189.1532405	62.267988	0.843	$0.88^{+0.00}_{-0.05}$	$0.86^{+0.22}_{-0.00}$	$0.87^{+0.00}_{-0.03}$	199.97	1.54	0.08	22.85
110870	GOODS-S	53.1250970	−27.729791	0.670	$0.73^{+0.00}_{-0.02}$	$1.49^{+0.00}_{-0.00}$	$0.64^{+0.04}_{-0.06}$	1001.01	1.21	0.04	20.05
108795	GOODS-S	53.1529810	−27.735115	0.665	$0.75^{+0.00}_{-0.00}$	$1.49^{+0.00}_{-0.00}$	$0.75^{+0.00}_{-0.00}$	351.36	1.31	0.05	21.96
134044	GOODS-S	53.0776149	−27.685201	1.127	$1.03^{+0.02}_{-0.02}$	$1.07^{+0.06}_{-0.01}$	$1.06^{+0.01}_{-0.00}$	67.63	1.35	0.21	24.16
117138	GOODS-S	53.0723515	−27.718686	0.648	$0.61^{+0.00}_{-0.00}$	$0.41^{+0.00}_{-0.00}$	$0.58^{+0.00}_{-0.00}$	581.46	1.19	0.04	21.18
52097	GOODS-N	189.2170311	62.207323	1.224	$1.16^{+0.02}_{-0.00}$	$1.13^{+0.17}_{-0.01}$	$1.15^{+0.02}_{-0.01}$	71.03	1.62	0.23	24.30
117070	GOODS-S	53.0579876	−27.720001	0.681	$0.44^{+0.02}_{-0.01}$	$0.69^{+0.00}_{-0.00}$	$0.47^{+0.00}_{-0.00}$	89.10	1.25	0.13	23.42
88566	GOODS-N	189.1720747	62.271681	0.850	$0.86^{+0.00}_{-0.01}$	$0.85^{+0.00}_{-0.00}$	$0.85^{+0.00}_{-0.00}$	202.17	1.69	0.09	23.19
53362	GOODS-N	189.1383792	62.209994	1.141	$1.03^{+0.02}_{-0.02}$	$1.21^{+0.01}_{-0.00}$	$1.10^{+0.00}_{-0.01}$	150.60	1.25	0.11	23.34
68104	GOODS-S	53.1912106	−27.817277	1.158	$1.05^{+0.04}_{-0.02}$	$1.07^{+0.00}_{-0.01}$	$1.07^{+0.01}_{-0.00}$	84.93	1.18	0.15	24.05
112339	GOODS-N	189.2730568	62.314237	0.856	$1.22^{+0.02}_{-0.08}$	$1.49^{+0.00}_{-0.25}$	$1.24^{+0.01}_{-0.06}$	132.44	1.18	0.10	23.44
47115	GOODS-N	189.1235786	62.200005	1.015	$1.28^{+0.02}_{-0.01}$	$1.11^{+0.01}_{-0.01}$	$1.10^{+0.01}_{-0.01}$	163.08	1.48	0.12	23.68
74060	GOODS-S	53.1634179	−27.799548	0.650	$0.68^{+0.00}_{-0.00}$	$0.66^{+0.01}_{-0.00}$	$0.67^{+0.00}_{-0.00}$	921.77	1.72	0.05	21.05
65145	GOODS-S	53.1473583	−27.822427	0.670	$1.47^{+0.02}_{-0.01}$	$0.33^{+0.06}_{-0.00}$	$1.49^{+0.00}_{-0.01}$	155.37	1.11	0.07	23.15
42277	GOODS-S	53.1756668	−27.862315	0.880	$0.84^{+0.01}_{-0.01}$	$0.89^{+0.00}_{-0.05}$	$0.84^{+0.01}_{-0.00}$	108.66	1.50	0.12	23.71
13986	GOODS-S	53.1720940	−27.920529	0.620	$0.54^{+0.01}_{-0.02}$	$0.62^{+0.01}_{-0.01}$	$0.61^{+0.00}_{-0.01}$	128.63	1.53	0.16	23.52
39835	GOODS-S	53.1780338	−27.866458	1.123	$1.04^{+0.01}_{-0.02}$	$1.10^{+0.00}_{-0.00}$	$1.09^{+0.01}_{-0.00}$	148.01	1.39	0.09	23.33
65404	GOODS-N	189.1931178	62.234639	0.961	$1.20^{+0.00}_{-0.00}$	$1.12^{+0.00}_{-0.00}$	$1.19^{+0.01}_{-0.00}$	647.93	1.44	0.04	21.48
59482	GOODS-S	53.2063116	−27.832483	1.227	$1.18^{+0.02}_{-0.02}$	$1.14^{+0.01}_{-0.00}$	$1.14^{+0.01}_{-0.00}$	67.99	1.31	0.21	24.28
37429	GOODS-S	53.1508874	−27.868331	0.761	$0.78^{+0.00}_{-0.04}$	$0.75^{+0.01}_{-0.00}$	$0.77^{+0.01}_{-0.00}$	304.78	1.60	0.07	21.71

continued . . .

. . . continued

PearsID	Field	RA	DEC	z_{spec}	z_{phot}	z_{grism}	z_{SPZ}	$\mathcal{N}$	D4000	$\sigma_{\rm D4000}$	i(AB)
55935	GOODS-N	189.2363417	62.214606	1.231	$1.12^{+0.01}_{-0.01}$	$1.18^{+0.00}_{-0.00}$	$1.11^{+0.01}_{-0.01}$	80.20	1.48	0.18	24.19
73058	GOODS-N	189.1245808	62.244721	0.761	$0.73^{+0.06}_{-0.00}$	$0.80^{+0.00}_{-0.00}$	$0.76^{+0.00}_{-0.03}$	259.31	1.37	0.06	22.52
41388	GOODS-N	189.1714112	62.190279	1.020	$0.98^{+0.03}_{-0.00}$	$1.05^{+0.00}_{-0.00}$	$0.99^{+0.02}_{-0.00}$	147.07	1.77	0.11	23.32
46603	GOODS-S	53.1371453	−27.852164	0.734	$0.72^{+0.02}_{-0.02}$	$0.75^{+0.01}_{-0.00}$	$0.75^{+0.00}_{-0.01}$	152.60	1.62	0.13	23.17
105095	GOODS-N	189.2455451	62.302763	0.943	$0.92^{+0.03}_{-0.03}$	$0.30^{+0.00}_{-0.00}$	$0.89^{+0.00}_{-0.00}$	150.85	1.18	0.07	23.15
110487	GOODS-S	53.1411224	−27.732656	0.979	$0.98^{+0.01}_{-0.02}$	$0.98^{+0.00}_{-0.02}$	$0.98^{+0.00}_{-0.00}$	138.30	1.74	0.11	23.45
87259	GOODS-S	53.1094858	−27.775934	0.738	$0.63^{+0.02}_{-0.02}$	$0.76^{+0.00}_{-0.00}$	$0.95^{+0.00}_{-0.00}$	51.22	1.72	0.19	22.82
36121	GOODS-S	53.1734378	−27.865976	0.779	$0.80^{+0.00}_{-0.00}$	$0.79^{+0.00}_{-0.01}$	$0.78^{+0.00}_{-0.00}$	838.35	1.76	0.06	20.76
69419	GOODS-S	53.1323758	−27.814240	0.750	$0.79^{+0.00}_{-0.00}$	$0.77^{+0.00}_{-0.00}$	$0.77^{+0.00}_{-0.00}$	251.62	1.70	0.09	23.03
73333	GOODS-S	53.1498462	−27.803301	0.605	$0.56^{+0.00}_{-0.00}$	$0.61^{+0.00}_{-0.01}$	$0.56^{+0.00}_{-0.00}$	720.32	1.43	0.05	21.59
71893	GOODS-N	189.2549969	62.241894	0.839	$0.85^{+0.06}_{-0.02}$	$0.72^{+0.01}_{-0.00}$	$0.81^{+0.00}_{-0.00}$	75.06	1.18	0.12	23.75
42703	GOODS-S	53.1363881	−27.850696	0.735	$0.72^{+0.00}_{-0.00}$	$0.75^{+0.00}_{-0.01}$	$0.75^{+0.00}_{-0.02}$	580.47	1.75	0.06	21.12
93370	GOODS-S	53.1138912	−27.767554	0.668	$0.63^{+0.01}_{-0.01}$	$0.64^{+0.03}_{-0.00}$	$0.64^{+0.00}_{-0.00}$	264.66	1.57	0.10	22.66
89655	GOODS-N	189.2711131	62.274348	1.121	$1.04^{+0.01}_{-0.01}$	$1.06^{+0.00}_{-0.01}$	$1.06^{+0.01}_{-0.00}$	141.73	1.11	0.08	23.36
99452	GOODS-N	189.2495025	62.293273	0.660	$0.64^{+0.01}_{-0.00}$	$0.41^{+0.00}_{-0.01}$	$0.58^{+0.04}_{-0.02}$	541.65	1.21	0.04	21.62
118434	GOODS-S	53.0496934	−27.718128	1.108	$1.09^{+0.02}_{-0.04}$	$1.11^{+0.01}_{-0.12}$	$1.10^{+0.01}_{-0.03}$	59.45	1.46	0.20	24.38
16151	GOODS-S	53.1318058	−27.917095	1.089	$0.98^{+0.02}_{-0.02}$	$1.09^{+0.01}_{-0.05}$	$1.00^{+0.03}_{-0.01}$	77.21	1.24	0.14	24.30
39801	GOODS-N	189.2217308	62.188003	0.938	$0.94^{+0.03}_{-0.02}$	$1.02^{+0.00}_{-0.00}$	$0.94^{+0.03}_{-0.03}$	333.14	1.41	0.05	21.78
94177	GOODS-N	189.1534424	62.282258	1.014	$0.97^{+0.02}_{-0.01}$	$0.97^{+0.01}_{-0.00}$	$0.99^{+0.01}_{-0.01}$	99.68	1.20	0.10	23.93
125963	GOODS-N	189.4135715	62.349900	0.837	$1.44^{+0.00}_{-0.00}$	$1.10^{+0.01}_{-0.00}$	$1.40^{+0.00}_{-0.01}$	995.43	1.11	0.03	20.50
70001	GOODS-S	53.2005520	−27.812487	0.670	$0.68^{+0.00}_{-0.00}$	$0.66^{+0.00}_{-0.00}$	$0.68^{+0.00}_{-0.00}$	424.52	1.75	0.08	21.88
41945	GOODS-N	189.2564439	62.191325	0.778	$0.83^{+0.05}_{-0.01}$	$0.36^{+0.00}_{-0.00}$	$0.81^{+0.04}_{-0.02}$	487.92	1.25	0.05	21.50
44746	GOODS-N	189.2420311	62.193817	0.680	$0.73^{+0.00}_{-0.01}$	$0.46^{+0.00}_{-0.00}$	$0.68^{+0.00}_{-0.00}$	193.01	1.12	0.06	23.11

continued . . .

...continued

PearsID	Field	RA	DEC	z_{spec}	z_{phot}	z_{grism}	z_{SPZ}	$\mathcal{N}$	D4000	$\sigma_{\rm D4000}$	i(AB)
126478	GOODS-S	53.0351877	−27.696088	0.730	$0.71^{+0.00}_{-0.00}$	$1.07^{+0.04}_{-0.03}$	$0.65^{+0.00}_{-0.00}$	656.87	1.21	0.04	21.94
47065	GOODS-N	189.1533358	62.203663	0.848	$0.84^{+0.00}_{-0.00}$	$1.07^{+0.00}_{-0.01}$	$0.84^{+0.00}_{-0.01}$	718.63	1.41	0.04	20.56
105709	GOODS-N	189.3056225	62.304234	1.082	$0.99^{+0.02}_{-0.01}$	$1.07^{+0.00}_{-0.01}$	$1.07^{+0.00}_{-0.00}$	136.82	1.27	0.10	23.31
52440	GOODS-N	189.1438811	62.211395	1.224	$1.40^{+0.00}_{-0.04}$	$1.20^{+0.00}_{-0.01}$	$1.41^{+0.08}_{-0.15}$	213.30	1.26	0.07	22.64
53237	GOODS-S	53.1799555	−27.843025	0.905	$1.10^{+0.00}_{-0.01}$	$0.82^{+0.01}_{-0.18}$	$1.13^{+0.00}_{-0.00}$	125.45	1.38	0.11	23.97
36105	GOODS-N	189.1914885	62.183611	0.931	$0.98^{+0.00}_{-0.01}$	$0.93^{+0.00}_{-0.00}$	$0.94^{+0.00}_{-0.01}$	248.73	1.82	0.10	22.40
48397	GOODS-N	189.2609274	62.204579	1.226	$1.17^{+0.03}_{-0.06}$	$1.42^{+0.00}_{-0.00}$	$1.16^{+0.04}_{-0.04}$	117.41	1.49	0.12	23.49
37225	GOODS-N	189.2081580	62.182990	0.683	$0.69^{+0.04}_{-0.03}$	$0.55^{+0.00}_{-0.16}$	$0.67^{+0.03}_{-0.01}$	241.33	1.25	0.06	22.67
123066	GOODS-S	53.0508125	−27.707512	0.735	$0.85^{+0.01}_{-0.03}$	$0.51^{+0.00}_{-0.01}$	$0.78^{+0.00}_{-0.01}$	116.91	1.32	0.10	23.65
75943	GOODS-N	189.1116870	62.249965	0.794	$0.81^{+0.01}_{-0.01}$	$0.82^{+0.01}_{-0.02}$	$0.80^{+0.01}_{-0.00}$	110.86	1.68	0.19	23.05
35156	GOODS-N	189.1994651	62.179304	1.223	$1.21^{+0.04}_{-0.05}$	$1.23^{+0.01}_{-0.00}$	$1.22^{+0.03}_{-0.06}$	189.96	1.33	0.08	22.62
86439	GOODS-N	189.2517898	62.268030	0.941	$0.85^{+0.05}_{-0.02}$	$0.34^{+0.58}_{-0.00}$	$0.91^{+0.01}_{-0.00}$	79.98	1.41	0.14	23.91
66729	GOODS-S	53.1363320	−27.816537	0.671	$0.65^{+0.00}_{-0.00}$	$0.61^{+0.00}_{-0.00}$	$0.65^{+0.00}_{-0.00}$	506.23	1.28	0.04	21.95
63902	GOODS-S	53.1617459	−27.824573	0.820	$0.82^{+0.00}_{-0.00}$	$0.82^{+0.00}_{-0.00}$	$0.82^{+0.00}_{-0.00}$	221.30	1.61	0.08	22.96
81011	GOODS-S	53.1603539	−27.784002	0.954	$0.90^{+0.00}_{-0.04}$	$0.97^{+0.00}_{-0.01}$	$0.90^{+0.01}_{-0.00}$	418.65	1.58	0.05	21.92
99892	GOODS-S	53.0951005	−27.755100	1.087	$1.01^{+0.01}_{-0.02}$	$1.03^{+0.01}_{-0.00}$	$1.02^{+0.01}_{-0.00}$	93.64	1.15	0.11	23.78
125952	GOODS-S	53.0335122	−27.701204	1.042	$1.00^{+0.01}_{-0.02}$	$1.29^{+0.02}_{-0.02}$	$1.02^{+0.02}_{-0.01}$	227.76	1.36	0.07	23.36
98997	GOODS-N	189.3637473	62.293080	1.011	$0.95^{+0.02}_{-0.02}$	$0.95^{+0.06}_{-0.00}$	$0.95^{+0.01}_{-0.00}$	143.34	1.34	0.08	23.12
86203	GOODS-N	189.1572727	62.268766	0.841	$0.81^{+0.01}_{-0.02}$	$0.84^{+0.00}_{-0.00}$	$0.80^{+0.02}_{-0.00}$	271.28	1.69	0.08	22.32
105455	GOODS-N	189.2603162	62.305642	0.767	$0.77^{+0.01}_{-0.01}$	$0.50^{+0.25}_{-0.14}$	$0.75^{+0.00}_{-0.01}$	258.67	1.36	0.06	22.58
54823	GOODS-S	53.1449423	−27.840218	0.978	$0.95^{+0.00}_{-0.01}$	$0.90^{+0.00}_{-0.00}$	$0.96^{+0.00}_{-0.01}$	196.85	1.12	0.07	22.80
28271	GOODS-N	189.1626963	62.168415	0.636	$0.85^{+0.00}_{-0.00}$	$0.58^{+0.01}_{-0.12}$	$0.68^{+0.00}_{-0.00}$	479.15	1.33	0.05	21.51
34457	GOODS-S	53.1465972	−27.876704	0.782	$0.69^{+0.00}_{-0.01}$	$0.50^{+0.00}_{-0.00}$	$0.77^{+0.00}_{-0.00}$	193.22	1.32	0.06	22.70

continued ...

. . . continued

PearsID	Field	RA	DEC	z_{spec}	z_{phot}	z_{grism}	z_{SPZ}	$\mathcal{N}$	D4000	$\sigma_{\rm D4000}$	i(AB)
118148	GOODS-N	189.3873210	62.323195	0.936	$0.92^{+0.01}_{-0.03}$	$0.36^{+0.00}_{-0.00}$	$0.82^{+0.04}_{-0.00}$	150.37	1.16	0.07	23.27
82267	GOODS-N	189.2077989	62.261628	0.942	$0.94^{+0.02}_{-0.01}$	$0.95^{+0.01}_{-0.00}$	$0.94^{+0.02}_{-0.02}$	175.92	1.46	0.08	22.83
102886	GOODS-N	189.2677677	62.300502	0.639	$0.66^{+0.02}_{-0.01}$	$0.74^{+0.00}_{-0.00}$	$0.65^{+0.01}_{-0.00}$	125.11	1.39	0.18	23.32
51003	GOODS-N	189.2044409	62.205905	0.954	$0.94^{+0.00}_{-0.00}$	$0.32^{+0.01}_{-0.00}$	$0.90^{+0.00}_{-0.00}$	242.66	1.21	0.05	22.46
115462	GOODS-S	53.0975207	−27.721266	0.615	$0.62^{+0.00}_{-0.02}$	$0.37^{+0.00}_{-0.00}$	$0.61^{+0.01}_{-0.00}$	994.16	1.32	0.04	20.79
126094	GOODS-S	53.0533614	−27.700461	1.018	$0.99^{+0.00}_{-0.00}$	$0.38^{+0.00}_{-0.01}$	$0.98^{+0.02}_{-0.03}$	294.31	1.31	0.05	21.90
127420	GOODS-N	189.3570418	62.349206	1.083	$1.00^{+0.00}_{-0.00}$	$1.02^{+0.00}_{-0.00}$	$0.99^{+0.00}_{-0.00}$	328.55	1.15	0.05	22.64
106613	GOODS-N	189.2741667	62.304796	0.855	$0.91^{+0.03}_{-0.01}$	$1.49^{+0.00}_{-1.18}$	$0.88^{+0.01}_{-0.00}$	122.25	1.14	0.07	23.52
65833	GOODS-N	189.2253789	62.231777	0.850	$0.83^{+0.01}_{-0.02}$	$0.33^{+0.01}_{-0.01}$	$0.84^{+0.00}_{-0.04}$	212.70	1.32	0.06	22.51
117087	GOODS-N	189.4419188	62.321199	1.012	$1.00^{+0.02}_{-0.05}$	$0.84^{+0.05}_{-0.01}$	$1.00^{+0.01}_{-0.07}$	50.91	1.27	0.20	23.50
53563	GOODS-N	189.1922296	62.212921	0.905	$0.89^{+0.00}_{-0.01}$	$0.90^{+0.01}_{-0.01}$	$0.89^{+0.00}_{-0.00}$	297.44	1.63	0.07	22.44
49261	GOODS-N	189.2010933	62.203861	0.961	$0.95^{+0.00}_{-0.01}$	$1.38^{+0.01}_{-1.07}$	$0.94^{+0.01}_{-0.00}$	170.27	1.33	0.09	22.55
101785	GOODS-N	189.2603805	62.297084	1.018	$0.99^{+0.01}_{-0.00}$	$0.99^{+0.00}_{-0.00}$	$0.98^{+0.01}_{-0.00}$	275.89	1.18	0.05	22.55
44204	GOODS-S	53.1658616	−27.858858	1.036	$0.98^{+0.02}_{-0.15}$	$1.01^{+0.01}_{-0.00}$	$1.00^{+0.02}_{-0.00}$	39.90	1.40	0.26	24.38
119489	GOODS-S	53.0551239	−27.711379	0.605	$0.78^{+0.00}_{-0.00}$	$0.34^{+0.01}_{-0.00}$	$0.78^{+0.00}_{-0.00}$	1689.60	1.20	0.03	19.88
97904	GOODS-N	189.3000232	62.290841	0.681	$0.68^{+0.00}_{-0.00}$	$1.48^{+0.01}_{-0.01}$	$0.65^{+0.01}_{-0.01}$	488.29	1.17	0.04	21.68
113696	GOODS-N	189.3371364	62.317026	0.747	$0.93^{+0.01}_{-0.07}$	$0.33^{+1.14}_{-0.01}$	$0.92^{+0.02}_{-0.07}$	117.12	1.29	0.11	23.63
21612	GOODS-S	53.1758193	−27.903717	0.737	$0.69^{+0.01}_{-0.02}$	$0.47^{+0.00}_{-0.00}$	$0.66^{+0.01}_{-0.02}$	203.85	1.19	0.06	22.75
107152	GOODS-N	189.3790634	62.305686	1.012	$0.95^{+0.02}_{-0.04}$	$1.08^{+0.39}_{-0.00}$	$1.00^{+0.01}_{-0.00}$	252.11	1.30	0.06	23.15
55434	GOODS-S	53.2043350	−27.837635	0.605	$1.17^{+0.07}_{-0.10}$	$1.20^{+0.00}_{-0.07}$	$1.17^{+0.09}_{-0.10}$	135.54	1.38	0.18	23.18
70878	GOODS-S	53.1643086	−27.810825	0.736	$0.92^{+0.01}_{-0.01}$	$0.51^{+0.01}_{-0.00}$	$0.81^{+0.03}_{-0.15}$	149.93	1.35	0.09	23.66
93907	GOODS-N	189.2616602	62.282144	1.019	$0.99^{+0.00}_{-0.02}$	$1.48^{+0.00}_{-0.00}$	$0.97^{+0.03}_{-0.01}$	297.39	1.41	0.06	23.17
44078	GOODS-N	189.2026831	62.194841	1.013	$0.95^{+0.00}_{-0.00}$	$1.01^{+0.00}_{-0.00}$	$1.01^{+0.00}_{-0.00}$	453.54	1.72	0.06	22.09

continued . . .

. . . continued

PearsID	Field	RA	DEC	z_{spec}	z_{phot}	z_{grism}	z_{SPZ}	$\mathcal{N}$	D4000	$\sigma_{\rm D4000}$	i(AB)
46914	GOODS-N	189.1977384	62.197467	0.912	$0.92^{+0.01}_{-0.04}$	$0.90^{+0.00}_{-0.04}$	$0.90^{+0.00}_{-0.03}$	81.89	1.24	0.11	24.04
103918	GOODS-S	53.1335047	−27.747705	0.895	$0.89^{+0.00}_{-0.00}$	$0.90^{+0.00}_{-0.01}$	$0.89^{+0.00}_{-0.00}$	389.83	1.61	0.06	22.25
38212	GOODS-N	189.2169023	62.183097	0.954	$0.93^{+0.01}_{-0.01}$	$0.36^{+0.00}_{-0.01}$	$0.94^{+0.00}_{-0.00}$	126.20	1.48	0.10	23.18
28029	GOODS-N	189.1688286	62.167595	0.748	$0.90^{+0.01}_{-0.06}$	$0.61^{+0.01}_{-0.01}$	$0.88^{+0.03}_{-0.07}$	111.46	1.26	0.11	22.32
60092	GOODS-N	189.1512002	62.222202	0.680	$0.68^{+0.00}_{-0.00}$	$0.48^{+0.00}_{-0.01}$	$0.64^{+0.00}_{-0.00}$	243.99	1.26	0.06	22.37
88279	GOODS-S	53.1207384	−27.773213	0.737	$0.87^{+0.07}_{-0.06}$	$0.53^{+0.47}_{-0.02}$	$0.87^{+0.06}_{-0.08}$	203.36	1.52	0.09	22.35
120498	GOODS-N	189.3974034	62.329535	1.147	$1.14^{+0.09}_{-0.00}$	$1.49^{+0.00}_{-0.00}$	$1.22^{+0.00}_{-0.00}$	111.17	1.54	0.13	24.09
93102	GOODS-S	53.1004687	−27.767594	1.225	$1.16^{+0.02}_{-0.03}$	$1.10^{+0.01}_{-0.01}$	$1.14^{+0.00}_{-0.00}$	98.60	1.21	0.14	23.81
74794	GOODS-N	189.1923008	62.247729	0.679	$0.58^{+0.01}_{-0.01}$	$0.51^{+0.00}_{-0.00}$	$0.58^{+0.00}_{-0.01}$	123.09	1.22	0.10	23.41
53471	GOODS-N	189.1798216	62.211731	0.846	$0.85^{+0.00}_{-0.01}$	$0.84^{+0.01}_{-0.00}$	$0.84^{+0.00}_{-0.00}$	485.24	1.72	0.06	21.81
103094	GOODS-N	189.3215519	62.301278	0.972	$0.96^{+0.01}_{-0.03}$	$0.36^{+0.01}_{-0.00}$	$0.94^{+0.01}_{-0.03}$	184.73	1.34	0.07	22.61
106861	GOODS-S	53.0665957	−27.739707	0.735	$0.68^{+0.00}_{-0.00}$	$0.75^{+0.01}_{-0.01}$	$0.68^{+0.00}_{-0.02}$	242.81	1.41	0.07	21.77
96481	GOODS-S	53.1252702	−27.759500	0.647	$0.61^{+0.00}_{-0.00}$	$0.45^{+0.00}_{-0.00}$	$0.59^{+0.00}_{-0.00}$	441.75	1.25	0.04	21.70
62528	GOODS-S	53.1898804	−27.826710	0.680	$0.79^{+0.00}_{-0.00}$	$0.69^{+0.02}_{-0.02}$	$0.74^{+0.00}_{-0.00}$	501.83	1.50	0.05	21.81
15005	GOODS-S	53.1282508	−27.915264	0.687	$0.69^{+0.01}_{-0.02}$	$1.49^{+0.00}_{-0.00}$	$0.66^{+0.02}_{-0.02}$	197.59	1.18	0.07	21.70
75267	GOODS-N	189.2208937	62.252423	0.938	$0.93^{+0.00}_{-0.00}$	$0.99^{+0.01}_{-0.05}$	$0.94^{+0.00}_{-0.00}$	282.91	1.70	0.07	22.27
119345	GOODS-N	189.3451894	62.326802	0.839	$0.75^{+0.01}_{-0.02}$	$0.79^{+0.00}_{-0.03}$	$0.76^{+0.02}_{-0.00}$	229.18	1.11	0.05	22.64
114108	GOODS-S	53.0958923	−27.725411	0.740	$0.73^{+0.00}_{-0.00}$	$0.72^{+0.00}_{-0.00}$	$0.72^{+0.01}_{-0.00}$	321.70	1.72	0.09	22.46
81470	GOODS-S	53.1975860	−27.786397	1.098	$1.24^{+0.00}_{-0.06}$	$1.19^{+0.01}_{-0.00}$	$1.22^{+0.05}_{-0.02}$	61.14	1.68	0.28	24.54
109801	GOODS-N	189.2890067	62.309933	0.851	$0.81^{+0.02}_{-0.03}$	$0.30^{+0.00}_{-0.00}$	$0.79^{+0.01}_{-0.00}$	170.70	1.25	0.06	23.26
44286	GOODS-N	189.2395284	62.193104	1.013	$0.98^{+0.01}_{-0.00}$	$0.94^{+0.00}_{-0.00}$	$0.97^{+0.00}_{-0.00}$	151.54	1.17	0.07	23.24
109167	GOODS-S	53.1416778	−27.736678	0.895	$0.99^{+0.03}_{-0.06}$	$0.86^{+0.01}_{-0.01}$	$0.95^{+0.08}_{-0.14}$	62.03	1.41	0.19	24.10
100157	GOODS-S	53.1835471	−27.756741	1.221	$1.13^{+0.03}_{-0.00}$	$1.19^{+0.29}_{-0.08}$	$1.19^{+0.00}_{-0.11}$	71.52	1.53	0.23	24.31

continued . . .

. . . continued

PearsID	Field	RA	DEC	z_{spec}	z_{phot}	z_{grism}	z_{SPZ}	$\mathcal{N}$	D4000	$\sigma_{\rm D4000}$	i(AB)
62719	GOODS-N	189.2165408	62.225615	0.961	$0.95^{+0.00}_{-0.00}$	$0.94^{+0.00}_{-0.00}$	$0.94^{+0.00}_{-0.00}$	157.73	1.42	0.08	23.23
89212	GOODS-S	53.1285126	−27.772701	1.018	$0.97^{+0.00}_{-0.00}$	$1.00^{+0.00}_{-0.00}$	$0.96^{+0.00}_{-0.00}$	454.38	1.55	0.05	22.26
89790	GOODS-N	189.1514720	62.273922	0.852	$0.92^{+0.00}_{-0.01}$	$0.82^{+0.02}_{-0.01}$	$0.82^{+0.05}_{-0.01}$	131.01	1.44	0.10	23.59
80987	GOODS-N	189.3423963	62.258581	0.772	$0.93^{+0.01}_{-0.01}$	$0.76^{+0.00}_{-0.29}$	$0.76^{+0.00}_{-0.00}$	75.99	1.28	0.13	23.71
94851	GOODS-N	189.2148947	62.283940	0.955	$0.89^{+0.02}_{-0.01}$	$0.94^{+0.00}_{-0.00}$	$0.89^{+0.00}_{-0.00}$	82.39	1.22	0.11	23.43
95997	GOODS-S	53.1537600	−27.763753	0.765	$0.69^{+0.05}_{-0.15}$	$0.56^{+0.00}_{-0.03}$	$0.66^{+0.01}_{-0.00}$	45.93	1.37	0.30	25.13
120898	GOODS-S	53.1076976	−27.712801	1.183	$1.02^{+0.01}_{-0.04}$	$1.02^{+0.00}_{-0.01}$	$1.03^{+0.01}_{-0.02}$	88.90	1.46	0.16	24.10
125086	GOODS-N	189.3660802	62.342984	1.148	$1.12^{+0.00}_{-0.01}$	$1.15^{+0.00}_{-0.01}$	$1.13^{+0.00}_{-0.00}$	242.15	1.70	0.08	23.00
119016	GOODS-S	53.1209150	−27.715390	0.925	$1.07^{+0.02}_{-0.09}$	$1.01^{+0.00}_{-0.00}$	$1.07^{+0.01}_{-0.06}$	227.45	1.61	0.08	22.46
126769	GOODS-S	53.0761629	−27.701149	0.847	$0.96^{+0.00}_{-0.01}$	$0.69^{+0.00}_{-0.20}$	$0.83^{+0.00}_{-0.00}$	233.94	1.18	0.05	23.00
12378	GOODS-S	53.1379561	−27.923834	0.630	$0.65^{+0.00}_{-0.00}$	$0.66^{+0.00}_{-0.00}$	$0.66^{+0.00}_{-0.01}$	537.31	1.68	0.06	21.52
104292	GOODS-S	53.1616111	−27.746921	0.735	$0.86^{+0.00}_{-0.00}$	$0.71^{+0.01}_{-0.00}$	$0.86^{+0.00}_{-0.00}$	199.46	1.51	0.09	21.98
52774	GOODS-S	53.1598218	−27.841340	0.629	$0.63^{+0.00}_{-0.00}$	$0.32^{+0.01}_{-0.00}$	$0.60^{+0.00}_{-0.02}$	505.41	1.18	0.04	21.61
95024	GOODS-N	189.3590094	62.285243	0.778	$0.73^{+0.02}_{-0.02}$	$0.74^{+0.00}_{-0.00}$	$0.74^{+0.00}_{-0.01}$	193.82	1.28	0.07	22.77
23172	GOODS-S	53.1452086	−27.897243	0.683	$0.67^{+0.00}_{-0.00}$	$0.67^{+0.01}_{-0.01}$	$0.66^{+0.00}_{-0.00}$	491.99	1.65	0.06	21.80
50422	GOODS-N	189.1817895	62.205071	0.751	$0.73^{+0.00}_{-0.01}$	$0.71^{+0.01}_{-0.00}$	$0.73^{+0.01}_{-0.00}$	230.07	1.22	0.06	22.69
70264	GOODS-S	53.1681747	−27.812932	0.963	$0.94^{+0.01}_{-0.00}$	$0.93^{+0.00}_{-0.00}$	$0.93^{+0.00}_{-0.00}$	175.30	1.16	0.06	23.38
39116	GOODS-S	53.1665649	−27.867970	0.648	$0.65^{+0.02}_{-0.01}$	$0.41^{+0.00}_{-0.00}$	$0.65^{+0.00}_{-0.01}$	152.68	1.29	0.09	22.89
123811	GOODS-N	189.3980841	62.341783	0.681	$0.65^{+0.01}_{-0.01}$	$0.76^{+0.00}_{-0.29}$	$0.64^{+0.01}_{-0.02}$	310.64	1.29	0.05	22.06
102153	GOODS-S	53.1237704	−27.751992	0.736	$0.74^{+0.00}_{-0.02}$	$0.65^{+0.00}_{-0.00}$	$0.75^{+0.00}_{-0.01}$	278.79	1.17	0.05	22.47
59375	GOODS-N	189.1713667	62.220700	1.016	$0.98^{+0.00}_{-0.00}$	$1.04^{+0.00}_{-0.05}$	$0.98^{+0.00}_{-0.01}$	211.11	1.34	0.06	22.83
77522	GOODS-S	53.1725238	−27.788092	0.640	$0.65^{+0.00}_{-0.00}$	$0.85^{+0.02}_{-0.05}$	$0.64^{+0.00}_{-0.00}$	958.58	1.50	0.05	20.99
78177	GOODS-S	53.1306425	−27.790259	0.665	$0.70^{+0.01}_{-0.02}$	$0.46^{+0.01}_{-0.00}$	$0.69^{+0.01}_{-0.04}$	782.25	1.25	0.04	21.23

continued . . .

. . . continued

PearsID	Field	RA	DEC	z_{spec}	z_{phot}	z_{grism}	z_{SPZ}	$\mathcal{N}$	D4000	$\sigma_{\rm D4000}$	i(AB)
122267	GOODS-N	189.4193151	62.335444	0.741	$0.70^{+0.01}_{-0.00}$	$0.44^{+0.06}_{-0.01}$	$0.70^{+0.00}_{-0.00}$	214.75	1.19	0.05	22.77
56922	GOODS-S	53.2181238	−27.833686	0.850	$0.89^{+0.00}_{-0.05}$	$0.31^{+0.00}_{-0.01}$	$0.87^{+0.01}_{-0.05}$	279.21	1.27	0.05	22.00
109592	GOODS-N	189.3562126	62.313886	0.841	$0.83^{+0.00}_{-0.01}$	$0.84^{+0.00}_{-0.09}$	$0.83^{+0.01}_{-0.03}$	658.94	1.34	0.04	20.98
99014	GOODS-S	53.1052463	−27.756648	0.664	$0.59^{+0.00}_{-0.00}$	$0.47^{+0.00}_{-0.00}$	$0.69^{+0.00}_{-0.00}$	641.43	1.29	0.04	21.37
17163	GOODS-S	53.1833072	−27.915043	0.908	$0.89^{+0.05}_{-0.06}$	$1.28^{+0.19}_{-0.07}$	$0.90^{+0.04}_{-0.07}$	143.06	1.19	0.08	24.53
47740	GOODS-S	53.1618859	−27.845847	1.015	$1.05^{+0.02}_{-0.04}$	$1.13^{+0.00}_{-0.00}$	$1.10^{+0.00}_{-0.00}$	304.31	1.41	0.06	21.80
117828	GOODS-N	189.2958433	62.324542	1.145	$1.17^{+0.00}_{-0.00}$	$1.22^{+0.00}_{-0.03}$	$1.12^{+0.00}_{-0.00}$	371.34	1.51	0.07	22.00
107836	GOODS-S	53.1501264	−27.739938	1.040	$0.99^{+0.00}_{-0.04}$	$0.34^{+0.01}_{-0.00}$	$1.02^{+0.00}_{-0.07}$	262.43	1.23	0.05	22.26
36639	GOODS-N	189.1726884	62.180919	0.937	$0.92^{+0.00}_{-0.01}$	$0.91^{+0.01}_{-0.10}$	$0.90^{+0.01}_{-0.00}$	160.27	1.37	0.08	22.82
77103	GOODS-N	189.2580853	62.252898	0.938	$0.89^{+0.00}_{-0.00}$	$0.35^{+0.00}_{-0.00}$	$0.90^{+0.00}_{-0.00}$	265.21	1.30	0.05	22.00
86854	GOODS-N	189.2822288	62.271106	0.940	$0.95^{+0.00}_{-0.01}$	$1.03^{+0.02}_{-0.01}$	$0.96^{+0.01}_{-0.02}$	398.34	1.50	0.05	21.85
105980	GOODS-S	53.1453463	−27.744600	0.677	$0.60^{+0.00}_{-0.01}$	$0.70^{+0.00}_{-0.05}$	$0.61^{+0.00}_{-0.01}$	146.99	1.46	0.11	23.13
48311	GOODS-S	53.1466198	−27.850945	0.981	$0.96^{+0.05}_{-0.15}$	$0.95^{+0.05}_{-0.01}$	$1.00^{+0.01}_{-0.02}$	41.46	1.25	0.22	24.84
134787	GOODS-S	53.0902606	−27.682261	1.045	$1.27^{+0.02}_{-0.07}$	$1.02^{+0.00}_{-0.01}$	$1.24^{+0.02}_{-0.06}$	123.16	1.40	0.10	23.31
102547	GOODS-S	53.1318547	−27.751345	1.098	$0.99^{+0.01}_{-0.01}$	$1.06^{+0.01}_{-0.66}$	$1.00^{+0.07}_{-0.03}$	89.87	1.25	0.14	23.72
90791	GOODS-S	53.1149475	−27.767561	0.670	$0.75^{+0.00}_{-0.00}$	$0.50^{+0.00}_{-0.01}$	$0.75^{+0.00}_{-0.02}$	545.22	1.37	0.05	20.78
115775	GOODS-S	53.1304757	−27.723096	1.097	$1.02^{+0.01}_{-0.02}$	$1.06^{+0.01}_{-0.00}$	$1.06^{+0.01}_{-0.00}$	97.59	1.27	0.12	23.71
23215	GOODS-S	53.1477455	−27.900513	1.089	$1.03^{+0.02}_{-0.05}$	$1.12^{+0.01}_{-0.03}$	$1.05^{+0.04}_{-0.07}$	75.85	1.46	0.17	24.40
48650	GOODS-N	189.2090322	62.204725	0.906	$0.93^{+0.02}_{-0.00}$	$1.11^{+0.00}_{-0.12}$	$0.93^{+0.00}_{-0.00}$	293.92	1.49	0.06	22.57
99579	GOODS-N	189.2778410	62.293851	1.144	$1.02^{+0.01}_{-0.03}$	$1.08^{+0.00}_{-0.02}$	$1.06^{+0.00}_{-0.01}$	188.40	1.16	0.07	22.75
81336	GOODS-N	189.3431863	62.262050	0.938	$0.92^{+0.00}_{-0.00}$	$0.94^{+0.00}_{-0.00}$	$0.92^{+0.00}_{-0.00}$	199.44	1.81	0.09	22.38
121232	GOODS-N	189.3648261	62.332437	0.855	$0.74^{+0.02}_{-0.04}$	$0.77^{+0.00}_{-0.00}$	$0.77^{+0.00}_{-0.01}$	122.17	1.24	0.08	23.37
87372	GOODS-S	53.1931062	−27.775560	1.220	$1.25^{+0.02}_{-0.02}$	$1.15^{+0.04}_{-0.15}$	$1.25^{+0.03}_{-0.02}$	55.70	1.30	0.25	24.54

continued . . .

. . . continued

PearsID	Field	RA	DEC	z_{spec}	z_{phot}	z_{grism}	z_{SPZ}	$\mathcal{N}$	D4000	σ_{D4000}	i(AB)
92570	GOODS-N	189.2638248	62.279586	0.744	$0.97^{+0.00}_{-0.01}$	$0.42^{+0.00}_{-0.00}$	$0.96^{+0.00}_{-0.23}$	335.65	1.15	0.04	22.42
52998	GOODS-N	189.1516111	62.210383	0.962	$0.97^{+0.00}_{-0.01}$	$0.99^{+0.00}_{-0.02}$	$0.97^{+0.00}_{-0.01}$	220.56	1.50	0.07	22.57
23407	GOODS-S	53.1594748	−27.898455	0.690	$0.62^{+0.03}_{-0.00}$	$0.68^{+0.05}_{-0.00}$	$0.65^{+0.00}_{-0.00}$	350.54	1.46	0.07	22.09
58084	GOODS-N	189.2297950	62.217689	0.955	$0.95^{+0.00}_{-0.00}$	$0.96^{+0.00}_{-0.01}$	$0.96^{+0.00}_{-0.00}$	133.67	1.77	0.12	23.78
78354	GOODS-N	189.2587331	62.254839	0.745	$0.82^{+0.01}_{-0.02}$	$0.49^{+0.01}_{-0.00}$	$0.72^{+0.04}_{-0.05}$	120.91	1.26	0.09	23.32
51522	GOODS-S	53.1843014	−27.844309	1.122	$1.01^{+0.06}_{-0.02}$	$1.25^{+0.22}_{-0.18}$	$1.07^{+0.00}_{-0.04}$	56.38	1.19	0.23	25.02
77715	GOODS-N	189.1926147	62.257590	0.851	$0.90^{+0.15}_{-0.00}$	$0.34^{+0.02}_{-0.01}$	$1.04^{+0.07}_{-0.06}$	310.37	1.22	0.05	21.99
37495	GOODS-N	189.1501810	62.183402	0.934	$0.88^{+0.03}_{-0.04}$	$0.30^{+0.07}_{-0.00}$	$0.82^{+0.06}_{-0.00}$	118.26	1.19	0.08	23.73
108448	GOODS-N	189.3793856	62.308392	1.199	$1.08^{+0.01}_{-0.01}$	$1.13^{+0.08}_{-0.00}$	$1.13^{+0.00}_{-0.01}$	326.05	1.36	0.06	23.32
80411	GOODS-N	189.1932733	62.258074	0.850	$0.84^{+0.00}_{-0.00}$	$0.85^{+0.02}_{-0.00}$	$0.84^{+0.00}_{-0.00}$	268.81	1.69	0.08	22.67
77927	GOODS-N	189.2379471	62.253144	0.849	$0.83^{+0.01}_{-0.01}$	$0.37^{+0.33}_{-0.07}$	$0.83^{+0.00}_{-0.00}$	143.19	1.33	0.08	23.39
84478	GOODS-S	53.1392830	−27.780668	0.733	$0.68^{+0.00}_{-0.00}$	$0.49^{+0.01}_{-0.02}$	$0.70^{+0.03}_{-0.00}$	204.33	1.23	0.06	23.11
75659	GOODS-N	189.1866640	62.248714	0.845	$0.85^{+0.05}_{-0.00}$	$0.30^{+0.00}_{-0.00}$	$0.83^{+0.00}_{-0.00}$	199.17	1.25	0.06	22.82
82986	GOODS-N	189.3028992	62.262840	0.936	$0.97^{+0.00}_{-0.04}$	$0.31^{+0.00}_{-0.00}$	$0.94^{+0.03}_{-0.03}$	366.57	1.22	0.04	22.11
119774	GOODS-S	53.0594358	−27.715070	0.814	$0.81^{+0.04}_{-0.01}$	$0.81^{+0.01}_{-0.01}$	$0.80^{+0.01}_{-0.00}$	98.98	1.36	0.11	23.84
71198	GOODS-N	189.1762207	62.241568	0.849	$1.03^{+0.01}_{-0.01}$	$1.38^{+0.00}_{-0.00}$	$1.04^{+0.00}_{-0.00}$	110.54	1.13	0.08	23.77
22917	GOODS-S	53.1709179	−27.900476	0.671	$0.65^{+0.02}_{-0.00}$	$0.66^{+0.00}_{-0.00}$	$0.67^{+0.00}_{-0.00}$	226.47	1.65	0.12	22.84
83883	GOODS-S	53.1903515	−27.782001	0.743	$1.19^{+0.01}_{-0.01}$	$1.26^{+0.01}_{-0.01}$	$1.29^{+0.00}_{-0.00}$	98.72	1.11	0.10	24.13
122855	GOODS-N	189.3990766	62.335984	1.082	$1.04^{+0.01}_{-0.01}$	$0.98^{+0.01}_{-0.01}$	$1.06^{+0.00}_{-0.00}$	172.91	1.17	0.07	23.51
13499	GOODS-S	53.1698435	−27.918154	0.978	$0.98^{+0.02}_{-0.03}$	$1.00^{+0.00}_{-0.01}$	$0.98^{+0.02}_{-0.03}$	456.14	1.40	0.05	21.54
98333	GOODS-S	53.1264391	−27.756544	1.223	$1.20^{+0.05}_{-0.03}$	$1.22^{+0.03}_{-0.02}$	$1.20^{+0.07}_{-0.05}$	177.44	1.42	0.10	22.68
96475	GOODS-N	189.3574708	62.287353	0.915	$0.92^{+0.00}_{-0.00}$	$0.77^{+0.00}_{-0.00}$	$0.92^{+0.00}_{-0.09}$	216.75	1.27	0.06	22.66
94262	GOODS-N	189.1744817	62.282598	0.851	$0.85^{+0.04}_{-0.02}$	$0.83^{+0.01}_{-0.00}$	$0.84^{+0.00}_{-0.00}$	165.17	1.30	0.07	23.58

continued . . .

. . . continued

PearsID	Field	RA	DEC	z_{spec}	z_{phot}	z_{grism}	z_{SPZ}	$\mathcal{N}$	D4000	$\sigma_{\rm D4000}$	i(AB)
121837	GOODS-S	53.0788672	−27.711738	1.021	$1.33^{+0.02}_{-0.01}$	$0.41^{+0.00}_{-0.01}$	$0.86^{+0.07}_{-0.04}$	68.31	1.42	0.17	24.56
117385	GOODS-N	189.3155191	62.321239	1.224	$1.13^{+0.01}_{-0.04}$	$1.14^{+0.00}_{-0.00}$	$1.14^{+0.00}_{-0.01}$	120.03	1.11	0.13	23.95
72730	GOODS-N	189.1379719	62.243688	1.224	$1.29^{+0.13}_{-0.38}$	$1.17^{+0.00}_{-0.01}$	$1.27^{+0.01}_{-0.34}$	83.29	1.25	0.19	23.85
110397	GOODS-S	53.1440704	−27.734604	0.937	$0.92^{+0.03}_{-0.01}$	$1.00^{+0.01}_{-0.13}$	$0.92^{+0.01}_{-0.01}$	88.05	1.34	0.11	23.80
66753	GOODS-N	189.2062393	62.235220	0.752	$0.83^{+0.06}_{-0.01}$	$0.74^{+0.00}_{-0.27}$	$0.83^{+0.03}_{-0.03}$	395.31	1.31	0.05	21.87
59747	GOODS-S	53.2155269	−27.830838	0.736	$0.69^{+0.00}_{-0.00}$	$0.46^{+0.00}_{-0.00}$	$0.69^{+0.00}_{-0.00}$	699.21	1.20	0.04	21.36
87585	GOODS-N	189.1798913	62.273634	0.851	$0.85^{+0.00}_{-0.01}$	$0.85^{+0.00}_{-0.00}$	$0.85^{+0.00}_{-0.00}$	564.01	1.71	0.08	21.21
84715	GOODS-N	189.3234267	62.265232	0.805	$0.71^{+0.11}_{-0.01}$	$1.26^{+0.03}_{-0.02}$	$0.76^{+0.21}_{-0.01}$	191.27	1.19	0.07	23.91
41478	GOODS-S	53.1965788	−27.863206	1.114	$1.11^{+0.00}_{-0.04}$	$1.12^{+0.00}_{-0.00}$	$1.11^{+0.00}_{-0.00}$	176.04	1.46	0.08	22.99
110801	GOODS-S	53.0620302	−27.732863	1.109	$1.07^{+0.03}_{-0.07}$	$1.10^{+0.01}_{-0.69}$	$1.10^{+0.00}_{-0.09}$	54.58	1.31	0.21	24.50
37044	GOODS-N	189.2136461	62.181028	1.226	$1.25^{+0.04}_{-0.04}$	$1.20^{+0.00}_{-0.01}$	$1.26^{+0.02}_{-0.06}$	88.27	1.77	0.18	24.01
131165	GOODS-S	53.0746292	−27.689635	1.041	$1.07^{+0.01}_{-0.00}$	$1.03^{+0.00}_{-0.00}$	$1.04^{+0.00}_{-0.00}$	197.49	1.72	0.09	22.98
112002	GOODS-N	189.2731624	62.313660	0.857	$0.92^{+0.10}_{-0.10}$	$1.04^{+0.01}_{-0.02}$	$1.02^{+0.10}_{-0.19}$	166.12	1.45	0.09	23.66
42430	GOODS-N	189.1616880	62.189869	1.005	$0.97^{+0.01}_{-0.01}$	$0.96^{+0.00}_{-0.00}$	$0.96^{+0.00}_{-0.00}$	118.87	1.17	0.08	23.45
84259	GOODS-N	189.1318744	62.267803	0.784	$0.80^{+0.01}_{-0.00}$	$0.74^{+0.00}_{-0.01}$	$0.75^{+0.00}_{-0.00}$	663.46	1.29	0.04	21.40
113298	GOODS-S	53.0418275	−27.725868	1.010	$1.00^{+0.00}_{-0.00}$	$1.01^{+0.00}_{-0.00}$	$1.01^{+0.00}_{-0.00}$	345.89	1.83	0.07	22.16
106859	GOODS-S	53.0965076	−27.739684	0.738	$0.90^{+0.01}_{-0.04}$	$0.30^{+0.00}_{-0.00}$	$0.91^{+0.00}_{-0.10}$	305.43	1.29	0.05	22.28
96098	GOODS-N	189.3939587	62.289808	0.641	$0.83^{+0.05}_{-0.00}$	$1.00^{+0.01}_{-0.00}$	$0.83^{+0.12}_{-0.00}$	552.13	1.37	0.05	20.86
114275	GOODS-N	189.3170025	62.316902	1.027	$0.97^{+0.01}_{-0.00}$	$0.93^{+0.00}_{-0.00}$	$0.94^{+0.01}_{-0.00}$	169.77	1.12	0.06	23.48
81269	GOODS-N	189.3327660	62.258972	0.842	$0.95^{+0.01}_{-0.01}$	$1.47^{+0.01}_{-0.00}$	$0.79^{+0.01}_{-0.01}$	175.66	1.12	0.07	23.35
72646	GOODS-N	189.1495348	62.243344	1.018	$1.23^{+0.01}_{-0.01}$	$1.23^{+0.01}_{-0.01}$	$1.06^{+0.01}_{-0.00}$	68.78	1.31	0.18	23.78
116653	GOODS-S	53.0776253	−27.721495	0.734	$0.71^{+0.01}_{-0.02}$	$0.68^{+0.01}_{-0.00}$	$0.74^{+0.00}_{-0.01}$	122.59	1.30	0.09	23.08
97147	GOODS-N	189.4000646	62.290546	0.709	$0.71^{+0.00}_{-0.00}$	$0.70^{+0.12}_{-0.00}$	$0.69^{+0.00}_{-0.00}$	462.18	1.53	0.06	21.49

continued . . .

. . . continued

PearsID	Field	RA	DEC	z_{spec}	z_{phot}	z_{grism}	z_{SPZ}	$\mathcal{N}$	D4000	σ_{D4000}	i(AB)
108336	GOODS-S	53.1046138	−27.740445	1.220	$1.17^{+0.02}_{-0.04}$	$1.11^{+0.01}_{-0.01}$	$1.21^{+0.01}_{-0.01}$	62.11	1.30	0.32	24.85
80348	GOODS-N	189.1610350	62.257246	0.632	$0.57^{+0.01}_{-0.01}$	$0.46^{+0.31}_{-0.00}$	$0.60^{+0.01}_{-0.00}$	189.66	1.28	0.08	23.20
36944	GOODS-N	189.1703780	62.181871	0.874	$0.89^{+0.00}_{-0.00}$	$0.30^{+0.00}_{-0.00}$	$0.85^{+0.00}_{-0.01}$	280.71	1.20	0.04	22.49
87433	GOODS-N	189.1871437	62.271319	0.747	$0.69^{+0.00}_{-0.01}$	$0.67^{+0.00}_{-0.00}$	$0.68^{+0.01}_{-0.00}$	293.13	1.27	0.05	22.17
87827	GOODS-S	53.1601613	−27.775527	0.630	$0.61^{+0.00}_{-0.00}$	$0.62^{+0.00}_{-0.00}$	$0.62^{+0.00}_{-0.00}$	482.50	1.67	0.08	22.20
39487	GOODS-N	189.2072622	62.185225	1.019	$0.96^{+0.01}_{-0.02}$	$0.38^{+0.01}_{-0.02}$	$0.97^{+0.01}_{-0.02}$	134.13	1.17	0.08	23.10
78415	GOODS-S	53.1694751	−27.791939	0.667	$0.66^{+0.00}_{-0.00}$	$0.85^{+0.04}_{-0.02}$	$0.66^{+0.00}_{-0.00}$	700.45	1.53	0.05	21.68
54327	GOODS-N	189.1841386	62.211217	0.874	$0.83^{+0.06}_{-0.02}$	$0.61^{+0.00}_{-0.02}$	$0.81^{+0.01}_{-0.00}$	112.75	1.10	0.08	23.34
103049	GOODS-S	53.1607879	−27.749989	0.979	$0.98^{+0.01}_{-0.05}$	$0.90^{+0.07}_{-0.00}$	$0.97^{+0.01}_{-0.05}$	46.16	1.21	0.20	23.34
92755	GOODS-S	53.0983783	−27.766944	1.033	$1.22^{+0.00}_{-0.00}$	$1.07^{+0.39}_{-0.01}$	$1.21^{+0.02}_{-0.01}$	58.16	1.49	0.22	23.35
122722	GOODS-S	53.0355561	−27.704930	0.730	$0.71^{+0.00}_{-0.00}$	$1.04^{+0.00}_{-0.00}$	$0.73^{+0.00}_{-0.00}$	751.82	1.47	0.05	21.27
35475	GOODS-S	53.1949430	−27.874946	1.227	$1.11^{+0.02}_{-0.01}$	$1.24^{+0.00}_{-0.00}$	$1.25^{+0.00}_{-0.07}$	143.49	1.37	0.12	23.15
117153	GOODS-N	189.3762979	62.321320	0.836	$0.83^{+0.03}_{-0.04}$	$0.64^{+0.01}_{-0.00}$	$0.79^{+0.00}_{-0.00}$	107.77	1.23	0.09	23.05
69850	GOODS-N	189.2097716	62.238518	0.818	$0.73^{+0.06}_{-0.02}$	$0.46^{+0.00}_{-0.01}$	$0.71^{+0.02}_{-0.00}$	100.30	1.14	0.10	23.21
47561	GOODS-N	189.2458031	62.202469	0.852	$0.91^{+0.00}_{-0.05}$	$0.96^{+0.06}_{-0.00}$	$0.91^{+0.01}_{-0.02}$	339.30	1.44	0.05	21.95
121405	GOODS-S	53.1220735	−27.712453	0.880	$1.09^{+0.01}_{-0.09}$	$0.89^{+0.00}_{-0.00}$	$1.06^{+0.00}_{-0.08}$	99.87	1.66	0.16	23.91

Chapter 4

CONSTRAINING AGN FEEDBACK THROUGH THE THERMAL SUNYAEV-ZEL'DOVICH EFFECT WITHIN STACKED CMB DATA

Note to the reader: *This chapter is based on work I did as part of Spacek et al. 2016 and Spacek et al. 2017, with permission from the co-authors. I suggest reading Spacek et al. 2016 in its entirety for a more complete description of the sample selection, the stacking process, and a discussion of the final results; particularly the analysis of the South Pole Telescope data.*

4.1 Background

The cosmic microwave background (CMB) is radiation released ∼380,000 years after the Big Bang (z∼1100) when the Universe had cooled down enough to allow free protons and electrons to form neutral Hydrogen in an event known as recombination (Dicke et al. 1965; Penzias and Wilson 1965). Prior to recombination the Universe was opaque (i.e., the mean free path of a CMB photon is shorter than the horizon length) because there are enough photons (even in the tail of the CMB blackbody) with energies above the Hydrogen ionization potential of 13.6eV to keep the Universe ionized. Although the CMB radiation is extremely close to an isotropic blackbody, temperature anisotropies on the order of 1 part in 10^5 exist (Peebles and Yu 1970; Smoot et al. 1992; Mather et al. 1994; White, Scott, and Silk 1994; Hu and Dodelson 2002) which are seeded by quantum density fluctuations occurring before the inflationary phase (i.e., at $t \lesssim 10^{-36}$ seconds) (Guth 1981; Linde 1982).

Galaxies, galaxy clusters, and the cosmic web forming the large scale structure in the Universe condense at the locations of these density fluctuations (Peebles 1965; Sachs and Wolfe 1967; Silk 1968; Press and Schechter 1974). CMB temperature fluctuations also have a dependence on angular scale which is encoded in the CMB temperature power spectrum shown in figure 23. The angular scale in the figure goes from angles much larger than a degree at the largest scales to fractions of a degree at the smallest scales (angle on sky $\sim 180/l$). The locations and the relative strengths of the peaks in the power spectrum are key to measuring the amounts of the baryon and dark components of the Universe, the Hubble constant, and the spectral index of the initial density perturbations, among other standard model observables. Measurements of the primary anisotropies of the CMB radiation have now helped precipitate the standard model of cosmology (see, for e.g., Hinshaw et al. 2013; Planck Collaboration et al. 2018b).

The utility of the CMB radiation reaches beyond providing the parameters of the concordance model of cosmology. Within the context of galaxy evolution, the interaction of the CMB with ionized gas along its path from the surface of last scattering to z=0, produces secondary anisotropies that can encode information about the thermal and kinematic properties of the ionized gas. The inverse Compton-scattering of CMB photons to higher energies due to high energy electrons is termed the thermal Sunyaev-Zel'dovich (tSZ) effect (Sunyaev and Zeldovich 1970, 1972).

The tSZ effect showing the distortion in the CMB blackbody spectrum is shown in figure 24. This figure shows the change in the CMB spectrum as it passes through hot intracluster gas. In the direction of the cluster, the CMB energy density decreases (relative to the blackbody) below a frequency of ∼218 GHz, and increases above it.

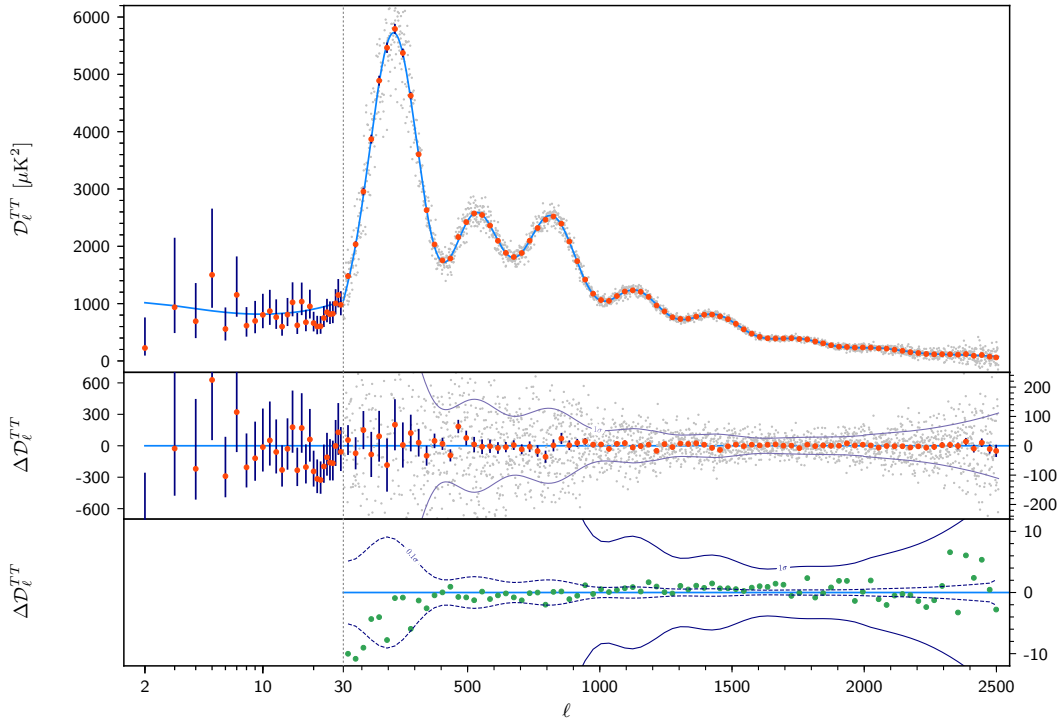

Figure 23. The temperature power spectrum of the CMB based on results from the Planck mission (Planck Collaboration et al. 2019). The top panel shows the power spectrum computed based on the 2018 data, the middle panel shows the residuals with respect to the model, and the bottom panel is a comparison to the 2015 data from Planck. The grey (red) points are the unbinned (binned) data points. The ΛCDM model is shown in blue. The green data points in the bottom panel are differences between the 2018 and the 2015 data. Note that the horizontal axis changes from logarithmic to linear at multipole values $l > 30$.

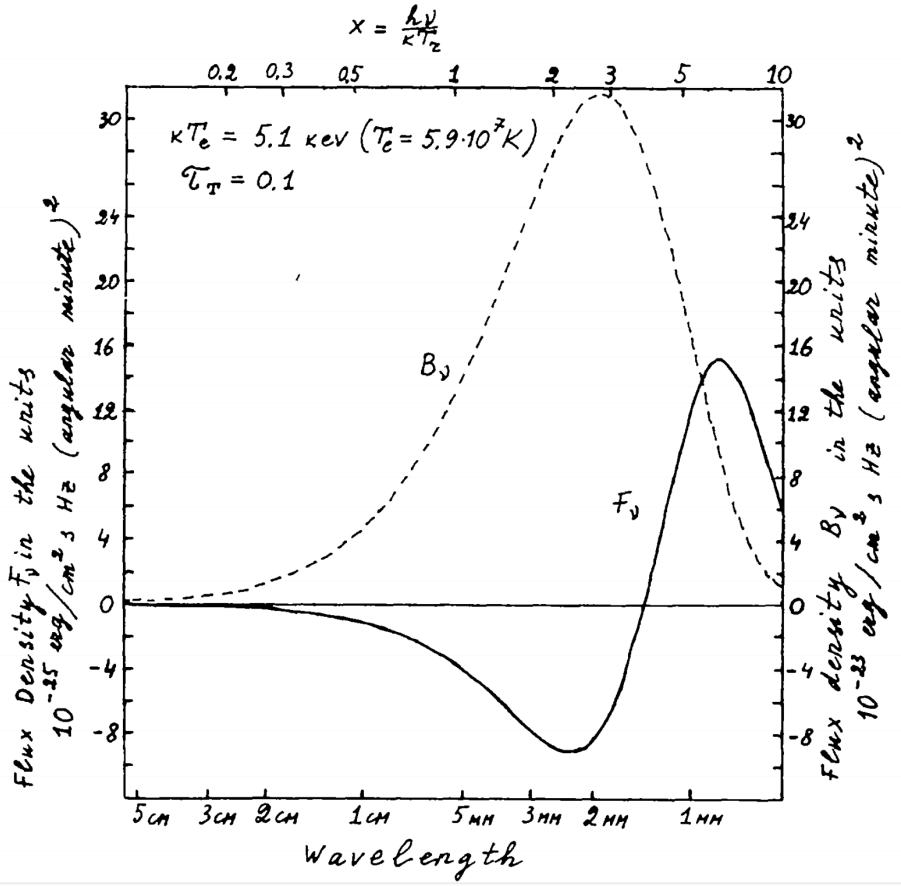

Figure 24. The SZ effect from Sunyaev and Zeldovich 1980, showing the change (solid line) in the CMB spectrum due to Compton scattering from interaction with hot gas within a galaxy cluster. The CMB blackbody spectrum is shown as the dashed line.

It is expected that feedback from supermassive black holes at the centers of active galaxies should contribute significant amounts of energetic input (kinematically and through radiation) into the surroundings of the galaxies, resulting in reservoirs of ionized gas around quiescent galaxies. The tSZ effect causes a distortion to the CMB spectrum that is uniquely identifiable (see figure 24), and therefore a convenient probe for the properties of the ionized gas and active galactic nuclei (AGN) feedback. The above mentioned reservoirs of ionized gas should then, in principle, be detectable via the tSZ effect. However, the signal from the tSZ effect is too small to be directly

detected for individual galaxies, therefore, stacks of CMB data are employed in Spacek et al. 2016 and Spacek et al. 2017 to quantify the energetic input from AGN feedback, and place constraints on models of galaxy evolution.

Below in section 4.2, I describe the method used to constrain contaminating emission from dusty sources, using CMB data from the Planck mission (Planck Collaboration et al. 2016), along with a brief description of the results.

4.2 Stacking Method and Final Result

The sample selection process is described in detail in Spacek et al. 2016 and Spacek et al. 2017. Briefly, massive quiescent elliptical galaxies are chosen from pre-existing survey data (Desai et al. 2012; McMahon 2012, Blanco Cosmology Survey and VISTA Hemisphere Survey). These galaxies are chosen for their high stellar masses and passive natures, i.e., the circumgalactic medium around a massive galaxy is likely to be correspondingly massive, the lack of star-formation implying the occurrence of past quenching event(s), and the lack of an AGN providing a cleaner signal without contaminating emission from the AGN. Also, these galaxies are chosen because they are more numerous than AGN, and therefore a stack of massive quiescent ellipticals offers a better chance of detecting the faint SZ signal.

I stack Planck data from the high-frequency bands at 857, 545, 353, and 217 GHz from the 2015 public data release of the Planck mission (Planck Collaboration et al. 2016) at the locations of galaxies in the sample. The effective full width at half maximum (FWHM) beam size for this data is $\sim$5 arcmin (varies between $\sim$4.6 to $\sim$5 arcmin for the aforementioned frequencies). Unfortunately, these beam sizes cannot spatially resolve the tSZ signal. This data does, however, provide useful

information about dusty sources which should be brighter at these frequencies. These measurements can therefore distinguish between contaminant models of dust. A modified blackbody with a free emissivity index β and dust temperature T_{dust} was considered by Spacek et al. 2016.

I convolve each map, corresponding to the high-frequency Planck bands, with a 7 arcmin FWHM Gaussian beam which filters out the primary CMB signal. This filtered map is then subtracted from the original. The Planck data at each of the source locations is then coadded to generate a separate final stack for each frequency band.

Since the Planck maps are normalized to an average value of 0, and the sample selection process excluded any galaxies close to potential contaminating sources, a negative bias gets introduced (since all contaminants only add positive signal; see section 7.2 of Spacek et al. 2016). Therefore, to account for this bias, I also stacked Planck data at 3000 random points on the sky in order to determine the offset value required to be added to each band to rescale it to an average of zero.

In the low-z bin of $0.5 \leq z \leq 1.0$, with the Planck data taken into account, Spacek et al. 2016 detected a tSZ signal at a significance of 3.6σ, while in the high-z bin of $1.0 \leq z \leq 1.5$ a hint of an excess tSZ signal at 0.9σ is detected. Based on these detections, Spacek et al. 2016 inferred thermal energies of $7.6^{+3.0}_{-2.3} \times 10^{60}$ erg and $6.0^{+7.7}_{-6.3} \times 10^{60}$ erg within the low-z and high-z bins, respectively.

Chapter 5

STAR-FORMATION HISTORIES OF MASSIVE GALAXIES AT INTERMEDIATE REDSHIFTS

This chapter is reproduced from a manuscript in preparation for submission to The Astrophysical Journal, with permission from the co-authors.

5.1 Introduction

Over most of cosmic history (the last ∼12 Gyr), galaxies show a bimodal distribution in their colors, star-formation rates (SFRs), morphologies, colors, and other key parameters (see, for e.g., Kauffmann, Heckman, White, Charlot, Tremonti, Brinchmann, et al. 2003; Baldry et al. 2004; Faber et al. 2007). These two distinct populations of galaxies are the "blue-cloud" (blue+actively star-forming) and the "red-sequence" (red+passively evolving), while the transitional population in between the two peaks, containing fewer galaxies, is the "green-valley". Deep observations have confirmed the existence of a red-sequence, containing massive quiescent galaxies, as far back as $z\sim2$ (e.g., Franx et al. 2003; Cimatti et al. 2004; Labbé et al. 2005; Arnouts et al. 2007). There are also indications that a population of massive quiescent galaxies could exist as early as $z\sim4$ from photometric data (Straatman et al. 2014).

5.1.1 Cosmic Downsizing and α-Element Enhancement in Massive Galaxies

Several lines of observational evidence support the paradigm of cosmic downsizing by which massive galaxies form their stars at higher redshifts and are also quenched relatively earlier than less massive galaxies (see Cowie et al. 1996, for the original definition of "downsizing"; also see, e.g., Fontanot et al. 2009 for a detailed discussion of the different types of downsizing). It is also well known that massive galaxies are enhanced in α-elements relative to lower mass galaxies in the local Universe. For example, some of the early studies like Worthey, Faber, and Gonzalez (1992) and Faber, Worthey, and Gonzales (1992) reported that local elliptical galaxies have larger [Mg/Fe] ratios than the most metal-rich stars in the solar neighborhood. Later studies confirmed these observed trends (e.g., Davies, Sadler, and Peletier 1993; Thomas, Greggio, and Bender 1999; Trager et al. 2000; Thomas et al. 2005; Renzini 2006; Thomas et al. 2010; Johansson, Thomas, and Maraston 2012).

An enhancement of α-elements relative to Iron typically implies shorter star-formation timescales due to their different synthesis pathways (Matteucci and Greggio 1986): α-elements are predominantly synthesized within Type-II core-collapse supernovae (SNe), while Iron (along with a small fraction of α-elements) is predominantly synthesized in Type-Ia SNe caused by white-dwarf explosions. Type-II SNe occur on a timescale of tens of Myr with progenitor masses >8 $M_\odot$, whereas Type-Ia SNe are caused by a slowly accreting white dwarf exploding after exceeding the Chandrasekhar limit of $\sim$1.4 $M_\odot$, which occur on timescales of $\sim$Gyr.

Another piece of evidence for cosmic downsizing comes from the observations of quiescent, massive galaxies at high-redshifts (e.g., Kriek et al. 2008; Williams et al. 2009; Whitaker et al. 2013; Man et al. 2016), which suggest faster quenching timescales

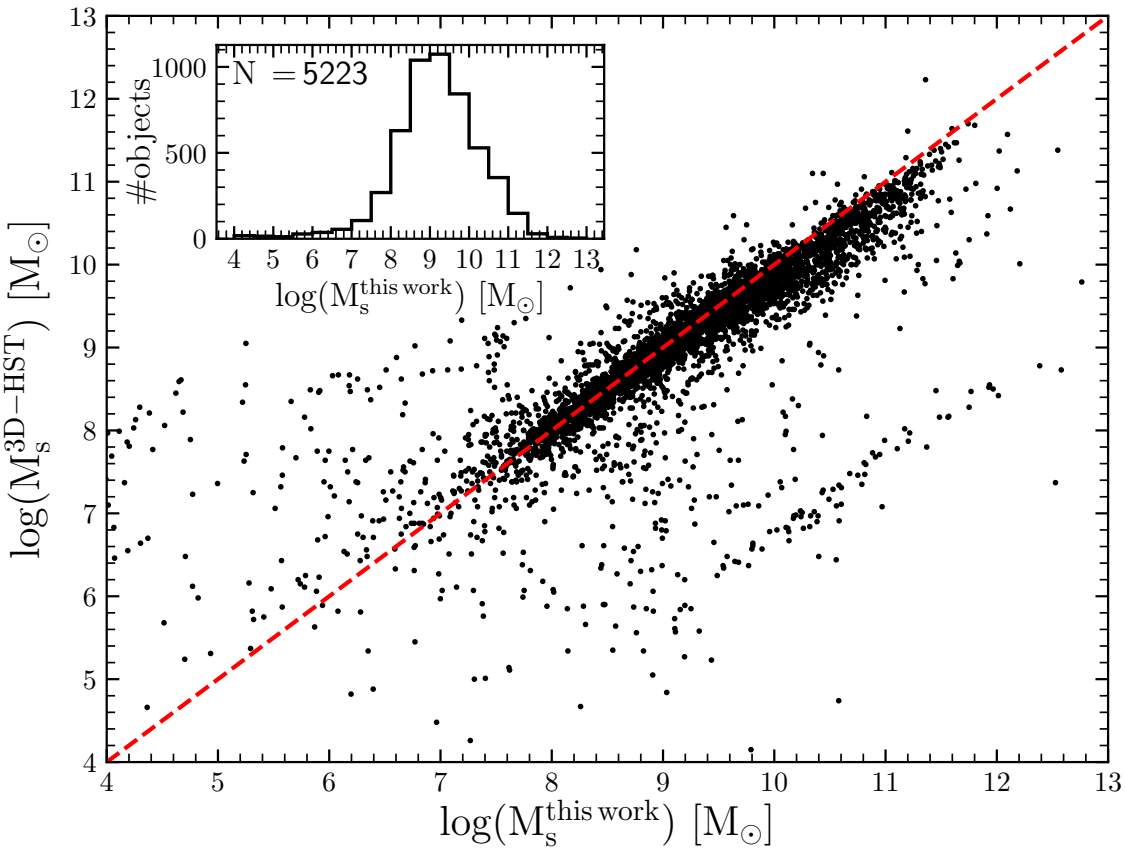

Figure 25. Comparing the stellar masses within the 3D-HST survey and PEARS. The red dashed line is the 1:1 line. The PEARS stellar masses are derived based on multi-wavelength SED fits to 12-band photometric data (this photometric data is the same as in chapter 3). A Chabrier initial mass function was assumed for the models used in the SED fitting. The 3D-HST stellar masses are from Skelton et al. (2014). The inset figure shows the histogram for the distribution of stellar masses within PEARS.

for the most massive galaxies in the Universe. In this work, I will present an analysis of the [Mg/Fe] ratio for massive galaxies at intermediate and high-redshifts.

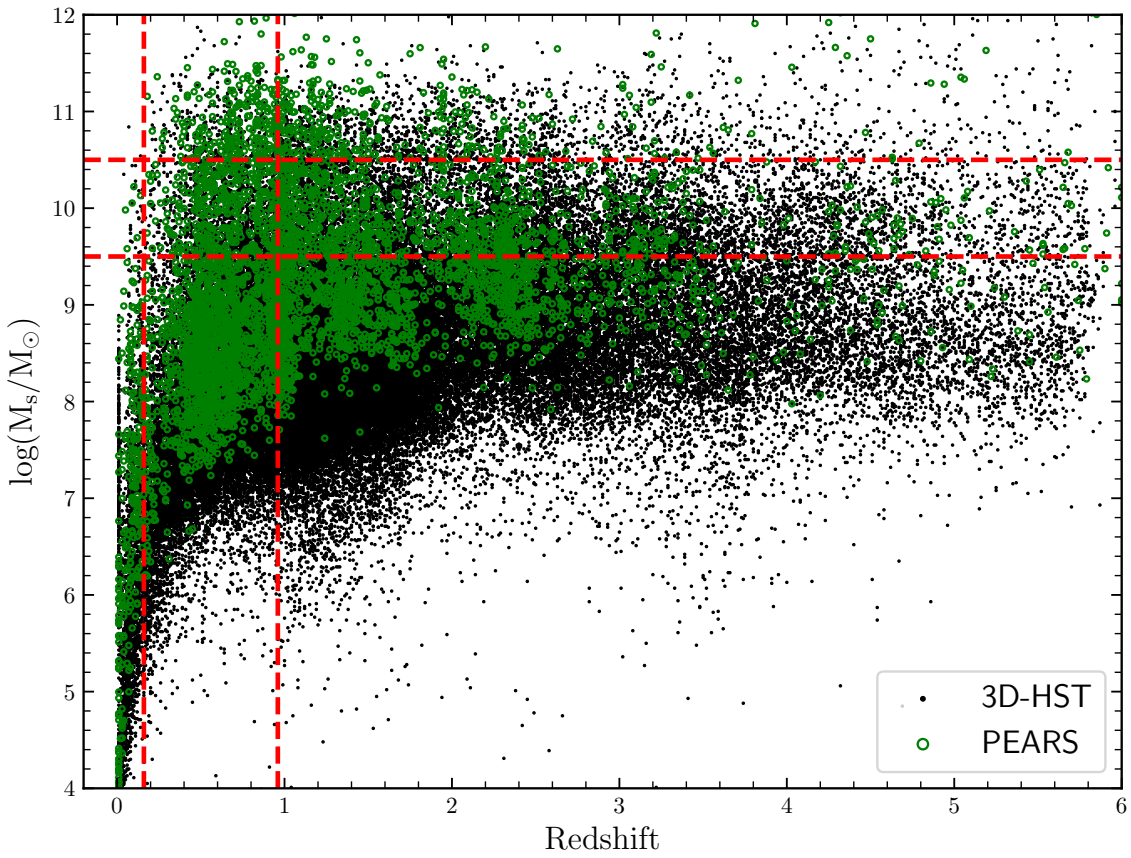

Figure 26. Showing the distribution of stellar masses in the PEARS catalog vs redshift. The green and black points are the PEARS and 3D-HST galaxies, respectively. The vertical dashed red lines indicate the redshift range for the sample in this paper. The horizontal dashed red lines indicate the stellar mass ranges of $10^{9.5} \leq M_s[M_\odot] \leq 10^{10.5}$ and $10^{10.5} \leq M_s[M_\odot] \leq 10^{12}$ considered in this paper.

5.2 Data and Sample Selection

Similar to chapter 3, the data for this chapter come from the PEARS survey. Please refer to section 3.2 in chapter 3 for details on the observed grism data from PEARS. To recap briefly, the PEARS survey is a 200 orbit HST grism survey with the ACS/G800L grism. It covers 8 pointings within the GOODS regions (4 in GOODS-N and 4 in GOODS-S) with 20 orbits per pointing and 3-4 roll angles per pointing. An

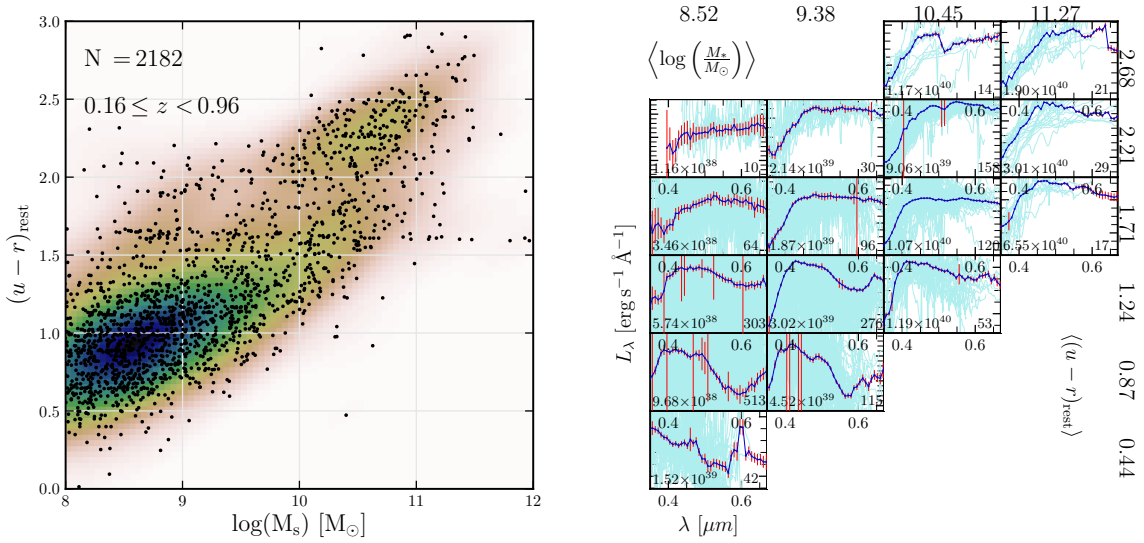

Figure 27. Left panel: $(u-r)$ restframe color vs stellar mass for all the galaxies in the PEARS sample within $0.16 \leq z \leq 0.96$. This panel also shows the stacking grid I used for the right panel overlaid. Right panel: Shows stacked spectra on the same grid. They show the individual spectra in light blue and the median stacked spectrum in blue. The numbers along the top are the average stellar masses for galaxies in that column and the numbers along the right are average $(u-r)$ restframe colors for galaxies in those rows. The number at the bottom right of each cell is the total number of individual galaxies in the stacked spectrum. The number at the bottom left of each cell is the median of the values (in cgs units) that were used to rescale spectra in that cell. The Y-axis tick labels are suppressed for clarity.

additional 40 orbits cover the HUDF in GOODS-S with 4 roll angles. Multiple roll angles serve the significant purposes of disentangling overlapping spectra, identifying localized emission/absorption sources within a source, and to a lesser extent of yielding higher spectral resolution relative to a single roll angle (see, e.g., Norbert Pirzkal et al. 2018; Ryan, Casertano, and Pirzkal 2018). I also use data from the 3D-HST survey (Brammer et al. 2012; Skelton et al. 2014) for comparing the stellar masses derived in this work. The 3D-HST survey is 248 orbit HST grism survey with the WFC3/G102 grism covering all CANDELS fields (except GOODS-N which is covered by a separate survey) at a depth of 2 orbits per pointing with a single roll angle.

5.2.1 Stellar Mass Completeness

Prior to selecting my sample, I conduct a preliminary check for the consistency of the stellar masses (i.e., comparing stellar masses obtained by two independent methods – by the 3D-HST collaboration and by my pipeline introduced in chapter 3), along with checking of the mass limits for completeness is done. Figure 25 shows a comparison between the stellar masses within the 3D-HST survey and the PEARS survey. It can be clearly seen that the stellar masses within both surveys agree quite well. Figure 26 shows the distribution of stellar masses vs redshift within PEARS and 3D-HST. It can be seen that both distributions follow each other reasonably well especially at $M_s \geq 10^{9.5} M_\odot$ and $z \leq 2.5$. Therefore, for this work I will consider galaxies which satisfy those limits.

5.2.2 Sample Selection

To analyze [Mg/Fe] I divide the mass range into two bins, a less massive bin of $10^{9.5} \leq M_s[M_\odot] < 10^{10.5}$ and a more massive bin of $10^{10.5} \leq M_s[M_\odot] < 10^{12}$, along with requiring $(u-r)_{\rm restframe} \geq 1.8$. For the more massive bin, the aforementioned selection criteria give me 157 galaxies within $0.16 \leq z \leq 0.96$. The redshift range is chosen to ensure coverage of the Hβ, Mgb and Fe absorption features at 4861Å, 5175Å, and 5270Å + 5335Å + 5406Å, respectively, within the PEARS wavelength coverage of $6500 \leq \lambda[\text{Å}] \leq 9000$, which are the absorption features I am considering in this chapter.

Although currently not used for analysis, it is also worthwhile to look at figure 27, which shows a color vs stellar mass diagram (left panel) and spectra stacked

on a superimposed grid as shown (right panel), for all 2182 PEARS galaxies within $0.16 \leq z \leq 0.96$. On the left panel, the separation between the blue-cloud and red-sequence is clearly visible. It can also be seen that my mass and color selection mentioned above does indeed select red-sequence and green-valley galaxies.

5.3 Stacking Method

Since the individual spectra can be quite noisy, to increase signal-to-noise I employ a median stacking procedure. The final measurement of [Mg/Fe] is done on the stacked spectrum. The individual grism spectra to be stacked are first fit by a fifth-degree polynomial. A polynomial is chosen because I am interested in measuring the emission and absorption features within the spectra of massive galaxies, therefore the slope of the continuum is accounted for before stacking. The polynomial fit is done while the expected emission and absorption features are kept masked. The original grism spectrum is then divided by the best-fit polynomial, and de-redshifted, leaving a residual spectrum which is then stacked. The median stacking is done over a restframe wavelength range of $3400 \leq \lambda[\text{Å}] \leq 7600$ within bins of $\Delta\lambda = 25$Å.

5.4 Discussion and Results

The resultant stack for my sample of massive galaxies is shown in figure 28. The Mg_2 and Mgb absorption features at $\sim$5175Å along with Hβ and Fe absorption features at 5270Å, 5335Å, and 5406Å can clearly be observed. Many other absorption features

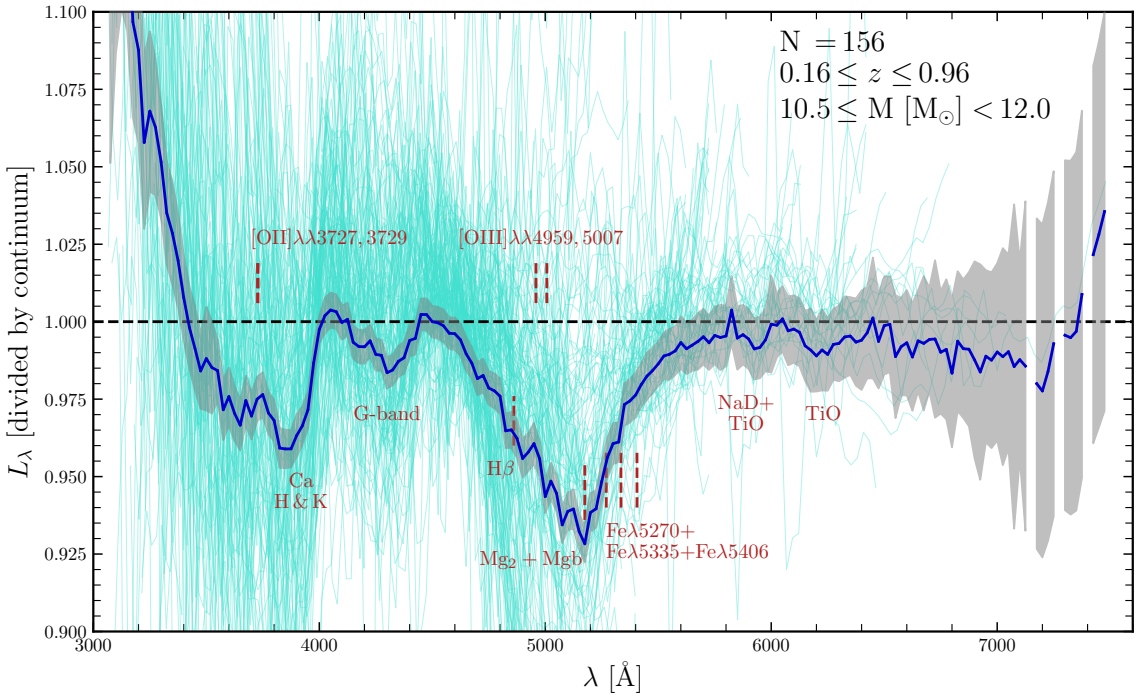

Figure 28. The final stack (blue) of 156 massive galaxies with $M_s \geq 10^{10.5} M_\odot$ within $0.16 \leq z \leq 0.96$. 1-σ errors on the stack are shown in gray. The grism spectra for all the individual galaxies in the stack are shown in teal. The legend shows the redshift and stellar mass ranges for the galaxies in the stack. Individual absorption and emission features are also marked.

can also be seen, such as, the Ca H & K lines (i.e., the 4000Å break), the G-band, NaD+TiO at ∼5900Å, and TiO at ∼6230Å.

It is worth noting that the absorption profile centered approximately on 5175Å appears unusually broad even for low-resolution grism data. This large line width is likely a combination of broadening caused by uncertainties in redshift estimates for galaxies in the stack along with broadening due to the line spread function (LSF). To asses the broadening caused by these effects, I approximate this broadening simply by adding the uncertainties in quadrature, i.e., $\Delta w^2 = \langle |\Delta z/(1+z)| \rangle^2 + \Delta l^2$, where w is the observed width of an individual absorption line in the stack and Δl is the effective LSF broadening. If I consider a typical 2.9% error in redshifts (see section 3.5) and

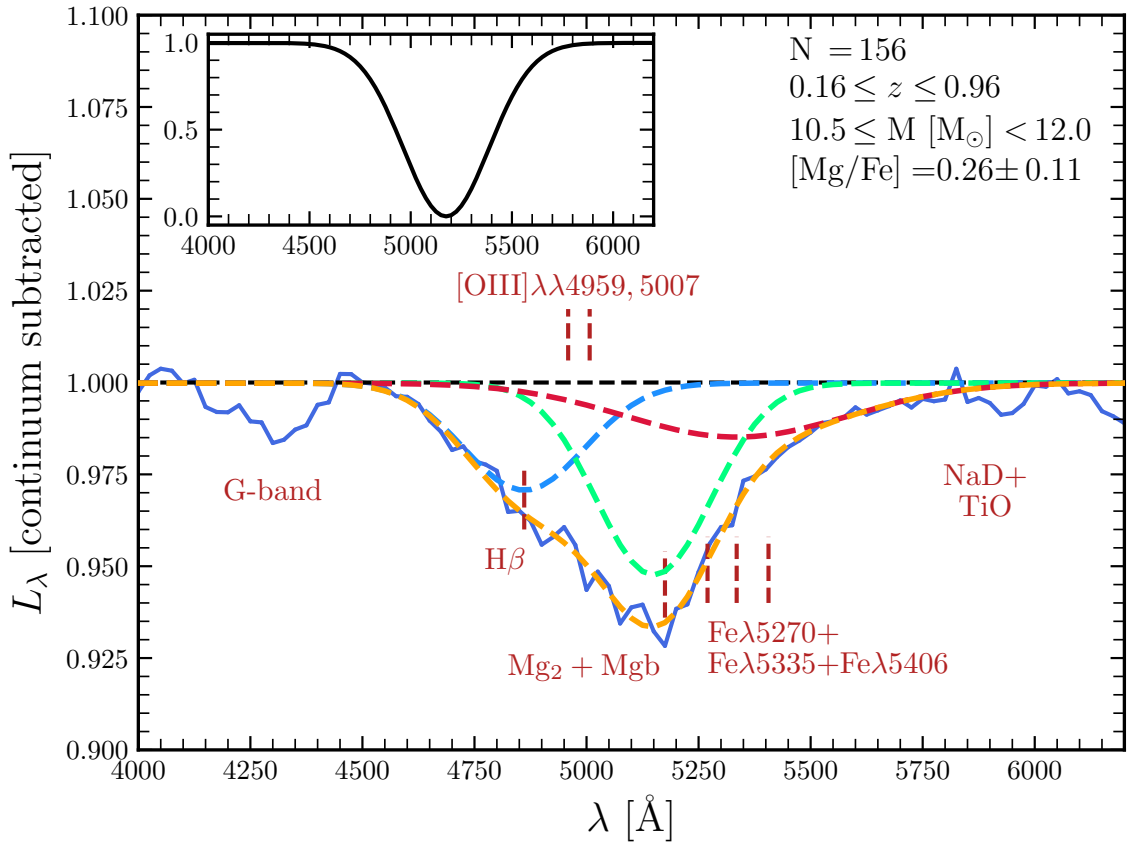

Figure 29. Simultaneous fit of three Gaussian absorption features to the stack between 4600Å to 5650Å. The blue, light-green, and red curves are fits to Hβ, Mg_2+Mgb, and Fe absorption features, respectively. The orange curve is the sum of the three individual Gaussians. The inset figure shows the broadening of an absorption line at 5175Å due to uncertainties in the redshift estimates and the line spread function. The legend shows the parameters of the galaxies in the stack and the final [Mg/Fe] value.

the size of a typical galaxy in the stack to be 3 ACS pixels, then the two effects appear to contribute equally to final observed width. For reference, I assume an absorption line centered on 5175Å and simulate a Gaussian absorption line broadened by the above mentioned two effects. This simulated absorption line is shown by the inset figure in figure 29. It can be clearly seen that the width of the simulated line matches the width of the observed line quite well.

The [Mg/Fe] value is obtained by simultaneously fitting an absorption model of three Gaussians to represent Hβ, Mg_2 + Mgb, and the Fe lines. This fit is shown in figure 29. The value of [Mg/Fe] I obtain is 0.26 ± 0.11. This value is consistent with that obtained by other studies (see, for e.g., Onodera et al. 2015), and provides further evidence for early formation and short quenching timescales for massive galaxies.

Chapter 6

CONCLUSION

Here I summarize the conclusions from each of the chapters in this dissertation.

In Chapter 2, Using visible IFU data from the VIRUS-P instrument on 2.7 m telescope at McDonald Observatory for the Taffy system, I have shown the results listed below.

a. I detect widespread ionized gas within the disks of the Taffy galaxies and the bridge which exhibit very disturbed kinematics, including many regions with double line profiles and emission regions that do not follow regular rotation.

b. An analysis of the excitation of the ionized gas through diagnostic line ratios shows that a significant fraction of the emission shows a mix of HII-region and LINER-type emission, especially in the areas where two velocity components can be clearly distinguished. I observe emission line ratios in the high-velocity component, for the east bridge and the low-velocity component of the west bridge, that are consistent with the gas being excited by shocks with velocities of $\sim$175-200 km/s, and a range of pre-shock densities.

c. Balmer absorption lines are strongest in regions where the ionized and molecular gas distributions are weak, suggesting that parts of the Taffy system have experienced a burst of star formation in the past, perhaps from a previous close passage of the two galaxies.

In Chapter 3, I note three important aspects of our continuum derived redshifts relevant to future redshift surveys –

a. SPZs improve over the photo-zs for all D4000 values by $\sim$17–60%.

b. I predict a total of $\sim$700–4400 galaxies/degree^2 which can be used to obtain redshifts accurate to $|\Delta z/(1+z_s)| \leq 0.02$, within the WFIRST and Euclid redshift ranges to a limiting depth of i_{AB}=24 mag.

c. I argue that – (i) since the expected number densities of objects with redshifts based on the 4000Å/Balmer breaks and objects with emission line redshifts are comparable, and (ii) since grism continuum redshifts can be done from space to fainter continuum levels compared to continuum-based redshifts from the ground (e.g., this work goes as faint as i_{AB}=24 mag) – continuum-based redshifts can thus provide redshifts for galaxies which will not have emission line based redshifts from grism observations with WFIRST and Euclid, and therefore contribute additional redshifts which would otherwise not be available.

In Chapter 4, I describe the motivation for constraining AGN feedback around quiescent elliptical galaxies, and the process used to stack the Planck data. The stacks were used to characterize contaminating emission from dusty galaxies. I stacked CMB data at the locations of galaxies in two redshift bins – a "low-z" $0.5 \leq z \leq 1.0$ and a "high-z" $1.0 \leq z \leq 1.5$ stack.

And in Chapter 5, I describe the motivation for studying the star-formation histories (SFHs) of massive galaxies. I also describe the stacking process used to create a coadded spectrum of 156 massive galaxies with stellar masses $\mathrm{M_s} \geq 10^{10.5}\mathrm{M_\odot}$ within $0.16 \leq z \leq 0.96$. Analysis of the coadded spectrum clearly shows several

important absorption features – CaII H & K, G-band, Mg_2 + Mgb, Fe, and NaD. These absorption features serve as useful constraints on the SFHs of massive galaxies through the [Mg/Fe] ratio along with other Lick indices.

REFERENCES

Adams, Joshua J., Guillermo A. Blanc, Gary J. Hill, Karl Gebhardt, Niv Drory, Lei Hao, Ralf Bender, et al. 2011. "The HETDEX Pilot Survey. I. Survey Design, Performance, and Catalog of Emission-line Galaxies." *ApJS* 192, no. 1, 5 (January): 5. doi:10.1088/0067-0049/192/1/5. arXiv: 1011.0426 [astro-ph.CO].

Alatalo, K., P. N. Appleton, U. Lisenfeld, T. Bitsakis, L. Lanz, M. Lacy, V. Charmandaris, et al. 2015. "Star Formation Suppression in Compact Group Galaxies: A New Path to Quenching?" *ApJ* 812, no. 2, 117 (October): 117. doi:10.1088/0004-637X/812/2/117. arXiv: 1509.05779 [astro-ph.GA].

Allen, Mark G., Brent A. Groves, Michael A. Dopita, Ralph S. Sutherland, and Lisa J. Kewley. 2008. "The MAPPINGS III Library of Fast Radiative Shock Models." *ApJS* 178, no. 1 (September): 20–55. doi:10.1086/589652. arXiv: 0805.0204 [astro-ph].

Allington-Smith, Jeremy. 2006. "Basic principles of integral field spectroscopy." *Nature Astronomy Reviews* 50, nos. 4-5 (June): 244–251. doi:10.1016/j.newar.2006.02.024.

Anders, P., and U. Fritze-v. Alvensleben. 2003. "Spectral and photometric evolution of young stellar populations: The impact of gaseous emission at various metallicities." *A&A* 401 (April): 1063–1070. doi:10.1051/0004-6361:20030151. arXiv: astro-ph/0302146 [astro-ph].

Andrae, Rene, Tim Schulze-Hartung, and Peter Melchior. 2010. "Dos and don'ts of reduced chi-squared." *arXiv e-prints,* arXiv:1012.3754 (December): arXiv:1012.3754. arXiv: 1012.3754 [astro-ph.IM].

Appleton, P. N., P. Guillard, A. Togi, K. Alatalo, F. Boulanger, M. Cluver, G. Pineau des Forêts, U. Lisenfeld, P. Ogle, and C. K. Xu. 2017. "Powerful H_2 Line Cooling in Stephan's Quintet. II. Group-wide Gas and Shock Modeling of the Warm H_2 and a Comparison with [C II] 157.7 μm Emission and Kinematics." *ApJ* 836, no. 1, 76 (February): 76. doi:10.3847/1538-4357/836/1/76. arXiv: 1701.03226 [astro-ph.GA].

Appleton, P. N., L. Lanz, T. Bitsakis, J. Wang, B. W. Peterson, U. Lisenfeld, K. Alatalo, et al. 2015. "X-Ray Emission from the Taffy (VV254) Galaxies and Bridge." *ApJ* 812, no. 2, 118 (October): 118. doi:10.1088/0004-637X/812/2/118. arXiv: 1509.05314 [astro-ph.GA].

Appleton, P. N., Kevin C. Xu, William Reach, Michael A. Dopita, Y. Gao, N. Lu, C. C. Popescu, J. W. Sulentic, R. J. Tuffs, and M. S. Yun. 2006. "Powerful High-Velocity Dispersion Molecular Hydrogen Associated with an Intergalactic Shock Wave in Stephan's Quintet." *ApJL* 639, no. 2 (March): L51–L54. doi:10.1086/502646. arXiv: astro-ph/0602554 [astro-ph].

Armus, L., J. M. Mazzarella, A. S. Evans, J. A. Surace, D. B. Sanders, K. Iwasawa, D. T. Frayer, et al. 2009. "GOALS: The Great Observatories All-Sky LIRG Survey." *PASP* 121, no. 880 (June): 559. doi:10.1086/600092. arXiv: 0904.4498 [astro-ph.CO].

Armus, Lee, Timothy Heckman, and George Miley. 1987. "Multicolor Optical Imaging of Powerful Far-Infrared Galaxies: More Evidence for a Link Between Galaxy Mergers and Far-Infrared Emission." *AJ* 94 (October): 831. doi:10.1086/114517.

Arnouts, S., C. J. Walcher, O. Le Fèvre, G. Zamorani, O. Ilbert, V. Le Brun, L. Pozzetti, et al. 2007. "The SWIRE-VVDS-CFHTLS surveys: stellar mass assembly over the last 10 Gyr. Evidence for a major build up of the red sequence between z = 2 and z = 1." *A&A* 476, no. 1 (December): 137–150. doi:10.1051/0004-6361:20077632. arXiv: 0705.2438 [astro-ph].

Baldry, Ivan K., Karl Glazebrook, Jon Brinkmann, Željko Ivezić, Robert H. Lupton, Robert C. Nichol, and Alexander S. Szalay. 2004. "Quantifying the Bimodal Color-Magnitude Distribution of Galaxies." *ApJ* 600, no. 2 (January): 681–694. doi:10.1086/380092. arXiv: astro-ph/0309710 [astro-ph].

Baldwin, J. A., M. M. Phillips, and R. Terlevich. 1981. "Classification parameters for the emission-line spectra of extragalactic objects." *PASP* 93 (February): 5–19. doi:10.1086/130766.

Balogh, Michael L., Simon L. Morris, H. K. C. Yee, R. G. Carlberg, and Erica Ellingson. 1999. "Differential Galaxy Evolution in Cluster and Field Galaxies at z~0.3." *ApJ* 527, no. 1 (December): 54–79. doi:10.1086/308056. arXiv: astro-ph/9906470 [astro-ph].

Beckwith, Steven V. W., Massimo Stiavelli, Anton M. Koekemoer, John A. R. Caldwell, Henry C. Ferguson, Richard Hook, Ray A. Lucas, et al. 2006. "The Hubble Ultra Deep Field." *AJ* 132, no. 5 (November): 1729–1755. doi:10.1086/507302. arXiv: astro-ph/0607632 [astro-ph].

Bezanson, Rachel, David A. Wake, Gabriel B. Brammer, Pieter G. van Dokkum, Marijn Franx, Ivo Labbé, Joel Leja, et al. 2016. "Leveraging 3D-HST Grism

Redshifts to Quantify Photometric Redshift Performance." *ApJ* 822, no. 1, 30 (May): 30. doi:10.3847/0004-637X/822/1/30. arXiv: 1510.07049 [astro-ph.GA].

Blanc, G. A., K. Gebhardt, A. Heiderman, II Evans N. J., S. Jogee, R. van den Bosch, I. Marinova, et al. 2010. "The VIRUS-P Exploration of Nearby Galaxies (VENGA): Survey Design and First Results." In *New Horizons in Astronomy: Frank N. Bash Symposium 2009,* edited by L. M. Stanford, J. D. Green, L. Hao, and Y. Mao, 432:180. Astronomical Society of the Pacific Conference Series.

Blanc, Guillermo A., Tim Weinzirl, Mimi Song, Amanda Heiderman, Karl Gebhardt, Shardha Jogee, II Evans Neal J., et al. 2013. "The VIRUS-P Exploration of Nearby Galaxies (VENGA): Survey Design, Data Processing, and Spectral Analysis Methods." *AJ* 145, no. 5, 138 (May): 138. doi:10.1088/0004-6256/145/5/138. arXiv: 1303.1552 [astro-ph.CO].

Braine, J., E. Davoust, M. Zhu, U. Lisenfeld, C. Motch, and E. R. Seaquist. 2003. "A molecular gas bridge between the Taffy galaxies." *A&A* 408 (September): L13–L16. doi:10.1051/0004-6361:20031148. arXiv: astro-ph/0308476 [astro-ph].

Brammer, Gabriel B., Pieter G. van Dokkum, and Paolo Coppi. 2008. "EAZY: A Fast, Public Photometric Redshift Code." *ApJ* 686, no. 2 (October): 1503–1513. doi:10.1086/591786. arXiv: 0807.1533 [astro-ph].

Brammer, Gabriel B., Pieter G. van Dokkum, Marijn Franx, Mattia Fumagalli, Shannon Patel, Hans-Walter Rix, Rosalind E. Skelton, et al. 2012. "3D-HST: A Wide-field Grism Spectroscopic Survey with the Hubble Space Telescope." *ApJS* 200, no. 2, 13 (June): 13. doi:10.1088/0067-0049/200/2/13. arXiv: 1204.2829 [astro-ph.CO].

Bruzual A., G. 1983. "Spectral evolution of galaxies. I. Early-type systems." *ApJ* 273 (October): 105–127. doi:10.1086/161352.

Bruzual, G., and S. Charlot. 2003. "Stellar population synthesis at the resolution of 2003." *MNRAS* 344, no. 4 (October): 1000–1028. doi:10.1046/j.1365-8711.2003.06897.x. arXiv: astro-ph/0309134 [astro-ph].

Bushouse, H. A. 1986. "Star-formation rates in the nuclei of violently interacting galaxies." *AJ* 91 (February): 255–270. doi:10.1086/114005.

Bushouse, Howard A. 1987. "Global Properties of Interacting Disk-Type Galaxies." *ApJ* 320 (September): 49. doi:10.1086/165523.

Calzetti, Daniela. 2001. "The Dust Opacity of Star-forming Galaxies." *PASP* 113, no. 790 (December): 1449–1485. doi:10.1086/324269. arXiv: astro-ph/0109035 [astro-ph].

Calzetti, Daniela, Lee Armus, Ralph C. Bohlin, Anne L. Kinney, Jan Koornneef, and Thaisa Storchi-Bergmann. 2000. "The Dust Content and Opacity of Actively Star-forming Galaxies." *ApJ* 533, no. 2 (April): 682–695. doi:10.1086/308692. arXiv: astro-ph/9911459 [astro-ph].

Cappellari, Michele, and Eric Emsellem. 2004. "Parametric Recovery of Line-of-Sight Velocity Distributions from Absorption-Line Spectra of Galaxies via Penalized Likelihood." *PASP* 116, no. 816 (February): 138–147. doi:10.1086/381875. arXiv: astro-ph/0312201 [astro-ph].

Charlot, Stéphane, and S. Michael Fall. 2000. "A Simple Model for the Absorption of Starlight by Dust in Galaxies." *ApJ* 539, no. 2 (August): 718–731. doi:10.1086/309250. arXiv: astro-ph/0003128 [astro-ph].

Cimatti, A., E. Daddi, A. Renzini, P. Cassata, E. Vanzella, L. Pozzetti, S. Cristiani, et al. 2004. "Old galaxies in the young Universe." *Nature* 430, no. 6996 (July): 184–187. doi:10.1038/nature02668. arXiv: astro-ph/0407131 [astro-ph].

Cluver, M. E., P. N. Appleton, F. Boulanger, P. Guillard, P. Ogle, P. -A. Duc, N. Lu, et al. 2010. "Powerful H_2 Line Cooling in Stephan's Quintet. I. Mapping the Significant Cooling Pathways in Group-wide Shocks." *ApJ* 710, no. 1 (February): 248–264. doi:10.1088/0004-637X/710/1/248. arXiv: 0912.0282 [astro-ph.CO].

Cluver, M. E., P. N. Appleton, P. Ogle, T. H. Jarrett, J. Rasmussen, U. Lisenfeld, P. Guillard, et al. 2013. "Enhanced Warm H_2 Emission in the Compact Group Mid-infrared "Green Valley"." *ApJ* 765, no. 2, 93 (March): 93. doi:10.1088/0004-637X/765/2/93. arXiv: 1301.4549 [astro-ph.CO].

Colbert, James W., Harry Teplitz, Hakim Atek, Andrew Bunker, Marc Rafelski, Nathaniel Ross, Claudia Scarlata, et al. 2013. "Predicting Future Space Near-IR Grism Surveys Using the WFC3 Infrared Spectroscopic Parallels Survey." *ApJ* 779, no. 1, 34 (December): 34. doi:10.1088/0004-637X/779/1/34. arXiv: 1305.1399 [astro-ph.CO].

Condon, J. J., G. Helou, D. B. Sanders, and B. T. Soifer. 1993. "The "Taffy" Galaxies UGC 12914/5." *AJ* 105 (May): 1730. doi:10.1086/116549.

Cowie, Lennox L., Antoinette Songaila, Esther M. Hu, and J. G. Cohen. 1996. "New Insight on Galaxy Formation and Evolution From Keck Spectroscopy of the

Hawaii Deep Fields." *AJ* 112 (September): 839. doi:10.1086/118058. arXiv: astro-ph/9606079 [astro-ph].

Croton, Darren J., Volker Springel, Simon D. M. White, G. De Lucia, C. S. Frenk, L. Gao, A. Jenkins, G. Kauffmann, J. F. Navarro, and N. Yoshida. 2006. "The many lives of active galactic nuclei: cooling flows, black holes and the luminosities and colours of galaxies." *MNRAS* 365, no. 1 (January): 11–28. doi:10.1111/j.1365-2966.2005.09675.x. arXiv: astro-ph/0508046 [astro-ph].

Davies, Roger L., Elaine M. Sadler, and Reynier F. Peletier. 1993. "Line-strength gradients in elliptical galaxies." *MNRAS* 262 (June): 650–680. doi:10.1093/mnras/262.3.650.

Dekel, A., and J. Silk. 1986. "The Origin of Dwarf Galaxies, Cold Dark Matter, and Biased Galaxy Formation." *ApJ* 303 (April): 39. doi:10.1086/164050.

Desai, S., R. Armstrong, J. J. Mohr, D. R. Semler, J. Liu, E. Bertin, S. S. Allam, et al. 2012. "The Blanco Cosmology Survey: Data Acquisition, Processing, Calibration, Quality Diagnostics, and Data Release." *ApJ* 757, no. 1, 83 (September): 83. doi:10.1088/0004-637X/757/1/83. arXiv: 1204.1210 [astro-ph.CO].

Dicke, R. H., P. J. E. Peebles, P. G. Roll, and D. T. Wilkinson. 1965. "Cosmic Black-Body Radiation." *ApJ* 142 (July): 414–419. doi:10.1086/148306.

Driver, S. P., D. T. Hill, L. S. Kelvin, A. S. G. Robotham, J. Liske, P. Norberg, I. K. Baldry, et al. 2011. "Galaxy and Mass Assembly (GAMA): survey diagnostics and core data release." *MNRAS* 413, no. 2 (May): 971–995. doi:10.1111/j.1365-2966.2010.18188.x. arXiv: 1009.0614 [astro-ph.CO].

Driver, Simon P., Cristina C. Popescu, Richard J. Tuffs, Jochen Liske, Alister W. Graham, Paul D. Allen, and Roberto de Propris. 2007. "The Millennium Galaxy Catalogue: the B-band attenuation of bulge and disc light and the implied cosmic dust and stellar mass densities." *MNRAS* 379, no. 3 (August): 1022–1036. doi:10.1111/j.1365-2966.2007.11862.x. arXiv: 0704.2140 [astro-ph].

Eisenstein, Daniel J., Idit Zehavi, David W. Hogg, Roman Scoccimarro, Michael R. Blanton, Robert C. Nichol, Ryan Scranton, et al. 2005. "Detection of the Baryon Acoustic Peak in the Large-Scale Correlation Function of SDSS Luminous Red Galaxies." *ApJ* 633, no. 2 (November): 560–574. doi:10.1086/466512. arXiv: astro-ph/0501171 [astro-ph].

Elbaz, D., C. J. Cesarsky, P. Chanial, H. Aussel, A. Franceschini, D. Fadda, and R. R. Chary. 2002. "The bulk of the cosmic infrared background resolved by

ISOCAM." *A&A* 384 (March): 848–865. doi:10.1051/0004-6361:20020106. arXiv: astro-ph/0201328 [astro-ph].

Faber, S. M., C. N. A. Willmer, C. Wolf, D. C. Koo, B. J. Weiner, J. A. Newman, M. Im, et al. 2007. "Galaxy Luminosity Functions to z~1 from DEEP2 and COMBO-17: Implications for Red Galaxy Formation." *ApJ* 665, no. 1 (August): 265–294. doi:10.1086/519294. arXiv: astro-ph/0506044 [astro-ph].

Faber, S. M., G. Worthey, and J. J. Gonzales. 1992. "Absorption-Line Spectra of Elliptical Galaxies and Their Relation to Elliptical Formation." In *The Stellar Populations of Galaxies,* edited by Beatriz Barbuy and Alvio Renzini, 149:255. IAU Symposium. January.

Fabian, A. C. 2012. "Observational Evidence of Active Galactic Nuclei Feedback." *ARA&A* 50 (September): 455–489. doi:10.1146/annurev-astro-081811-125521. arXiv: 1204.4114 [astro-ph.CO].

Ferreras, Ignacio, Anna Pasquali, Sangeeta Malhotra, James Rhoads, Seth Cohen, Rogier Windhorst, Nor Pirzkal, et al. 2009. "Early-Type Galaxies in the PEARS Survey: Probing the Stellar Populations at Moderate Redshift." *ApJ* 706, no. 1 (November): 158–169. doi:10.1088/0004-637X/706/1/158. arXiv: 0908.0739 [astro-ph.CO].

Finkelstein, Steven L., Jr. Ryan Russell E., Casey Papovich, Mark Dickinson, Mimi Song, Rachel S. Somerville, Henry C. Ferguson, et al. 2015. "The Evolution of the Galaxy Rest-frame Ultraviolet Luminosity Function over the First Two Billion Years." *ApJ* 810, no. 1, 71 (September): 71. doi:10.1088/0004-637X/810/1/71. arXiv: 1410.5439 [astro-ph.GA].

Fontanot, Fabio, Gabriella De Lucia, Pierluigi Monaco, Rachel S. Somerville, and Paola Santini. 2009. "The many manifestations of downsizing: hierarchical galaxy formation models confront observations." *MNRAS* 397, no. 4 (August): 1776–1790. doi:10.1111/j.1365-2966.2009.15058.x. arXiv: 0901.1130 [astro-ph.CO].

Franx, Marijn, Ivo Labbé, Gregory Rudnick, Pieter G. van Dokkum, Emanuele Daddi, Natascha M. Förster Schreiber, Alan Moorwood, et al. 2003. "A Significant Population of Red, Near-Infrared-selected High-Redshift Galaxies." *ApJL* 587, no. 2 (April): L79–L82. doi:10.1086/375155. arXiv: astro-ph/0303163 [astro-ph].

French, K. Decker, Iair Arcavi, and Ann Zabludoff. 2016. "Tidal Disruption Events Prefer Unusual Host Galaxies." *ApJL* 818, no. 1, L21 (February): L21. doi:10.3847/2041-8205/818/1/L21. arXiv: 1601.04705 [astro-ph.GA].

Fujita, Yutaka. 2004. "Pre-Processing of Galaxies before Entering a Cluster." *Proceedings of the Astronomical Society of Japan* 56 (February): 29–43. doi:10.1093/pasj/56.1.29. arXiv: astro-ph/0311193 [astro-ph].

Gao, Yu, Ming Zhu, and E. R. Seaquist. 2003. "Star Formation Across the Taffy Bridge: UGC 12914/15." *AJ* 126, no. 5 (November): 2171–2184. doi:10.1086/378611. arXiv: astro-ph/0307490 [astro-ph].

Gardner, Jonathan P. 1998. "An Extendable Galaxy Number Count Model." *PASP* 110, no. 745 (March): 291–305. doi:10.1086/316141. arXiv: astro-ph/9802037 [astro-ph].

Giavalisco, M., H. C. Ferguson, A. M. Koekemoer, M. Dickinson, D. M. Alexander, F. E. Bauer, J. Bergeron, et al. 2004. "The Great Observatories Origins Deep Survey: Initial Results from Optical and Near-Infrared Imaging." *ApJL* 600, no. 2 (January): L93–L98. doi:10.1086/379232. arXiv: astro-ph/0309105 [astro-ph].

Gibson, N. P., S. Aigrain, S. Roberts, T. M. Evans, M. Osborne, and F. Pont. 2012. "A Gaussian process framework for modelling instrumental systematics: application to transmission spectroscopy." *MNRAS* 419, no. 3 (January): 2683–2694. doi:10.1111/j.1365-2966.2011.19915.x. arXiv: 1109.3251 [astro-ph.EP].

Grogin, Norman A., Dale D. Kocevski, S. M. Faber, Henry C. Ferguson, Anton M. Koekemoer, Adam G. Riess, Viviana Acquaviva, et al. 2011. "CANDELS: The Cosmic Assembly Near-infrared Deep Extragalactic Legacy Survey." *ApJS* 197, no. 2, 35 (December): 35. doi:10.1088/0067-0049/197/2/35. arXiv: 1105.3753 [astro-ph.CO].

Guillard, P., F. Boulanger, G. Pineau Des Forêts, and P. N. Appleton. 2009. "H_2 formation and excitation in the Stephan's Quintet galaxy-wide collision." *A&A* 502, no. 2 (August): 515–528. doi:10.1051/0004-6361/200811263. arXiv: 0904.4239 [astro-ph.CO].

Guth, Alan H. 1981. "Inflationary universe: A possible solution to the horizon and flatness problems." *Physical Review D* 23, no. 2 (January): 347–356. doi:10.1103/PhysRevD.23.347.

Güver, Tolga, and Feryal Özel. 2009. "The relation between optical extinction and hydrogen column density in the Galaxy." *MNRAS* 400, no. 4 (December): 2050–2053. doi:10.1111/j.1365-2966.2009.15598.x. arXiv: 0903.2057 [astro-ph.GA].

Hamilton, D. 1985. "The spectral evolution of galaxies. I. an observational approach." *ApJ* 297 (October): 371–389. doi:10.1086/163537.

Hampton, E. J., B. Groves, A. Medling, R. Davies, M. Dopita, I. -T. Ho, M. Kaasinen, et al. 2017. "Using an Artificial Neural Network to Classify Multi-component Emission Line Fits." In *Astronomical Data Analysis Software and Systems XXV,* edited by N. P. F. Lorente, K. Shortridge, and R. Wayth, 512:221. Astronomical Society of the Pacific Conference Series.

Harrison, C. M. 2017. "Impact of supermassive black hole growth on star formation." *Nature Astronomy* 1, 0165 (July): 0165. doi:10.1038/s41550-017-0165. arXiv: 1703.06889 [astro-ph.GA].

Hathi, N. P., I. Ferreras, A. Pasquali, S. Malhotra, J. E. Rhoads, N. Pirzkal, R. A. Windhorst, and C. Xu. 2009. "Stellar Populations of Late-Type Bulges at z≃1 in the Hubble Ultra Deep Field." *ApJ* 690, no. 2 (January): 1866–1882. doi:10.1088/0004-637X/690/2/1866. arXiv: 0805.0791 [astro-ph].

Heckman, Timothy M., Lee Armus, and George K. Miley. 1990. "On the Nature and Implications of Starburst-driven Galactic Superwinds." *ApJS* 74 (December): 833. doi:10.1086/191522.

Heckman, Timothy M., Matthew D. Lehnert, David K. Strickland, and Lee Armus. 2000. "Absorption-Line Probes of Gas and Dust in Galactic Superwinds." *ApJS* 129, no. 2 (August): 493–516. doi:10.1086/313421. arXiv: astro-ph/0002526 [astro-ph].

Hernán-Caballero, Antonio, Almudena Alonso-Herrero, Pablo G. Pérez-González, Nicolás Cardiel, Antonio Cava, Ignacio Ferreras, Guillermo Barro, et al. 2013. "SHARDS: stellar populations and star formation histories of a mass-selected sample of 0.65 < z < 1.1 galaxies." *MNRAS* 434, no. 3 (September): 2136–2152. doi:10.1093/mnras/stt1165. arXiv: 1306.5581 [astro-ph.CO].

Hildebrandt, H., T. Erben, K. Kuijken, L. van Waerbeke, C. Heymans, J. Coupon, J. Benjamin, et al. 2012. "CFHTLenS: improving the quality of photometric redshifts with precision photometry." *MNRAS* 421, no. 3 (April): 2355–2367. doi:10.1111/j.1365-2966.2012.20468.x. arXiv: 1111.4434 [astro-ph.CO].

Hill, Gary J., Phillip J. MacQueen, Michael P. Smith, Joseph R. Tufts, Martin M. Roth, Andreas Kelz, Joshua J. Adams, et al. 2008. "Design, construction, and performance of VIRUS-P: the prototype of a highly replicated integral-field spectrograph for HET." In *Proceedings of SPIE,* 7014:701470. Society of Photo-Optical Instrumentation Engineers (SPIE) Conference Series. doi:10.1117/12.790235.

Hinshaw, G., D. Larson, E. Komatsu, D. N. Spergel, C. L. Bennett, J. Dunkley, M. R. Nolta, et al. 2013. "Nine-year Wilkinson Microwave Anisotropy Probe (WMAP) Observations: Cosmological Parameter Results." *ApJS* 208, no. 2, 19 (October): 19. doi:10.1088/0067-0049/208/2/19. arXiv: 1212.5226 [astro-ph.CO].

Ho, I. -Ting, Anne M. Medling, Brent Groves, Jeffrey A. Rich, David S. N. Rupke, Elise Hampton, Lisa J. Kewley, et al. 2016. "LZIFU: an emission-line fitting toolkit for integral field spectroscopy data." *APSS* 361, no. 9, 280 (September): 280. doi:10.1007/s10509-016-2865-2. arXiv: 1607.06561 [astro-ph.GA].

Hogg, David W., Jo Bovy, and Dustin Lang. 2010. "Data analysis recipes: Fitting a model to data." *arXiv e-prints,* arXiv:1008.4686 (August): arXiv:1008.4686. arXiv: 1008.4686 [astro-ph.IM].

Hu, Wayne, and Scott Dodelson. 2002. "Cosmic Microwave Background Anisotropies." *ARA&A* 40 (January): 171–216. doi:10.1146/annurev.astro.40.060401.093926. arXiv: astro-ph/0110414 [astro-ph].

Hummer, D. G., and P. J. Storey. 1987. "Recombination-line intensities for hydrogenic ions - I. Case B calculations for H I and He II." *MNRAS* 224 (February): 801–820. doi:10.1093/mnras/224.3.801.

Jarrett, T. H., G. Helou, D. Van Buren, E. Valjavec, and J. J. Condon. 1999. "A Near- and Mid-Infrared Study of the Interacting Galaxy Pair UGC 12914/12915: "Taffy"." *AJ* 118, no. 5 (November): 2132–2147. doi:10.1086/301080. arXiv: astro-ph/0004268 [astro-ph].

Johansson, Jonas, Daniel Thomas, and Claudia Maraston. 2012. "Chemical element ratios of Sloan Digital Sky Survey early-type galaxies." *MNRAS* 421, no. 3 (April): 1908–1926. doi:10.1111/j.1365-2966.2011.20316.x. arXiv: 1112.0322 [astro-ph.CO].

Jones, D. Heath, Will Saunders, Matthew Colless, Mike A. Read, Quentin A. Parker, Fred G. Watson, Lachlan A. Campbell, et al. 2004. "The 6dF Galaxy Survey: samples, observational techniques and the first data release." *MNRAS* 355, no. 3 (December): 747–763. doi:10.1111/j.1365-2966.2004.08353.x. arXiv: astro-ph/0403501 [astro-ph].

Joseph, R. D., and G. S. Wright. 1985. "Recent star formation in interacting galaxies - II. Super starbursts in merging galaxies." *MNRAS* 214 (May): 87–95. doi:10.1093/mnras/214.2.87.

Joshi, Bhavin A., Philip N. Appleton, Guillermo A. Blanc, Pierre Guillard, Jeffrey Rich, Curtis Struck, Emily E. Freeland, Bradley W. Peterson, George Helou, and Katherine Alatalo. 2019. "Evidence for Shock-heated Gas in the Taffy Galaxies and Bridge from Optical Emission-line IFU Spectroscopy." *ApJ* 878, no. 2, 161 (June): 161. doi:10.3847/1538-4357/ab2124. arXiv: 1812.07743 [astro-ph.GA].

Joshi, Bhavin A., Seth Cohen, Rogier A. Windhorst, Rolf Jansen, Norbert Pirzkal, and Nimish P. Hathi. 2019. "Spectrophotometric Redshifts for z∼1 Galaxies and Predictions for Number Densities with WFIRST and Euclid." *ApJ* 883, no. 2, 157 (October): 157. doi:10.3847/1538-4357/ab3a4e. arXiv: 1903.08705 [astro-ph.GA].

Kauffmann, Guinevere, Timothy M. Heckman, Simon D. M. White, Stéphane Charlot, Christy Tremonti, Jarle Brinchmann, Gustavo Bruzual, et al. 2003. "Stellar masses and star formation histories for 10^5 galaxies from the Sloan Digital Sky Survey." *MNRAS* 341, no. 1 (May): 33–53. doi:10.1046/j.1365-8711.2003.06291.x. arXiv: astro-ph/0204055 [astro-ph].

Kauffmann, Guinevere, Timothy M. Heckman, Simon D. M. White, Stéphane Charlot, Christy Tremonti, Eric W. Peng, Mark Seibert, et al. 2003. "The dependence of star formation history and internal structure on stellar mass for 10^5 low-redshift galaxies." *MNRAS* 341, no. 1 (May): 54–69. doi:10.1046/j.1365-8711.2003.06292.x. arXiv: astro-ph/0205070 [astro-ph].

Kawata, Daisuke, and John S. Mulchaey. 2008. "Strangulation in Galaxy Groups." *ApJL* 672, no. 2 (January): L103. doi:10.1086/526544. arXiv: 0707.3814 [astro-ph].

Kelvin, Lee S., Simon P. Driver, Aaron S. G. Robotham, Alister W. Graham, Steven Phillipps, Nicola K. Agius, Mehmet Alpaslan, et al. 2014. "Galaxy And Mass Assembly (GAMA): ugrizYJHK Sérsic luminosity functions and the cosmic spectral energy distribution by Hubble type." *MNRAS* 439, no. 2 (April): 1245–1269. doi:10.1093/mnras/stt2391. arXiv: 1401.1817 [astro-ph.CO].

Kennicutt, Jr., Robert C. 1998. "Star Formation in Galaxies Along the Hubble Sequence." *ARA&A* 36 (January): 189–232. doi:10.1146/annurev.astro.36.1.189. arXiv: astro-ph/9807187 [astro-ph].

Kewley, L. J., C. A. Heisler, M. A. Dopita, and S. Lumsden. 2001. "Optical Classification of Southern Warm Infrared Galaxies." *ApJS* 132, no. 1 (January): 37–71. doi:10.1086/318944.

Kewley, Lisa J., Brent Groves, Guinevere Kauffmann, and Tim Heckman. 2006. "The host galaxies and classification of active galactic nuclei." *MNRAS* 372, no. 3 (November): 961–976. doi:10.1111/j.1365-2966.2006.10859.x. arXiv: astro-ph/0605681 [astro-ph].

Koekemoer, Anton M., S. M. Faber, Henry C. Ferguson, Norman A. Grogin, Dale D. Kocevski, David C. Koo, Kamson Lai, et al. 2011. "CANDELS: The Cosmic Assembly Near-infrared Deep Extragalactic Legacy Survey—The Hubble Space Telescope Observations, Imaging Data Products, and Mosaics." *ApJS* 197, no. 2, 36 (December): 36. doi:10.1088/0067-0049/197/2/36. arXiv: 1105.3754 [astro-ph.CO].

Komugi, S., K. Tateuchi, K. Motohara, T. Takagi, D. Iono, H. Kaneko, J. Ueda, et al. 2012. "The Schmidt-Kennicutt Law of Matched-age Star-forming Regions; Paα Observations of the Early-phase Interacting Galaxy Taffy I." *ApJ* 757, no. 2, 138 (October): 138. doi:10.1088/0004-637X/757/2/138. arXiv: 1208.0315 [astro-ph.CO].

Kriek, Mariska, Arjen van der Wel, Pieter G. van Dokkum, Marijn Franx, and Garth D. Illingworth. 2008. "The Detection of a Red Sequence of Massive Field Galaxies at z 2.3 and Its Evolution to z 0." *ApJ* 682, no. 2 (August): 896–906. doi:10.1086/589677. arXiv: 0804.4175 [astro-ph].

Kulkarni, Samridhi, D. K. Sahu, Laxmikant Chaware, N. K. Chakradhari, and S. K. Pandey. 2014. "Study of dust and ionized gas in early-type galaxies." *New Astronomy* 30 (July): 51–63. doi:10.1016/j.newast.2014.01.003. arXiv: 1402.5545 [astro-ph.GA].

Labbé, Ivo, Jiasheng Huang, Marijn Franx, Gregory Rudnick, Pauline Barmby, Emanuele Daddi, Pieter G. van Dokkum, et al. 2005. "IRAC Mid-Infrared Imaging of the Hubble Deep Field-South: Star Formation Histories and Stellar Masses of Red Galaxies at z>2." *ApJL* 624, no. 2 (May): L81–L84. doi:10.1086/430700. arXiv: astro-ph/0504219 [astro-ph].

Laureijs, R., J. Amiaux, S. Arduini, J. -L. Auguères, J. Brinchmann, R. Cole, M. Cropper, et al. 2011. "Euclid Definition Study Report." *arXiv e-prints,* arXiv:1110.3193 (October): arXiv:1110.3193. arXiv: 1110.3193 [astro-ph.CO].

Li, Cheng, Enci Wang, Lin Lin, Matthew A. Bershady, Kevin Bundy, Christy A. Tremonti, Ting Xiao, et al. 2015. "P-MaNGA: Gradients in Recent Star Formation Histories as Diagnostics for Galaxy Growth and Death." *ApJ* 804, no. 2, 125 (May): 125. doi:10.1088/0004-637X/804/2/125. arXiv: 1502.07040 [astro-ph.GA].

Linde, A. D. 1982. "A new inflationary universe scenario: A possible solution of the horizon, flatness, homogeneity, isotropy and primordial monopole problems." *Physics Letters B* 108, no. 6 (February): 389–393. doi:10.1016/0370-2693(82)91219-9.

Lisenfeld, U., K. Alatalo, C. Zucker, P. N. Appleton, S. Gallagher, P. Guillard, and K. Johnson. 2017. "The role of molecular gas in galaxy transition in compact groups." *A&A* 607, A110 (November): A110. doi:10.1051/0004-6361/201730898. arXiv: 1708.09159 [astro-ph.GA].

Lisenfeld, U., and H. J. Völk. 2010. "Shock acceleration of relativistic particles in galaxy-galaxy collisions." *A&A* 524, A27 (December): A27. doi:10.1051/0004-6361/201015083. arXiv: 1009.1659 [astro-ph.CO].

Mac Low, Mordecai-Mark, and Andrea Ferrara. 1999. "Starburst-driven Mass Loss from Dwarf Galaxies: Efficiency and Metal Ejection." *ApJ* 513, no. 1 (March): 142–155. doi:10.1086/306832. arXiv: astro-ph/9801237 [astro-ph].

Macchetto, F., M. Pastoriza, N. Caon, W. B. Sparks, M. Giavalisco, R. Bender, and M. Capaccioli. 1996. "A survey of the ISM in early-type galaxies. I. The ionized gas." *A&AS* 120 (December): 463–488.

Madau, Piero, and Mark Dickinson. 2014. "Cosmic Star-Formation History." *ARA&A* 52 (August): 415–486. doi:10.1146/annurev-astro-081811-125615. arXiv: 1403.0007 [astro-ph.CO].

Man, Allison W. S., Thomas R. Greve, Sune Toft, Benjamin Magnelli, Alexander Karim, Olivier Ilbert, Mara Salvato, et al. 2016. "Confirming the Existence of a Quiescent Galaxy Population out to z=3: A Stacking Analysis of Mid-, Far-Infrared and Radio Data." *ApJ* 820, no. 1, 11 (March): 11. doi:10.3847/0004-637X/820/1/11. arXiv: 1411.2870 [astro-ph.GA].

Mather, J. C., E. S. Cheng, D. A. Cottingham, Jr. Eplee R. E., D. J. Fixsen, T. Hewagama, R. B. Isaacman, et al. 1994. "Measurement of the Cosmic Microwave Background Spectrum by the COBE FIRAS Instrument." *ApJ* 420 (January): 439. doi:10.1086/173574.

Matteucci, F., and L. Greggio. 1986. "Relative roles of type I and II supernovae in the chemical enrichment of the interstellar gas." *A&A* 154, nos. 1-2 (January): 279–287.

McMahon, Richard. 2012. "The VISTA Hemisphere Survey(VHS) Science Goals and Status." In *Science from the Next Generation Imaging and Spectroscopic Surveys,* 37. October.

Mehta, Vihang, Claudia Scarlata, James W. Colbert, Y. S. Dai, Alan Dressler, Alaina Henry, Matt Malkan, et al. 2015. "Predicting the Redshift 2 Hα Luminosity Function Using [OIII] Emission Line Galaxies." *ApJ* 811, no. 2, 141 (October): 141. doi:10.1088/0004-637X/811/2/141. arXiv: 1505.07843 [astro-ph.GA].

Merson, Alexander, Yun Wang, Andrew Benson, Andreas Faisst, Daniel Masters, Alina Kiessling, and Jason Rhodes. 2018. "Predicting Hα emission-line galaxy counts for future galaxy redshift surveys." *MNRAS* 474, no. 1 (February): 177–196. doi:10.1093/mnras/stx2649. arXiv: 1710.00833 [astro-ph.GA].

Muratov, Alexander L., Dušan Kereš, Claude-André Faucher-Giguère, Philip F. Hopkins, Eliot Quataert, and Norman Murray. 2015. "Gusty, gaseous flows of FIRE: galactic winds in cosmological simulations with explicit stellar feedback." *MNRAS* 454, no. 3 (December): 2691–2713. doi:10.1093/mnras/stv2126. arXiv: 1501.03155 [astro-ph.GA].

National Research Council. 2010. *New Worlds, New Horizons in Astronomy and Astrophysics.* Washington, DC: The National Academies Press. doi:10.17226/12951.

Oke, J. B., and J. E. Gunn. 1983. "Secondary standard stars for absolute spectrophotometry." *ApJ* 266 (March): 713–717. doi:10.1086/160817.

Onodera, M., C. M. Carollo, A. Renzini, M. Cappellari, C. Mancini, N. Arimoto, E. Daddi, et al. 2015. "The Ages, Metallicities, and Element Abundance Ratios of Massive Quenched Galaxies at z1.6." *ApJ* 808, no. 2, 161 (August): 161. doi:10.1088/0004-637X/808/2/161. arXiv: 1411.5023 [astro-ph.GA].

Pasquali, A., N. Pirzkal, S. Larsen, J. R. Walsh, and M. Kümmel. 2006. "Slitless Grism Spectroscopy with the Hubble Space Telescope Advanced Camera for Surveys." *PASP* 118, no. 840 (February): 270–287. doi:10.1086/498731. arXiv: astro-ph/0510428 [astro-ph].

Pasquali, A., N. Pirzkal, J. R. Walsh, R. N. Hook, W. Freudling, R. Albrecht, and R. A. E. Fosbury. 2001. *The Effective Spectral Resolution of the WFC and HRC Grism.* ST-ECF Instrument Science Report ACS 2001-002, March.

Peebles, P. J. E. 1965. "The Black-Body Radiation Content of the Universe and the Formation of Galaxies." *ApJ* 142 (November): 1317. doi:10.1086/148417.

Peebles, P. J. E., and J. T. Yu. 1970. "Primeval Adiabatic Perturbation in an Expanding Universe." *ApJ* 162 (December): 815. doi:10.1086/150713.

Peng, Y., R. Maiolino, and R. Cochrane. 2015. "Strangulation as the primary mechanism for shutting down star formation in galaxies." *Nature* 521, no. 7551 (May): 192–195. doi:10.1038/nature14439. arXiv: 1505.03143 [astro-ph.GA].

Penzias, A. A., and R. W. Wilson. 1965. "A Measurement of Excess Antenna Temperature at 4080 Mc/s." *ApJ* 142 (July): 419–421. doi:10.1086/148307.

Peterson, B. W., P. N. Appleton, T. Bitsakis, P. Guillard, K. Alatalo, F. Boulanger, M. Cluver, et al. 2018. "Herschel Spectroscopy of the Taffy Galaxies (UGC 12914/12915 = VV 254): Enhanced [C II] Emission in the Collisionally Formed Bridge." *ApJ* 855, no. 2, 141 (March): 141. doi:10.3847/1538-4357/aaac2c. arXiv: 1801.10230 [astro-ph.GA].

Peterson, B. W., P. N. Appleton, G. Helou, P. Guillard, T. H. Jarrett, M. E. Cluver, P. Ogle, C. Struck, and F. Boulanger. 2012. "Detection of Powerful Mid-IR H_2 Emission in the Bridge between the Taffy Galaxies." *ApJ* 751, no. 1, 11 (May): 11. doi:10.1088/0004-637X/751/1/11. arXiv: 1203.4203 [astro-ph.CO].

Pharo, John, Sangeeta Malhotra, James Rhoads, Russell Ryan, Vithal Tilvi, Norbert Pirzkal, Steven Finkelstein, et al. 2018. "Spectrophotometric Redshifts in the Faint Infrared Grism Survey: Finding Overdensities of Faint Galaxies." *ApJ* 856, no. 2, 116 (April): 116. doi:10.3847/1538-4357/aaadfc. arXiv: 1802.02239 [astro-ph.GA].

Pirzkal, N., C. Xu, S. Malhotra, J. E. Rhoads, A. M. Koekemoer, L. A. Moustakas, J. R. Walsh, et al. 2004. "GRAPES, Grism Spectroscopy of the Hubble Ultra Deep Field: Description and Data Reduction." *ApJS* 154, no. 2 (October): 501–508. doi:10.1086/422582. arXiv: astro-ph/0403458 [astro-ph].

Pirzkal, Nor, Barry Rothberg, Chun Ly, Sangeeta Malhotra, James E. Rhoads, Norman A. Grogin, Tomas Dahlen, et al. 2013. "Emission-line Galaxies from the Hubble Space Telescope Probing Evolution and Reionization Spectroscopically (PEARS) Grism Survey. II. The Complete Sample." *ApJ* 772, no. 1, 48 (July): 48. doi:10.1088/0004-637X/772/1/48. arXiv: 1208.5535 [astro-ph.GA].

Pirzkal, Norbert, Sangeeta Malhotra, Russell E. Ryan, Barry Rothberg, Norman Grogin, Steven L. Finkelstein, Anton M. Koekemoer, et al. 2017. "FIGS—Faint Infrared Grism Survey: Description and Data Reduction." *ApJ* 846, no. 1, 84 (September): 84. doi:10.3847/1538-4357/aa81cc. arXiv: 1706.02669 [astro-ph.GA].

Pirzkal, Norbert, Barry Rothberg, Russell E. Ryan, Sangeeta Malhotra, James Rhoads, Norman Grogin, Emma Curtis-Lake, et al. 2018. "A Two-dimensional Spectroscopic Study of Emission-line Galaxies in the Faint Infrared Grism Survey (FIGS). I. Detection Method and Catalog." *ApJ* 868, no. 1, 61 (November): 61. doi:10.3847/1538-4357/aae585. arXiv: 1806.01787 [astro-ph.GA].

Planck Collaboration, R. Adam, P. A. R. Ade, N. Aghanim, Y. Akrami, M. I. R. Alves, F. Argüeso, et al. 2016. "Planck 2015 results. I. Overview of products and scientific results." *A&A* 594, A1 (September): A1. doi:10.1051/0004-6361/201527101. arXiv: 1502.01582 [astro-ph.CO].

Planck Collaboration, N. Aghanim, Y. Akrami, M. Ashdown, J. Aumont, C. Baccigalupi, M. Ballardini, et al. 2018a. "Planck 2018 results. VI. Cosmological parameters." *arXiv e-prints,* arXiv:1807.06209 (July): arXiv:1807.06209. arXiv: 1807.06209 [astro-ph.CO].

———. 2018b. "Planck 2018 results. VI. Cosmological parameters." *arXiv e-prints,* arXiv:1807.06209 (July): arXiv:1807.06209. arXiv: 1807.06209 [astro-ph.CO].

Planck Collaboration, N. Aghanim, Y. Akrami, M. Ashdown, J. Aumont, C. Baccigalupi, M. Ballardini, et al. 2019. "Planck 2018 results. V. CMB power spectra and likelihoods." *arXiv e-prints,* arXiv:1907.12875 (July): arXiv:1907.12875. arXiv: 1907.12875 [astro-ph.CO].

Poggianti, B. M., and G. Barbaro. 1997. "Indicators of star formation: 4000 Å break and Balmer lines." *A&A* 325 (September): 1025–1030. arXiv: astro-ph/9703067 [astro-ph].

Press, William H., and Paul Schechter. 1974. "Formation of Galaxies and Clusters of Galaxies by Self-Similar Gravitational Condensation." *ApJ* 187 (February): 425–438. doi:10.1086/152650.

Renzini, Alvio. 2006. "Stellar Population Diagnostics of Elliptical Galaxy Formation." *ARA&A* 44, no. 1 (September): 141–192. doi:10.1146/annurev.astro.44.051905.092450. arXiv: astro-ph/0603479 [astro-ph].

Rich, J. A., L. J. Kewley, and M. A. Dopita. 2011. "Galaxy-wide Shocks in Late-merger Stage Luminous Infrared Galaxies." *ApJ* 734, no. 2, 87 (June): 87. doi:10.1088/0004-637X/734/2/87. arXiv: 1104.1177 [astro-ph.CO].

———. 2014. "Composite Spectra in Merging U/LIRGs Caused by Shocks." *ApJL* 781, no. 1, L12 (January): L12. doi:10.1088/2041-8205/781/1/L12. arXiv: 1310.3441 [astro-ph.CO].

Rich, J. A., L. J. Kewley, and M. A. Dopita. 2015. "Galaxy Mergers Drive Shocks: An Integral Field Study of GOALS Galaxies." *ApJS* 221, no. 2, 28 (December): 28. doi:10.1088/0067-0049/221/2/28. arXiv: 1509.08468 [astro-ph.GA].

Robotham, A. S. G., S. P. Driver, L. J. M. Davies, A. M. Hopkins, I. K. Baldry, N. K. Agius, A. E. Bauer, et al. 2014. "Galaxy And Mass Assembly (GAMA): galaxy close pairs, mergers and the future fate of stellar mass." *MNRAS* 444, no. 4 (November): 3986–4008. doi:10.1093/mnras/stu1604. arXiv: 1408.1476 [astro-ph.GA].

Ryan, Jr., R. E., S. Casertano, and N. Pirzkal. 2018. "Linear: A Novel Algorithm for Reconstructing Slitless Spectroscopy from HST/WFC3." *PASP* 130, no. 985 (March): 034501. doi:10.1088/1538-3873/aaa53e. arXiv: 1801.03936 [astro-ph.IM].

Ryan, Jr., R. E., N. P. Hathi, S. H. Cohen, S. Malhotra, J. Rhoads, R. A. Windhorst, T. Budavári, et al. 2007. "The Galaxy Luminosity Function at z = 1 in the HUDF: Probing the Dwarf Population." *ApJ* 668, no. 2 (October): 839–845. doi:10.1086/519307. arXiv: astro-ph/0703743 [astro-ph].

Sachs, R. K., and A. M. Wolfe. 1967. "Perturbations of a Cosmological Model and Angular Variations of the Microwave Background." *ApJ* 147 (January): 73. doi:10.1086/148982.

Sanders, D. B., J. M. Mazzarella, D. -C. Kim, J. A. Surace, and B. T. Soifer. 2003. "The IRAS Revised Bright Galaxy Sample." *AJ* 126, no. 4 (October): 1607–1664. doi:10.1086/376841. arXiv: astro-ph/0306263 [astro-ph].

Sanders, D. B., and I. F. Mirabel. 1996. "Luminous Infrared Galaxies." *ARA&A* 34 (January): 749. doi:10.1146/annurev.astro.34.1.749.

Sanders, D. B., B. T. Soifer, J. H. Elias, B. F. Madore, K. Matthews, G. Neugebauer, and N. Z. Scoville. 1988. "Ultraluminous Infrared Galaxies and the Origin of Quasars." *ApJ* 325 (February): 74. doi:10.1086/165983.

Sanders, D. B., B. T. Soifer, J. H. Elias, G. Neugebauer, and K. Matthews. 1988. "Warm Ultraluminous Galaxies in the IRAS Survey: The Transition from Galaxy to Quasar?" *ApJL* 328 (May): L35. doi:10.1086/185155.

Schawinski, Kevin, Daniel Thomas, Marc Sarzi, Claudia Maraston, Sugata Kaviraj, Seok-Joo Joo, Sukyoung K. Yi, and Joseph Silk. 2007. "Observational evidence for AGN feedback in early-type galaxies." *MNRAS* 382, no. 4 (December): 1415–1431. doi:10.1111/j.1365-2966.2007.12487.x. arXiv: 0709.3015 [astro-ph].

Schechter, P. 1976. "An analytic expression for the luminosity function for galaxies." *ApJ* 203 (January): 297–306. doi:10.1086/154079.

Silk, Joseph. 1968. "Cosmic Black-Body Radiation and Galaxy Formation." *ApJ* 151 (February): 459. doi:10.1086/149449.

Silk, Joseph, and Martin J. Rees. 1998. "Quasars and galaxy formation." *A&A* 331 (March): L1–L4. arXiv: astro-ph/9801013 [astro-ph].

Skelton, Rosalind E., Katherine E. Whitaker, Ivelina G. Momcheva, Gabriel B. Brammer, Pieter G. van Dokkum, Ivo Labbé, Marijn Franx, et al. 2014. "3D-HST WFC3-selected Photometric Catalogs in the Five CANDELS/3D-HST Fields: Photometry, Photometric Redshifts, and Stellar Masses." *ApJS* 214, no. 2, 24 (October): 24. doi:10.1088/0067-0049/214/2/24. arXiv: 1403.3689 [astro-ph.GA].

Smoot, G. F., C. L. Bennett, A. Kogut, E. L. Wright, J. Aymon, N. W. Boggess, E. S. Cheng, et al. 1992. "Structure in the COBE Differential Microwave Radiometer First-Year Maps." *ApJL* 396 (September): L1. doi:10.1086/186504.

Soifer, B. T., and G. Neugebauer. 1991. "The Properties of Infrared Galaxies in the Local Universe." *AJ* 101 (February): 354. doi:10.1086/115691.

Soifer, B. T., D. B. Sanders, B. F. Madore, G. Neugebauer, G. E. Danielson, J. H. Elias, Carol J. Lonsdale, and W. L. Rice. 1987. "The IRAS Bright Galaxy Sample. II. The Sample and Luminosity Function." *ApJ* 320 (September): 238. doi:10.1086/165536.

Spacek, Alexander, Evan Scannapieco, Seth Cohen, Bhavin Joshi, and Philip Mauskopf. 2016. "Constraining AGN Feedback in Massive Ellipticals with South Pole Telescope Measurements of the Thermal Sunyaev-Zel'dovich Effect." *ApJ* 819, no. 2, 128 (March): 128. doi:10.3847/0004-637X/819/2/128. arXiv: 1601.01330 [astro-ph.GA].

———. 2017. "Searching for Fossil Evidence of AGN Feedback in WISE-selected Stripe-82 Galaxies by Measuring the Thermal Sunyaev-Zel'dovich Effect with the Atacama Cosmology Telescope." *ApJ* 834, no. 2, 102 (January): 102. doi:10.3847/1538-4357/834/2/102. arXiv: 1610.02068 [astro-ph.GA].

Spergel, D., N. Gehrels, C. Baltay, D. Bennett, J. Breckinridge, M. Donahue, A. Dressler, et al. 2015. "Wide-Field InfrarRed Survey Telescope-Astrophysics Focused Telescope Assets WFIRST-AFTA 2015 Report." *arXiv e-prints,* arXiv:1503.03757 (March): arXiv:1503.03757. arXiv: 1503.03757 [astro-ph.IM].

Straatman, Caroline M. S., Ivo Labbé, Lee R. Spitler, Rebecca Allen, Bruno Altieri, Gabriel B. Brammer, Mark Dickinson, et al. 2014. "A Substantial Population of Massive Quiescent Galaxies at z 4 from ZFOURGE." *ApJL* 783, no. 1, L14 (March): L14. doi:10.1088/2041-8205/783/1/L14. arXiv: 1312.4952 [astro-ph.GA].

Straughn, Amber N., Norbert Pirzkal, Gerhardt R. Meurer, Seth H. Cohen, Rogier A. Windhorst, Sangeeta Malhotra, James Rhoads, et al. 2009. "Emission-Line Galaxies from the Hubble Space Telescope Probing Evolution and Reionization Spectroscopically (PEARS) Grism Survey. I. The South Fields." *AJ* 138, no. 4 (October): 1022–1031. doi:10.1088/0004-6256/138/4/1022. arXiv: 0907.2254 [astro-ph.CO].

Struck, Curtis. 1997. "Simulations of Collisions between Two Gas-rich Galaxy Disks with Heating and Cooling." *ApJS* 113, no. 2 (December): 269–309. doi:10.1086/313055.

Sunyaev, R. A., and Ya. B. Zeldovich. 1970. "Small-Scale Fluctuations of Relic Radiation." *APSS* 7, no. 1 (April): 3–19. doi:10.1007/BF00653471.

———. 1972. "The Observations of Relic Radiation as a Test of the Nature of X-Ray Radiation from the Clusters of Galaxies." *Comments on Astrophysics and Space Physics* 4 (November): 173.

———. 1980. "Microwave background radiation as a probe of the contemporary structure and history of the universe." *ARA&A* 18 (January): 537–560. doi:10.1146/annurev.aa.18.090180.002541.

Thomas, D., L. Greggio, and R. Bender. 1999. "Constraints on galaxy formation from alpha-enhancement in luminous elliptical galaxies." *MNRAS* 302, no. 3 (January): 537–548. doi:10.1046/j.1365-8711.1999.02138.x. arXiv: astro-ph/9809261 [astro-ph].

Thomas, Daniel, Claudia Maraston, Ralf Bender, and Claudia Mendes de Oliveira. 2005. "The Epochs of Early-Type Galaxy Formation as a Function of Environment." *ApJ* 621, no. 2 (March): 673–694. doi:10.1086/426932. arXiv: astro-ph/0410209 [astro-ph].

Thomas, Daniel, Claudia Maraston, Kevin Schawinski, Marc Sarzi, and Joseph Silk. 2010. "Environment and self-regulation in galaxy formation." *MNRAS* 404, no. 4 (June): 1775–1789. doi:10.1111/j.1365-2966.2010.16427.x. arXiv: 0912.0259 [astro-ph.CO].

Trager, S. C., S. M. Faber, Guy Worthey, and J. Jesús González. 2000. "The Stellar Population Histories of Early-Type Galaxies. II. Controlling Parameters of the Stellar Populations." *AJ* 120, no. 1 (July): 165–188. doi:10.1086/301442. arXiv: astro-ph/0004095 [astro-ph].

Unterborn, Cayman T., and Barbara S. Ryden. 2008. "Inclination-Dependent Extinction Effects in Disk Galaxies in the Sloan Digital Sky Survey." *ApJ* 687, no. 2 (November): 976–985. doi:10.1086/591898. arXiv: 0801.2400 [astro-ph].

Valentino, F., E. Daddi, J. D. Silverman, A. Puglisi, D. Kashino, A. Renzini, A. Cimatti, et al. 2017. "Predicting emission line fluxes and number counts of distant galaxies for cosmological surveys." *MNRAS* 472, no. 4 (December): 4878–4899. doi:10.1093/mnras/stx2305. arXiv: 1709.01936 [astro-ph.GA].

van Dokkum, Pieter G. 2001. "Cosmic-Ray Rejection by Laplacian Edge Detection." *PASP* 113, no. 789 (November): 1420–1427. doi:10.1086/323894. arXiv: astro-ph/0108003 [astro-ph].

Veilleux, Sylvain, Gerald Cecil, and Joss Bland-Hawthorn. 2005. "Galactic Winds." *ARA&A* 43, no. 1 (September): 769–826. doi:10.1146/annurev.astro.43.072103.150610. arXiv: astro-ph/0504435 [astro-ph].

Veilleux, Sylvain, and Donald E. Osterbrock. 1987. "Spectral Classification of Emission-Line Galaxies." *ApJS* 63 (February): 295. doi:10.1086/191166.

Vollmer, B., J. Braine, and M. Soida. 2012. "A dynamical model for the Taffy galaxies UGC 12914/5." *A&A* 547, A39 (November): A39. doi:10.1051/0004-6361/201219668. arXiv: 1209.6052 [astro-ph.CO].

Weilbacher, Peter M., Ana Monreal-Ibero, Anne Verhamme, Christer Sandin, Matthias Steinmetz, Wolfram Kollatschny, Davor Krajnović, et al. 2018. "Lyman-continuum leakage as dominant source of diffuse ionized gas in the Antennae galaxy." *A&A* 611, A95 (April): A95. doi:10.1051/0004-6361/201731669. arXiv: 1712.04450 [astro-ph.GA].

Weinberg, David H., Michael J. Mortonson, Daniel J. Eisenstein, Christopher Hirata, Adam G. Riess, and Eduardo Rozo. 2013. "Observational probes of cosmic acceleration." *Physics Reports* 530, no. 2 (September): 87–255. doi:10.1016/j.physrep.2013.05.001. arXiv: 1201.2434 [astro-ph.CO].

Whitaker, Katherine E., Pieter G. van Dokkum, Gabriel Brammer, Ivelina G. Momcheva, Rosalind Skelton, Marijn Franx, Mariska Kriek, et al. 2013. "Quiescent Galaxies in the 3D-HST Survey: Spectroscopic Confirmation of a Large Number

of Galaxies with Relatively Old Stellar Populations at z 2." *ApJL* 770, no. 2, L39 (June): L39. doi:10.1088/2041-8205/770/2/L39. arXiv: 1305.1943 [astro-ph.CO].

White, Martin, Douglas Scott, and Joseph Silk. 1994. "Anisotropies in the Cosmic Microwave Background." *ARA&A* 32 (January): 319–370. doi:10.1146/annurev.astro.32.1.319.

Williams, Rik J., Ryan F. Quadri, Marijn Franx, Pieter van Dokkum, and Ivo Labbé. 2009. "Detection of Quiescent Galaxies in a Bicolor Sequence from Z = 0-2." *ApJ* 691, no. 2 (February): 1879–1895. doi:10.1088/0004-637X/691/2/1879. arXiv: 0806.0625 [astro-ph].

Windhorst, Rogier A., Seth H. Cohen, Nimish P. Hathi, Patrick J. McCarthy, Jr. Ryan Russell E., Haojing Yan, Ivan K. Baldry, et al. 2011. "The Hubble Space Telescope Wide Field Camera 3 Early Release Science Data: Panchromatic Faint Object Counts for 0.2-2 μm Wavelength." *ApJS* 193, no. 2, 27 (April): 27. doi:10.1088/0067-0049/193/2/27. arXiv: 1005.2776 [astro-ph.CO].

Worthey, Guy, S. M. Faber, and J. J. Gonzalez. 1992. "MG and Fe Absorption Features in Elliptical Galaxies." *ApJ* 398 (October): 69. doi:10.1086/171836.

Worthey, Guy, and D. L. Ottaviani. 1997. "Hγ and Hδ Absorption Features in Stars and Stellar Populations." *ApJS* 111, no. 2 (August): 377–386. doi:10.1086/313021.

Xia, Lifang, Sangeeta Malhotra, James Rhoads, Norbert Pirzkal, Zhenya Zheng, Gerhardt Meurer, Amber Straughn, Norman Grogin, and David Floyd. 2011. "Spectroscopic Study of the HST/ACS PEARS Emission-line Galaxies." *AJ* 141, no. 2, 64 (February): 64. doi:10.1088/0004-6256/141/2/64. arXiv: 1011.4064 [astro-ph.CO].

Yang, Yujin, Ann I. Zabludoff, Dennis Zaritsky, Tod R. Lauer, and J. Christopher Mihos. 2004. "E+A Galaxies and the Formation of Early-Type Galaxies at z~0." *ApJ* 607, no. 1 (May): 258–273. doi:10.1086/383259. arXiv: astro-ph/0402062 [astro-ph].

Yang, Yujin, Ann I. Zabludoff, Dennis Zaritsky, and J. Christopher Mihos. 2008. "The Detailed Evolution of E+A Galaxies into Early Types." *ApJ* 688, no. 2 (December): 945–971. doi:10.1086/591656. arXiv: 0801.1190 [astro-ph].

Yeager, Travis R., and Curtis Struck. 2020. "Splash bridge models of inclined, gas-rich, direct galaxy collisions." *MNRAS* 492, no. 4 (March): 4892–4916. doi:10.1093/mnras/staa121. arXiv: 2001.03795 [astro-ph.GA].

York, Donald G., J. Adelman, Jr. Anderson John E., Scott F. Anderson, James Annis, Neta A. Bahcall, J. A. Bakken, et al. 2000. "The Sloan Digital Sky Survey: Technical Summary." *AJ* 120, no. 3 (September): 1579–1587. doi:10.1086/301513. arXiv: astro-ph/0006396 [astro-ph].

Zabludoff, Ann I., Dennis Zaritsky, Huan Lin, Douglas Tucker, Yasuhiro Hashimoto, Stephen A. Shectman, Augustus Oemler, and Robert P. Kirshner. 1996. "The Environment of "E+A" Galaxies." *ApJ* 466 (July): 104. doi:10.1086/177495. arXiv: astro-ph/9512058 [astro-ph].

Zahid, H. Jabran, and Margaret J. Geller. 2017. "Velocity Dispersion, Size, Sérsic Index, and D $_n$4000: The Scaling of Stellar Mass with Dynamical Mass for Quiescent Galaxies." *ApJ* 841, no. 1, 32 (May): 32. doi:10.3847/1538-4357/aa7056. arXiv: 1701.01350 [astro-ph.GA].

Zhu, Ming, Yu Gao, E. R. Seaquist, and Loretta Dunne. 2007. "Gas and Dust in the Taffy Galaxies: UGC 12914/15." *AJ* 134, no. 1 (July): 118–134. doi:10.1086/517996. arXiv: astro-ph/0703200 [astro-ph].

APPENDIX A

ERRORS ON THE D4000 MEASUREMENT

We use a simple trapezoidal rule to estimate the definite integrals to measure the continuum flux within the two bandpasses employed in the measure of D4000. The error on the D4000 measurement is obtained analytically using equation A.2, where f_- and f_+ are the measurements of integrated flux in the bluer and red bandpasses in the definition of D4000, respectively. The flux measurements, f_- and f_+, are given by equations A.3 and A.4, respectively, and σ_- and σ_+ are their respective errors which are given by equations A.5 and A.6. In the equations below, f_λ and σ_λ are the values of the flux and its corresponding error respectively at the stated λ:

$$\mathrm{D4000} = \frac{f_+}{f_-} \tag{A.1}$$

$$\sigma_{\mathrm{D4000}} = \frac{1}{f_-^2}\sqrt{\sigma_+^2\, f_-^2 \;+\; \sigma_-^2\, f_+^2} \tag{A.2}$$

$$f_- = \frac{(3950-3750)}{2N_-}\left(f_{3750} + f_{3950} + 2\, f_{\Sigma_-}\right) \tag{A.3}$$

$$f_+ = \frac{(4250-4050)}{2N_+}\left(f_{4050} + f_{4250} + 2\, f_{\Sigma_+}\right) \tag{A.4}$$

$$\sigma_- = \sqrt{\frac{(3950-3750)^2}{(2N_-)^2}\left(\sigma_{3750}^2 + \sigma_{3950}^2 + 4\,\sigma_{\Sigma_-}^2\right)} \tag{A.5}$$

$$\sigma_+ = \sqrt{\frac{(4250-4050)^2}{(2N_+)^2}\left(\sigma_{4050}^2 + \sigma_{4250}^2 + 4\,\sigma_{\Sigma_+}^2\right)} \tag{A.6}$$

In the above equations, there are N_-+1 and N_++1 spectral points in the blue and red wavelength intervals, respectively, over which the continuum flux is measured. In most spectra, where a flux measurement at the exact wavelengths of the bandpass limits did not exist, we used a simple linear interpolation to compute the flux measurement at the exact wavelength, using the flux measurements on either side of it. These flux points are referenced by their exact wavelengths in the above equations, i.e. f_{3750}, f_{3950}, f_{4050}, f_{4250}. Also, f_{Σ_-} and f_{Σ_+} are flux measurements excluding the end points in the blue and red wavelength intervals, respectively.

APPENDIX B

NET SPECTRAL SIGNIFICANCE

The Net Spectral Significance ($\mathcal{N}$) is a way of measuring the amount of useful information in a spectrum (N. Pirzkal et al. 2004). It is defined as the maximum cumulative signal to noise ratio (SNR) in a spectrum.

The Net Spectral Significance is measured in the following way. The SNR at each flux point is measured and then sorted in descending order. This sorted array is used to create signal and noise arrays, with the first element in these arrays corresponding to the signal and noise from the highest SNR point in the spectrum. The second element in the signal array would then be the sum of the signals from the point with the highest SNR and the point with the second-highest SNR. The second element in the noise array are the noise values summed in quadrature for the same two points. The rest of the arrays are filled similarly.

The signal and noise arrays are divided element-wise to make the final cumulative SNR array (shown in Eq. B.1 as a sequence). The Net Spectral Significance is then the maximum value in this cumulative SNR array.

$$\text{Cumulative SNR} : \frac{S_1}{\sqrt{N_1^2}}, \frac{S_1+S_2}{\sqrt{N_1^2+N_2^2}}, \frac{S_1+S_2+S_3}{\sqrt{N_1^2+N_2^2+N_3^2}}, \text{etc} \ldots \tag{B.1}$$

$$\mathcal{N} = \max\left(\text{Cumulative SNR}\right) \tag{B.2}$$

APPENDIX C

COVARIANCE MATRIX ESTIMATION

The covariance matrix is estimated using a squared exponential kernel (see for example the brief pedagogical introduction given by Gibson et al. 2012, appendix A1). We estimate individual elements of the inverse of the covariance matrix directly. The 'ij'th element of the inverse of the covariance matrix 'C^{-1}' is given by,

$$\mathrm{C}_{\mathrm{ij}}^{-1} = \delta_{\mathrm{ij}} \frac{1}{\sigma_{\mathrm{ij}}^2} + (1 - \delta_{\mathrm{ij}}) \frac{1}{\theta_0} \exp\left(-\frac{(\lambda_{\mathrm{i}} - \lambda_{\mathrm{j}})^2}{2\,\mathcal{L}^2} \right). \tag{C.1}$$

In the above equation, θ_0 is the maximum covariance which is used as a normalization constant. We simply used the square of the maximum of errors on all flux points within a given spectrum. The effective correlation length is given by $\mathcal{L}$, and depends on the galaxy size along the dispersion direction. The wavelength corresponding to the 'i'th flux point and the variance on the data is given by λ_i and σ_{ii}^2, respectively. Here δ_{ij} is the Kronecker delta function which populates elements only on the diagonal of the matrix. In the ideal case of each grism data point being completely uncorrelated to any other data point in the grism spectrum, the inverse of the covariance matrix is a diagonal matrix containing only the reciprocals of the variances on the individual data points.

To arrive at the effective correlation length, $\mathcal{L}$, we fit the measured LSF of each galaxy with a Gaussian and set $\mathcal{L} = 3\,\sigma_{LSF}$, where σ_{LSF} is the best-fit Gaussian standard deviation for the LSF. This takes into account the correlation induced by the morphology of each galaxy along the dispersion direction. The above measure of the effective correlation length essentially indicates that the data becomes uncorrelated $\pm 3\,\sigma_{LSF}$ away from any individual data point in the grism spectrum.

Below we provide a short derivation for the vertical scaling factor given in equation 3.5. The χ^2 statistic is defined by $\chi^2 = (F - \alpha M)^T\, C^{-1}\, (F - \alpha M)$ which can be written as,

$$\chi^2 = \sum_{ij}^{N} (F_i - \alpha M_i)\, (F_j - \alpha M_j) \left(\frac{1}{\sigma_{ij}^2} \right). \tag{C.2}$$

In the above equation, the 'i'th flux and model elements are denoted by F_i and M_i, respectively. The 'ij'th element of C^{-1} is denoted by $1/\sigma_{ij}^2$ which is the result of evaluating equation C.1. For example, $C_{11}^{-1} = 1/\sigma_{11}^2$ where σ_{11}^2 is the variance on the 'i'th flux point and $C_{12}^{-1} = 1/\sigma_{12}^2 = (1/\theta_0) \exp(-(\lambda_1 - \lambda_2)^2/(2\,\mathcal{L}))$. The size of the flux and model vectors is 'N' elements and the size of C^{-1} is N × N. We can now evaluate,

$$\frac{\partial \chi^2}{\partial \alpha} = \sum_{ij}^{N} \left(\frac{1}{\sigma_{ij}^2} \right) \left[(F_i - \alpha M_i)\,. - M_j + (F_j - \alpha M_j)\,. - M_i \right] = 0, \tag{C.3}$$

for the α that minimizes χ^2. This then gives us,

$$\sum_{ij}^{N} \left(\frac{1}{\sigma_{ij}^2} \right) \left[-F_i M_j - F_j M_i + 2\alpha M_i M_j \right] = 0. \tag{C.4}$$

Which directly leads to the α given by equation 3.5.